Special Applications and Advanced Techniques for

Crack Size Determination

John J. Ruschau
and
J. Keith Donald,
editors

ASTM
STP 1251

STP 1251

Special Applications and Advanced Techniques for Crack Size Determination

John J. Ruschau and J. Keith Donald, editors

ASTM Publication Code Number (PCN)
04-012510-30

ASTM
1916 Race Street
Philadelphia, PA 19103
Printed in the U.S.A.

Library of Congress Cataloging-in-Publication Data

Symposium on Special Applications and Advanced Techniques for Crack Size Determination (1993: Atlanta, Ga.)
Special applications and advanced techniques for crack size determination/John J. Ruschau and J. Keith Donald, editors.
(STP; 1251)
"ASTM publication code number (PCN) 04-012510-30."
Includes bibliographical references.
ISBN 0-8031-2003-6
1. Metals—Cracking—Measurement—Congresses. 2. Fracture mechanics—Congresses. 3. Measuring instruments—Congresses.
I. Ruschau, John J., 1950– . II. Donald, J. Keith, 1949–
III. Title. IV. Series: ASTM special technical publication; 1251.
TA460.S9393 1995
620.1'126—dc20 94-49349
CIP

Photocopy Rights

Peer Review Policy

Each paper published in this volume was evaluated by three peer reviewers. The authors addressed all of the reviewers' comments to the satisfaction of both the technical editor(s) and the ASTM Committee on Publications.

The quality of the papers in this publication reflects not only the obvious efforts of the authors and the technical editor(s), but also the work of these peer reviewers. The ASTM Committee on Publications acknowledges with appreciation their dedication and contribution to time and effort on behalf of ASTM.

Printed in Ann Arbor, MI
April 1995

Foreword

The symposium on Special Applications and Advanced Techniques for Crack Size Determination was held in Atlanta, Georgia, on 19 May 1993. ASTM Committee E8 on Fatigue and Fracture sponsored the symposium. J. J. Ruschau, University of Dayton Research Institute, Dayton, Ohio, and J. K. Donald, Fracture Technology Associates, Bethlehem, Pennsylvania, presided as symposium chairmen and are editors of this publication.

Contents

Overview

In the past four decades, the field of fracture mechanics has transitioned from a fundamental research topic to a mature, engineering discipline. Begun with the work by Griffith on glass and later extended to metals by Irwin, engineers today are equipped with the tools and techniques to characterize the behavior of cracks for a majority of structural materials and service conditions. Methodologies have been developed by researchers to model fracture in linear-elastic, elastic-plastic, and viscoelastic/viscoplastic materials and conditions. Regardless of the method used, however, the fundamental ingredients required to properly characterize fracture behavior are the stress state and crack size. With the increasing availability of analytical tools such as finite element analysis, engineers can describe the stress on a component with excellent accuracy. Likewise for the experimentalist tasked with empirically characterizing fracture related properties of materials, test equipment has matured to the point that loading conditions on a component or specimen can be determined accurately and maintained to well within a percentage of desired conditions. However, the ability to accurately measure crack size and similarly crack extensions in the range of tens of microns often remains a formidable task, even for the most experienced researcher.

Historically, crack size measurements for most test applications began with visual examination of the specimen under test. Situations quickly arose, however, where such visual measurements were either inaccurate or impractical, forcing researchers to develop nonvisual means for determining crack size. Refinements in automated crack size methodology have evolved over the years to include the now commonly employed compliance and electric potential difference techniques. These methods, though pioneered years ago, have been incorporated eventually into the ASTM standards for crack size determination under fatigue (E 647), static (E 1457), and quasi-static (E 813 and E 1152) loading conditions, just to name a few. Though such procedures are carefully outlined for a majority of standardized tests, unique situations or materials or both often require the experimentalist to modify or devise new procedures for the precise measurement of crack size.

Sensing the need of researchers to keep abreast of continual improvements, as well as providing a better understanding of existing methods for crack measurement techniques, the ASTM Committee on Fatigue and Fracture (E8) sponsored a one-day symposium in Atlanta, Georgia, on 19 May 1993 to review a number of unique applications and advanced techniques that researchers are currently employing for crack size determination. Information presented at the symposium and included in this volume should prove useful to the most experienced experimentalist as well as those less familiar with such nonvisual approaches. Methods are described for the measurement of surface crack size, multiple site cracking, and cracking under nonisothermal conditions using AC potential difference procedures. Influences of crack deflection and crack splitting on DC potential calibrations are discussed. Compliance techniques using a laser micrometer, as well as a load-ratio method for predicting crack size, are described for standard laboratory test specimens. Ultrasonic methods for crack measurement are presented for situations involving specimens containing large closure regions, metal matrix composites, and the in situ measurement of crack size and crack opening parameters during actual testing conditions. Finally, a novel approach using an AC magnetic bridge device for quantifying crack size in aluminum specimens is described in detail.

The editors would like to express their sincere appreciation first to all the authors and co-authors for their valuable time in both preparing the presentations as well as the formal papers that comprise this publication; to the reviewers whose high degree of professionalism and timely response ensure the quality of this publication; and to all the attendees for their open and often fruitful participation at the symposium. The editors also wish to express their appreciation to the ASTM symposium planning and publications staff for their assistance in setting up the symposium and preparing this special technical publication.

John J. Ruschau

University of Dayton Research Institute,
Dayton, OH 45469-0136;
symposium chairman and coeditor.

J. Keith Donald

Fracture Technology Associates,
Bethlehem, PA 18015;
symposium cochairman and coeditor.

Mark P. Connolly[1]

The Measurement of Regular and Irregular Surface Cracks Using the Alternating Current Potential Difference Technique

REFERENCE: Connolly, M. P., **"The Measurement of Regular and Irregular Surface Cracks Using the Alternating Current Potential Difference Technique,"** *Special Applications and Advanced Techniques for Crack Size Determination, ASTM STP 1251,* J. J. Ruschau and J. K. Donald, Eds., American Society for Testing and Materials, Philadelphia, 1995, pp. 3–16.

ABSTRACT: The alternating current (AC) potential difference technique for measuring the growth of regular and irregular surface cracks is described. This technique is based on injecting high frequency alternating current into the metal specimen and measuring the change in voltage on the surface produced by the presence of a crack. The high frequency current tends to flow in a thin layer of the metal surface; therefore, low currents are required to produce measurable voltages on the specimen surface. Although AC techniques are increasingly employed for the measurement of surface cracks, one of the difficulties with the approach is the problem of interpreting the measured data in terms of crack shape and size. The objective of this paper is to present an inversion algorithm that can be used to determine the shape and size of surface cracks from measurements of the surfaces' voltage. This inversion algorithm is based on a model of the electromagnetic field problem, and the algorithm enables the voltage data obtained from measurements in the crack region to be interpreted directly in terms of the crack shape and size. Examples of the application of the inversion algorithm to the interpretation of voltage measurements obtained from a single semielliptical and two semielliptical intersecting surface cracks are described.

KEYWORDS: nondestructive evaluation, surface cracks, alternating current, potential difference, alternating current potential difference (ACPD), inversion

Many fatigue failures in engineering structures are due to the growth of surface cracks. These cracks may initiate either from localized stress concentrations or alternatively from preexisting manufacturing defects. In order to conduct a remaining life assessment of surface cracks, nondestructive evaluation (NDE) techniques to size the crack must be used in tandem with a fracture mechanics analysis. The fracture mechanics approach to the analysis of surface cracks is reasonably well established as a result of the many stress intensity factor solutions available for the surface crack, such as the solution given by Newman and Raju [*1*]. The measurement of surface cracks is more problematic since no general techniques are available to measure both the size and shape of surface cracks. Common practice is to measure the surface length and to infer the crack depth from an assumed crack aspect ratio.

A further advantage of surface crack measurement techniques is the ability to conduct laboratory crack growth rate tests on surface cracks in the actual service environment. This is particularly important for applications where environmental effects may exist that can

[1] Senior research engineer, Southwest Research Institute, P. O. Drawer 28510, San Antonio, TX 78228-0510.

result in interactions with the surface crack. These interactions, such as crack closure effects due to corrosion debris, may not be manifested from tests conducted on specimens with through-thickness cracks. Consequently, for these situations the crack growth rate data obtained from the through-thickness tests may not represent crack growth rates experienced by surface cracks in service.

Electric potential techniques have been used to measure the size and growth of surface cracks in metals and these electric techniques can be subdivided into either direct or alternating current methods. One promising technique called the alternating current potential difference (ACPD) method is described here, and has been adopted for the measurement of the depth and length of surface cracks [*2*]. This technique was pioneered by Dover et al. [*3*] in the United Kingdom and numerous papers have been published describing both the theory [*4–6*] and experimental applications [*7,8*] of the technique. The objective of this paper is to describe the application of the AC potential difference technique to the measurement of both regular and irregular surface cracks. The regular cracks correspond to semielliptical surface cracks and the irregular cracks correspond to two intersecting semielliptical surface cracks.

The Alternating Current Potential Difference (ACPD) Technique

The alternating current potential difference technique is based on applying high frequency alternating current (3 to 100 kHz) to the specimen and measuring the surface voltages. This high frequency alternating current tends to flow in a thin skin along the metal surface. This "skin effect" produces a higher resistive effect as compared to DC potential difference techniques, and consequently much lower currents are required to produce a measurable voltage on the specimen surface. The so-called skin depth, δ, is dependent on the permeability μ and the conductivity σ of the metal and the frequency of the alternating current f and is given in Ref *3* as

$$\delta = \frac{1}{\sqrt{\pi\mu\sigma f}} \tag{1}$$

For the ferromagnetic mild steel considered here, an AC frequency of 5 kHz gives a skin depth of about 0.1 mm, but for nonmagnetic materials such as stainless steel or nickel the skin depth at 5 kHz can range from 1 to 20 mm. For the ferromagnetic mild steels used here the skin-depths are typically on a scale smaller than the crack depth and the thin-skin modeling theory described in Ref *3* will be used.

The basis of the ACPD crack measurement technique can be illustrated by means of the example shown in Fig. 1. Consider an infinite plate containing an infinitely long surface crack of uniform depth a as shown in the figure. The current is injected through point I_1 and flows along the metal surface, down and up the crack, and out through point I_2. The procedure commonly used to determine the crack depth in this case is shown in the figure. The voltage difference is measured by a probe whose contacts form a gap of length Δ; when placed near the crack at position ST, it gives a voltage difference V_1, and when across the crack at position $S'T'$ it gives a voltage difference V_2. Since V_1 is proportional to Δ and V_2 is proportional to $\Delta + 2a$ ($2a$ since the current has to flow up and down the crack), then the crack depth a can be obtained from the ratio of the two voltages and is given as

$$a = \left(\frac{V_2}{V_1} - 1\right)\frac{\Delta}{2} \tag{2}$$

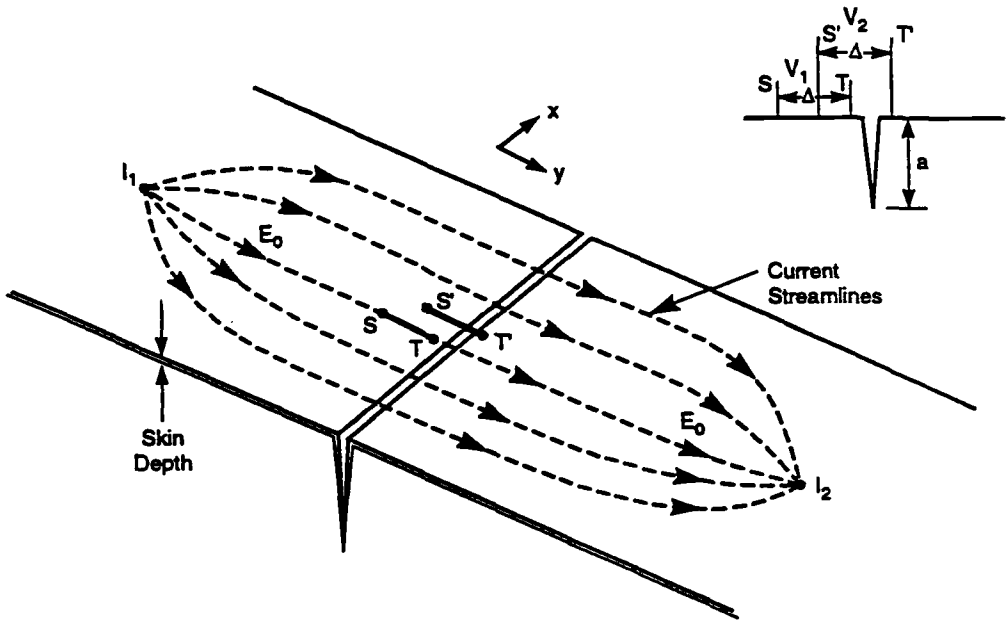

FIG. 1—*Schematic diagram illustrating the measurement of surface cracks using the ACPD technique. For the case shown the crack is of depth* a *in a uniform field which is created by injecting current into the specimen at* I_1 *which flows out at* I_2.

A key feature of this equation is that no prior calibration is required. Equation 2 is known as the one-dimensional interpretation of the crack depth and is exact in the case of an infinitely long surface crack of uniform depth in a uniform field, but it can also be applied with small error to shallow surface cracks, with large aspect ratios, in plates of finite width. A useful analogy in understanding the current flow is the concept of fluid flow, since there is a direct correspondence between fluid and current flow. In the one-dimensional case shown in Fig. 1 the fluid streamlines are straight and parallel everywhere and are a function of y only. Consequently for this situation, Eq 2 is exact.

For the more practical case of surface cracks with smaller aspects ratios, Eq 2 does not apply and can produce a serious underestimate of the crack depth. This is due to the fact that for larger aspect ratio cracks, such as thumbnail, the current flow is no longer a simple function of y. For this case, as the current streamlines approach the crack they will diverge in the x-direction. Consequently, both the current and corresponding voltages are functions of both x and y, and the interpretation of the measured voltages in terms of crack size and shape cannot be accomplished using the simple relationship given by Eq 2. This is a class of the general inversion problem where it is required to find the size and shape of flaws by analysis of the field scattering produced by them. An algorithm is described here that is used to solve this inversion problem for the cases of both regular and irregular surface cracks and is based on a detailed analysis developed in Ref *9*. Prior to outlining the approach in detail, an instrument is described which has been used here to perform the ACPD measurements.

The ACPD measurements were performed using a commercially available instrument [*10*], that provides a current source to give the appropriate current magnitude and stability at the

chosen and adjustable frequency. It also contains a voltage measurement circuit that includes a synchronous rectifier circuit phase locked to the current and capable of measuring the small voltages on the specimen surface. This instrument was used to obtain the voltage measurements on the specimen surface—the theoretical algorithm used to interpret these measured voltages is now described.

Formulation of Inversion Algorithm

The inversion algorithm has been described in a recent paper [*9*] and will only be summarized here. The basis of the approach is that for thin-skin situations, the problem can be modelled in terms of a plane Laplacian field for which the following equation holds

$$\nabla^2\phi = 0 \tag{3}$$

The potentials given by ϕ are directly analogous to the measured voltages represented by V_1 and V_2 in Fig. 1. It has been shown in Ref *3* that for thin-skin situations such as those considered here, the problem can be reduced to a two-dimensional potential problem in the domain formed by conceptually "unfolding" the crack plane so that it becomes coplanar with the metal surface as shown in Fig. 2. This is the approach that was developed by Collins et al. [*4*] and has been used to solve a variety of field problems in ACPD. Using this technique it is relatively straightforward to solve the forward problem wherein the crack shape and size are known and the potentials on the surface are required. Standard techniques such as Fourier analysis, finite difference, or even finite element methods can be used.

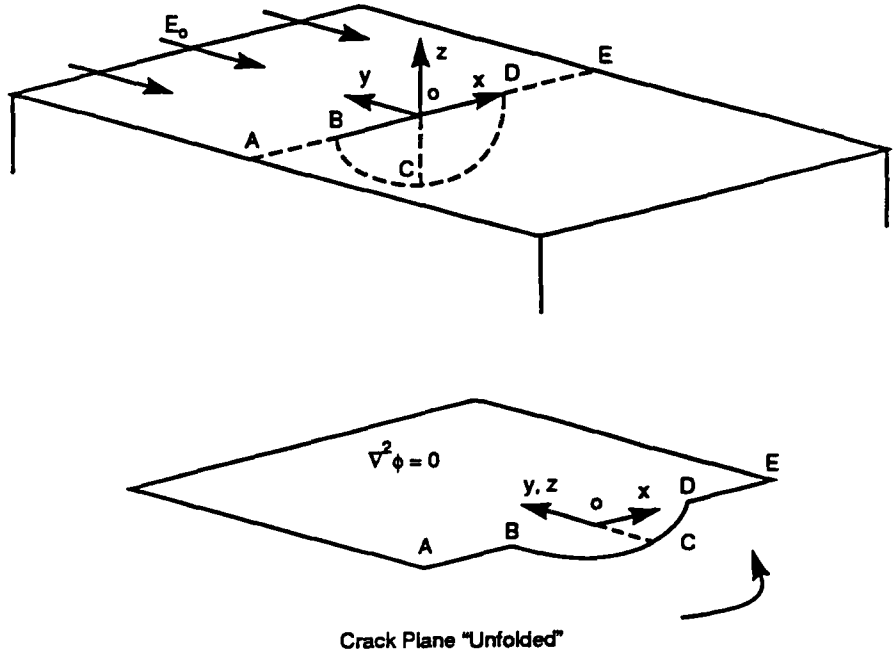

FIG. 2—*Schematic diagram showing unfolding of the crack problem in order to produce the plane potential problem.*

However, in practice it is the surface voltages, and corresponding potentials, that are known, and it is required to determine the crack shape and size. This is known as the inverse problem and is represented in Fig. 3 where the crack boundary R, given by the line BCD is unknown. Obtaining a solution to the inverse problem requires solving Laplace's equation given by Eq 3, subject to the boundary conditions that are shown in Fig. 3. The square region in Fig. 3 is the metal surface for which voltages and corresponding potentials are measured. The edge $ABCDE$ is a line of symmetry for this problem, and from potential theory the potentials ϕ can be arbitrarily set to zero along this edge. Far from the crack edges the field becomes uniformly distributed so $\phi = E_0 y$ as $y \rightarrow \infty$.

For practical crack measurement the voltages are obtained normally at a number of discrete points along the length of the crack. An example of typical voltage readings taken on a semielliptical surface crack are shown in Fig. 4. These voltage readings correspond to those taken by a probe straddling the crack as shown in Fig. 1, and traversing along the crack in the x direction. These results clearly show the influence of the crack on the voltage readings on the metal surface where a large increase in the voltages is obtained as the probe moves from the crack edge to the central and deepest point of the crack. The voltages in Fig. 4 represents the amplified and conditioned output from the ACPD instrument. To incorporate these voltages into the field problem shown in Fig. 3 they must first be converted to potentials ϕ, and this is accomplished by taking a reading of the voltage upstream from the crack, termed V_1, with a probe of spacing Δ, and using the relationship $V_1 = E_0\Delta$ in order to determine the unknown scaling term E_0. All of the voltages measured in Fig. 4 are divided by this scaling term in order to obtain the corresponding potentials ϕ, and it is these potentials taken at different points which are shown schematically by ϕ_i in Fig. 3.

Before the inversion algorithm is described, supplemental information is also required on the length of the crack in order to fix the points B and D in Fig. 3. Fixing the crack ends

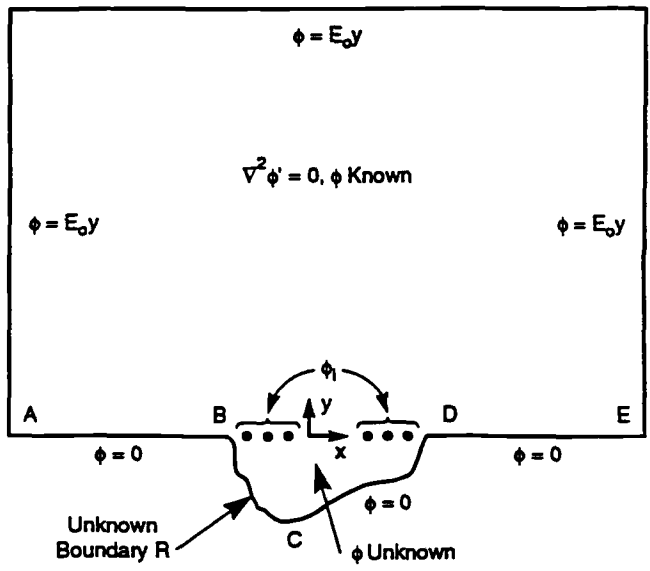

FIG. 3—*Representation of the inversion problem. The square region corresponds to the metal surface. The potentials given by* ϕ_i *corresponds to the measured voltages. The solution of the inverse problem requires determining the unknown boundary* BCD *which is compatible with the other boundary condition and the measured potentials.*

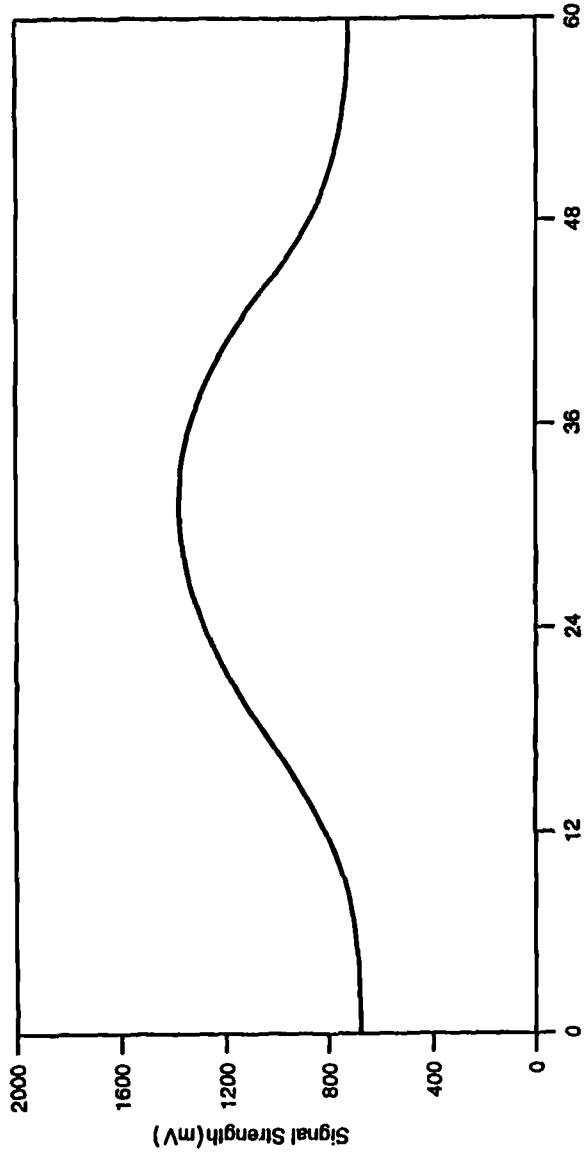

FIG. 4—*Examples of the measured voltage output from ACPD instrument for the case of scan performed along the length of a semielliptical surface crack.*

enforces an important limitation on the solution—otherwise the inversion of the surface potentials to determine the crack size and shape would not be feasible. The crack ends *B* and *D* can be obtained either from optical measurements or from other NDE techniques or can also be determined from the voltage measurements in Fig. 4 where the slope of the voltage readings can be related to the crack ends, and this was the approach that was used in Ref *2*. In this paper the crack length was determined from an optical microscope mounted on a vernier scale.

An algorithm is now described which enables the crack shape to be determined from the measured surface voltages. The steps in the algorithm are as follows:

1. Obtain voltage measurements both across the crack as shown in Fig. 4 and also upstream from the crack.
2. Convert these voltage readings to absolute potential values ϕ_i along the edge *BD* in Fig. 3.
3. Assume a starting crack shape by applying the one dimensional solution given by Eq 2 to each of the potentials ϕ_i along the crack edge.
4. Solve the boundary value problem with the assumed crack shape obtained from Step 3 to compute the potentials along *BD*. Boundary element methods were used here although finite element or finite difference techniques can also be used.
5. Compare these computed potentials with the measured potentials and then update the crack shape.
6. Repeat the process until the difference between the measured and computed potential are negligible. The crack shape now corresponds to the solution of the inverse problem.

Although the above algorithm is relatively straightforward, the implementation of the algorithm is slightly more involved. This is due to the fact that at the crack ends *B* and *D* in Fig. 3 the potentials are singular. The implication of these singularities at *B* and *D* for practical crack measurement is that the crack shape near the ends is very sensitive to measurements near these points. In fact, in mathematical terms the problem at these locations is referred to as ill-posed where small changes in the input data can result in large changes in the crack shape. In order to overcome this problem, the algorithm given previously incorporates the important feature wherein the field problem in Fig. 3 is transformed from a Cartesian to a bipolar coordinate system, since the crack problem is solved more easily in bipolar (α, β) coordinates. This transformation is accomplished by applying the following equation between points in the (x, y) and (α, β) plane

$$x = \frac{(c \sinh \alpha)}{d} \qquad y = \frac{(c \sin \beta)}{d} \tag{4}$$

where $d = \cosh \alpha + \cos \beta$ and $2c$ is the crack surface length. This transformation is shown in Fig. 5 where the x, y plane is transformed to the α, β plane. The key point from this figure is the mapping of the crack ends *B* and *D* to infinity. Consequently, the singular regions around *B* and *D* are not included in the inversion algorithm. The lines $\alpha = C_1$ and $\alpha = C_2$ in Fig. 5 correspond to circular regions around the singular points *B* and *D* where the potential is determined by the singular behavior in this region. The line $\beta = -\pi/2$ in Fig. 5 corresponds to a semicircular crack and $\beta = \pi$ corresponds to the far field in (x, y) where the field is uniform. As shown in Fig. 5, it is advantageous to formulate the field problem in terms of the dependent variable ϕ^1 where $\phi^1 = \phi - E_0 y$ is the perturbation potential, as

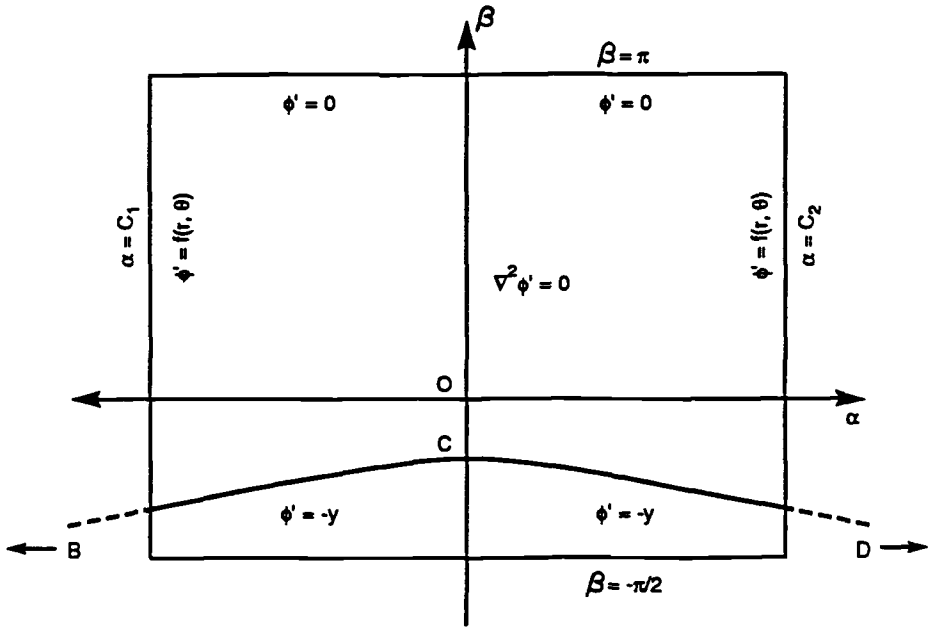

FIG. 5—*Conversion of the field problem from Cartesian to bipolar coordinates.*

this representation results in more convenient computations when transformed to the bipolar (α, β) plane.

The algorithm was implemented in a FORTRAN computer program on a Microvax computer. This program is capable of operating directly on the measured surface voltages and converting them to a final crack shape. In order to demonstrate the utility of this algorithm we consider the case of a semicircular crack for which the potentials to the forward problem are known exactly from a closed form solution to this problem given in Ref *11*. These potentials were input to the program and the objective was to determine if the algorithm was capable of recovering the semicircular crack shape. Nineteen values of the potential along the x-axis from both crack ends were used as input to the program. Stages in the iterative process for the semicircular crack in the (x, y) and (α, β) planes are shown in Fig. 6 which shows that after four iterations the crack shape is close to the semicircular crack. The iteration stops when the difference between the computed and measured potential is less than 1×10^{-4}. The number of iterations required for the semicircular crack was 10 and the final crack depth predictions are given in Table 1. Table 1 shows that the predictions of the crack depth are, in all cases, within 0.3% of the exact value. We now consider the more practical cases of measurements obtained from tests conducted on actual cracks.

Experimental Measurements on Surface Cracks

Experiments were conducted on two sets of surface cracks. The first case considered is a semielliptical surface crack. The second case considered is intersecting semielliptical surface cracks.

The semielliptical surface crack was obtained by machining a small starter notch and subjecting the specimen to alternating stress cycles so that the cracks grew from the notch

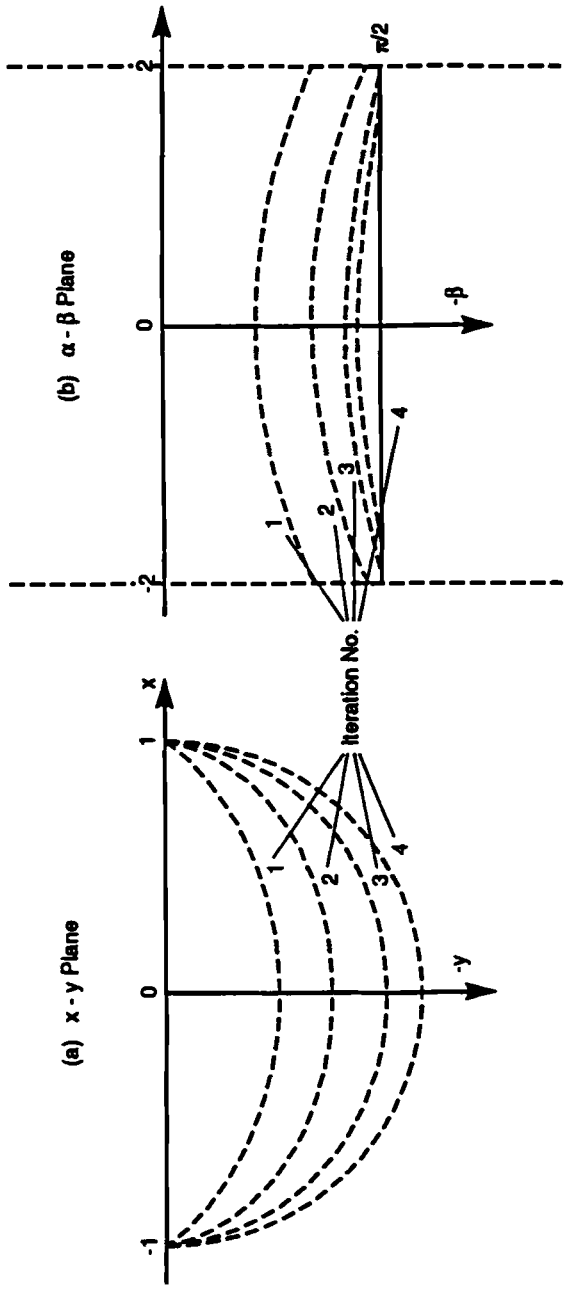

FIG. 6—*Illustration of the inversion technique for a semi-circular crack in the Cartesian* (x, y) *and the bipolar* (α, β) *planes. Figure shows that after four iterations the algorithm has almost fully recovered the semicircular crack shape.*

TABLE 1—*Comparison for the exact and computed crack depths for a semicircular crack.*

Semicircular $a/c = 1.0$		
x	Exact Depth	Computed Depth
1.0	0.0	0.0
0.9	0.435	0.435
0.8	0.600	0.600
0.7	0.714	0.714
0.6	0.800	0.800
0.5	0.866	0.867
0.4	0.916	0.918
0.3	0.953	0.956
0.2	0.979	0.982
0.1	0.995	0.997
0.0	1.000	1.003

by the process of fatigue crack growth. The specimens were tested in tension with a R-ratio of 0 and a cyclic frequency of 1 Hz. In order to obtain the desired crack geometry, the starter notch was machined to a circular arc shape so that the crack grew to the desired semielliptical crack shape. The specimens were machined from BS 4360 50D mild steel plates. The plates were 80 mm wide, 12 mm thick, and 250 mm long, and the starter notch was machined midway along the length of the specimen. The experimental arrangement used to measure the surface voltages is shown schematically in Fig. 7. The specimen was placed under an x-y table. A probe was attached to the table which was controlled by stepper motors under computer control. This enabled the probe to be moved to any x and y position on the specimen surface. An ACPD instrument was used to supply the high frequency alternating current and to measure the small voltages on the metal surface detected by the probe. The current was injected at the ends of the specimen by means of magnets at locations shown in Fig. 7. The crack measurements were obtained by a probe with a 5.4 mm spacing that straddled the crack and a typical example of the surface voltages is shown in Fig. 4. The data shown in the figure represent actual measured voltages; because the probes were controlled by a stepper motor at very small intervals, the data form a continuous curve. In this figure the probe readings V taken at each point correspond to the cross crack voltage V_2. A voltage reading was also taken of the upstream voltage, known here as V_1, and this voltage reading was used to obtain the scaling term E_0. All of the cross crack voltages V_2 were scaled by dividing them by this E_0 term. Optical readings were also taken to determine the surface crack length $2c$, which was used to normalize the crack length to the range of $-1 < x < 1$, and all the other dimensions were scaled according to this dimension.

After the measurements had been performed, the specimens were destructively sectioned and the actual crack shape was compared with the predicted crack shape. This comparison is shown in Fig. 8. In this case, 13 iterations were required for the results to converge, and it is clear from this figure that the inversion algorithm produces a significant improvement on the one-dimensional solution and predicts the actual crack shape quite well. It is for these cases that the inversion algorithm is particularly well suited. We now consider the case of the measurement of intersecting surface flaws.

For the case of the intersecting surface cracks two starter notches were machined on the specimen surface. The specimen size was 80 mm wide, 12 mm thick, and 250 mm long and the starter notches were machined midway along the length of the specimen. The starter

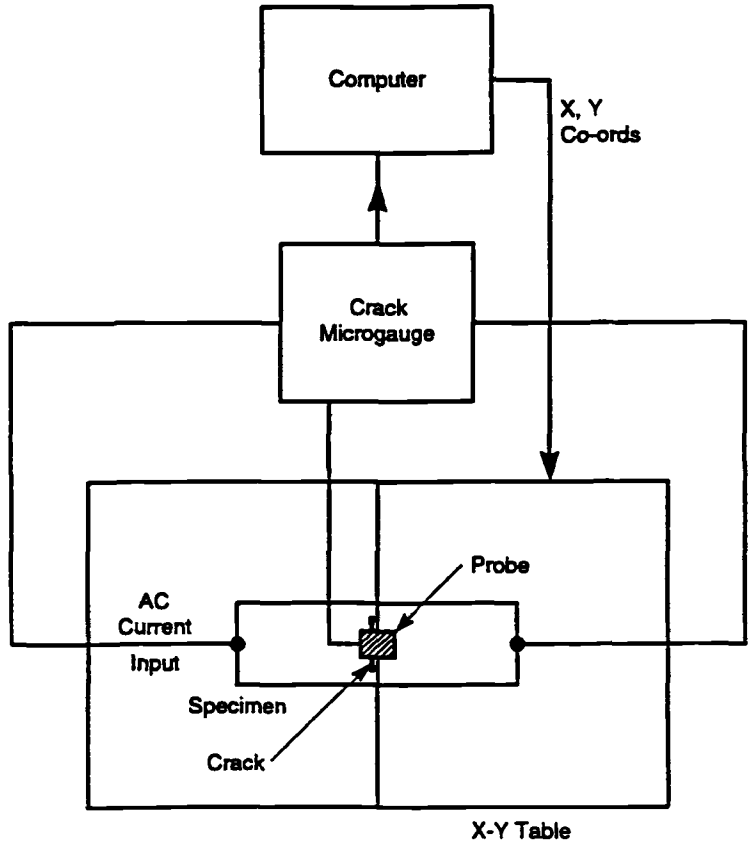

FIG. 7—*Schematic diagram of the experimental setup used to measure the surface cracks.*

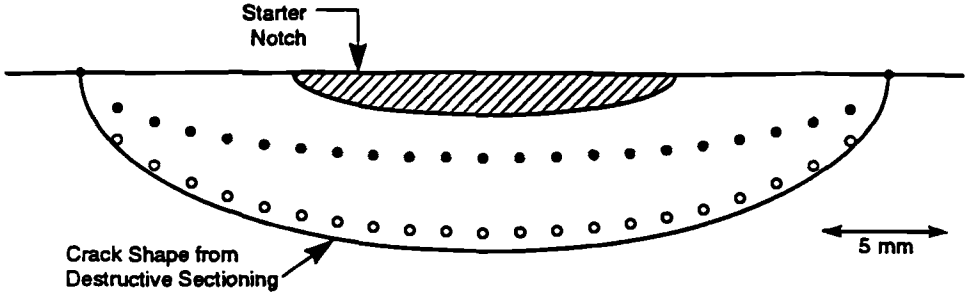

• 1-Dimensional

o Prediction Using Inversion Algorithm

FIG. 8—*Comparison between the measured and predicted crack depth showing good agreement obtained using the inversion algorithm. Also shown is the crack depth obtained from the one-dimensional prediction given by Eq 2.*

notches were 10 mm long and 1.5 mm deep and were separated from each other by a distance of 12 mm. The specimens were again subject to alternating tension-tension fatigue loading with an *R*-ratio of 0 and a frequency of 1 Hz. At periodic intervals the specimens were removed from the fatigue testing machine and were placed on the *x-y* table where an ACPD scan was performed, and the cross crack voltages at different numbers of cycles are shown in Fig. 9. The inversion algorithm was used to operate on the data shown in Fig. 9, and the resulting crack shape changes are shown in Fig. 10. Figure 10 shows that initially the two cracks grew independently, but eventually, coalesced to form one large crack. Although the crack growth behavior is not germane to this paper, a feature of this coalescence was the very rapid growth that occurred as the crack ends approached each other, and this is evident from Fig. 10 which shows very rapid growth in the region between the cracks following Scan I. The crack ends were not coplanar as they coalesced, and a small overlap occurred resulting in a small fissure on the surface as shown in Fig. 10. A comparison with the crack shape obtained from the destructive sectioning of the specimen is also shown in Fig. 10.

Figure 10 shows that for the final crack shape the agreement between the predicted and actual crack shapes is good. The presence of the small fissure is significant since it has been shown in Ref *12* that crack surface features such as fissures can produce electrical short circuits between the crack faces and anomalously low crack depth predictions. The inversion algorithm presented here is not capable of accounting for these surface contacts. Clearly, the good agreement between predicted and actual crack shapes in Fig. 10 indicates that crack face contact did not occur probably as a result of oxide formation around the fissure that prevented electrical contact between the crack faces. For the smaller crack size, before crack coalescence, the accuracy of the inversion algorithm is not known although the algorithm did reproduce differences in the size of the two cracks that is evident from the asymmetric voltage readings from Fig. 9, but that is difficult to discern from Fig. 10. For example, for the scan taken before coalescence (Scan I in Figs. 9 and 10), the maximum crack depth calculated from the inversion algorithm was 4.6 mm for crack A and 4.75 mm for crack *B*.

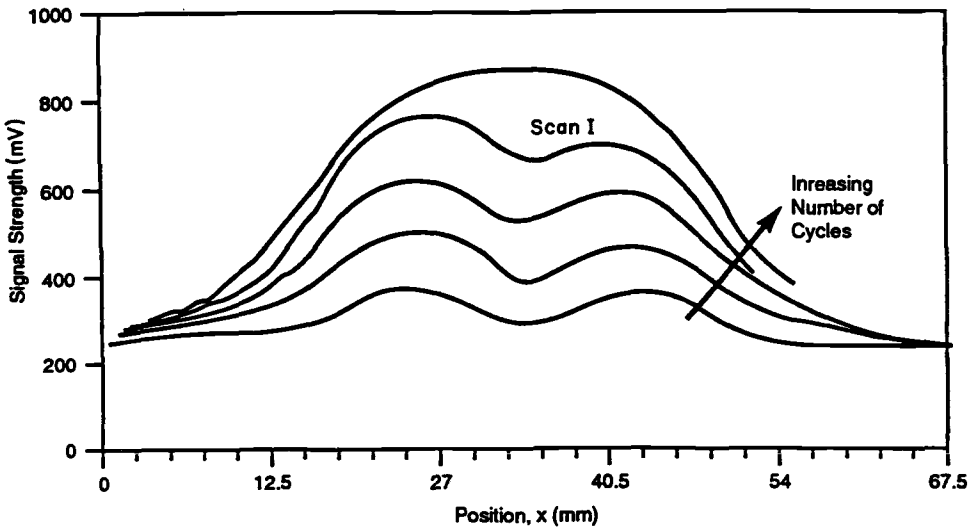

FIG. 9—*ACPD surface voltages obtained from measurements conducted on two starter notches, a distance 12 mm apart which were subject to tension-tension fatigue loading. The cracks which grew from the two notches eventually coalesced to form one large crack.*

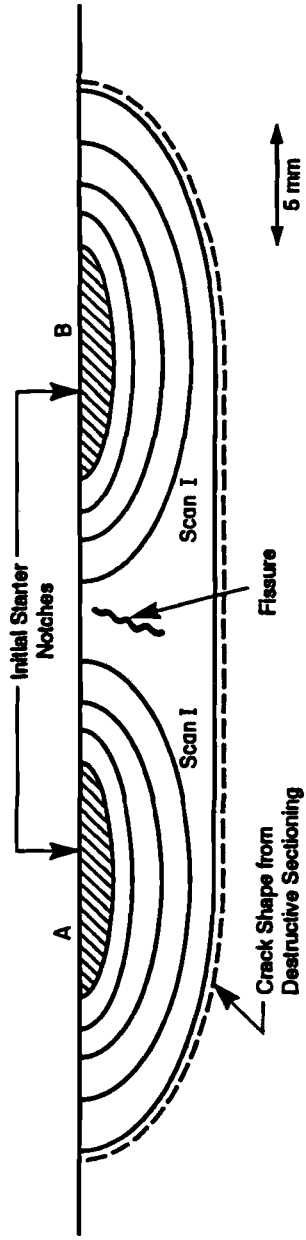

FIG. 10—*Crack shape changes for intersecting surface flaws obtained from an analysis of the ACPD data shown in Fig. 9.*

Conclusion

The preceding results have highlighted the utility of the alternating current potential difference (ACPD) technique for crack depth measurement. The work has also outlined the importance of detailed interpretation of the measured voltages in order to determine the crack depth. An inversion algorithm is described that is capable of operating on the measured surface voltages, and this inversion algorithm is used to measure the growth of both regular semielliptical and also intersecting surface flaws.

Acknowledgments

The author wishes to acknowledge the support of Professor Bill Dover and Dr. Roy Collins of University College London where the work was performed.

References

[*1*] Newman, J. C., Jr. and Raju, I. S., "An Empirical Stress Intensity Factor Equation for the Surface Crack," *Engineering Fracture Mechanics,* Vol. 15, 1981, pp. 185–192.

[*2*] Connolly, M. P. and Collins, R., "The Measurement and Analysis of Semielliptical Surface Fatigue Crack Growth," *Engineering Fracture Mechanics,* Vol. 26, No. 6, 1987, pp. 897–911.

[*3*] Dover, W. D., Collins, R., and Michael, D. H., "Review of Developments in ACPD and ACFM," *British Journal of Non-Destructive Testing,* Vol. 33, No. 3, 1991, pp. 121–127.

[*4*] Collins, R., Dover, W. D., and Michael, D. H., "The Use of AC Field Measurement for NDT," *Research Techniques in NDT,* Vol. VIII, Chapter 5, R. S. Sharpe, Ed., Academic Press, New York, 1985, pp. 211–267.

[*5*] Michael, D. H., Waechter, R. T., and Collins, R., "The Measurement of Surface Cracks in Metals Using AC Electric Fields," *Proceedings* Royal Society, A381, 1982, pp. 139–159.

[*6*] Dover, W. D., Collins, R., and Michael, D. H., "The Use of AC Field Measurements for Crack Detection and Sizing in Air and Underwater," *Philosophical Transactions* Royal Society London, A320, 1986, pp. 271–283.

[*7*] Topp, D., McGugan, J., and Dover, W. D., "Automated Inspection System for Drill String Threaded Connections Using AC Field Measurement (ACFM) Techniques," *Proceedings,* Offshore Drilling Technology Conference, Aberdeen, Nov. 1990.

[*8*] Dover, W. D., Glinka, G., and Collins, R., "Automated Crack Detection and Monitoring of Crack Shape Evolution in Tubular Welded Joints and T-Butt Welds," *Proceedings,* International Conference on NDT in Fitness for Purpose Assessments of Welded Constructions, The Welding Institute, 1984, pp. 83–90.

[*9*] Connolly, M. P., Michael, D. H., and Collins, R., "The Inversion of Surface Potential Measurements to Determine Crack Size and Shape," *Journal of Applied Physics,* Vol. 64, No. 5, 1988, pp. 2638–2647.

[*10*] Crack Microgauge Instrument, TSC Ltd., 6 Mill Square, Featherston Road, Wolverton Mill, Milton Keynes, UK.

[*11*] Collins, R., Michael, D. H., and Ranger, K. B., "The AC Field Around a Plane Semielliptical Crack in a Metal Surface," *Proceedings* 13th Symposium on Non-Destructive Evaluation, B. E. Leonard, Ed., Non-destructive Testing Information Center, San Antonio, TX, 1981, pp. 470–479.

[*12*] Haq, R., Michael, D. H., and Collins, R., "The Detection and Measurement of Overlapping Fatigue Cracks at Welded Joints by Thin-Skin Electromagnetic Fields," *Proceedings* Royal Society, London, A419, 1988, pp. 69–89.

Y. Dai,[1] *N. J. Marchand,*[2] *and M. Hongoh*[3]

Fatigue Crack Growth Measurements in TMF Testing of Titanium Alloys Using an ACPD Technique

REFERENCE: Dai, Y., Marchand, N. J., and Hongoh, M., **"Fatigue Crack Growth Measurements in TMF Testing of Titanium Alloys Using an ACPD Technique,"** *Special Applications and Advanced Techniques for Crack Size Determination, ASTM STP 1251,* J. J. Ruschau and J. K. Donald, Eds., American Society for Testing and Materials, Philadelphia, 1995, pp. 17–32.

ABSTRACT: A thermal-mechanical fatigue (TMF) testing system has been developed which is capable of studying the fatigue behaviors of gas turbine materials under simultaneous changes of temperatures and strains (or stresses). Furthermore, an advanced alternating current potential difference (ACPD) measurement technique has been developed successfully to perform on-line monitoring of fatigue crack initiation and growth in specimens tested under isothermal and TMF conditions. In this paper, the basic principles of the ACPD technique as well as all the relevant experimental procedures for performing ACPD measurements, including probe setup, choice of alternating currents (AC) and frequencies, noise rejection, data acquisition, and signal processing, are described. The linear relationship between ACPD signals and crack lengths, as well as the effects of thermal cycling on the ACPD signal, are presented and discussed. The capabilities of the TMF and ACPD systems are well illustrated by fatigue crack initiation and growth test results under isothermal and TMF conditions. These tests were performed on two titanium forgings, Ti-6Al-4V (Ti64) and Ti-6Al-2Sn-6Mo (Ti6246), respectively. Alloy Ti64 was TMF cycled between 150 and 400°C, while Ti6246 was cycled between 200 and 482°C. The resolution for detecting crack initiation at the root of notches was found to be 50 μm with 95% confidence while the resolution for crack growth was 2 μm per mV change of ACPD. An environmental assisted cracking model applied to TMF crack growth is proposed for rationalizing the data.

KEYWORDS: fatigue crack growth, crack initiation, potential difference, thermal cycling, thermal-mechanical fatigue test, titanium alloy, crack size measurement

The demand for further improvement in thrust-to-weight ratios for high performance aero-engines now requires that higher temperatures be used in all stages of the engines. As a result, titanium-based components used in fan and compressor sections of the engines are expected to sustain temperatures that were not considered in the early engine designs. These increases in temperature are accompanied by significant increases in stress which arise from the higher rotational speeds and by accelerated fatigue damage accumulation due to a more aggressive operating environment. The application of damage tolerance design (DTD) concepts to engine design and maintenance requires additional material characterization, more

[1] Stress engineer, Bombardier Inc., Canadair Group, Saint-Laurent, Quebec, Canada, H4R-1K2.
[2] Associate professor, Department of Materials Engineering, École Polytechnique, Montreal, Quebec, Canada, H3C-3A7.
[3] Stress engineer, Pratt & Whitney Canada, 1000 Marie-Victorin, Longueuil, Quebec, Canada, J4G-1A1.

analysis, and increased testing. This new situation has prompted the gas turbine manufacturers to reassess the fatigue lives of their materials and components. In particular, the lives of all components containing geometric discontinuities are being evaluated under simulated service conditions. Hence, the thermal-mechanical fatigue (TMF) tests described in this paper were devised to study material fatigue damage under varying strain (or stress) and temperature histories.

Fatigue crack size determination is essential to the study of material fatigue crack growth (FCG) behavior at elevated temperatures. Conventional direct current potential difference (DCPD) methods use constant DC currents passing through the specimen and measure the potential between the probes on either side of the crack or notch. The crack sizes are sensed through an increase in electrical resistance of the conducting material due to crack initiation and growth. However, DCPD requires relatively large current to produce a measurable potential difference. This is problematic for measuring small cracks with high resolution and can cause undesired crack tip overheating. In addition, signal compensation techniques to correct for current instability and to deal with thermal EMF (TEMF) are difficult to apply under nonisothermal test conditions [*1*].

The alternating current potential difference (ACPD) methods use high frequency currents of constant amplitude (passing through the specimen), and, as for DCPD methods, the potential difference between the probes is measured. Since the high frequency currents are self-confined in thin layers near the surface (skin depth), much higher potentials due to the high current densities can be expected with the ACPD as compared to DCPD methods. The presence of "thin skins" of current also entails that the ACPD technique is more sensitive to small cracks than DCPD methods and that changes of potential with crack depth should be more linear than with DCPD [*1*]. However, a major inconvenience of ACPD, as compared to DCPD, is that ACPD systems require complex high stability electronics. This requirement has severely limited the accuracy and thus the use of the ACPD method [*1*]. Using modern generation lock-in amplifiers and advanced phase shift detection (PSD) circuits, the accuracy and sensitivity of AC potential measurement systems have been improved vastly in the recent years.

When an alternating current (AC) is passed through a conductive material, the distribution of the electric field strength ($\hat{E}$) in the specimen obeys Maxwell's wave equations and Ohm's law. In a simplified form this behavior can be written as

$$\nabla^2\hat{E} = \mu\sigma_c \frac{\partial \hat{E}}{\partial t} \tag{1}$$

where μ is the magnetic permeability and σ_c is the conductivity of the material. Thus the potential difference (ΔV) between any two points on the surface of the specimen can be computed provided the $\hat{E}$ field is known. Unfortunately, the analytical solution for Eq 1 is only available for simple two-dimensional (2D) axisymmetric cases (that is, long cylindrical conductor). For cases such as the specimens used in this study, general analytical solutions are not available and numerical solutions are being developed [*2*]. For example, three dimensional numerical analyses of DC potential fields were performed by Ikeda [*3*]. The theoretical calibration curve for a penny-shaped crack was found in very good agreement with the experimental data. However, the analytical formulas and numerical results, which did not consider skin effects, cannot be applied to the AC potential methods.

A simplified procedure can be used to estimate the distribution of the AC electrical field when high frequencies are used. In this procedure, the depth of penetration (δ) of the field is defined as

$$\delta = \frac{1}{\sqrt{\pi f \sigma_c \mu}} \tag{2}$$

where f is the frequency of the AC. For titanium alloy Ti-6Al-4V (Ti64), the skin depth δ is estimated to be 3.7 mm for a 30 kHz current and 2.4 mm for a 100 kHz current. Although this value is much larger than that of magnetic materials such as ferritic steels, the current density at the surface of a specimen will still be much higher than that of the average values in the cross section. As mentioned already, the skin effect increases the potential difference for a given total current, and results in an increased sensitivity for detecting material damage. The sensitivity increases with increasing AC frequency as can be seen from Eq 2.

The increased sensitivity with increasing AC frequency has been demonstrated by Verpoest et al. [*4*] who performed theoretical and experimental analysis of the ACPD response of cylindrical specimens with smooth surfaces. In their study, the minimum detectable crack was claimed to be 65 μm (area of 0.0066 mm^2 or 0.05% of cross section) for a steel specimen. Due to the limitation of the signal processing technique at that time, the PD signal outputs were in μV scale (15 μV ACPD change corresponded to a 600 μm crack). In fact, the scatter of data obtained at high frequencies ($f > 40$ kHz) by Verpoest et al. [*4*] can be attributed to their signal processing scheme. Nevertheless, in a recent study of the few available data pertaining to crack monitoring using ACPD techniques, Lugg [*5*] also showed a linear relationship between ACPD and crack length for both thin-skin and thick-skin materials.

Hwang and Ballinger [*6*] recently developed a multifrequency ACPD system (17 to 203 kHz). They performed measurements on a nickel-based alloy, using round bar specimens, fatigued at room temperature, and at 350°C in an aqueous environment. Detection of single crack initiation was reported with a resolution of 50 μm. A linear relationship between the measured ACPD and the crack depth at high frequencies was also measured. In their study, the amplitude as well as the phase shift of the ACPD signals were shown to be extremely sensitive to probe spacing and configuration at high frequencies. Their study suggests that the ACPD technique is more suitable for constant load testing than for dynamic loading and that extreme care is required when mounting the probes to ensure reproducibility of the data.

The application of high frequency ACPD techniques (>30 KHz) to fatigue testing of aerospace materials is still in its early stage, although some applications of the reversed DCPD method, which is not "skin effect" based but rather a signal differential technique, have been reported in the gas turbine industry for long crack growth measurement [*7*]. Hence, very little data are available in the open literature regarding the application of ACPD techniques to monitoring cracks in nonmagnetic materials such as titanium-based alloys [*8*]. The purpose of this paper is to present a newly developed ACPD system capable of accurate and reproducible crack initiation and growth measurements at elevated temperatures. The capabilities of this system will be demonstrated by fatigue crack initiation tests and fatigue crack growth tests under isothermal and thermal-mechanical fatigue (TMF) conditions.

Experimental Procedures

Materials, Specimen Geometry, and Testing Conditions

Two titanium alloys were chosen for this study: respectively, Ti-6Al-4V (Ti64) and Ti-6Al-2Sn-4Zr-6Mo (Ti6246). The specimens were fabricated from PWC engine compressor disk forgings. The specimen blanks (16.5 by 16.5 by 82 mm) were taken out by electrical discharge machining EDM along the circumferential directions of the disk forgings.

Single edge notched (SEN) specimens were used in the test program. The effective gage section of the specimens was 25.4 mm long (L), 10.67 mm in width (W), and 5.33 mm of thickness. Some specimens were provided with a semicircular notch to study isothermal crack initiation at the root of these notches. The radius (ρ) of the notches was 1.06 mm (or $\rho/W = 0.1$). The notch geometry and machining procedure were chosen as to duplicate the notch features (that is, stress concentration factor K_t, machining procedures, and surface finish, etc.) encountered at bolt holes of compressor disk.

The specimens were cycled under "far-field back face strain" controlled conditions at room and elevated temperatures. The maximum temperatures investigated in the study of crack initiation, were 400°C (750°F) and 483°C (900°F) for Ti64 and Ti6246 respectively [*9*]. Note that a 450 kHz inductive furnace (15 kW TOCCO) was used to heat the specimens with an accuracy, on the control of the temperature, better than 2.5°C.

A detailed description of the TMF test system has been presented elsewhere [*8,10*]. In the TMF tests, the temperature and mechanical strain imposed on the specimen were controlled independently. Two baseline TMF tests with proportional phasings, that is, out-of-phase (OP) (maximum strain at minimum temperature) and in-phase (IP) (maximum strain at maximum temperature), as well as a counter clockwise diamond TMF cycle type, were performed. The SEN specimens were preflawed by EDM.

The TMF tests were carried-out between 150 and 400°C for Ti64 and between 200 and 482°C for Ti6246. A total of 35 specimens were tested for the crack initiation studies while more than 22 specimens were tested under TMF conditions. To demonstrate the capabilities of the present ACPD system to confidently detect crack initiation and growth during TMF testing, few but key data will be presented in this paper.

ACPD Probe Setup and Measurement Techniques

A schematic of the ACPD probe setup is illustrated in Fig. 1. It can be seen that ceramic spacers were used to protect and control the probe configuration during the tests. Two sets of probes, namely, the working probes (PD) and reference probes (RP), were used to sense the ACPD signals. The working probes (vertically spaced 2.13 mm apart) were welded across the notch to sense the fatigue damage that developed at the root of the notch, while the reference probes (located at some distance from the notch) were used to sense any drifts in current and testing temperatures. The AC current leads used were 0.5 mm (0.020 in.) in diameter while the PD and RP probes were 0.127 mm (0.005 in.) in diameter. Both types of wires were made of pure titanium to minimize junction effects. Spot welding of the probes was carried out using a specially designed holder and spot welding system [*8*]. With this system the positioning of the welds and the pressure applied by the welding head can be controlled accurately to guarantee reproducibility of the spot welds [*8*]. Since the specimens were heated by a RF inductive heating coil, the ACPD probes and current leads were set parallel to the RF magnetic field to minimize undesired EMF noise pickup.

The ACPD signals were amplified by an extensively modified CGM5[4] system which consists of an advanced two channel preamplifier, a multi-high frequency current source, and an automatic AC signal phase shift control circuit (PSD). A similar system has been described in detail by Marchand et al. [*11*]. In the present study, a current of 30 kHz with 1000 mA amplitude was used for both titanium alloys. Note that such current is insufficient

[4] The ACPD signal amplifier used here is a modified CGM5 crack growth monitor. It is a trademark of MATELECT Ltd., Bedford Gardens, London, W8-7EF, UK.

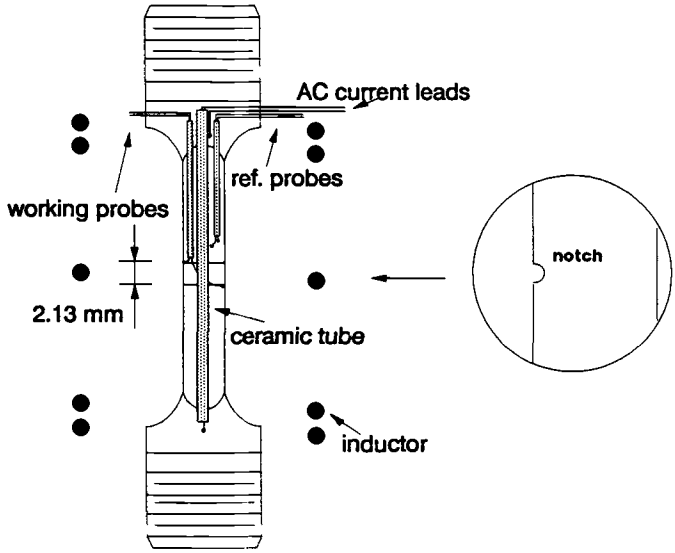

FIG. 1—*Schematic of the ACPD probe setup used for notch crack initiation and crack growth monitoring.*

to generate any notable heating of the specimen. During the tests, the ACPD signals from the probes were continuously phase shifted and amplified by the crack growth monitor. An amplification gain of 60 dB (or 70 dB) was selected for the low temperature tests, while 50 dB (or 60 dB) was selected for the elevated temperature tests. Here a smaller gain was used to reduce the emf interferences caused by the 15 kW inductive heating system. The output signals of the CGM5, along with all the mechanical parameters (that is, stress, strain, and temperature) of the specimens were digitized and recorded by a data acquisition and control system (Hewlett-Packard model 3852).

The probe connections and the linearity of the CGM5 system were checked after mounting each specimen. This was accomplished by measuring the ACPD signals as a function of increasing current. Typical results are shown in Fig. 2. Since the initial ACPD readings are a function of current and frequency (for a given probe configuration), the output of the CGM5 were offsetted (as indicated in the plot) to make use of the full resolution (100 nV) of the lower voltage range (<50 mV) of the digital voltmeter (DVM); thus enhancing the capability for detecting crack initiation (or growth increment) at elevated temperatures. On the other hand, if the ACPD response as a function of current was not as shown in Fig. 2, the specimen was removed from the servohydraulic machine, and the probes checked and reconfigured thoroughly.

ACPD Responses During Isothermal and TMF Testing

Isothermal Fatigue: Crack Initiation and Growth

Isothermal fatigue tests were performed at room and high temperatures using SEN specimens with semicircular notches. In these fatigue tests, the cracks initiated randomly at the

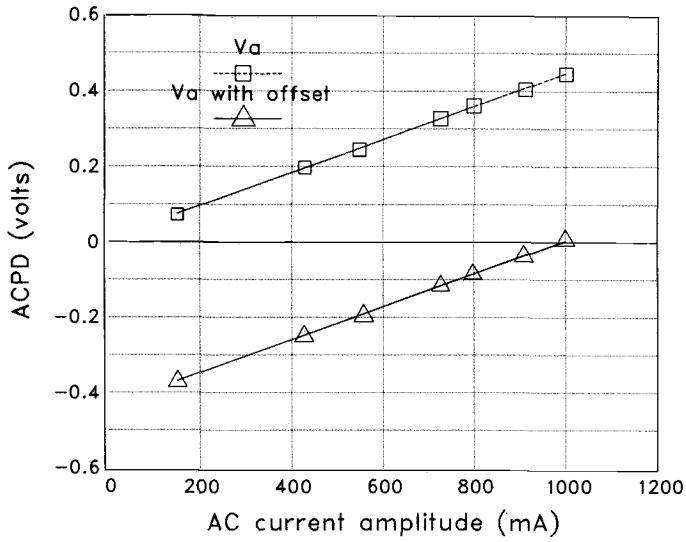

FIG. 2—*Typical result of ACPD readings as a function of current setting (Ti64, 30 KHz).*

roots of the notches and further propagated. All the tests were stopped when a well-defined through thickness crack was present.

Typical ACPD responses (working probe) at RT as a function of time for two load cycles, are displayed in Fig. 3. It can be seen that the ACPD signal continuously changes during each load cycle, as a result of straining, crack opening/closure, and complex mechanical-magnetic interactions. By plotting the ACPD change as a function of the far field stresses,

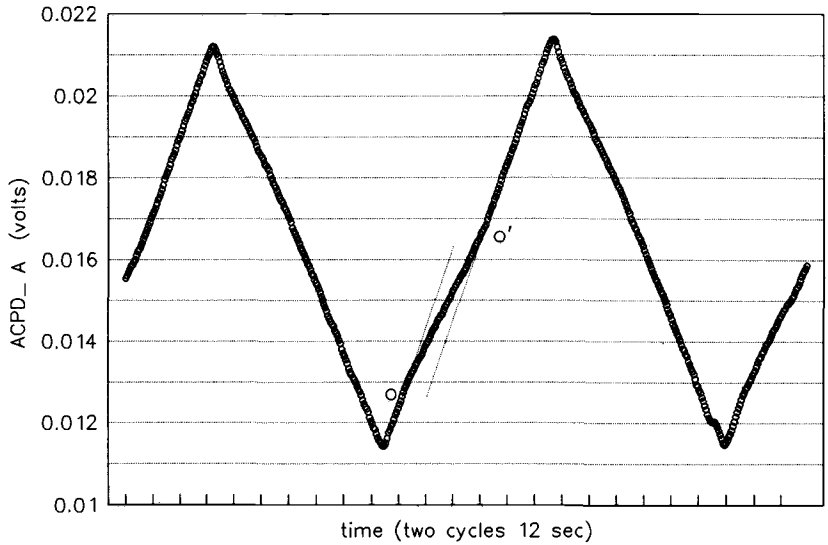

FIG. 3—*Close view of the ACPD signal as a function of time for two load cycles (Ti6246, RT).*

Fig. 4, an hysteresis loop behavior can be observed for both short and long cracks. This behavior is associated with the stress-strain relationship at the root of the notch and with crack closure effects. For long cracks, the crack tip closure effects can be clearly observed. Since the ACPD responses are plotted for two consecutive cycles, a small shift of the ACPD signal near the maximum load can be found. This small shift is the result of the average crack growth within one cycle. Detailed study of the ACPD response during each load cycle can be carried out to allow quantification of the different phenomena occurring during fatigue loading (opening, closure, plasticity, etc.). These measurements were not carried out systematically for the present fatigue tests because the purpose of the testing program was to determine the number of cycles to crack initiation (number of cycles to a_0 = 400 μm).

With increasing damage with the number of cycles, the AC potential versus time curve gradually shifted upward. Figure 5 shows "the peak values" of the ACPD loops plotted as a function of the number of cycles for Ti64 tested at 400°C. From this plot, a clearer picture of the crack initiation and early growth processes is obtained. The reference ACPD signal is constant which indicates that the testing temperature and the far field strain remained stable throughout the test. The gradual change of the ACPD (working probes) signal is due to crack initiation and growth at the root of the notch. At the end of this particular test (defined as 60 mV change), the specimen was broken. The crack depth was measured to be 1.07 mm (0.042 in.) which entails that the average ACPD crack initiation monitoring resolution is about 18 μm per 1 mV ACPD change. It can also be noted that the peak stresses remain almost unchanged during the test. This clearly shows that load drop criterion cannot be used to quantify the fatigue crack initiation life of materials.

Figure 6 shows another example of the sensitivity of the ACPD system to detect short crack initiating at the root of the notch. After about 40 mV change of the ACPD signal, the specimen was marked (heat tint technique) and broken into liquid nitrogen. The microcracks can be detected confidently using this procedure. As can be seen, there are several microcracks with the largest having about 400 μm in depth. In most tested specimens, at least

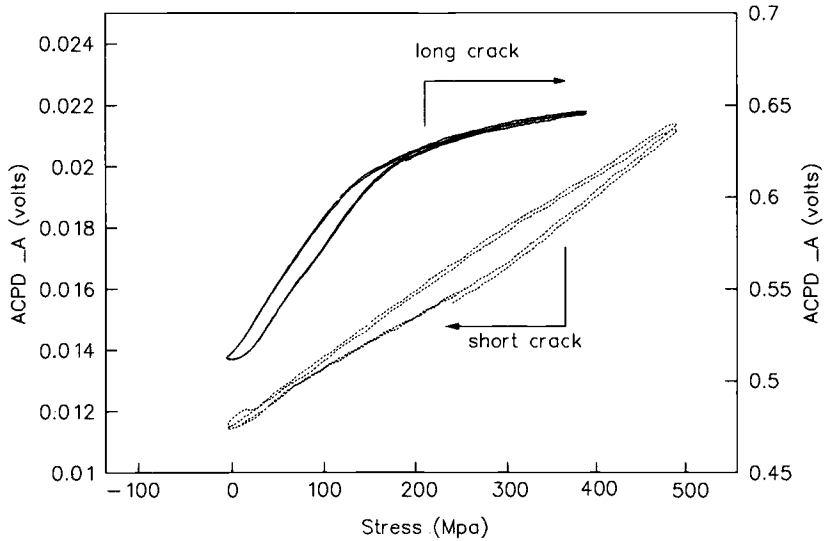

FIG. 4—*Typical ACPD signal as a function of the applied stress for short and long cracks (Ti6246, RT).*

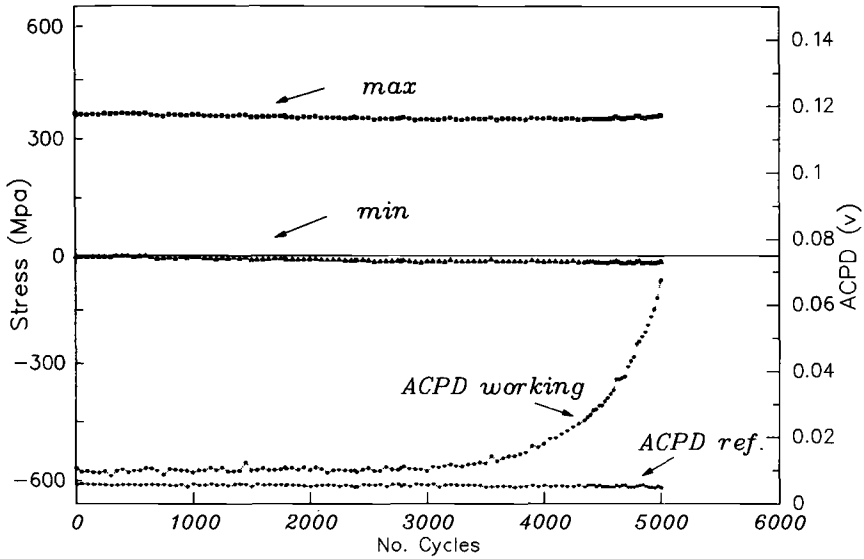

FIG. 5—*Far field stresses and ACPD signals as a function of number of cycles for a crack initiation and growth test (Ti64, 400°C).*

three microcracks were found. After analyzing the ACPD curves obtained from the different tests, it was confirmed that cracks as small as 50 μm (99% probability of detection and 95% confidence) could be detected reliably with the present system. Higher crack detection resolution was achieved for tests carried out at room temperature since no RF noise, coming from the induction heating system, interfered with the ACPD signals. Furthermore, crack growth measurements were performed with a resolution better than 2 μm per mV ACPD change (at 60 dB) with the present specimen geometry and ACPD probe setup.

Since multiple cracking was encountered (also often found in service), it is necessary to define an equivalent crack length (or depth) if a calibration curve, relating a change in potential to a given crack depth, is to be produced. For the present study, the equivalent crack depths were obtained by dividing the measured total cracked area by the thickness. Several specimens were marked and broken in liquid nitrogen after reaching specific changes in ACPD. Calibration curves were thus obtained at several temperatures. A linear relationship was found between the ACPD responses and the (physically) measured crack lengths as shown in Fig. 7. As can be seen, the slope of the curve depends on the testing temperature as a result of the changing electrical resistivity and magnetic permeability with changing temperature. The higher the temperature, the lower the sensitivity for the same AC frequency. Note that it is this linearity between the ACPD and the crack depth which constitutes the most important advantage of the ACPD technique over the other crack detection methods. This is particularly important for small cracks (<200 μm).

Because the initial value of the ACPD is sensitive to factors such as probe lengths, positioning, spacing, and connections, etc., a signal normalization processing procedure, like the one described by Hwang and Ballinger [5], is often required. However, because all the specimens were prepared using a very consistent procedure, and because the initial ACPD signals were offset close to zero volt at the beginning of each test (to fully utilize the high resolution of the DVM), normalization of the ACPD signal was found unnecessary.

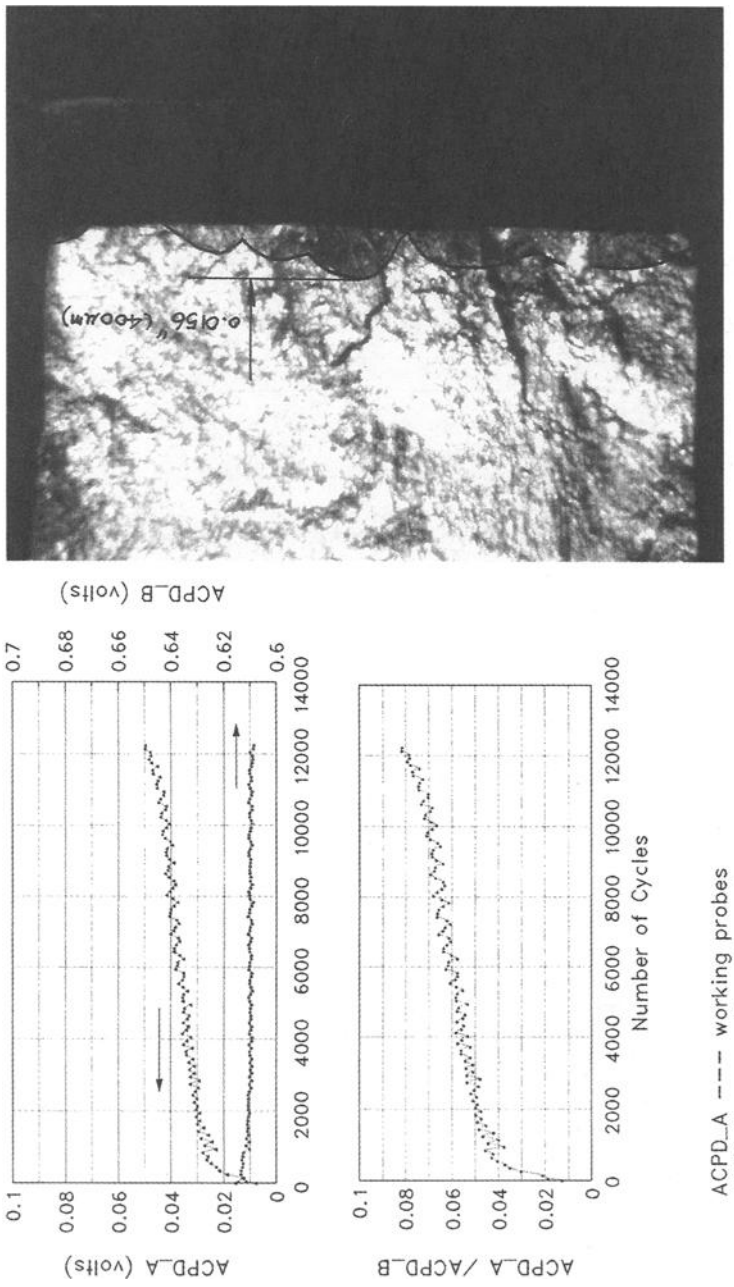

FIG. 6—*ACPD responses due to multiple fatigue crack initiation at the root of a notch (Ti64, RT).*

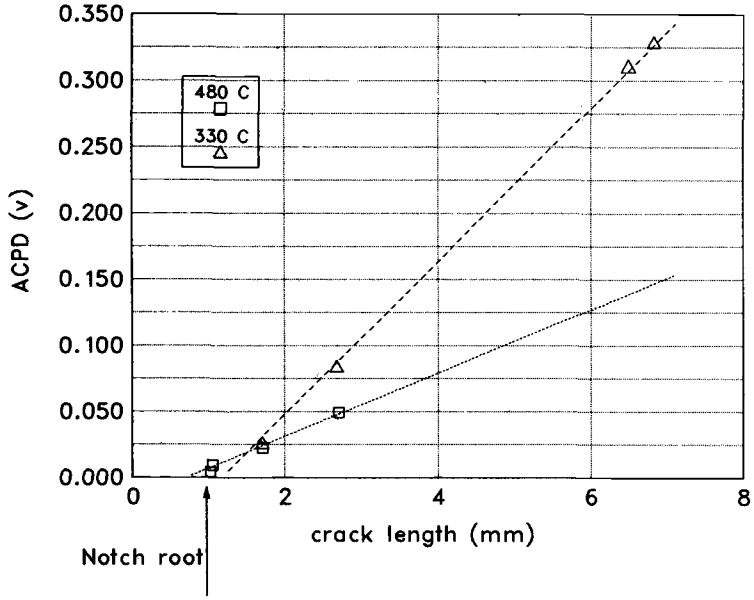

FIG. 7—*Calibration curves: ACPD signal versus crack length at two temperatures (Ti6246).*

TMF Crack Growth

Typical on-line (unfiltered) time series recorded during an in-phase TMF test (Ti6246) are presented in Fig. 8. Here the ACPD-A curve pertains to the working probe while ACPD-B pertains to the reference probe. As can be seen, the ACPD signal cycle curves are complicated by the TMF cycles. However, when the peak values of each cycle (obtained at a given temperature) are plotted as a function of the number of cycles (Fig. 9), the ACPD changes continuously with crack propagation. The ACPD data were also recorded during the thermal strain updating procedure which is used in mechanical strain controlled TMF test to measure the thermal strain of the material. In this procedure, the specimen is under zero stress control conditions while the temperature is cycled. A comparison between the ACPD data obtained from pure thermal cycling and from TMF cycling indicates that the change of the ACPD peak value depends only on crack growth, although the detailed ACPD change during each cycle is dependent on the TMF cycle type.

Figure 10 shows the complete ACPD peak to peak data (maximum and minimum ACPD measured in each cycle) and the far field stresses (σ_{max} and σ_{min}) observed during in-phase TMF testing of Ti64. As expected, the working probe signal increases continuously with the number of cycles as a result of crack growth. On the other hand, the reference ACPD signal is stable throughout the test indicating that the TMF cycles were accurately controlled.

Linear relationships between the ACPD response and the measured crack lengths were also found for TMF crack growth testing, as shown in Fig. 11. Here, the data pertains to Ti6246 cycled under IP and OP TMF conditions. The offset between the two curves is due to initial voltage offsetting procedure. Nevertheless, it can be seen that the linearity of the calibration curve is not affected by the TMF cycle type and that the slope of the curves are quite similar. A resolution of about 2 μm per mV change was obtained for the TMFCG tests.

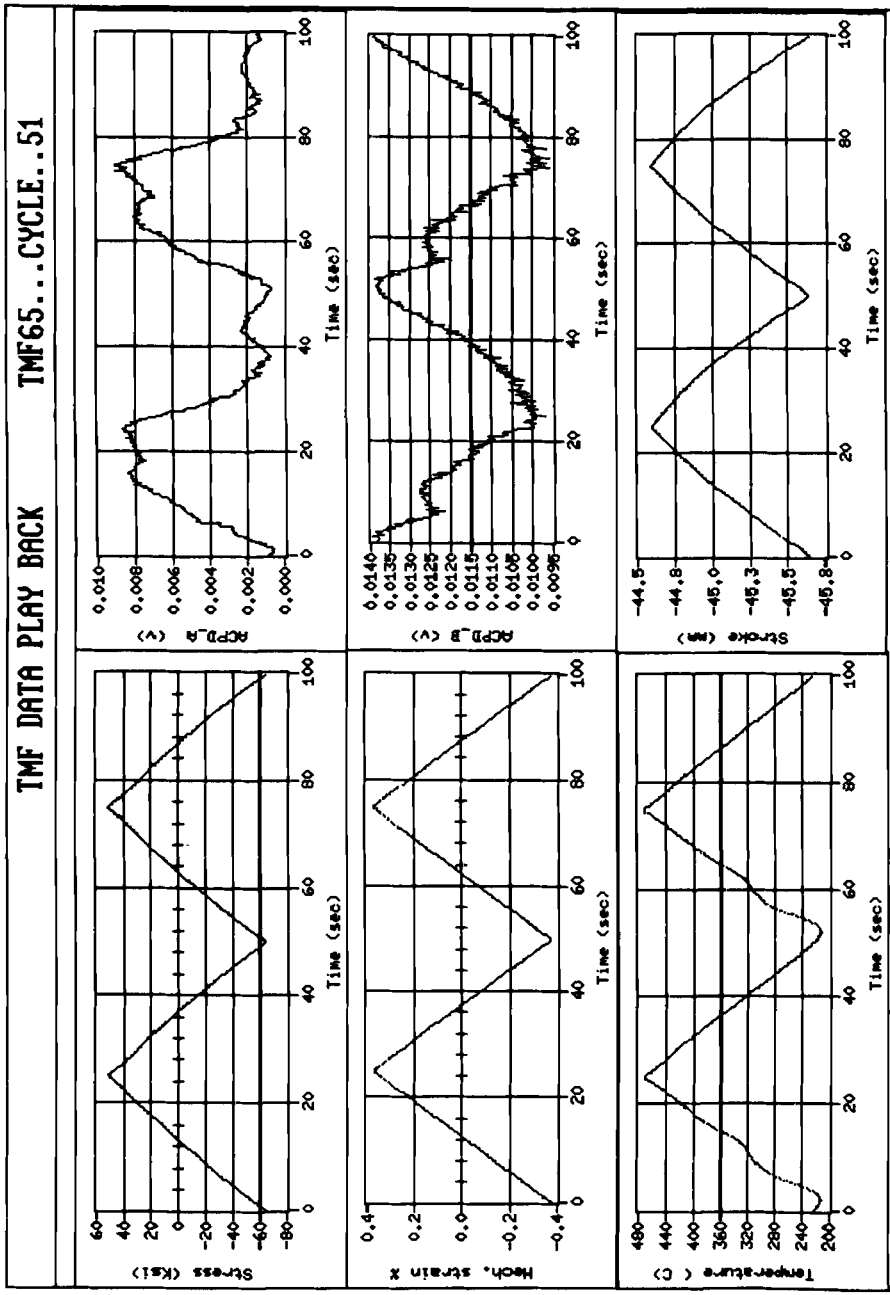

FIG. 8—*Typical time series (data) of an in-phase TMF test (Ti6246).*

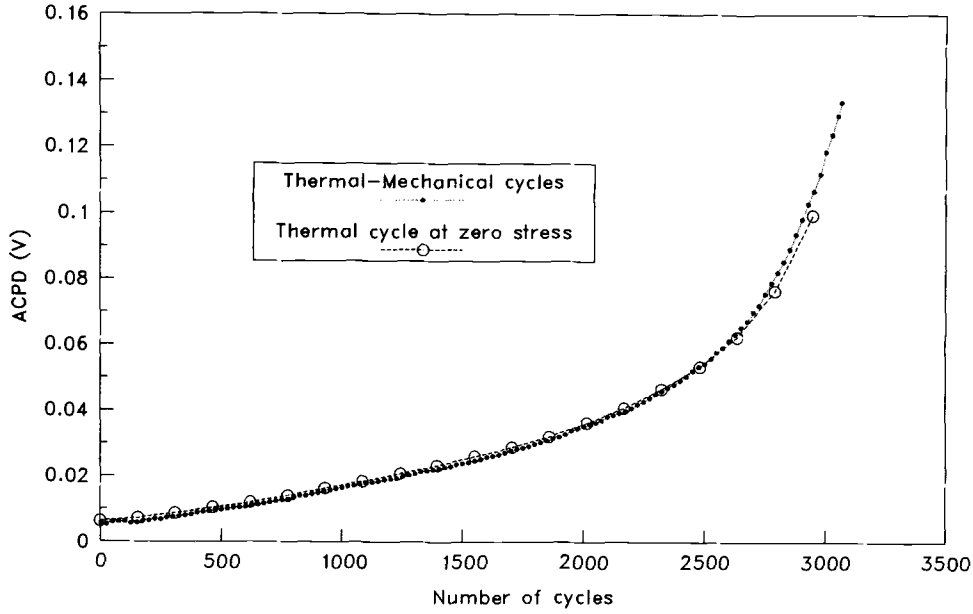

FIG. 9—*Effects of TMF cycling and pure thermal cycling on the ACPD responses.*

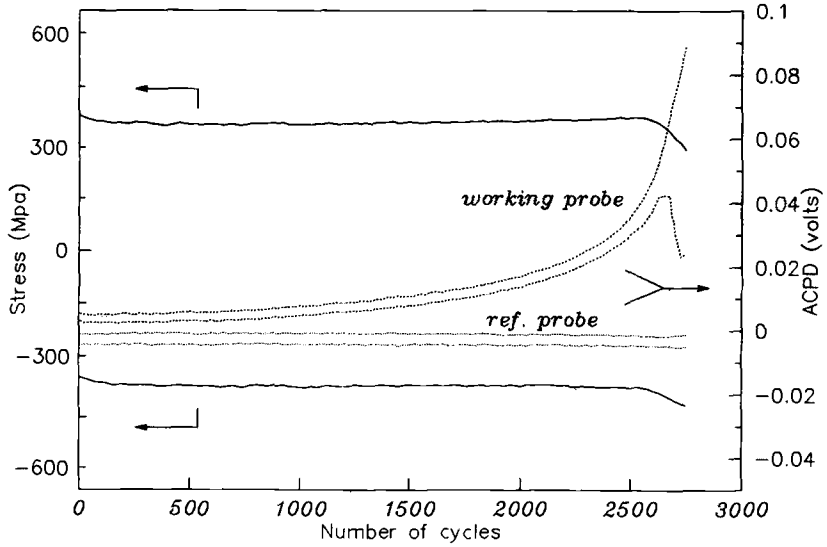

FIG. 10—*Changes of the far-field stresses and ACPD signals as a function of number of cycles in an in-phase TMF test (Ti64).*

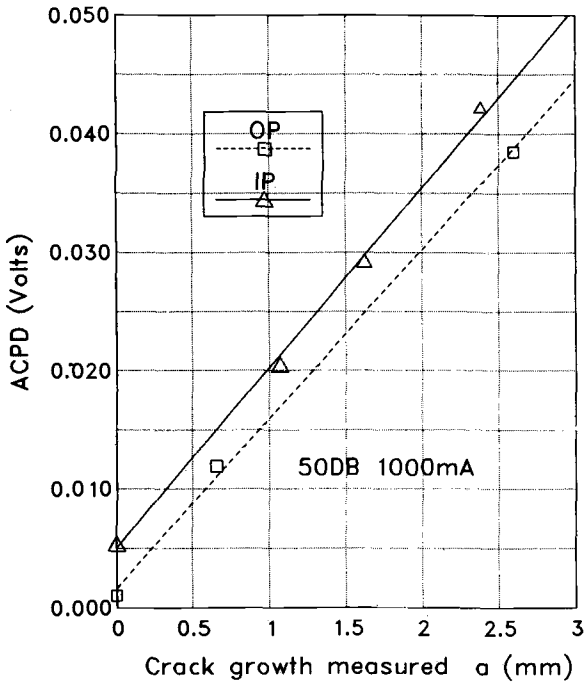

FIG. 11—*Calibration curves: ACPD signal versus length for TMF testing (Ti6246).*

ACPD Data Reduction

In order to determine accurately the *a-N* curves from the ACPD curves, the final crack lengths for each test needed to be measured. At the end of each test, the final crack fronts were marked using the heat tint technique and the fractured surface of the specimens were photographed under stereo microscopy (×80). The average final crack lengths were then measured from the color prints.

The recommended data reduction technique of the ASTM Test Method for Measurements of Fatigue Crack Growth Rates (E 647) was used to derive the *da/dN* data from the measured *a-N* curves. In this procedure, the coefficients of second order polynomials (parabola) of successive sets of seven successive data points are determined by the least squares method (that is, minimization of the square of the deviations between the observed and the fitted values of crack length). The crack growth rates are then obtained from the derivatives of the parabola.

TMF Crack Growth Test Results

Using the ACPD technique described previously, TMF crack growth rate data were obtained for the Ti64 and Ti6246 forgings. Here, only the long crack data are presented. The stress intensity factors (ΔK) for the through thickness cracks were computed using a formula developed elsewhere [*12*]. Since little or no closure was found for the TMF tests, the K_{max}'s were taken as the effective stress intensity factors (ΔK_{eff}). All the *da/dN* versus ΔK_{eff} curves were produced and compared. The following results are shown to demonstrate the capabilities of type TMF and ACPD systems.

The results pertaining to Ti6246 are shown in Fig. 12. As can be seen, the in-phase data are very close to the isothermal data obtained at T_{max} (480°C), while the out-of-phase TMF test results are close to the isothermal tests data obtained at T_{min} (200°C). The faithful TMF data (diamond) are found in-between the in-phase and out-of-phase data although closer to out-of-phase. The results obtained under isothermal T_{max} (480°C) and in-phase TMF conditions, show a behavior akin to corrosion fatigue. This indicates that crack growth is affected significantly by the environment in Ti64 and Ti6246, at least for growth rates lower than 10^{-3} mm/cycle. This conclusion is supported by the microfractographic study of the fractured surface [*13*]. It was found that the accelerated crack growth at elevated temperature was due to oxygen induced embrittlement of the material near the crack tip. At higher crack growth rates, all the data merge into a narrow scatter band because the environmental effects become less important.

A model has been proposed [*10,13*] to separate the *da/dN* component due to environmental effects $(da/dN)_{ox}$ from the total crack growth rate $(da/dN)_{tot}$.

Here the $(da/dN)_{ox}$'s are assumed to obey the following dependence with temperature

$$\left(\frac{da}{dN}\right)_{ox} = \left(\frac{da}{dN}\right)_{ox}^{\circ} \exp(-Q/RT) \tag{3}$$

where Q is the activation energy for oxygen embrittlement and $(da/dN)_{ox}^{\circ}$ the intrinsic maximum embrittlement of the material. Using the isothermal data only, the values of $(da/dN)_{ox}^{\circ}$ and Q were determined. The $(da/dN)_{ox}$ for TMF cycling were computed using the following formula

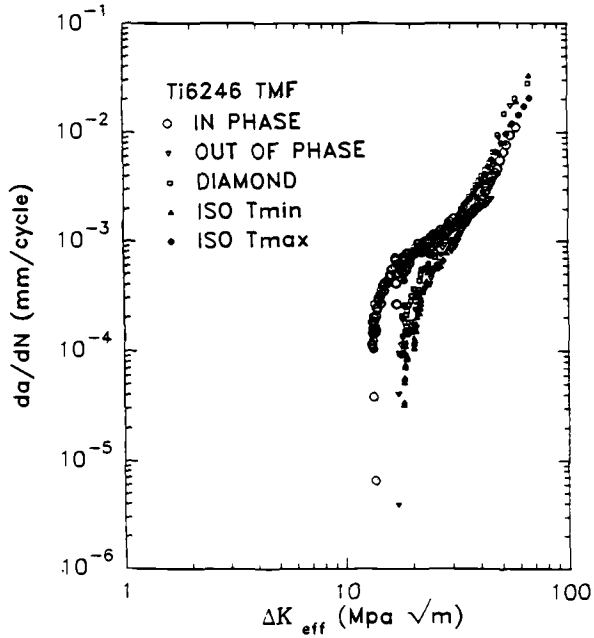

FIG. 12—*TMFCG and isothermal FCG data (Ti6246) as a function of* ΔK_{eff}

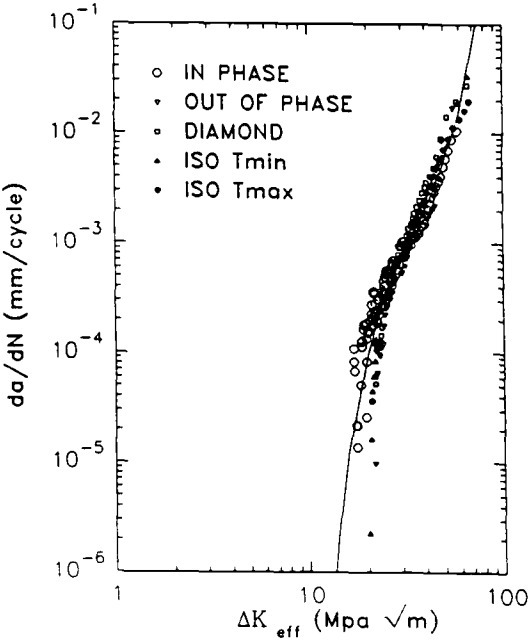

FIG. 13—*TMFCG and isothermal FCG data (Ti6246) as a function of the* ΔK_{eff} *after partitioning of the components due to the environment assisted cracking.*

$$\left(\frac{da}{dN}\right)_{ox} = \int_{t_1}^{t_2} \left(\frac{da}{dN}\right)_{ox}^{\circ} \exp(-Q/RT(t))\, dt \tag{4}$$

The integration limits (t_1 and t_2) were taken as the tensile going period of the TMF cycles. The pure fatigue contributions $(da/dN)_{fat}$ were evaluated by subtracting $(da/dN)_{ox}$ from $(da/dN)_{tot}$.

Figure 13 shows the pure fatigue contribution to the crack growth. As can be seen the $(da/dN)_{fat}$ due to fatigue damage follows the Paris law and does not depend on the cycle type and test temperature. These data are in good agreement with the Pratt & Whitney Aircraft database [*8,9*] obtained at high frequencies (>10 cpm). Note that all the TMF data (IP, OP, and CCD) are rationalized with the present model providing further support for the validity of the proposed model.

The expected $(da/dN)_{tot}$ of components are now obtained by adding $(da/dN)_{ox}$ to the $(da/dN)_{fat}$ data shown in Fig. 13. In turn, the $(da/dN)_{ox}$ are computed for each flight sequence (that is, temperature history) which vary according to airlines and flight paths. Comparisons of the predicted results crack lengths with those found in components removed from service have been excellent [*14*].

Conclusions

The major conclusions drawn from this paper can be summarized as follows:

1. An advanced ACPD technique has been developed and applied successfully to on-line monitoring of crack initiation and growth under isothermal and TMF conditions of titanium alloys.

2. The current ACPD system (with gain = 60 dB) has a crack initiation detection limit (99% POD) of 50 μm for the SEN specimen geometry used in this study. The long crack growth monitoring resolution was found to be 2 μm per mV ACPD change at elevated temperatures. The procedures to achieve these resolutions have been described in detail.
3. The capabilities of the TMF and ACPD systems have been demonstrated by fatigue testing performed under isothermal and TMF conditions.

Acknowledgments

The financial support provided by the National Science and Engineering Research Council of Canada (NSERC-Grant 661-001/89) and by Pratt & Whitney Canada is gratefully acknowledged. The authors would like to thank Dr. A. Koul (NRC/IAR) for many fruitful discussions.

References

[1] Watt, K. R., *The Measurement of Crack Length and Shape during Structure and Fracture,* C. J. Beevers, Ed., Engineering Materials Advisory Services, Ltd., West Midlands, UK, 1980, pp. 202–221.

[2] Marchand, N. J., "Feasibility Study of a Damage Measurement Sensor Based on the ACPD Technique," final report, prepared for the Department of National Defense, DAS ENG 6-6, Ottawa, Ont., Canada, Dec. 1990.

[3] Ikeda, K. et al., "Electrical Potential Drop Method for Evaluating Crack Depth," *International Journal of Fracture,* Vol. 47, 1991, pp. 25–38.

[4] Verpoest et al., "An Improved AC Potential Drop Method for Detecting Surface Microcracks during Fatigue Tests of Unnotched Specimens," *Fatigue of Engineering Material Structures,* Vol. 3, 1981, pp. 203–17.

[5] Lugg, M. C., "The Analysis of Sparse Data in ACPD Crack Growth Monitoring," *International Journal of Nondestructive Testing,* Vol. 21, No. 3, 1988, pp. 153–158.

[6] Hwang, I. S. and Ballinger, R. G., "A Multi-Frequency AC Potential Drop Technique for the Detection of Small Cracks," *Measurement of Science Technology,* Vol. 3, 1992, pp. 62–74.

[7] Pickard et al., "Crack Detection and Crack Length Measurement in the Gas Turbine Industry," *Fatigue Crack Measurement: Techniques and Applications,* K. J. Marsh, R. A. Smith, and R. O. Ritchie, Eds., Engineering Materials Advisory Services, Ltd., West Midlands, UK, 1992, pp. 457–486.

[8] Marchand, N. J., Dai, Y., and Hongoh, M., *Thermal-Mechanical Fatigue Crack Growth in Aircraft Engine Materials,* Pratt & Whitney Canada, WY-910069, April 1991.

[9] Dai, Y., Marchand, N. J., and Dickson, J. I., "Fatigue Crack Growth Mechanisms of Two Titanium Alloys at Room and Elevated Temperatures," *Proceedings,* Fifth International Conference on Titanium-92, S. Froes, Ed., ASM-AIME, 1992, pp. 1803–1811.

[10] Dai, Y., Marchand, N. J., and Hongoh, M., "Thermal Mechanical Fatigue Crack Growth in Titanium Alloys," *Proceedings,* Fifth International Conference on Fatigue 93, J. I. Dickson et al., Eds., Engineering Materials Advisory Services, Ltd., West Midlands, UK, 1993, pp. 82–90.

[11] Marchand, N. J., Dorner, W., and Ilschner, B., "A Novel Procedure to Study Crack Initiation and Growth in Thermal Fatigue Testing," *Surface-Crack Growth: Models, Experiments, and Structures, ASTM STP 1060,* American Society for Testing and Materials, Philadelphia, 1990, pp. 237–259.

[12] Marchand, N. J., Parks, D. M., and Pelloux, R.N., "K_I Solution for a SEN Geometry Under Fixed-end Displacement Conditions," *International Journal of Fracture,* Vol. 31, 1986, pp. 53–65.

[13] Dai, Y., Marchand, N. J., and Hongoh, M., "Thermal Mechanical Fatigue in Titanium Alloys: Experiments and Modelling," submitted to *Second Symposium on Thermo-Mechanical Fatigue Behavior of Materials,* Phoenix, AZ, 14–15 Nov. 1994, American Society for Testing and Materials.

[14] Hongoh, M., private communication, Pratt & Whitney Canada, February 1992.

David A. Jablonski[1]

Measurement of Multiple-Site Cracking in Simulated Aircraft Panels Using AC Potential Drop

REFERENCE: Jablonski, D. A., **"Measurement of Multiple-Site Cracking in Simulated Aircraft Panels Using AC Potential Drop,"** *Special Applications and Advanced Techniques for Crack Size Determination, ASTM STP 1251,* J. J. Ruschau and J. K. Donald, Eds., American Society for Testing and Materials, Philadelphia, 1995, pp. 33–50.

ABSTRACT: The characterization of multiple-site damage by use of laboratory test specimens is an important precursor to the understanding of multiple-site damage in aging aircraft. As the number of damage sites in the laboratory specimen increases, it becomes more time-consuming to measure crack initiation and growth from the various sites. Typically the crack initiation and crack growth would be measured either visually or with a low-power microscope. This technique is accurate, but it is labor-intensive. To decrease the time necessary to obtain multiple-site crack growth rate data, an automated crack length measuring technique, AC potential drop, was investigated.

This AC potential drop technique was applied to aluminum test specimens under fatigue cycling conditions as well as monotonic *R*-curve testing. Aluminum ALCLAD 2024 test specimens of three different specimen geometries were examined. Specimens with a single-hole were used to examine the effects of lead placement on the sensitivity of AC potential drop. Three-hole specimens were used to simulate multiple-site cracking from several holes. Riveted specimens containing one row of three rivets were used to examine multiple-site cracking from fasteners. Optimum current and potential lead geometries were determined for each specimen geometry. Relationships between the AC potential and crack length were determined for AC current frequencies of 3, 10, and 30 kHz. The sensitivity of AC potential drop in measuring crack initiation was investigated. The sensitivity was found to increase substantially with increasing AC current frequency.

KEYWORDS: Automation, ACPD, aluminum, crack initiation, crack growth, fasteners, fatigue, fracture mechanics, multiple site cracking, *R*-curve, rivet, scanning electron microscope

There are a variety of possible automated crack length techniques available for measuring cracking in test specimens and structures. The most popular are compliance [*1,2*], DC potential drop [*3,4*], and AC potential drop [*5,6*]. The compliance technique relates the specimen's normalized compliance to crack length by a multiple term polynomial relationship. To measure the compliance of an aircraft panel, it is necessary to attach a displacement gage at each location of interest. In the present study, this would require the attachment of six displacement gages in the case of the three-hole or the riveted specimens. The attachment of displacement gages to an aircraft panel would be difficult. The accuracy of this technique decreases as the specimen's compliance decreases. Since aluminum aircraft panels are not very compliant, this technique would not be able to measure crack length accurately.

[1] Manager of Research Laboratory, Instron Corporation, 100 Royall Street, Canton, MA 02021.

With the DC potential drop technique a constant DC current is applied to the specimen and the resulting potential is measured. The potential increases as the crack grows. The magnitude of the current necessary to produce repeatable and accurate potential readings depends upon the specimen geometry, size, and the material's resistivity. Materials with relatively high resistivity, such as alloy steels, require currents of the order of 10 to 50 amp. Materials with low resistivity, such as aluminum alloys, require currents of the order of 50 to 250 amp. Low resistivity materials require such high current densities for accurate potential measurements that there is a serious problem of specimen heating. Also, the DC potential drop technique is not sensitive to crack initiation and the measurement of short cracks.

The AC potential drop technique (ACPD) applies a high frequency (3 to 100 kHz) current to the specimen and measures the resulting potential. With the ACPD technique, phase-sensitive detection is used to measure the small voltages involved. Phase-sensitive detection means that the transmitted and received signals are filtered to pass only a narrow frequency band. Signals outside this band are rejected, thus reducing the noise. In ACPD the high current frequencies cause the current to be concentrated on the surface of the specimen, and it is this so-called "skin effect" that is responsible for the high sensitivity and low currents required (~1 amp). The current is carried in a thin layer of material which results in a high current density from a low input current. The skin thickness (δ) can be calculated by the following equation

$$\delta = 1 \div \sqrt{\pi\mu\sigma\nu} \tag{1}$$

where

μ = magnetic permeability,
σ = electrical conductivity, and
ν = current frequency

The skin depth, δ (depth of current penetration), for an alloy steel with current frequencies of 3, 10, and 30 kHz would be approximately 0.60, 0.15, and 0.08 mm. The skin depth for an aluminum alloy with the same current frequencies would be 2.0, 1.0, and 0.60 mm, respectively. The material used in this study is an ALCLAD 2024 aluminum alloy, which is a composite material consisting of thin aluminum layer (~0.05 mm) and a core of aluminum alloy 2024. The estimation of skin depth for this configuration would require a theoretical model, which is beyond the scope of this work. A quick estimate of the impedance of the clad versus unclad material shows that the impedance of the clad material is lower, thus the skin depths for the clad material should be greater.

With the ACPD technique it is possible to concentrate the current to only the area of interest by placing the current leads in a line directly above the area of interest. This is the so-called current-focusing technique. This intensifies the current field which in turn increases the sensitivity of the technique. A reported problem with the ACPD technique is that the potential can be affected by plastic deformation [*5*]. This effect was experimentally investigated on the single-hole specimens by use of monotonic *R*-curve testing.

The results of these experiments demonstrate the use of ACPD for other than thin skin conditions. Because of this the sensitivities are not much better than they are with DCPD. ACPD has the advantages of locally intensifying the electrical field to the area of interest and the ability to reduce the noise in the measured potentials by the use of phase locked amplifiers. This paper describes the benefits and problems of applying ACPD to aluminum aircraft panels. Three specimen types, single-hole, three-hole, and riveted panels were stud-

ied. Current and potential lead geometries were experimented with in order to obtain high sensitivity. Duplicate specimens were used to determine the repeatability of the technique.

Experimental Procedure

Three types of specimens were tested: single-hole, three-hole, and riveted panels. The specimens were manufactured from ALCLAD 2024 aluminum plates with a thickness of 1.0 mm. The single-hole specimens were 381 mm long, 50.8 mm wide, and had a centrally located hole with a diameter of 4 mm. The three-hole specimens, Fig. 1, were 381 mm long by 101.6 mm wide with three equally spaced 4 mm diameter holes. These specimens were gripped by a clamping arrangement using seven bolts at either end of the specimen. The riveted specimens, Fig. 2, were 254 mm long by 101.6 mm wide with three equally spaced rivets 6.1 mm in diameter. Aircraft grade rivets were used to join the specimen halves. Each half of the specimen overlapped the opposite side by 101.6 mm. These specimens were gripped the same way as the three-hole specimens.

The AC potential leads were 0.50 mm diameter 99.9999% aluminum wire and the AC current leads were 1.0 mm diameter 99.9999% aluminum wire. The leads were spot-welded to the specimen and were twisted to minimize noise pickup. Spot welding was performed under controlled conditions; constant power and pressure to ensure consistent welds. The spot weld positioning accuracy was ± 0.05 mm as measured from the center of the spot weld. The diameter of the spot weld was approximately 0.50 mm. Experiments were performed on a variety of different locations for placement of these leads. The positioning of the leads on the test specimens will be described in the results and discussion section. The specimens were tested on an Instron 8502 digital servohydraulic test machine. The crack

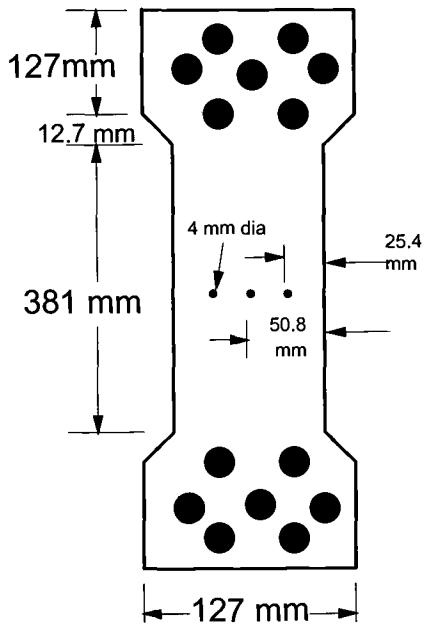

FIG. 1—*Schematic drawing of three-hole specimen.*

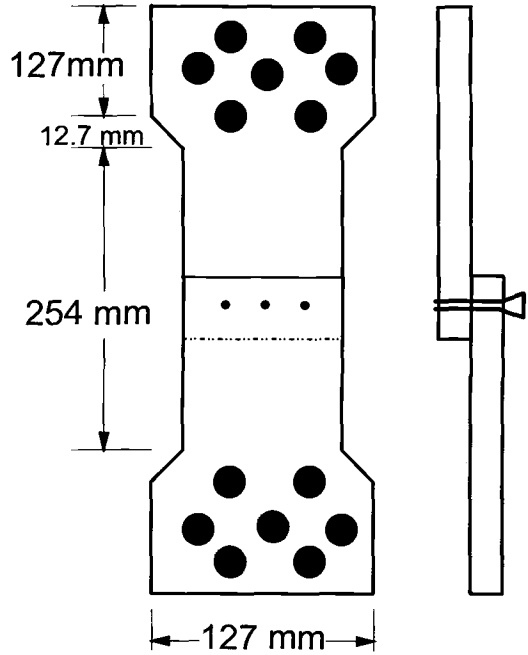

FIG. 2—*Schematic drawing of riveted panel specimen.*

length was measured visually with a Questar QRMS-M optical microscope system. The AC potential drop equipment consisted of a Matelect CGM5 ACPD unit, SC1 scan controller, SCM1 8-channel potential scanner, and a SCM2 8-channel current scanner. The AC current was fixed at 1 amp for all of the tests and the gain of the voltage measuring device was 80 dB (×10 000). No filtering was applied to the ACPD signal. The test specimen was not electrically isolated from the test machine. Electrical isolation was not necessary because of modifications made to the CGM-5 by Matelect. The resolution of the voltage measuring device (CGM5) was not determined, but it is estimated to be 10 nV by the manufacturer. The noise has been estimated to be less than 100 nV. The test was controlled and data collected with a personal computer (PC) with a custom designed software program. A schematic of the test system is shown in Fig. 3. Digital communication between the Instron 8502 and the PC was through an IEEE interface, and communication between the PC and both the Matelect and Questar equipment was by RS232.

Fatigue tests were controlled by a custom software program that cycled the specimen at a fixed stress ratio (0.10), frequency (10 Hz), and stress amplitude (75 to 100 MPa) for a specified number of cycles. After reaching the specified number of cycles, the load was slowly increased to maximum load and held constant. During the hold period the AC potentials were measured automatically by the Matelect system. The visual crack length measurements required an interactive procedure. The operator positioned the cross hairs on the microscope at the center of the hole or rivet and zeroed the x-y position; next the operator positioned the cross hairs at the crack tip to measure crack length. These values from the Questar were read by use of the RS232 interface and were stored in the computer. This procedure was repeated for both the left and right sides of the hole or rivet and for each hole or rivet. The crack lengths were defined relative to the edge of the hole or rivet. At the

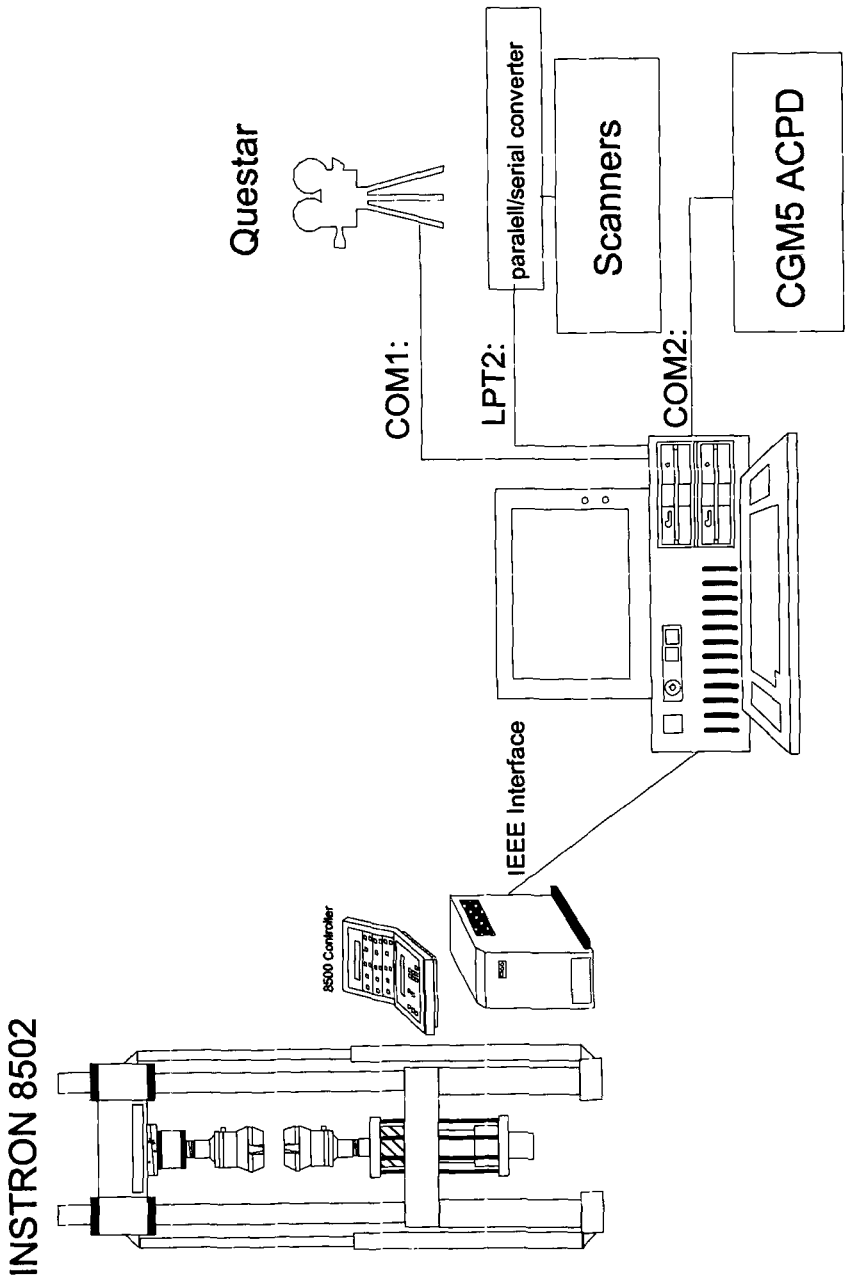

FIG. 3—*Schematic drawing of test equipment and test setup.*

end of the visual crack length measurements, the load was slowly decreased to the mean load and the load cycling was continued. All the pertinent test data were stored in an ASCII data file for post test analysis. The *R*-curve test was done in position control at a constant rate of 0.127 mm/min, and approximately 100 data points were collected during the test. The test data that consisted of position, load and crack length were logged to disk at a one second interval. The longest crack was followed manually with the Questar microscope with the operator attempting to smoothly follow the advancing crack tip.

Results and Discussion

The single-hole specimens were used to experiment with various current and potential lead geometries. It is not the purpose of this paper to describe all the geometries examined, but rather to describe the geometries that gave good results. A complete description of all the geometries experimented with can be found in Ref *7* which details the experiments done to determine optimum current and potential lead geometries. Briefly these experiments varied the current lead placement and examined differences between using separate current leads for the left and right sides of the hole versus using one centrally located current lead as well as the effect of the vertical separation distance of the current leads. The experiments also varied the potential lead placement by using those shown in Fig. 4 as well as a position which was midway between those shown in Fig 4. Optimization was defined as a probe position which gave high sensitivity in terms of the magnitude of the AC potentials and repeatable measurements with duplicate test specimens. It was assumed that because the specimen geometries of the single, three-hole and riveted panels were similar, that the results

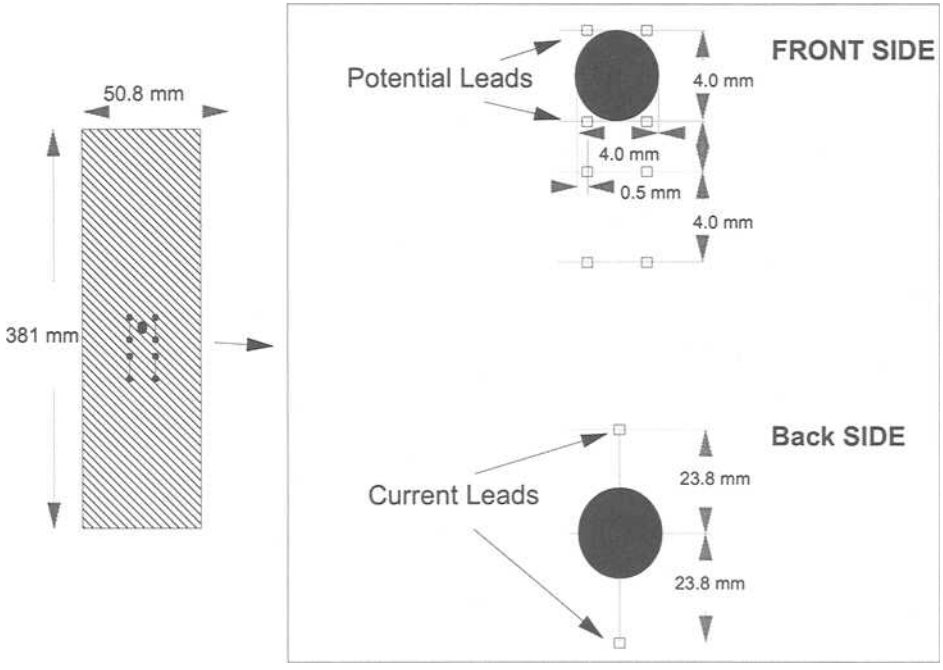

FIG. 4—*Diagram of single-hole specimen showing current and potential lead placement.*

of the optimization study performed on the single hole specimen would be applicable to all three geometries. The final current potential lead geometry is shown in Fig. 4. The potential leads were placed on the front of the specimen and the current leads were placed on the back of the specimen. Experiments showed that the placement of the current leads on either the front or back side of the specimen did not affect the relationship between the AC potential and crack length. Placing the current on the back side of the specimen had the advantage of the leads not obstructing the visual crack length measurements. The potential leads were placed on either side of the hole to measure the potential with the crack and below the hole so that a reference voltage could be measured.

The reference potentials were measured to determine if a theoretical crack sizing equation from the work of Collins, Dover, and Michael [*6*] could be used. The assumptions of the theoretical sizing equation are: a thin skin field exists and the current field is uniform. In the aluminum panels it is doubtful that these conditions were met completely, but it was thought that a test of the validity of this expression as applied to the aluminum panels was worthwhile. This expression [*7*] when applied to the single-hole specimen geometry, is formulated as follows

$$a = \frac{\Delta}{2}\left[\frac{P_{act}}{P_{ref}} - 2\left[\frac{\pi}{2} - \sin^{-1}\left(\frac{\Delta - 2X_{off}}{\Delta}\right)\right]\right] \tag{2}$$

where

Δ = spacing between potential leads,
P_{act} = active potential,
P_{ref} = reference potential, and
X_{off} = vertical distance from vertical edge of hole to potential lead.

A test was run on a single-hole specimen with current and potential leads attached, as shown in Fig. 4. The results are shown in Fig. 5, which is a plot of measured and calculated crack length versus cycle number. The curve labeled "a1meas" is the optically measured crack length for the crack on the left side of the hole and that labeled "a2meas" is for the crack on the right side of the hole. The other two curves are for the crack lengths calculated by Eq 2. The calculated crack lengths do not agree with the measured crack lengths, although they both show the same trends with cycle number. Duplicate experiments were performed in which the stress amplitude, stress ratio, and cyclic interval at which tests were stopped to make measurements were identical. The results which were the plots of AC potential versus crack growth were identical, and the underprediction when compared to Eq 2 was consistent. The theoretical sizing equation was derived assuming that a thin skin solution would apply and that the current field is uniform. Aluminum has a low resistivity and magnetic permeability; thus the assumption of a thin skin solution is probably not valid. An estimate of the skin thickness shows that it is the same order of the specimen thickness; thus, it is expected that the thin skin solution would be inaccurate. The current focusing technique produces a nonuniform current field which will affect the magnitude of both the active and reference potentials. Equation 2 has an inverse relationship with the reference potential which was a small value ~15 μV. This inverse relationship with reference potential makes the equation very sensitive to changes in magnitude of the reference potential. The nonuniformity of the current field would affect the value of the reference potential which could explain why negative crack lengths were predicted.

The effect of current frequency was investigated by measuring AC potential at frequencies of 3, 10, and 30 kHz. Repeatable correlations between crack length and AC potential were

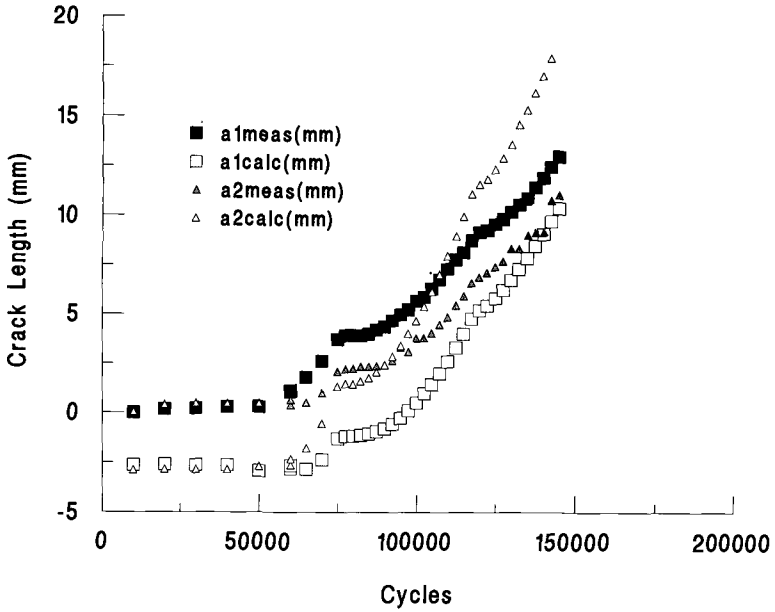

FIG. 5—*Plot of measured and calculated crack length versus cycle number for single-hole specimen.*

obtained when the measured AC potential of the uncracked hole, Pd_0, was subtracted from the measured potentials. The potential of the uncracked hole, Pd_0, was found to vary considerably from hole to hole and specimen to specimen. The cause of this variation was not determined, but it was probably due to pickup. Another cause for this variation could be a variation of the electrical resistance across the welded junction, though careful spot welding procedures were used to minimize this effect. A typical plot of crack length versus AC potential is shown in Fig. 6. This plot includes data from the crack growth at the left and right sides of the hole as well as their measured potentials. The crack grew at approximately the same rate from either side of the hole; therefore, the plots show little scatter due to this effect. The sensitivity to measuring crack length with AC potential drop increased as the current frequency increased. The ACPD method used in this study is not accurate for short crack lengths due to the lack of thin skin conditions. Consequently only larger crack lengths were related to the potential. The test data for crack growth greater than 1.0 mm could be represented by the followng equation

$$a = m \times (Pd - Pd_0) + b \tag{3}$$

where

Pd_0 = AC potential of uncracked hole, and
Pd = AC potential.

The slope "m" represents the sensitivity in units of $\mu m/\mu V$ and "b" represents the intercept of the least squares fit. The lower the value of m, the greater the sensitivity of ACPD in measuring crack length from the AC potential. The values of m for the plots shown in Fig. 6 are: 34.9, 68.9, and 140.1 $\mu m/\mu V$ for current frequencies of 30, 10, and 3 kHz,

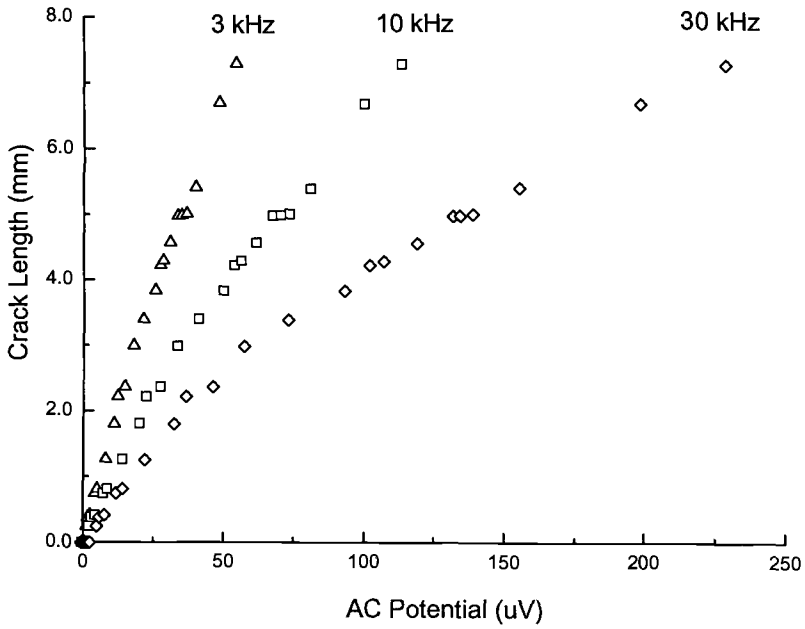

FIG. 6—*Plot of crack length versus AC potential for single-hole specimen for frequencies of 3, 10, and 30 kHz.*

respectively. Experiments were run with two current leads per hole. These current leads were placed directly in line with the potential leads, but on the opposite side of the specimen. The results were almost identical to those in Fig. 6 that had one centrally located current lead. The use of two current leads per hole gave a slope, *m*, that was approximately 10% less than the results shown in Fig. 6. This sensitivity difference was verified by running tests on two identical specimens, both of which showed the same 10% change in sensitivity. Clearly there was an advantage of using two current leads per hole, but the advantage was small (~10%). It was decided to simplify specimen preparation and use only one current lead per hole.

The knowledge that was gained from the single-hole specimen experiments was applied to tests run on three-hole specimens. The three-hole specimens were instrumented with current and potential leads as shown in Fig. 7. Each specimen had eight potential lead pairs and three current lead pairs attached to them. Experiments had shown that the results were the same when the current leads were on the same or opposite sides as the potential leads; thus, the current leads were placed on the specimen side opposite the potential leads to aid in the visual measurement of crack length. The potential lead pairs, numbers 4 and 5, in Fig. 7 were used to measure a reference voltage, but these values tended to change with crack growth. Stability experiments were run to verify that the change in the reference voltages was not due to drift.

The results of duplicate tests for specimens "ALH3 6" and "ALH3 7" are shown in Fig. 8. The results show the same trend as the single-hole specimen test showed: the sensitivity of ACPD in measuring crack length increased with increasing current frequency. The scatter in the data also increased with AC current frequency, but this is to be expected because the higher frequency signals are more susceptible to noise. The test data for crack growth greater than 0.5 mm was fit to Eq 3. The slopes were 29.3, 76.2, and 163.1 μm/μV for current

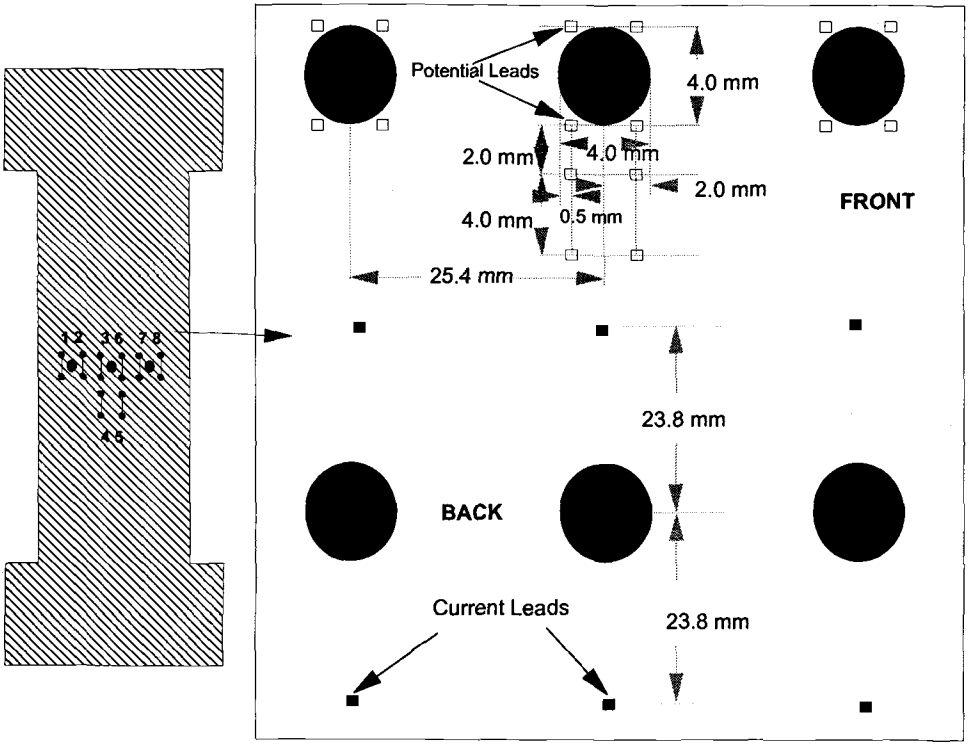

FIG. 7—*Diagram of three-hole specimen showing current and potential lead placement.*

frequencies of 30, 10, and 3 kHz, respectively. These values are similar to the single-hole specimen results, but not identical. At short crack lengths (<1.0 mm) the plots exhibited a nonlinear behavior. The resolution of the optical measurements was 0.010 mm, but it was difficult to see any cracks until they grew at least 0.50 mm from the edge of the hole. This was due to the poor surface finish around the holes, as well as the reflection of light around the holes.

A careful examination of the data in the initial stages of the test revealed some interesting results. Figure 9 shows a dual *y*-axis plot of AC potential and crack length versus cycle number for one of the cracks in specimen ALH3 6. The AC potential is observed to steadily increase with cycle number even when there is no visible cracking occurring on the surface as viewed with the Questar microscope. This observation implies that ACPD is able to measure crack initiation. This observation will be discussed further in the section on the riveted panel test results.

The riveted panels were instrumented with AC current and potential leads as shown in Fig. 10. The AC current leads were placed on the same side as the AC potential leads. It was not possible to place the current leads on the back side of the specimen because of the overlapping of the second half of the specimen in the riveted lap joint. Reference potentials were not measured because the single-hole and three-hole specimen tests showed that they were of little value because they varied with crack growth. A typical aircraft panel consists of three rows of rivets. The top and bottom rows prevent bending of the panel and the middle row, which is under tension-tension fatigue cycling, is where the fatigue cracks occur. To

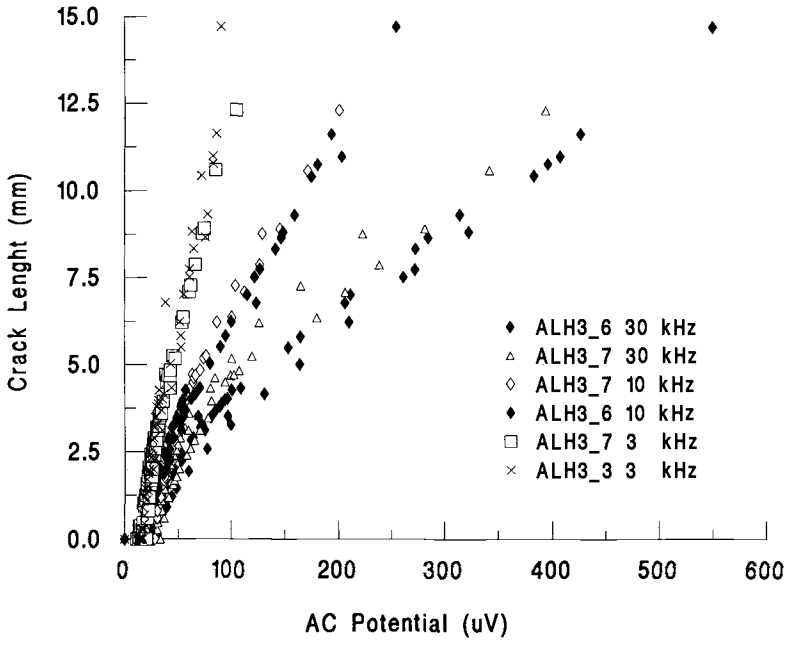

FIG. 8—*Plot of crack length versus AC potential for two duplicate three-hole specimens for frequencies of 3, 10, and 30 kHz.*

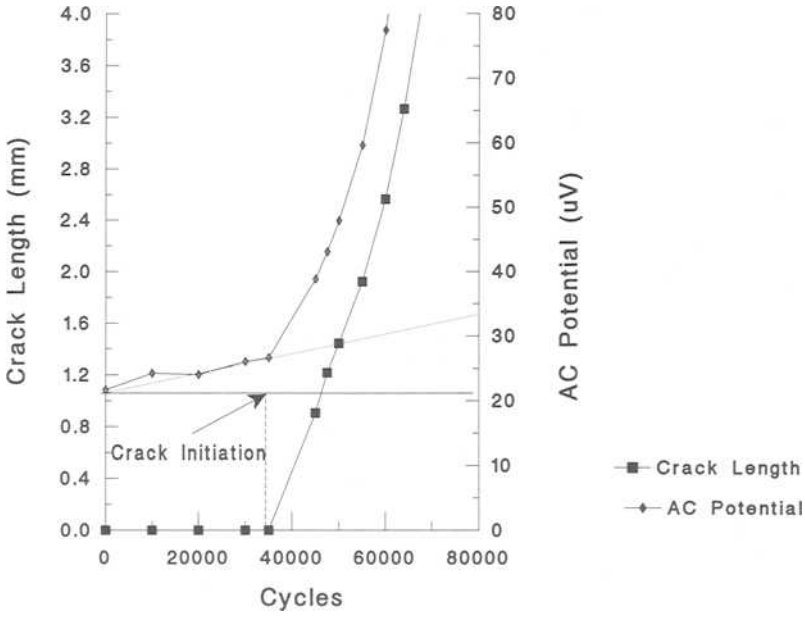

FIG. 9—*Plot of crack length and AC potential versus cycle number for a three-hole specimen showing AC potential increases before visible crack growth.*

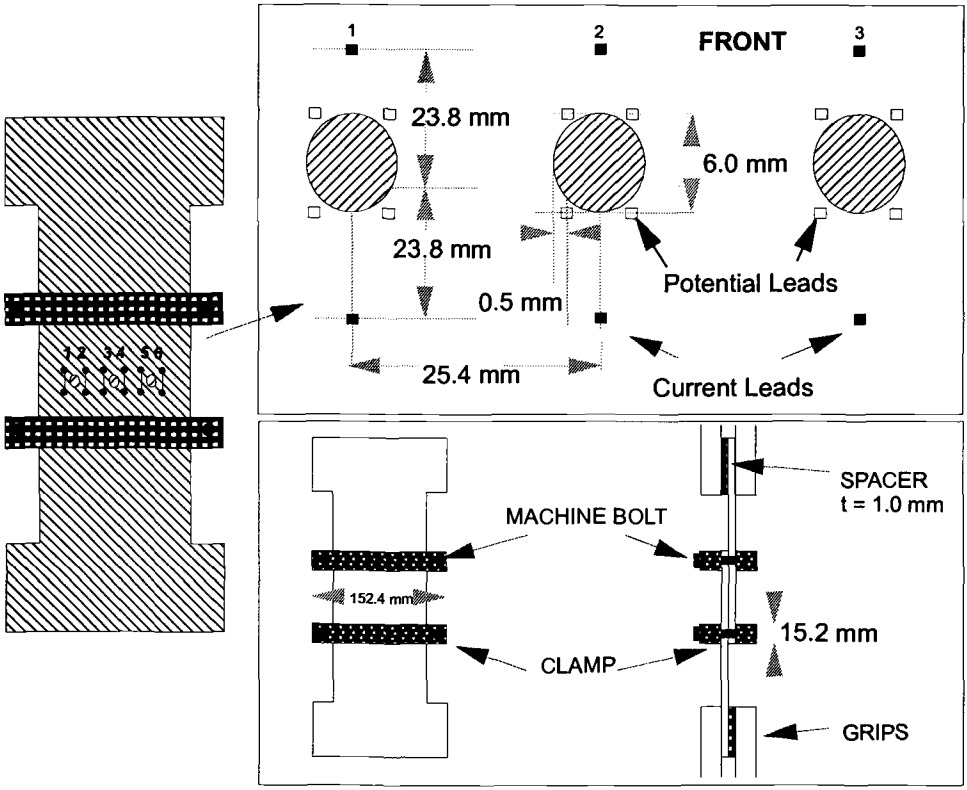

FIG. 10—Diagram of riveted panel specimen showing current and potential lead placement.

minimize the bending at the single row of rivets and to cause fatigue cracks to propagate under tension-tension cycling, two clamps were placed at either end of the lap joint. These clamps were effective in minimizing bending, and fatigue cracks were easily observed initiating from the rivets. The crack profiles indicated that there was no out of plane bending present.

The cracking initiation and initial crack growth is different for the riveted panels. The cracking from the riveted panels starts subsurface at the feather edge of the rivet. The crack grows subsurface until it passes through the chamfer in the panel and emerges to the surface. The cracks in the one and three-hole panels were through-cracks. The visual cracks observed in the riveted panels were always through-cracks, but they had to grow ~0.8 mm from the feather edge before they emerged to the surface and became through-cracks.

The effect of current frequency on the relation between crack length and potential was measured and the results are shown in Fig. 11. The sensitivity to the measurement of crack growth by ACPD increases with AC current frequency. For crack lengths greater than 1.0 mm the data were fit to Eq 3 and the slope m was 76.7, 159.7, and 259.0 $\mu m/\mu V$ for current frequencies of 30, 10, and 3 kHz. In the riveted panel test specimens, cracks were not generally observed until they reached a length of approximately 1.0 mm. Experiments on duplicate specimens were carried out to determine the repeatability of the measurement technique, and these results are shown in Fig. 12. The amount of scatter in the data increases with current frequency, as it did in the experiments on the three-hole experiments, but the

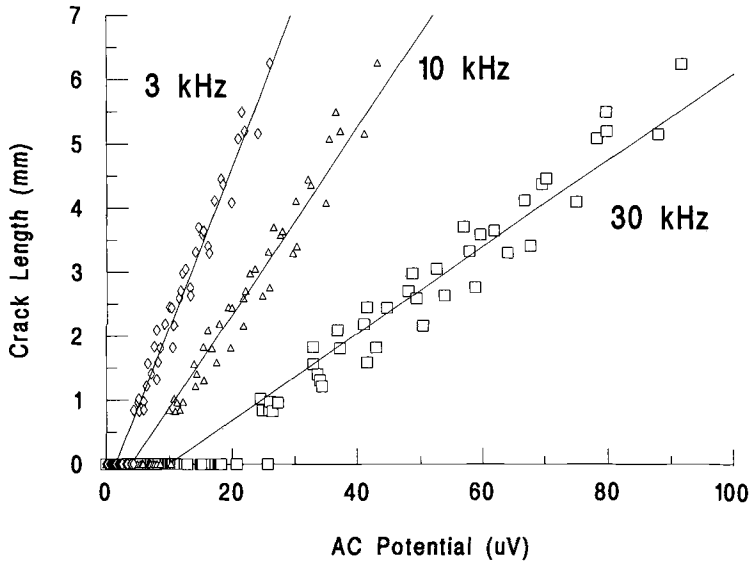

FIG. 11—*Plot of crack length versus AC potential for a riveted panel at frequencies of 3, 10, and 30 kHz. Least squares fit lines are plotted for the three frequencies.*

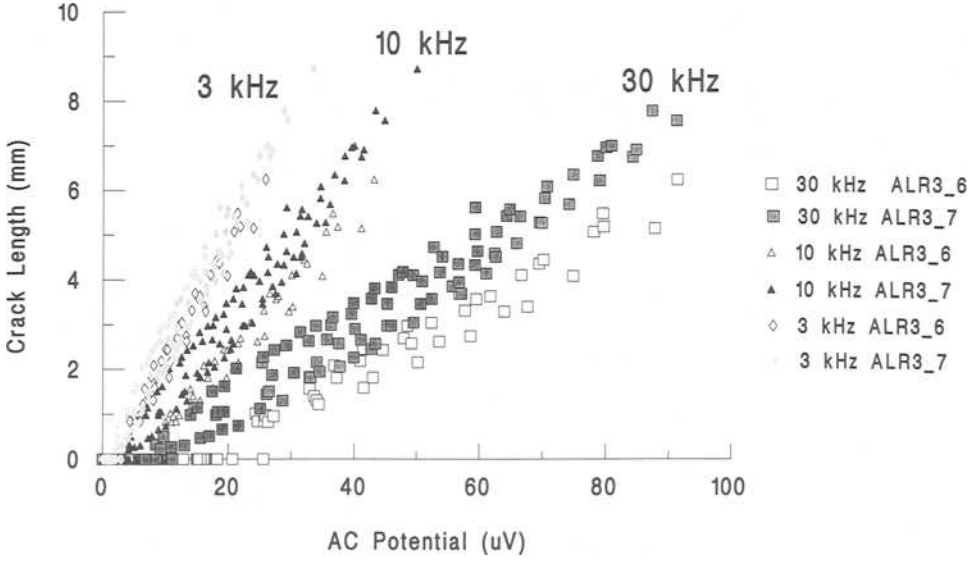

FIG. 12—*Plot of crack length versus AC potential for two duplicate riveted panel specimens for frequencies of 3, 10, and 30 kHz.*

amount of scatter is somewhat greater. The correlation coefficients for the linear fits varied from 0.95 for 30 kHz data to 0.98 for 3 kHz data.

The AC potential was observed to increase before any visible crack growth could be seen. Results similar to those shown in Fig. 9 for the three-hole panels were obtained. To determine if this effect was due to crack growth or to an inaccuracy in the visible crack length measurements, a series of crack initiation experiments were performed. A riveted panel was subjected to a stress waveform that consisted of alternating blocks of low-stress ratio (high-stress amplitude) and high-stress ratios (low-stress amplitude), with the maximum stress kept constant. The intent of this stress history was to grow the crack at the low-stress ratio cycling and to mark the crack front at the high-stress ratio cycling. A number of different combinations of stress ratios were examined, but the combination of a low-stress ratio of 0.10 and a high-stress ratio of 0.70 gave the best fracture surface banding. Figure 13 shows a plot of crack length versus change in AC potential from the start of stress cycling, as well as a schematic representation of the stress history. A current frequency of 30 kHz was used for these experiments. Typically each stress ratio band would represent 2000 to 5000 cycles. The crack length measured by fracture surface banding in the scanning electron microscope (SEM) showed a linear increase in crack length with AC potential. The optical measurements were unable to measure crack length until the crack had grown more than 1.0 mm. In the case of the data in Fig. 13, visible crack growth occurred somewhere between measurement numbers two and three. The cracking observed in the SEM showed that the crack initiated from the feather edge of the rivet. The crack had to grow ~0.80 mm before it became a through-crack at which point it would be visible on the surface. This experiment showed that the increase in potential before visible crack growth is detected is due to actual crack growth. The limited results shown in Fig. 13 suggest a linear relationship between crack growth and potential for short cracks, but more detailed experiments are needed to make a definite statement about this.

The effect that plastic deformation has on the relationship between AC potential and crack length was investigated on the single-hole specimens with an *R*-curve test. Gibson [*5*] has

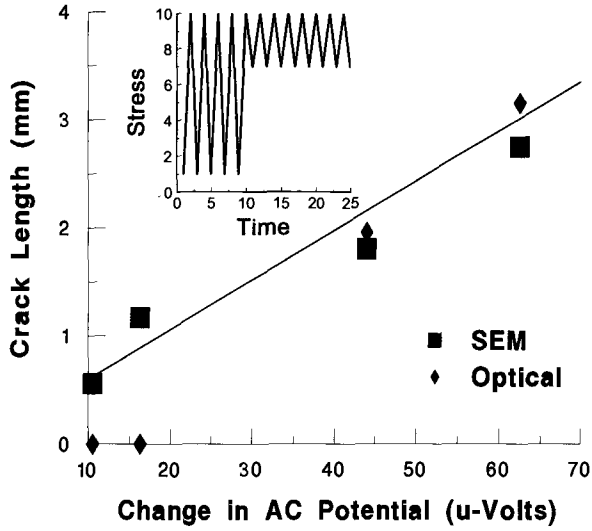

FIG. 13—*Plot of crack length versus change in AC potential for crack initiation test on riveted panel. Crack lengths measured by fracture surface banding in the SEM and that measured optically are shown.*

shown that in A533B steel there is a decrease in measured AC potential prior to crack growth. This is caused by a change in magnetic permeability due to the plastic deformation in an *R*-curve test. This effect was examined in the single-hole specimens. Three single-hole specimens were fatigue-precracked at a stress amplitude of 100 MPa and stress ratio of 0.10 to obtain crack lengths between 7 and 9 mm. The specimens were then tested in position control using a ramp rate of 0.127 mm/min. Load, position, AC potential, and crack length were measured at a one-second interval. Only the longest crack's length and potential were measured. A typical load displacement plot is shown in Fig. 14*a*. Figure 14*b* shows a plot of AC potential and visible crack length versus position. The initial rapid increase in AC potential is due to opening of the crack, which eliminated any fracture surface shorting which occurred due to fatigue crack closure. The steps in the crack length measurement occurred because it was difficult to continuously follow the crack tip. The rapid increase in potential and crack length occurs near maximum load. These data as well as the fatigue precracking data are replotted in Fig. 15, which is a plot of AC potential versus crack length. This plot shows that the *R*-curve data are simply a linear extension of the fatigue data. A careful examination of Fig. 15 shows that there is an approximate 20 μV linear shift in the *R*-curve data with respect to the fatigue precracking data. The author does not feel that this observation is of significance. Two other specimens tested under similar conditions did not show this effect. The visual measurement of the crack length during the *R*-curve test was not as accurate as that determined during fatigue precracking; therefore, it is likely that this apparent shift between fatigue and *R*-curve data is due to experimental error. The relationships determined in the fatigue experiments can be applied to the *R*-curve test results. The other two specimens tested showed similar result to that shown in Fig. 15. The large scale plasticity, which occurs in *R*-curve testing, had no effect in the AC potentials. The results reported by Gibson on A533B pressure vessel steel are not universal, and they do not apply to thin sheet high-strength aluminum alloys.

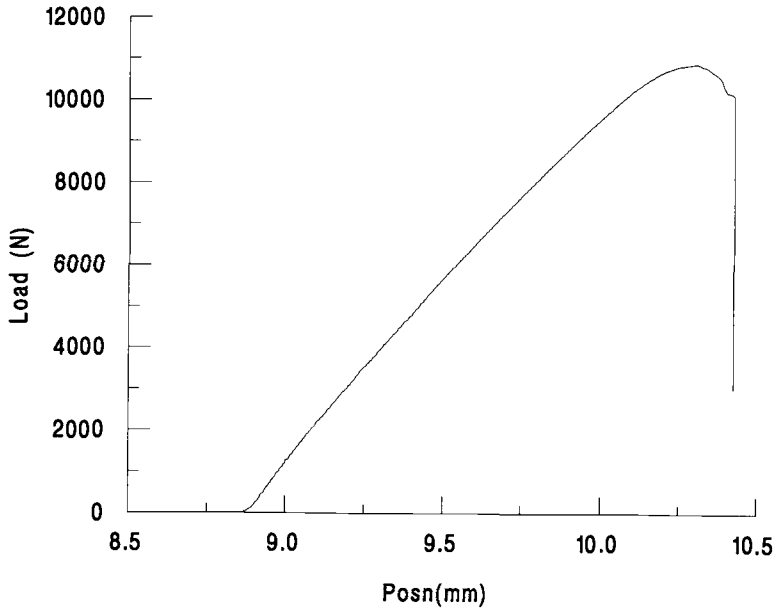

FIG. 14*a*—*Plot of load versus position for* R-*curve test.*

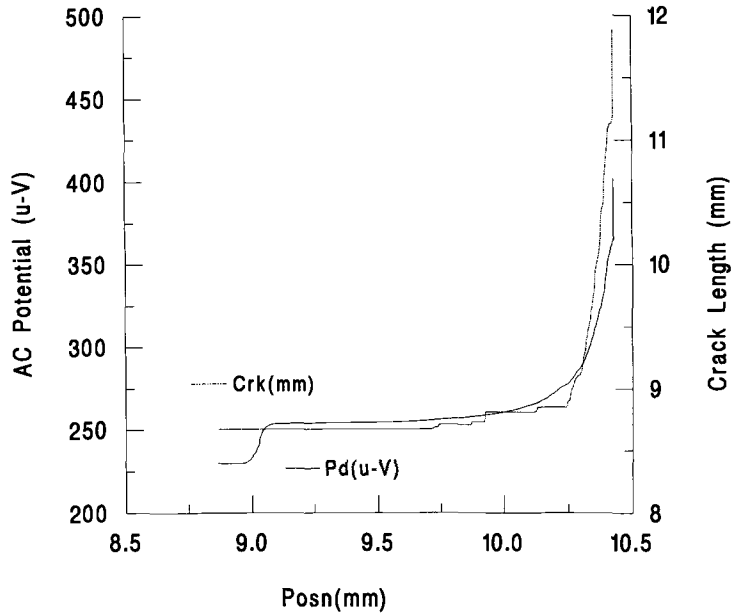

FIG. 14*b*—*Plot of crack length and AC potential versus position for* R-*curve test.*

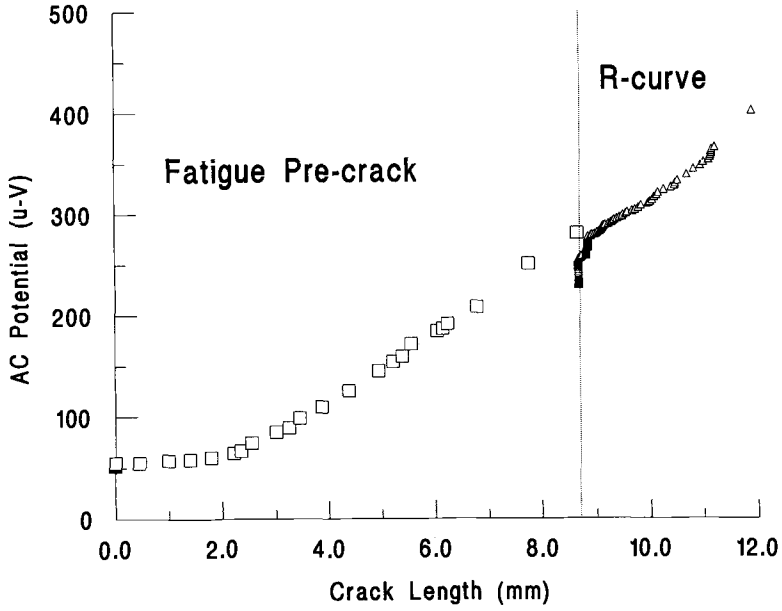

FIG. 15—*Plot of AC potential versus crack length, comparing fatigue precracking results to* R-*curve results.*

The theoretical crack length resolution of ACPD for the specimen geometries used in these experiments would be difficult to determine and would require a detailed finite element study. This is beyond the scope of the work reported herein. A relatively simple estimate of the crack length resolution can be made by substituting in Eq 3 a typical potential voltage and adding to that value the typical system noise (100 nV) and determine the effect of the noise on the calculated crack length. This was done for the three specimen geometries and AC current frequency using a potential of 50 μV with a noise of 100 nV. The results are tabulated below:

Frequency, kHz	Single-Hole Crack Error, μm	Three-Hole Crack Error, μm	Riveted Panels Crack Error, μm
30	3.49	2.93	7.67
10	6.89	7.62	15.97
3	14.01	16.31	25.9

The results in this table are estimates of the best crack length resolution obtainable for a particular specimen geometry and a particular current frequency. The actual resolutions were not determined, but would be greater than those shown in the table.

Summary and Conclusions

The technique of AC potential drop was applied to typical aluminum aircraft panel test specimens. The technique was evaluated to determine its sensitivity for measuring multiple-site crack initiation and growth under cyclic fatigue conditions. The technique was also evaluated for monotonic *R*-curve testing. The optimum locations for attaching both potential leads and current leads were determined for three-hole specimens and for specimens with a single row of three rivets. The effect of current frequency on the sensitivity of the technique to measure crack growth was also examined.

Theoretical and empirical correlations of AC potential with crack length were examined. The theoretical relationship, which predicted crack length from the ratio of active to reference potentials, worked poorly because the assumptions from which the theoretical relationship was developed were not met. It was found that the initial potential measured on an uncracked hole or rivet varied from specimen to specimen and from hole to hole. It was found that, if this initial potential was subtracted, a simple linear equation could be used to correlate the data. The equation used was as follows

$$a = m \times (Pd - Pd_0) + b$$

The slope m determines the sensitivity of ACPD in measuring crack length, with lower values of m representing increased sensitivity. A summary of the slopes, m, for all the specimen geometries tested is given as follows.

Frequency, kHz	Single-Hole, μm/μV	Three-Hole, μm/μV	Riveted Panels, μm/μV
30	34.9	29.34	76.7
10	68.9	76.24	159.7
3	140.1	163.1	259

The minimum visually detectable crack was 0.5 mm for three-hole specimens and 1.0 mm for riveted panels. Before cracks were detected visually, an increase in the potential was observed. Test specimens were subjected to low- to high-stress ratio cycling, which produced bands on the fracture surface. When these specimens were examined in the scanning electron microscope, the widths of these bands were correlated linearly to the measured AC potentials. It was shown that the AC potential increase was due to crack advance. Therefore, the AC potential can be used to detect the presence of cracks smaller than the visual detection limit in laboratory conditions.

R-curve testing was performed on single-hole specimens. These experiments showed that the AC potentials were not affected by the deformation in these tests. Correlations of crack length to potential measured during fatigue accurately predicted the crack advance in the *R*-curve tests. The crack length relationships developed herein are not affected by the monotonic loading conditions for the materials/specimens examined.

Acknowledgments

The author would like to acknowledge the financial support of the U.S. Department of Transportation's Volpe National Transportation Systems Center in Cambridge, Massachusetts. The technical support and advice from Dr. Oscar Orringer and the assistance of Steve Peltzman for performing most of the experimental work is also acknowledged.

References

[1] Saxena, A. and Hudak, S., *International Journal of Fracture,* Vol. 14, Oct. 1978, pp. 453–467.
[2] Jablonski, D., Journet, B., Vecchio, R., and Hertzberg, R., *Engineering Fracture Mechanics,* Vol. 22, No. 5, 1985, pp. 819–827.
[3] Newby, J., Ed., *Metals Handbook Volume 8 Mechanical Testing Ninth Edition,* American Society for Metals, Metals Park, OH, pp. 386–391.
[4] Ritchie, R. O., Garrett, G. G., and Knott, J. F., *International Journal of Fracture,* Vol. 7, 1971, pp. 462–467.
[5] Gibson, G. P., *Engineering Fracture Mechanics,* Vol. 32, No. 3, 1989, pp. 387–401.
[6] Collins, R., Dover, W. D., and Michael, D. H., *Nondestructive Testing,* Vol. 8, Academic Press, London, UK, 1985, pp. 211–267.
[7] Jablonski, D. A., "*Development of ACPD Procedures for Crack Detection in Aluminum Aircraft Panels,*" final report to U.S. Department of Transportation, Volpe National Transportation Center, Cambridge, MA, Dec. 1990.

Peter C. McKeighan,[1] *Christopher P. Tabrett,*[2] *and David J. Smith*[3]

The Influence of Crack Deflection and Bifurcation on DC Potential Drop Calibration

REFERENCE: McKeighan, P. C., Tabrett, C. P., and Smith, D. J., **"The Influence of Crack Deflection and Bifurcation on DC Potential Drop Calibration,"** *Special Applications and Advanced Techniques for Crack Size Determination, ASTM STP 1251,* J. J. Ruschau and J. K. Donald, Eds., American Society for Testing and Materials, Philadelphia, 1995, pp. 51–66.

ABSTRACT: Finite element and analog techniques are used to assess the influence of abnormal crack morphologies on the potential drop (PD) response of an M(T) specimen. All crack geometries considered, including simply deflected, bifurcated, and periodic sawtooth morphologies, result in higher potentials than observed for an undeflected crack. The greatest influence was observed with a bifurcated crack even with relatively short branch segment lengths. The potential drop responses are assessed in terms of the overestimates of stress intensity factor which result if a standard, undeflected crack PD calibration is applied to the PD response of the deflected geometry. The overestimate of stress intensity factor generally increases as deflection angle or crack length increases. Furthermore the PD response measured from a single probe set configuration is slightly less influenced by crack deflection than a dual probe configuration. This influence is also minimized by increasing the probe gage length and sacrificing overall sensitivity. Provided the deflection geometry of a given crack is constant, an effective probe gage length can be determined and used with the standard undeflected crack calibration to approximate closely the PD response of the deflected geometry.

KEYWORDS: potential drop (PD), crack deflection, crack bifurcation, crack roughness, finite element technique, analog technique, effective probe gage length

The electrical potential, or potential drop (PD) technique is used widely to remotely monitor crack length during fatigue testing. The technique was first introduced by Barnett and Troiano [*1*] who examined hydrogen embrittlement in notched tension specimens. Johnson [*2*] subsequently used the method of conjugate functions to generate a closed form analytical calibration for finite width cracked plates. Concurrent work by Gilbey and Pearson [*3*], using conformal transformation techniques and computer simulation, gave results very similar to Johnson. Furthermore Johnson's calibration was first verified experimentally by Li and Wei [*4*] using center-cracked specimens.

The potential drop method measures the change in the potential caused by a discontinuity (crack) in a current-carrying body (specimen). As the crack grows, the effective cross-sectional area of the specimen decreases and the electrical resistance increases. Given a constant current input, the magnitude of the voltage difference between two fixed points on either side of the crack depends on the size and shape of the crack. Whereas visual measurement

[1] Senior research engineer, Southwest Research Institute, San Antonio, TX 78228-0510.
[2] Research assistant, University of South Australia, South Australia 5095, Australia.
[3] Reader in Engineering Materials, Department of Mechanical Engineering, Queen's Building, University of Bristol, Bristol, BS8 1TR, UK.

of crack length is confined to a surface observation, crack lengths derived from the direct-current (DC) PD technique provide a total crack length measure including the effect of possible crack front curvature.

The vast majority of PD development work has focused on single cracks which grow perpendicular to the applied loading. However, there are practical circumstances where crack growth can occur at an angle θ from the expected growth direction normal to the applied loading direction. This has been observed during crack growth in Ni-based superalloys and Al-Li alloys, where the effects of crystallographic texture and slip plane cracking lead to noncoplanar crack growth [*5,6*]. It is not uncommon for these deflection angles to be quite large. For example, McKeighan and Hillberry [*7*] observed fatigue crack deflection angles of between 20 to 30° which remained relatively constant for extensive amounts of crack growth in an Al-Li-Zr alloy. Furthermore other more complex, branched, and bifurcated cracks have also been observed in Al-Li alloys [*8,9*].

Limited research has been carried out to examine the influence of deflected crack morphologies on PD measurement. Sakagami et al. [*10*] applied optimization techniques to identify the location, size, and inclination of a deflected crack using multiple current input locations. However, the method is limited to simple crack deflections, requires an estimate of the location, size, and inclination of the crack and consequently would appear difficult to implement. Green et al. [*11*] investigated how cracks with a periodic sawtooth morphology (simulating roughness) and cracks with large deflections ($\theta = 45°$) influence PD calibrations. They report poor correlation with the conventional undeflected crack PD calibration for both types considered.

The aim of the work reported in this paper is to investigate how deflected and bifurcated cracks influence PD calibrations for an M(T) specimen. This is particularly applicable to fatigue crack growth (FCG) testing where extensive visual observation of the crack may not be possible and noncoplanar crack morphologies occur. Fatigue crack growth testing in aggressive environments and tension-compression loading with antibuckling fixtures are examples of situations when visual observation of the crack is typically limited. Results from finite element and analog simulations of various geometries including deflected, periodic sawtooth and branched cracks are presented. The results are compared to a standard PD calibration and are assessed to consider possible errors in crack length measurement. These crack length errors are used to estimate the difference in the stress intensity factor if a standard PD calibration were used with the measured PD response of a noncoplanar crack. Finally, the influence of probe position, as well as possible methods for modifying the standard calibration, are also considered.

Numerical and Experimental Procedures

The steady-state electrical potential field in a current carrying body satisfies Laplace's equation

$$\nabla^2 V = 0 \tag{1}$$

where V is the electrical potential at a given point with cartesian coordinates x, y. If the boundary conditions of a specimen are relatively simple, closed form analytical solutions of Eq 1 can be derived [*2*]. As the boundary conditions increase in complexity, as is the case for a deflected or bifurcated crack, numerical methods such as conformal mapping must be used generally to solve Eq 1 [*12*]. This equation can also be simulated using analog techniques. Analog models for complex crack shapes and complicated specimen geometries have been created from graphetized conducting paper [*11–14*], rheoelectric tanks [*15*], and

graphite/wax blocks [*16*]. In this work the finite element (FE) method and a foil analog model of the M(T) specimen were used to obtain PD results. For both methods the specimen was treated as a two-dimensional body with the crack fully open.

Numerical Method

The governing mathematical formulation of a current flow problem, Eq 1, is identical to that of steady-state heat flow [*13*]. Consequently, the heat flow option in the ANSYS finite element package was used. A schematic of one half of the specimen is illustrated in Fig. 1*a*. The boundary conditions included:

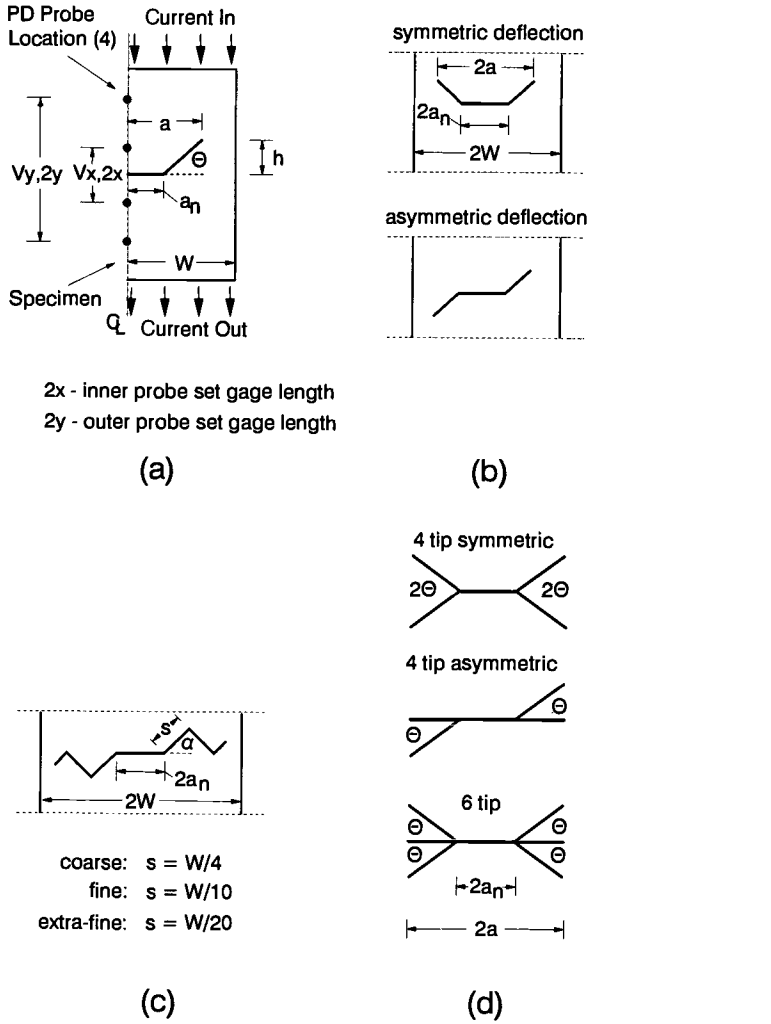

FIG. 1—*Schematics of* (a) *a deflected crack geometry,* (b) *crack symmetry and complex multisegmental morphologies including* (c) *sawtooth, and* (d) *bifurcated cracks.*

(*a*) constant current density along the top and bottom edges,
(*b*) no current flow across both of the vertical edges, and,
(*c*) no current flow across the entire crack face.

The symmetric boundary conditions imply that the results apply for both an M(T) as well as an SEN(T) specimen. For an M(T) specimen with the boundary conditions described previously, the crack geometry is symmetric about the specimen centerline as illustrated in Fig. 1*b*.

Four node, isoparametric elements were used in the FE model with a finer mesh density at the crack tip. The aspect ratio of the model, defined by the ratio of the height to the width, was 9:1. For all crack geometries the input current density was fixed. Potentials were recorded at various positions along the specimen centerline corresponding to width normalized, PD half gage lengths of 0.1, 0.2, 0.5, 1.0, 1.9, 2.0, and 2.5.

The crack geometry illustrated in Fig. 1*a* is bisegmental with an initial undeflected segment length a_n/W and a deflected segment at an angle θ from the conventional growth direction. The FE evaluations, summarized in Table 1, are subdivided into two geometric classifications:

Case A: fixed deflection geometry (a_n/W and θ), variable crack length (a/W), and,
Case B: fixed crack tip position (a/W and h), variable deflection geometry (a_n/W and θ).

The analyses included in Case A simulated a crack with an initial undeflected segment (possibly a starter notch or precracked region) followed by a segment with a constant deflection angle θ. This type of crack geometry is generally consistent with observations in Al-Li alloys [*7*] and Ni-based superalloys [*6*]. The analyses included in Case B were performed to gain further insight into the influence of crack path on the PD response.

TABLE 1—*Summary of the finite element simulations of simple deflection geometries.*

Geometric Description	a_n/W	θ°	Comments
		CASE A	
Fixed = a_n/W, θ	0.15	0	$0.20 \le a/W \le 0.85$
Variable = a/W		15	$0.20 \le a/W \le 0.85$
		30	$0.20 \le a/W \le 0.85$
		45	$0.20 \le a/W \le 0.85$
	0.30	30	$0.35 \le a/W \le 0.85$
		45	$0.35 \le a/W \le 0.85$
	0.45	30	$0.50 \le a/W \le 0.85$
		45	$0.50 \le a/W \le 0.85$
	0.60	30	$0.65 \le a/W \le 0.85$
		45	$0.65 \le a/W \le 0.85$
		CASE B	
Fixed = a/W, h	0.15 to 0.70	20 to 59	$a/W = 0.85$, $h = 0.25W$
Variable = a_n/W, θ	0.10 to 0.55	33 to 59	$a/W = 0.85$, $h = 0.50W$
	0.10 to 0.50	24 to 59	$a/W = 0.65$, $h = 0.25W$
	0.10 to 0.35	43 to 59	$a/W = 0.65$, $h = 0.50W$

Analog Method

The analog model used domestic aluminum foil as a conductive material which was cut to the dimensions of an M(T) specimen. The aspect ratio of the model, defined by the ratio of height to half width, was 7:1. By applying the appropriate boundary conditions, potentials measured on the analog geometry were then directly applicable to the specimen. Various crack geometries were simulated by cutting the analog model with a scalpel and inserting a nonconductor between the crack faces. Care was taken to properly simulate a narrow notch and sharp crack tip since the PD calibration can depend on both of these factors [*2*].

Current was supplied from a pulsed, direct current PD unit connected to the analog model. Potentials were measured through copper wires attached to the foil along the specimen centerline. A dual probe PD unit was used to measure the ratio of the potentials between two sets of probes attached to the specimen. The primary advantage of this arrangement is that compensation is automatically made for changes in the applied current or sample temperature as well as for material and instrumentation variations [*17*]. The definition of the probe gage lengths $2x$ and $2y$ is illustrated in Fig. 1*a*. In these analog studies the inner and outer probes were positioned with $x/W = 0.1$ and $y/W = 1.9$, respectively. These probe positions reflect the optimum possible with the M(T) specimen geometry currently used for FCG testing in the laboratory.

A summary of the analog simulations is given in Table 2. To verify the methods used, five identical trials for an undeflected ($\theta = 0°$) crack were performed. This consequently allowed an evaluation of the accuracy and repeatability of the analog technique. In addition the influence of crack asymmetry, defined along the specimen centerline and illustrated in Fig. 1*b*, was examined for simply deflected cracks. The analog technique was also used for more complicated crack geometries not easily modeled with finite elements. For example, three sawtooth crack geometries of differing roughness, Fig.1*c*, were examined. Furthermore, the effect of multiple crack branches with $\theta = 45°$, Fig. 1*d*, was also evaluated.

Results

Theoretical Calibration

For an M(T) specimen with a total width $2W$, Johnson [*2*] derived the following voltage ratio, valid for all a/W

TABLE 2—*Summary of M(T) specimen analog simulations, all with an initial undeflected segment length* $a_n/W = 0.15$.

Description	Number of Tests	Deflection of Angle	Number of Crack Tips	Comments
Undeflected crack	5	$\theta = 0°$	2	
Symmetric	1	$\theta = 45°$	2	
Asymmetric	2	$\theta = 45°$	2	
Periodic sawtooth	3	$\alpha = \pm 45°$	2	extra fine, $s = W/20$
	2	$\alpha = \pm 45°$	2	fine segment, $s = W/10$
	3	$\alpha = \pm 45°$	2	coarse segment, $s = W/4$
Multiple branches	1	$2\theta = 90°$	4	
	1	$\theta = 45°$	4	
	1	$\theta = 45°$	6	

$$\frac{V}{V_0} = \frac{\cosh^{-1}\left(\frac{\cosh(\pi x/2W)}{\cos(\pi a/2W)}\right)}{\cosh^{-1}\left(\frac{\cosh(\pi x/2W)}{\cos(\pi a_0/2W)}\right)} \tag{2}$$

where

x = half the potential probe gage length,
V = the measured potential at a crack length a/W, and
V_0 = a measured potential at an initial crack length a_0/W.

A theoretical calibration for the voltage ratio for a dual probe configuration can be obtained from Eq 2

$$\overline{V} = \frac{V_x}{V_y} = \frac{V_x/V_0}{V_y/V_0} = \frac{\cosh^{-1}\left(\frac{\cosh(\pi x/2W)}{\cos(\pi a/2W)}\right)}{\cosh^{-1}\left(\frac{\cosh(\pi y/2W)}{\cos(\pi a/2W)}\right)} \tag{3}$$

where

$\overline{V}$ = the dual probe potential ratio, and
y = half the probe gage length for the outer set of probes, Fig. 1*a*.

In addition to the advantages discussed earlier, the dual probe compared to the single probe configuration has the advantage of not requiring information about the initial crack length, a_0. However, this advantage is partially offset by a loss in sensitivity. For example, the ratio of the single probe voltage at $a/W = 0.7$ to that at $a/W = 0.15$ is approximately 5 for $x/W = 0.1$. When a dual probe arrangement is used, the ratio of the voltages at the same crack lengths is dependent on the probe gage length y/W. For instance, with $x/W = 0.1$ and $y/W = 2.5$, the ratio of the dual probe voltages at $a/W = 0.7$ to that at $a/W = 0.15$ is approximately 4.2 indicating a sensitivity loss of about 15% when compared to the single probe results. It is important to note that as y/W increases to large values, the dual probe arrangement is equivalent to the single probe configuration at a given probe gage length x/W. Hence the results denoted $y/W = \infty$ correspond to the single probe potentials.

Verification of Analog and FE Methods

A comparison between the theoretical calibration, Eq 3, and FE results for an undeflected crack reveals that the potential ratio $\overline{V}$ from the FE results was between 97 to 99% of the theoretical calibration. In general, the greater error occurred at shorter crack lengths. The analog results for the five replicate tests of an undeflected crack also compare favorably to the theoretical results. Crack length predictions using a curve fit to the results range from a 2% overestimate at $a/W = 0.2$ to less than a 0.4% underestimate for $a/W > 0.35$. No systematic errors were noted in either the analog or finite element results.

Simply Deflected Cracks

Finite element results for Case A are shown in Figs. 2 and 3 where the potential ratio Φ is defined by

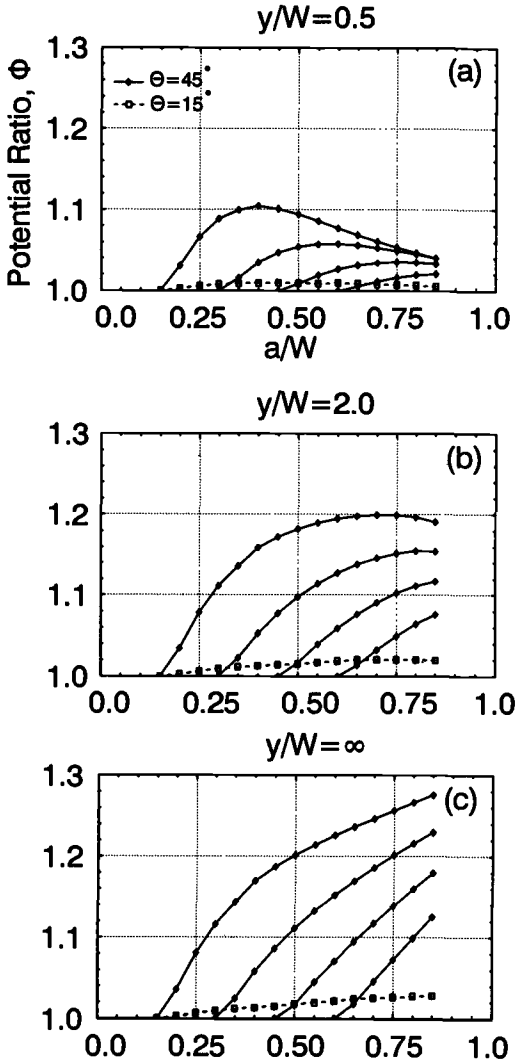

FIG. 2—*Finite element derived potential ratios* Φ *at* x/W = *0.1 and* θ = *15° and* θ = *45° for* (a) y/W = *0.5,* (b) y/W = *2.0, and* (c) y/W = ∞ (*single probe*).

$$\Phi = \frac{\overline{V}_\theta}{\overline{V}_{\theta=0^\circ}} \tag{4}$$

where $\overline{V}_\theta$ is the dual probe potential ratio for a deflected crack and $\overline{V}_{\theta=0^\circ}$ is for an undeflected crack. This potential ratio indicates the deviation from the undeflected crack calibration. For instance, a value of Φ = 1.1 implies that the deflected crack potential is 10% higher than the undeflected crack potential at a given *a/W.*

The influence of undeflected segment length, crack deflection angle, and probe position on potential ratio as crack length increases can be inferred from Figs. 2 and 3. As the

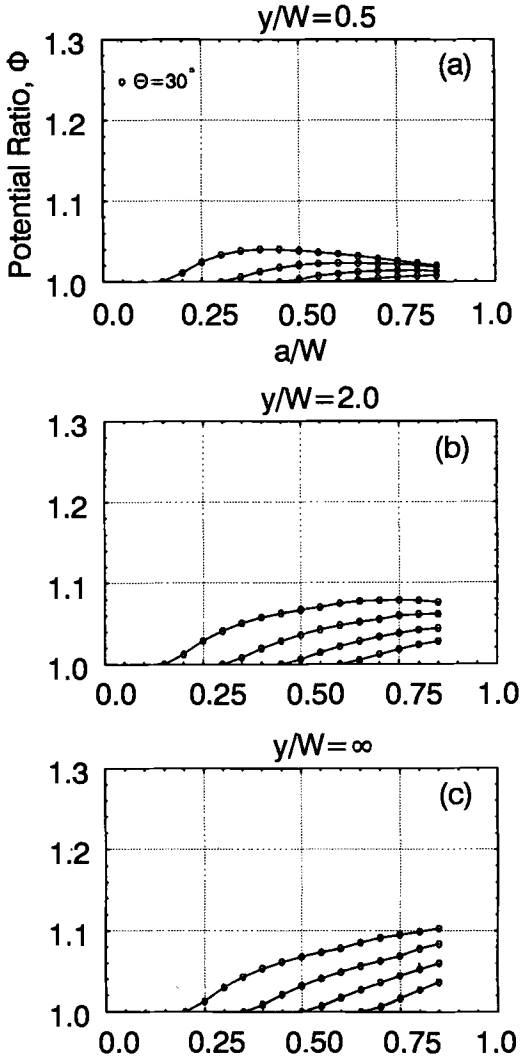

FIG. 3—*Finite element derived potential ratios* Φ *at* x/W = *0.1 and* θ = *30° for* (a) y/W = *0.5,* (b) y/W = *2.0, and* (c) y/W = ∞ (*single probe*).

undeflected segment length increases, Φ becomes lower over the crack length range. Also, as crack deflection angle θ increases, Φ increases. Both of these trends indicate that when the deflected crack tip is closer to the potential probes, the ratio of the PD voltage for the deflected crack to the undeflected crack increases. The ratios Φ for a deflection of 15° and various undeflected segment lengths are all less than 1.03; for θ = 30° less than 1.11 and for θ = 45° less than 1.28.

The position of the probes can quite dramatically affect both the magnitude of Φ as well as its variation with increasing crack length. In general the potential ratios for the dual probe

results reach a peak and subsequently decrease as a/W increases. Conversely, the Φ ratios for the single probe configuration ($y/W = \infty$) always increase with increasing crack length. The potential ratio at a given crack length also systematically increases as the outer probe gage length y/W increases. Since x/W is fixed for all the results presented, the potential ratio for the single probe configuration can be considered as an upper bound of the response.

The potential ratio Φ is shown in Fig. 4 as a function of deflection angle θ for the four fixed crack tip positions considered in Case B. Recall that for each of these evaluations, the crack tip position remained constant and the crack path to that position was varied. The deflected cracks with the higher out-of-plane deflection, h, exhibit consistently larger potential ratios. As was noted for the Case A results, the position of the outer probes can affect the potential ratio Φ significantly. The highest ratios occur when the outer probes are at larger gage lengths which is consistent with the Case A results. Moreover, it is interesting to note that Φ nearly varies linearly with deflection angle θ. Since each data point in the individual responses represents a fixed Δa_n interval, it is clear that Φ does *not* vary linearly with undeflected segment length a_n.

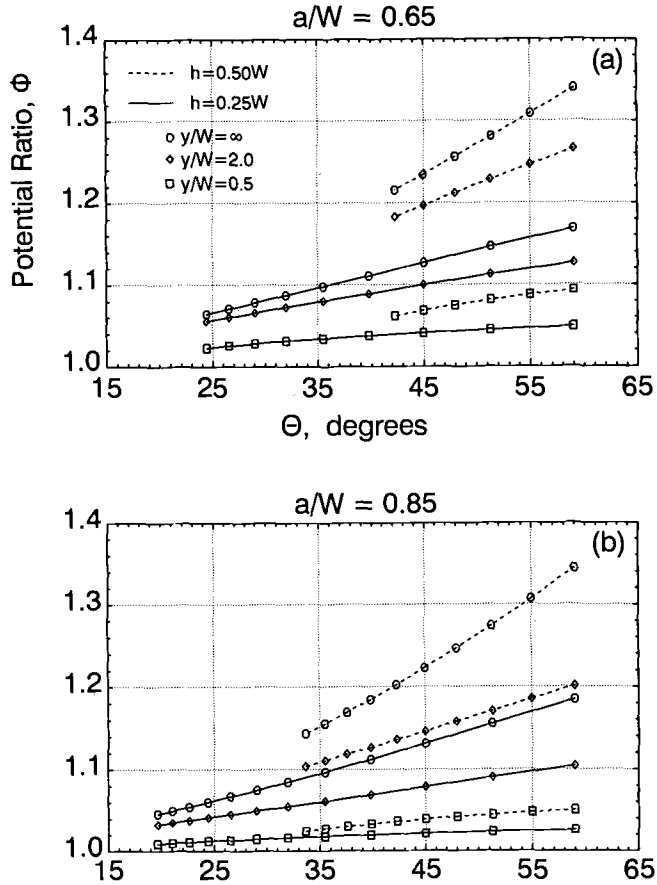

FIG. 4—*Finite element derived potential ratios* Φ *at* x/W = *0.1 for fixed crack tip positions of* (a) a/W = *0.65 and* (b) a/W = *0.85.*

Complex Crack Morphologies

The results from the analog experiments described in Table 2 are shown in Fig. 5. In practice fatigue cracks can exhibit varying levels of local roughness. The sawtooth crack geometries, illustrated in Fig. 1*c*, exhibited relatively low potential ratios with Φ typically less than 1.10. As the degree of roughness, or magnitude of s, increases, so too does the potential ratio Φ. In the limit as s increases, Φ should approach the results for the asymmetric $\theta = 45°$ crack geometry. Furthermore the significant decrease in Φ as a/W increases is probably a consequence of the periodicity of the sawtooth geometry. As the sawtooth crack increases in length, the effective gross angular deflection decreases. Hence at high a/W, the potential ratio should generally approach $\Phi = 1$ and the PD response should converge to the undeflected crack calibration. Green et al. [*11*] found that the fine roughness ($s = W/10$) case converged to the undeflected crack calibration. A greater difference, though, was observed in this work with even the extra-fine roughness case still differing from the undeflected crack results.

Unusual crack morphologies encountered during FCG testing are not necessarily symmetric, Fig. 1*b*. For the asymmetric case, the analog results in Fig. 5 show a decrease in potential ratio compared to the symmetric case. In one sense this is not surprising since for the symmetric case the two crack tips are closer together and contribute to a more perturbed potential field and higher net effect. Conversely, in the asymmetric geometry the crack tips are further apart and their net effect is decreased since it is distributed over a larger portion of the specimen. Moreover the symmetric analog results compare favorably to the equivalent finite element results indicated in Fig. 5. A similar trend with crack length can be observed with potential ratio differences between the analog and FE results typically less than 0.05.

The bifurcated, multiple crack tip results shown in Fig. 5 clearly exhibit much higher potential ratios than any of the other geometries considered. This implies that increasing the number of crack tips or branches evidently increases the disturbance in the potential field. Whereas the potential ratio increase between the two and four tip geometries is quite large, the potential ratio increase between the four and six tip geometries is much smaller. The striking similarity between the four tip and six tip bifurcations suggests that the outer

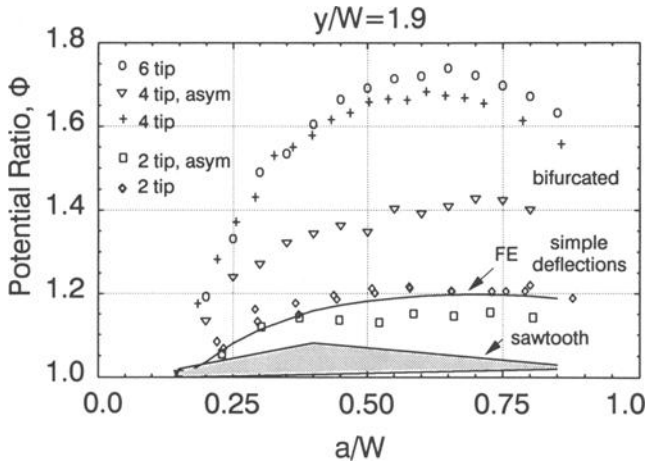

FIG. 5—*Potential ratios Φ from analog testing for more complex crack geometries with* x/W = *0.1 and* y/W = *1.9.*

branches dominate the potential measured along the specimen centerline. In effect it appears that these outer branches act to shield the influence of the included branch. Moreover the lower potential ratios for the asymmetric geometry when compared to the symmetric is consistent with the trend observed with the simply deflected, two-tip geometry.

Discussion

There are two features of the results that are examined in the following: the implications for estimating stress intensity factor (SIF) K and a modification to the standard theoretical PD calibration to take into account crack deflection. For the purposes of this analysis, it has been assumed that the crack length of interest in an abnormal crack morphology is the projected length. Moreover, it is important to note that provided information is available about the morphology of the deflected crack, the results given in the previous section will allow an experimentalist to estimate the influence of an abnormal crack morphology on the standard calibration curve.

Overestimations of K

Since the potential drop, $\bar{V}$ or V, for the deflected cracks examined in this work is always greater than that for the undeflected crack, using the standard calibration to determine the crack length will always give an overestimate of the actual projected length. Consequently there will also be an overestimate of the SIF as illustrated in Fig. 6 and based on projected crack length. Denoting the true projected crack length for the deflected crack as a/W and the apparent crack length determined from the standard calibration as a'/W, the ratio of the stress intensity factors at a/W and a'/W is

$$\Gamma = \frac{K(a'/W)}{K(a/W)} = \frac{\sqrt{\frac{a'}{W}\sec\left(\frac{\pi a'}{2W}\right)}}{\sqrt{\frac{a}{W}\sec\left(\frac{\pi a}{2W}\right)}} \tag{5}$$

where the standard M(T) calibration is used [*18*]. Thus, Γ represents the overestimate in K if a standard PD calibration for an undeflected crack were used for a deflected crack geometry.

The SIF ratio Γ is shown in Figs. 7 and 8 for representative Cases A and B results, respectively. In all cases there is an overestimate of K with the largest occurring when the

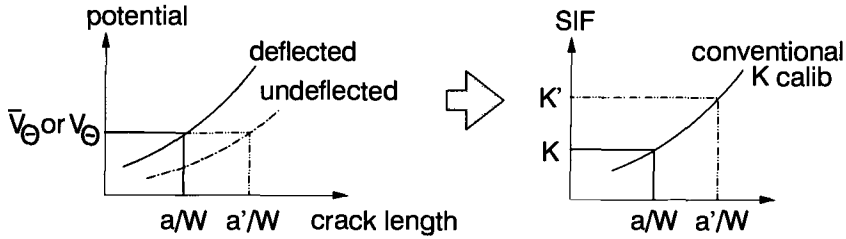

FIG. 6—*Methodology for calculating the overestimate of* K *resulting from an abnormal crack morphology.*

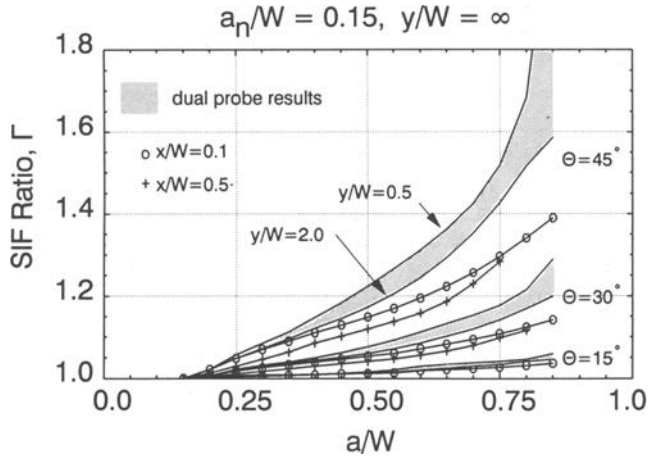

FIG. 7—*SIF ratio* Γ *for fixed deflection geometry (Case A) finite element results with* $a_n/W = 0.15$.

crack deflection angle is the greatest. The results shown in Figs. 7 and 8 indicate that for these simple deflections, the overestimate of K is generally in excess of 10% (that is, $\Gamma > 1.10$). However, for the lowest deflection angle, $\theta = 15°$, Γ is less than 1.06.

Whereas the potential ratio Φ had a tendency to reach a peak and decrease with a/W, Γ *always* increases. This is a consequence of the increasing sensitivity of K to crack length at longer crack lengths. It is also apparent that to minimize overestimates of K, the outer probes need to be located at higher y/W values for the dual probe case. Hence the lower limit of the SIF ratio variation is given by the single probe calibration $x/W = 0.1$ ($y/W = \infty$).

It is notable that with $x/W = 0.5$ for the single probe configuration, the lowest estimate of Γ is obtained. This is true for all of the deflection angles, crack lengths, and crack geometries considered in Figs. 7 and 8. Although the absolute magnitude of Γ is reduced with a single set of probes, the corresponding K overestimates can still be quite significant.

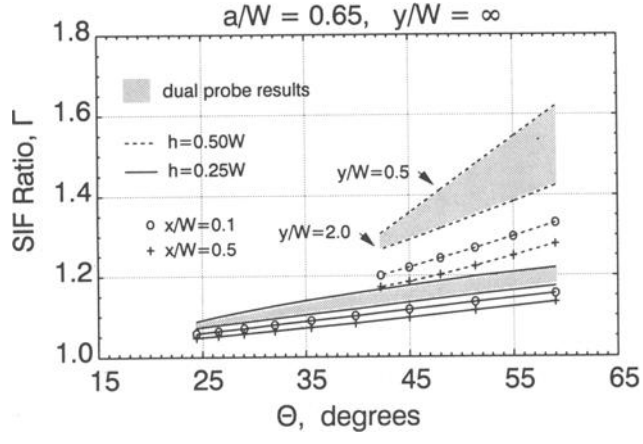

FIG. 8—*SIF ratio* Γ *for fixed crack tip position (Case B) finite element results at* $a/W = 0.65$.

This implies that x/W should be increased to minimize the overestimate of K. However, this may be offset by the significant loss in sensitivity with the increased gage length probes. For instance, with $x/W = 0.1$ the ratio of the single probe voltage at $a/W = 0.7$ to $a/W = 0.15$ is about 5 whereas with $x/W = 0.5$ this ratio is reduced to approximately 2. Yet another factor which will affect this decision is how the PD signal is being measured. Increasing the probe gage length should be considered only if the data acquisition system employed is robust enough to accurately measure smaller voltage changes at an offset voltage value.

If the overestimate of K is limited to 10%, the results shown in Fig. 7 can be interpreted to provide an estimate of the allowable deflected segment growth before this limit is exceeded. For the dual probe case, it is estimated that with $\theta = 45°$ and $a_n/W = 0.15$, the deflected segment can grow to a projected crack length of $a/W = 0.35$. For a single probe configuration this estimate increases to 0.4 for $x/W = 0.1$ and 0.45 for $x/W = 0.5$. Clearly at lower deflection angles these estimates are larger. For example with a dual probe configuration and $\theta = 30°$, the projected crack length must exceed 0.55 before Γ exceeds 1.10. For the lowest deflection angle, 15°, the K overestimate is *always* less than 10%. It should be noted that this deflection would be allowable with the newest crack deflection guidelines contained in the most recent draft ASTM E 647-93 [*18*].

It is interesting to note in Fig. 8 that the SIF ratio varies almost linearly with deflection angle θ. As observed with the potential ratio Φ, this linear variation is a function of θ and not a_n/W. This clearly indicates the primary significance of crack deflection angle in controlling the PD response of a deflected crack geometry. It is also apparent that the sensitivity of Γ to probe position increases as h increases. Finally, it appears as if the Γ difference between the dual probe $y/W = 2.0$ and all single probe configurations is a constant value dependent upon crack tip position and independent of deflection angle θ.

A summary of the overestimate of K arising from more complex crack morphologies, and derived from analog potential responses, is shown in Fig. 9. As might be expected from the potential ratio Φ results, the largest overestimate of K occurs for the bifurcated cracks. The extent of allowable crack growth before a 10% overestimate of K takes place is quite small, $\Delta a/W = 0.05$ to 0.10. Even though the high deflection angle $\theta = 45°$ may represent a limiting case, it is clear that a branched crack can severely influence the potential field in a

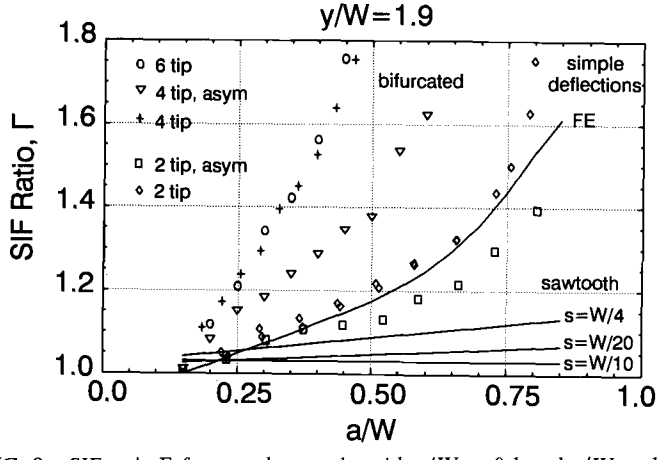

FIG. 9—*SIF ratio* Γ *from analog results with* x/W = *0.1 and* y/W = *1.9.*

specimen. The high Γ values, even at short crack lengths when K is *less* sensitive to crack length difference, are indicative of the significant potential field differences between a branched and an undeflected crack.

In contrast, the degree of allowable crack growth before Γ exceeds 1.10 is extensive for the sawtooth crack morphologies. In fact, only the coarse roughness sawtooth exceeds this value. It is interesting to note that Γ for the extra-fine case remains at a constant value insensitive to crack length. This implies that if a standard undeflected crack PD calibration were applied to this extra-fine periodic sawtooth geometry, a 3% overestimate of K would consistently occur regardless of total projected crack length. Nevertheless it should be reiterated that the magnitude of Γ for the periodic sawtooth cracks is generally low and on the order of the results observed with a constant deflection angle of 15° shown in Fig. 7.

Modifications to the Standard Calibration

It is apparent from the results presented that the PD response for a deflected crack geometry is significantly different than that of an undeflected crack. A simple method to closely approximate the PD response of a deflected crack geometry makes use of the observation that the potential field as measured on the centerline of a specimen, generally follows the form given by Eq 2. To modify the undeflected crack calibration, an "effective" probe gage length x'/W is introduced. This same technique has been used previously with undeflected crack PD results to correct for slight errors arising from physically positioning the probes [*17*] as well as minimizing the influence of initial PD value V_0 [*3*] in Eq 2. Further extending the technique to correct for abnormal crack morphologies is speculated to be possible due to the mathematical similarity of the solutions to Eq 1 for a deflected and undeflected crack.

This technique is evaluated by using single probe results from several finite element cases and Eq 2 with $a_0/W = 0.2$. Given a potential ratio V/V_0, Eq 2 was solved iteratively to yield an x'/W which represents an effective probe position for which Johnson's equation predicts the potential for a deflected geometry. Results of this analysis are presented in Fig. 10 in terms of the probe position variation defined by $x'/W - x/W$. The linear responses indicated in Fig. 10 were determined by considering three crack lengths spanning the total evaluated

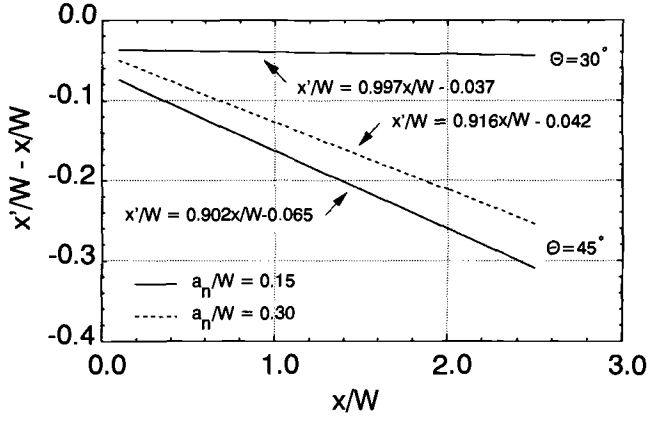

FIG. 10—*Effective single probe set gage length* x'/W *from FE results for deflected cracks with a fixed deflection geometry (Case A).*

range. The effective gage lengths varied minimally for the range in crack lengths considered with $\Delta x'/W < 0.04$ for $x/W = 2.5$ and $\Delta x'/W < 0.01$ for $x/W = 0.2$.

It is evident from Fig. 10 that the effective probe position is a function of both variables defining the deflection geometry, namely, a_n/W and θ. Furthermore it appears that the influence of deflection angle is greater than that of undeflected segment size. These results show that if the deflection geometry is relatively constant, an effective probe gage length x'/W can be employed in Eq 2 to predict the potential drop calibration.

This technique can be applied if a single visual crack length measurement is used to determine an effective gage length x'/W. However, the accuracy of this corrective procedure would be increased if more than one measurement were made.

Conclusions

1. The analog and finite element techniques utilized for predicting the PD response in an M(T) specimen with an undeflected crack were in excellent agreement with the theoretical calibration derived by Johnson [2].
2. Simply deflected, bifurcated and periodic sawtooth morphologies resulted in higher potentials than predicted from the theoretical analysis for an undeflected crack at an equal projected length. In general deflected cracks exhibiting symmetry about the specimen centerline resulted in higher measured potentials than asymmetric deflected cracks. Of all the unusual crack morphologies considered, a bifurcated crack, even of relatively short length, most influenced the PD response of the specimen.
3. Using an undeflected crack PD calibration for a deflected, bifurcated, or sawtooth crack results in an overestimate of the stress intensity factor based on projected crack lengths. This overestimate generally increases as the crack angle increases or the crack grows in length.
4. Results enable an analysis to be performed after FCG testing to correct crack length measurements on the basis of the actual crack geometry. Alternatively, limits are defined on the degree of crack deflection which gives less than or equal to 10% stress intensity factor overestimates.
5. A single probe set PD configuration is slightly less influenced by crack deflection than a dual probe configuration. Depending upon the particular potential drop recording system used, it may be best to sacrifice PD sensitivity by increasing probe gage length to consequently minimize the influence of crack deflection.
6. Given a constant crack morphology, an effective probe gage length x'/W derived from a visual crack length measurement can be used with Johnson's equation to closely approximate the PD response of the deflected geometry.

Acknowledgments

This work was undertaken as part of a project funded by British Aerospace, Airbus Ltd. (Filton, UK), whose support is gratefully acknowledged. Thanks are also due to Mr. Wu-Xue Zhu for several helpful discussions.

References

[1] Barnett, W. J. and Troiano, A. R., "Crack Propagation in the Hydrogen-Induced Brittle Fracture of Steel," *Transactions,* American Institute of Mining, Metallurgical, and Electronic Engineers, Vol. 209, No. 4, April 1957, pp. 486–494.

[2] Johnson, H. H., "Calibrating the Electrical Potential Method for Studying Slow Crack Growth," *Materials Research and Standards,* Vol. 5, No. 9, Sept. 1965, pp. 442–445.

[3] Gilbey, D. M. and Pearson, S., "Measurement of the Length of a Central Crack or Edge Crack in a Sheet of Metal by an Electrical Resistance Method," Technical Report 66402, Royal Aircraft Establishment, Farnborough, Hants, UK, Dec. 1966.

[4] Li, Che-Yu and Wei, R. P., "Calibrating the Electrical Potential Method for Studying Slow Crack Growth," *Materials Research and Standards,* Vol. 6, No. 8, Aug. 1966, pp. 392–394.

[5] Chan, K. S. and Cruse, T. A., "Stress Intensity Factors for Anisotropic Compact-Tension Specimens with Inclined Cracks," *Engineering Fracture Mechanics,* Vol. 23, No. 5, 1986, pp. 863–874.

[6] Chan, K. S., Fitzgerald, J. H., and Chang, T. C., "Growth Response of Inclined Fatigue Cracks in Compact-Tension Specimens," *Engineering Fracture Mechanics,* Vol. 40, No. 2, 1991, pp. 251–253.

[7] McKeighan, P. C. and Hillberry, B. M., "On the Uncertainties Involved in Quantifying the Fracture Toughness of Al-Li-X Alloys," submitted and accepted for the *Journal of Testing and Evaluation,* 1993.

[8] Vasudevan, A. K. and Suresh, S., "Microstructural Effects on Quasi-static Fracture Mechanisms in Al-Li Alloys: The Role of Crack Geometry," *Materials Science and Engineering,* Vol. 72, 1985, pp. 37–49.

[9] Suresh, S., Vasudevan, A. K., Tosten, M., and Howell, P. R., "Microscopic and Macroscopic Aspects of Fracture in Lithium-Containing Aluminum Alloys," *Acta Metallurgica,* Vol. 35, No. 1, 1987, pp. 25–46.

[10] Sakagami, T., Kubo, S., Hashimoto, T., Yamawaki, Y., and Ohji, K., "Quantitative Measurement of Two-Dimensional Inclined Cracks by the Electric-Potential CT Method with Multiple Current Applications," *JSME International Journal,* Series 1, Vol. 31, No. 1, 1988, pp. 76–86.

[11] Green, D. A., Kendall, J. M., and Knott, J. F., "Analytic and Analogue Techniques for Determining Potential Distributions around Angled Cracks," *International Journal of Fracture,* Vol. 37, 1988, pp. R3–R12.

[12] Clark, G. and Knott, J. F., "Measurement of Fatigue Cracks in Notched Specimens by Means of Theoretical Electrical Potential Calibrations," *Journal of the Mechanics and Physics of Solids,* Vol. 23, 1975, pp. 265–276.

[13] Pickard, A. C. and Hicks, M. A., "Crack Length Determination Using the D.C. Electrical P.D. Technique—A Comparison of Calibration Methods," *Advances in Crack Length Measurement,* C. J. Beevers, Ed., Engineering Materials Advisory Services, Ltd., Cradley Heath, UK, 1982, pp. 97–113.

[14] Ritchie, R. O., Garrett, G. G., and Knott, J. F., "Crack Growth Monitoring: Optimisation of the Electrical Potential Technique using an Analogue Method," *International Journal of Fracture Mechanics,* Vol. 7, 1971, pp. 462–467.

[15] Baudin, G. and Policella, H., "A Pulsed D.C.P.D. Technique—Applications to Three-Dimensional Crack Fronts," *Advances in Crack Length Measurement,* C. J. Beevers, Ed., Engineering Materials Advisory Services, Ltd., Cradley Heath, UK, 1982, pp. 159–174.

[16] Smith, R. A. and Cameron, A. D., "A Three-Dimensional Wax Analogue for the Calibration of the Electrical Potential Technique of Crack Growth Monitoring," *Advances in Fracture Research, Fracture 84,* Vol. 5, pp. 3371–3376.

[17] Donald, J. K. and Ruschau, J., "Direct Current Potential Difference Fatigue Crack Measurement Techniques," *Fatigue Crack Measurement: Techniques and Applications,* K. J. Marsh, R. O. Ritchie, and R. A. Smith, Eds., Engineering Materials Advisory Services, Ltd., Worley, UK, 1990.

[18] ASTM E 647-93, "Standard Test Method for Measurement of Fatigue Crack Growth Rates," *1993 Annual Book of ASTM Standards,* Vol. 3.01, 1993, pp. 679–706.

Laurent Legendre,[1] *Bertrand Journet,*[1] *Joel Delmotte,*[1]
Georges Millour,[1] *and Jean-Marc Schwab*[1]

Application of a Crack Length Measurement with a Laser Micrometer to *R*-Curve Tests

REFERENCE: Legendre, L., Journet, B., Delmotte, J., Millour, G., and Schwab, J.-M., **"Application of a Crack Length Measurement with a Laser Micrometer to *R*-Curve Tests,"** *Special Applications and Advanced Techniques for Crack Size Determination, ASTM STP 1251,* J. J. Ruschau and J. K. Donald, Eds., American Society for Testing and Materials, Philadelphia, 1995, pp. 67–82.

ABSTRACT: The application of the damage tolerance philosophy to aeronautical thin structures requires that *R*-curves tests be run. The automation of such tests can be achieved through crack length monitoring using the compliance technique. However such a method faces experimental errors when a clipon gage extensometer is used to record the crack opening displacement on a CCT specimen because of the out-of-plane displacements. In order to write these displacements off, it is proposed to resort to a noncontacting device such as a scanning plane laser micrometer.

The sensor used consists of two parts which are symmetrically placed on each side of the central notch of the specimen. The emitter sends a 60 mm high laser plane wave to the receiver. Only the beams passing through the central hole of the specimen hit the receiver. The intensity of the transmitted laser beam is then converted into an electrical signal by the sensor electronics. A numerical processing of the signal enables a calculation of the crack opening displacement of a machined slot with a resolution greater than 1 μm and an excellent digital stability.

The measurement is then integrated into a PC microcomputer, which calculates the corresponding effective crack length using the appropriate compliance formula (ASTM E 561).

The stress intensity factor is computed from the testing machine load signal. A stability test (no crack growth under constant applied load step) is checked out in order to store the relevant data points for plotting the *R*-curve and to decide for the next load increment the computer is going to apply.

This laser technique was validated in comparison to a classical mechanical extensometer method on an aluminum alloy.

This method bears fruitful applications in testing under controlled environment (temperature, moist or corrosive atmosphere).

KEYWORDS: *R*-curve test, aluminum alloys, crack length measurement, laser extensometer, test automation

The object of *R*-curve tests is to calculate the fracture toughness of thin sheets of metals. The theoretical aspects underlying these tests have been described in numerous publications [*1–3*], and experimental procedures have also been discussed by many scientists [*4,5*]. Technical recommendations were proposed by ASTM in Standard Practice for *R*-Curve Determination (ASTM E 561).

[1] Doctor engineers, research engineer, and computer scientist, respectively, Aerospatiale, Joint Research Center, Louis Bleriot 12, Rue Pasteur B P 76 152, Suresnes, France.

Test specimens are fatigue precracked prior to being submitted to displacement increments during which crack length at stability is assessed. Widely applied techniques for crack size determination based on compliance methods [*6*] rely on crack opening displacement (COD) extensometers that are clipped onto the specimen; even if the specimen is set up with anti-buckling devices, the out of plane displacements can be significant enough to alter the COD measurements.

This paper describes a new test technique, developed at Aérospatiale Louis Bleriot Joint Research Center, which overcomes this experimental problem inherent to conventional test methods. The present method uses a planar-scan laser micrometer to measure the COD. Moreover this noncontacting extensometer minimizes measurement scattering and turns out to be a first choice candidate for running such tests with environment.

Experimental Procedure

The testing machine is a 250 kN servohydraulic machine (MTS). The specimen is 200 mm wide and 1.6 mm thick with a central notch and complies with ASTM E 561 standard (Fig. 1). The grips are free to rotate and the specimen is tightened through rows of bolts (Fig. 2). An antibuckling system has been set up. A 5 mm ($= 2Y_0$) wide slot is machined in the middle of the specimen. The COD ($\nu = 2Y - 2Y_0$) of the specimen is taken as the variation of measurement of $2Y$ during the test using a laser micrometer. The crack length is then calculated computing the appropriate compliance formulation given by paragraph 10 in the E 561 ASTM standard. The tested material is a 2219 aluminum alloy in the T-L orientation. The sensor is used to measure the slot opening and is a planar-scan laser micrometer (Keyence LS 3060) which is coupled to a digital measurement signal processor (Keyence LS 3010).

Test Method

Using of the Laser Micrometer

The effective crack length is calculated with the help of the contact-free measurements of the central hole width in the specimen (see specimen drawing, Fig. 1). The procedure to determine the crack size derives from the compliance method described in standard ASTM E 561 and is briefly presented in the section on Test Control Mode. Figure 2 shows the test setup. The laser micrometer consists of an emitter and a receiver placed on either side of the specimen, a 60 mm high laser plane being generated between them.

A laser diode in the emitter illuminates a rotating octagonal mirror which reflects the beam in a plane perpendicular to its axis. A mirror then reflects the coplanar beams to a collimator which makes them parallel. This emitter outputs a 60 mm high parallel-beam plane which illuminates the specimen. Part of the beam passes through the central hole and is used to measure its aperture.

In the receiver, a lens again focuses the beams onto a photocell. The shaped signals contain pulses generated each time the scanning beam hits one of the edges of the hole in the specimen. These pulses trigger a pulse counter. The timebase for the counter is a high-speed clock (40 MHz), and the count start is synchronized with the signal from the photodiode in the emitter. The stability of the mirror-drive motor speed keeps the laser plane scanning rate constant. The slot width is given as follows

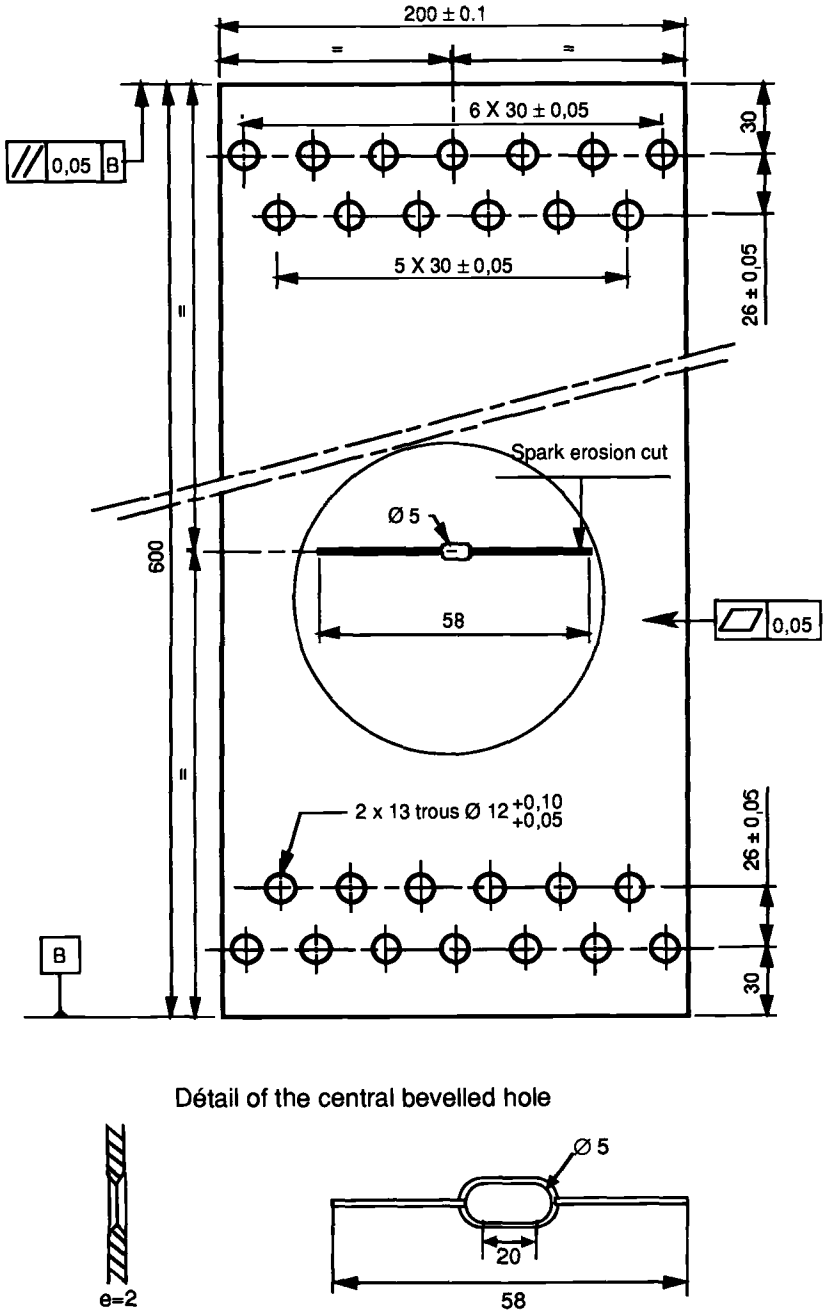

FIG. 1—*Drawing of* R-*curve specimen CCT W200.*

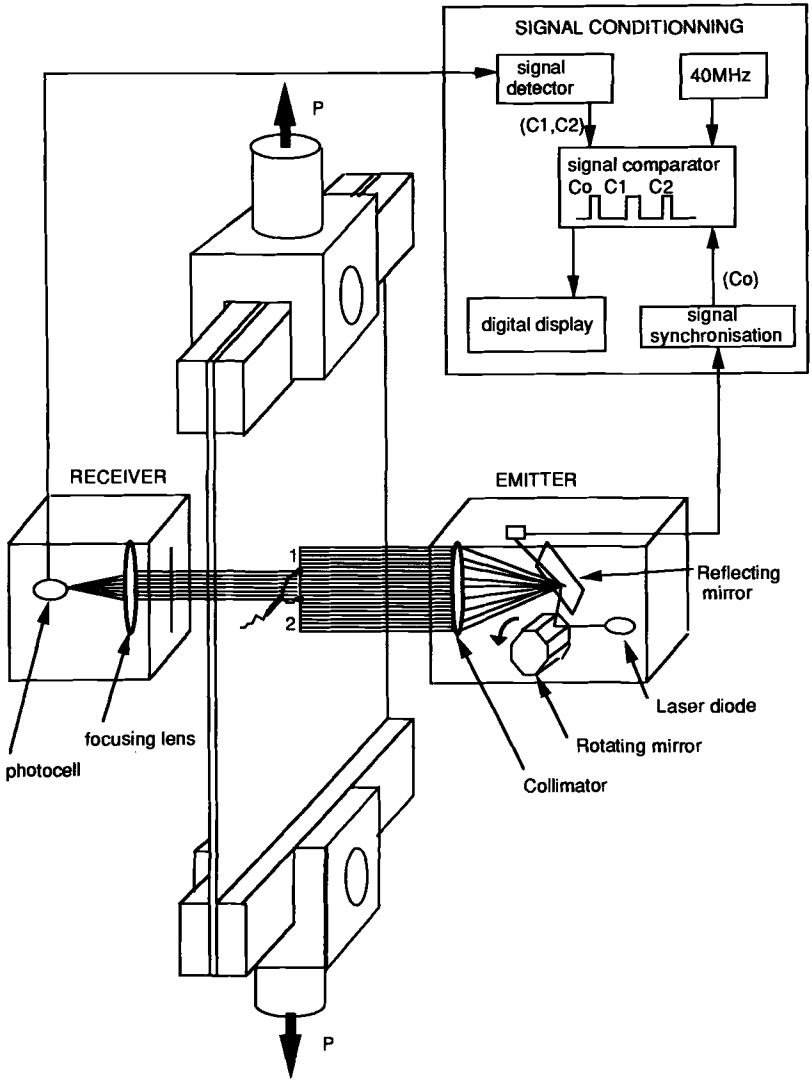

FIG. 2—*General view of the testing installation.*

$$d = [b_2 + M(C_2 - C_0)] - [b_1 + M(C_1 - C_0)]$$

or

$$d = b_2 - b_1 + M(C_2 - C_1) \tag{1}$$

where

d = diameter of the slot, $d = 2Y$,
C_0 = synchronization count,
C_1 and C_2 = counts corresponding to each edge of the hole,

M = a compensation factor proportional to this speed, and
b_2 and b_1 = factors to compensate for the angle of incidence of the focused beam.

The laser is accurate to within approximately 10^{-3} mm (resolution = 10^{-4} mm). The measurements are made every 2.5 to 20 ms, depending on whether a single measurement or an average of several measurements is required. In the latter case, the number of successive points can be selected between 2 and 1024. Increasing the number of points in the averaging step results in a more stable measurement but reduces the scanning rate. The measured value of the slot displacement ($v = d - d_0$) is then transmitted, in digital form, to a personal computer (PC) which processes the test results.

Test Control Mode

The test is run under displacement computer control. The displacement increment is 0.01 mm. The computer constantly scans the load signals (P) output by the machine and the measurement signals output by the laser micrometer (v). The specimen COD stability (v) is used to test the crack for stability. Once the crack is stable (that is, when propagation stops), the computer stores the corresponding load P and COD v-values and sends a signal to generate a new increment in the displacement. This acquisition-load incrementation sequence is repeated until the specimen fails. At the end of the test the computer file contains a series of 20 to 50 (depending on the test) pairs of load/COD values (the acquisition algorithm is shown in Fig. 3).

Determination of Crack Length

Standard ASTM E 561 gives the following equation of the normalized compliance with respect to crack length for the CCT specimen

$$EvB/P = f(a/W) \tag{2}$$

$$\frac{EvB}{P} = 2\sqrt{\frac{\pi a/W}{\sin(\pi a/W)}}\left\{\frac{2W}{\pi Y}\cosh - 1\left\{\frac{\cosh(\pi Y/W)}{\cos(\pi a/W)}\right\} + \frac{1+\mu}{\sqrt{1+\left\{\frac{\sin(\pi a/W)}{\sinh(\pi Y/W)}\right\}}} + \mu\right\}\frac{Y}{W}$$

where

E = Young's modulus,
v = COD measured by the laser sensor,
P = load in N,
B = specimen thickness in mm,
W = specimen width in mm,
Y = laser "gage length" (half the width between the bevel edges) in mm,
a = half the effective crack length in mm, and
μ = Poisson's ratio.

The operator enters the file of test parameters (characteristics of the material and specimens) into the analysis program at the start of each test (the data processing algorithm is shown in Fig. 4). The R-curve is calculated at the end of the test using the values recorded in the file (P, v). At the beginning of the test, the Young's modulus value is checked using the linear section of the curve produced by the acquired values (P, v, Fig. 5).

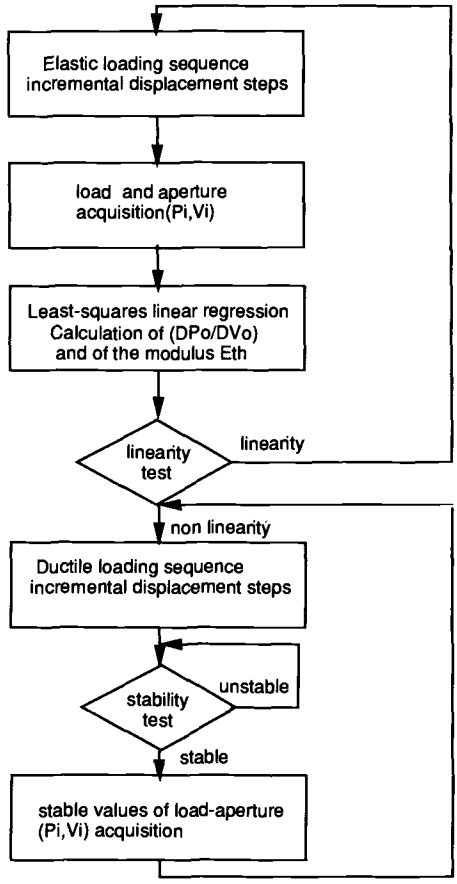

FIG. 3—*Data acquisition and test control program.*

During this part of the test, the material is elastic and the crack length remains equal to the initial fatigue crack length, a_0, and this value is verified after the specimen rupture. The modulus of elasticity of the material is therefore calculated from the formula

$$E_{th} = \frac{\Delta P_0}{B\Delta v_0} f(a_0/W) \tag{3}$$

where $\Delta P_0/\Delta v_0$ is the slope of the (v, P) curve (Fig. 5) calculated by regression using the least-squares method. This calculated modulus must not differ from the real modulus of the material (determined by a tension test) by more than 10%. If the crack length for the two modulus values (E_{th} and E_{real}) differ by more than 3%, the modulus is then remeasured after a verification of the testing setup (alignment, antibuckling resistance . . .).

Calculation of the Effective Crack Length, a_{eff}—A compliance measurement correction is applied to each pair of recorded data points $(v_i, P_i)_{mes}$ before calculating an estimate of the a_{eff} value from the reverse function of Eq 1 (compliance curve, Fig. 6).

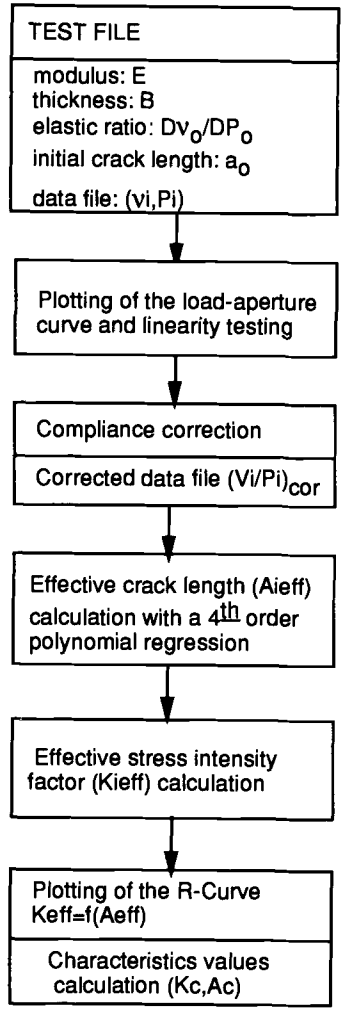

FIG. 4—*Data treatment program.*

The compliance correction applies to the initial (that is, during the elastic loading phase) difference between the measured compliance values

$$(v_0/P_0)_{mes} = \frac{\Delta v_0}{\Delta P_0} \tag{4}$$

and the compliance values calculated from Eq 1

$$(v_0/P_0)_{th} = \frac{1}{EB} f(a_0/W) \tag{5}$$

This compliance correction

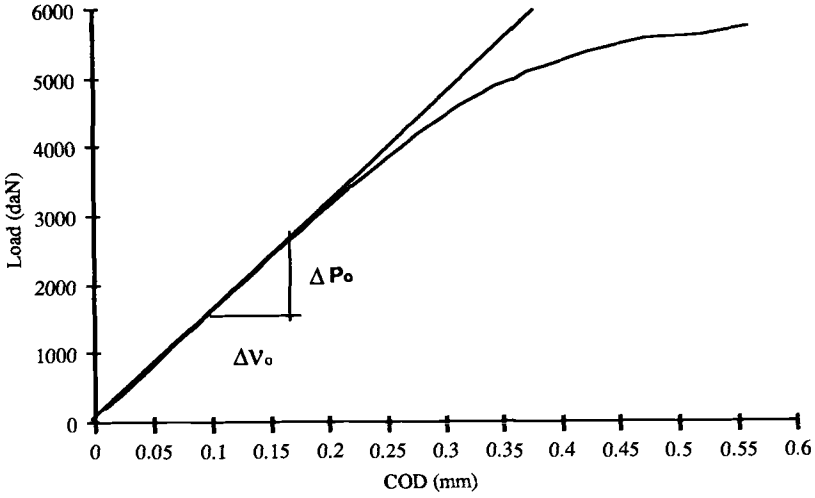

FIG. 5—*Elastic slope measurement on the load-COD curve.*

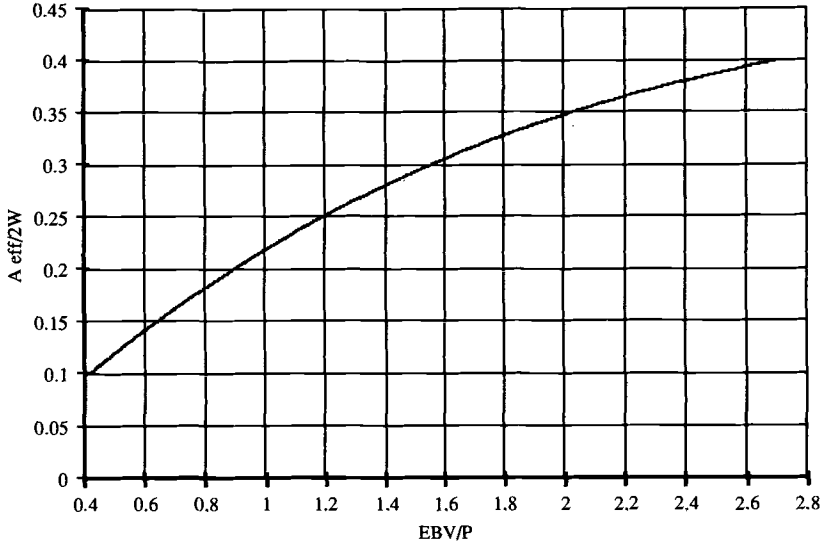

$$aeff/W=Co+C1EB(V/P)c+C2(EB(V/P)c)^2+C3(EB(V/P)c)^3+C4(EB(V/P)c)^4$$

	C_0	C_1	C_2	C_3	C_4
W=200	-0.009083	0.286254	-0.061294	0.002143	0.000769

FIG. 6—*Polynomial regression of the compliance curve (CCT W200 specimen).*

$$(v_0/P_0)_{mes} - (v_0/P_0)_{th} \tag{6}$$

is calculated from the compliance measurement $(v_i/P_i)_{mes}$ recorded for each test point. Therefore, we obtain corrected compliance values

$$(v_i/P_i)_{cor} = (v_i/P_i)_{mes} - \{(v_0/P_0)_{mes} - (v_0/P_0)_{th}\} \tag{7}$$

There is no simple literal expression of the inverse function of Eq 2 ($EvB/P = f(a/W)$). Consequently, to calculate a_{ieff} we must determine the real root of the equation

$$EB(v_i/P_i)_{cor} = f(a_{ieff}/W) \tag{8}$$

for each test point.

To make this equation easier to resolve, a 4th-order polynomial regression is applied to achieve a reliable estimation of a_{ieff} for each value of $(v_i/P_i)_{cor}$

$$a_{eff}/W = g(EB(v/P)_c) \tag{9}$$

$$\frac{a_{eff}}{W} = c_0 + c_1\, EB(v/P)_c + c_2(EB(v/P)_c)^2 + c_3(EB(v/P)_c)^3 + c_4(EB(v/P)_c)^4 \tag{10}$$

Figure 6 shows this polynomial and the compliance curve for the CCT $W = 200$ mm specimens. This dimensionless equation is independent of the specimen size. To ensure the measurements are reproducible and independent of the type of specimen chosen, the geometry of all specimens is homothetic except for the central notch (Y is constant for all specimens). The values of a_{ieff} are then stored in a file before the stress intensity factor K_{ieff} is calculated.

Calculation of the Effective Stress Intensity Factor, K_{ieff}:

The test file contains three values: a_{ieff}, v_i, and P_i. The values of the stress intensity factor K_{ieff} are estimated for each point by measuring the resistance to crack propagation K_R using the formula given in ASTM E 561 (paragraph 9)

$$K_R = \frac{P}{BW}\sqrt{\frac{\pi a}{\cos(\pi a/W)}} \tag{11}$$

therefore

$$K_{ieff} = \frac{P_i}{BW}\sqrt{\frac{\pi a_{ieff}}{\cos(\pi a_{ieff}/W)}} \tag{12}$$

Plotting the R*-Curve and Calculation of Characteristic Values*

The R-curve is plotted from the (a_{ieff}, K_{ieff}) points in the file. During the elastic loading (v and P are proportional) the slope of the curve is vertical, a_{ieff} remains equal to a_0. The validity of the points on the R-curve (as defined in ASTM E 561) is finally checked before plotting the curve itself (any invalid points are indicated, in the curve, by a star symbol).

The aim is to verify that the mean stress in the remaining ligament is still less than the yield strength.

The criterion used to assess validity of the measurement depends on the specimen geometry. A check is done, at each point, that

$$W \geq (27/2\pi)(K_{\text{eff}}/\sigma_y)^2 \tag{13}$$

The fracture toughness, $K_{\text{eff}} = K_c$, at the extreme test load ($P_{\max}$), is given as the limit of crack instability ($K_R = K_{\text{eff}}$ and $dK_R/da = K_{\text{eff}}/da$)

$$K_c = \frac{P_{\max}}{BW}\sqrt{\frac{\pi a_m}{\cos(\pi a_m/W)}} \tag{14}$$

a_m is the effective length of the crack corresponding to the maximum load point. *Note:* The value of K_c is only valid if it meets the W geometrical criterion (see Eq 13).

The final test report gives all results obtained and includes:

1. Information to identify the test (material, manufacturer, treatment, mechanical properties, sampling direction, type of specimen, and dimensions).
2. The file of test results (values of points on the R-curve).
3. The characteristic values for the R-curve (K_c, a_0).
4. The R-curve plotting.

Advantages of the Test Method

Compared to conventional methods, the use of a laser micrometer to measure crack lengths during the R-curve tests offers several advantages:

1. The test is automated.
2. The test is more reliable.
3. The measurements are more accurate.
4. The experimental device is improved.
5. The test environment can be varied.

Test Automation

Unlike conventional visual methods, this measurement technique, combined with digital data acquisition, means that the presence of an operator is required only for initial preparation before the test and for removal once the test has been completed. Values are acquired directly, eliminating risks of data entry errors. Continuous testing for crack stability ensures more accurate control. In addition, the measurement of the COD could be used directly as a test servocontrol parameter to further increase sensitivity. The analysis of results is easier and, above all, quicker since they are available as soon as the test is completed. Moreover, all the risks involved in manually reentering calculated results is eliminated.

Measurement Reliability

The test results are more reproducible since a quantified test is used to determine the crack stability instead of the subjective assessment of the operator. Moreover, unlike when the

crack length is measured directly, a plastic zone correction is integrated directly into the measured value. The measurements are also less sensitive to local phenomena which can occur at the crack tip, the crack front is never straight, and an optical measurement method minimizes the crack length.

Measurement Accuracy

The micrometer's resolution which, at $\pm 10^{-3}$ mm, is sufficient to allow the crack length to be measured to within approximately 0.05 mm which ensures crack measurement accuracy. An optical method provides a reproducibility of only ± 0.1 mm. Crack stability is also easier to assess thanks to digital acquisition which avoids the loss of measurement accuracy.

The laser sensor provides a more accurate measurement of the COD (v_l) since it is independent of the relative movement of the crack edges (δ) (Fig. 7); in contrast, with a clipon gage extensometer, there is a nonnegligible margin of error as calculated by the following relationship

$$v_g = \sqrt{\delta^2 + (2Y + v_l)^2} - 2Y \tag{15}$$

The out of plane displacement is maximum when the load is maximum and can reach 0.5 mm. The overestimation with a conventional extensometer is then of the order of 1 mm for a 45-mm long crack. In addition, the sensor gage length ($2Y$) is measured more precisely than with a conventional clipon extensometer.

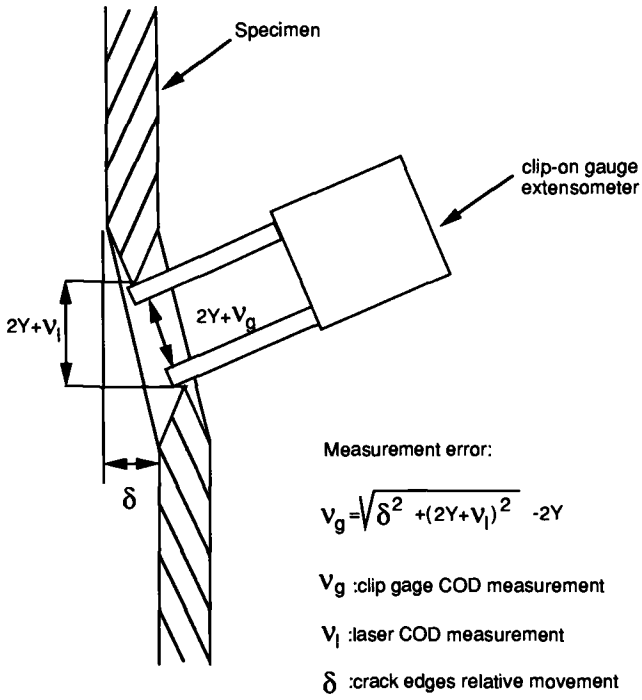

FIG. 7—*Clipon gage extensometer measurement error.*

The Experimental Device

The machined slot in the center of the specimen to allow measurement by the laser micrometer is small which means that extremely rigid antibuckling tools can be used. The preliminary fatigue cracks can be produced using the same test fixture and without removing the specimen from the servohydraulic machine, thanks to the high sensitivity of the compliance method which allows the initial crack length determination. The laser heads allow a misalignment of 0.1 mm and a maximum angle of 1 deg between themselves. Finally, a system with two measurement heads (Keyence) is also used to apply the method to other types of specimen, using the double compliance method on test specimens with lateral notch (ASTM E 561 CLWL type).

Test Medium

The laser measurement is not sensitive to the refractive index of the medium separating the emittor and the receptor of the micrometer. The field of investigations for R-curves determination will be extended to temperature controlled environments, but the choice of the test medium is spread to gaseous atmospheres (inerts, humids, and corrosives gas) and to liquid mediums (liquid nitrogen, water, etc.) in order to reproduce real service conditions for materials (pressure tanks, etc.).

Method Validation

The method validation measurement method has been validated during tests on aluminum alloy, 2219 T87. The tests described in this paragraph concern specimens of the CCT W = 200 mm type. The aim of this validation is to estimate, for each specimen, the measurement discrepancies induced by the two following methods.

The first method uses a traditional COD gage extensometer, the second method uses a planar-scan laser micrometer. Both types of test methods conform to the compliance method previously described, and they are applied simultaneously on the specimen. They compare two measures of the effective crack length whereas an optical method needs a plasticity correction to obtain an effective value; so, this latter method has not been taken into account here.

Figures 8 and 9 superimpose the two curves thus plotted for two distinct specimens. Both curves obtained with the laser extensometer are more regular than those obtained with the gage sensor. Differences appear between the two types of curves. The most serious difference is obtained for maximum values of crack length which are here the critical values limiting the stable propagation of cracks (Table 1). The mechanical extensometer measurement overestimates the length of the crack, and, hence, the value of the fracture toughness coefficient. The mean overestimate obtained for the crack length propagation is of the order of e = 8.5%, when using the gage sensor method. This gap calculation is $e = 1 - (a_{\text{eff}} - a_0)\text{gage}/(a_{\text{eff}} - a_0)\text{laser}$. This measurement difference is reflected on the fracture toughness coefficient measurement to a lower extent, however, it remains significant as the overestimation connected to the COD sensor method remains the average value of 1.8%. If the test had been performed without using antibuckling systems, the error would have been greater. Both laser curves are strictly superimposable. But, between 20 and 40 MPa$\sqrt{\text{m}}$, the limit of linear regression may be overestimated by the clip gage sensor (see Fig. 9). The gage sensor can then overestimate the value of the stress intensity factor by 10 MPa$\sqrt{\text{m}}$, and the test results are not reproducible.

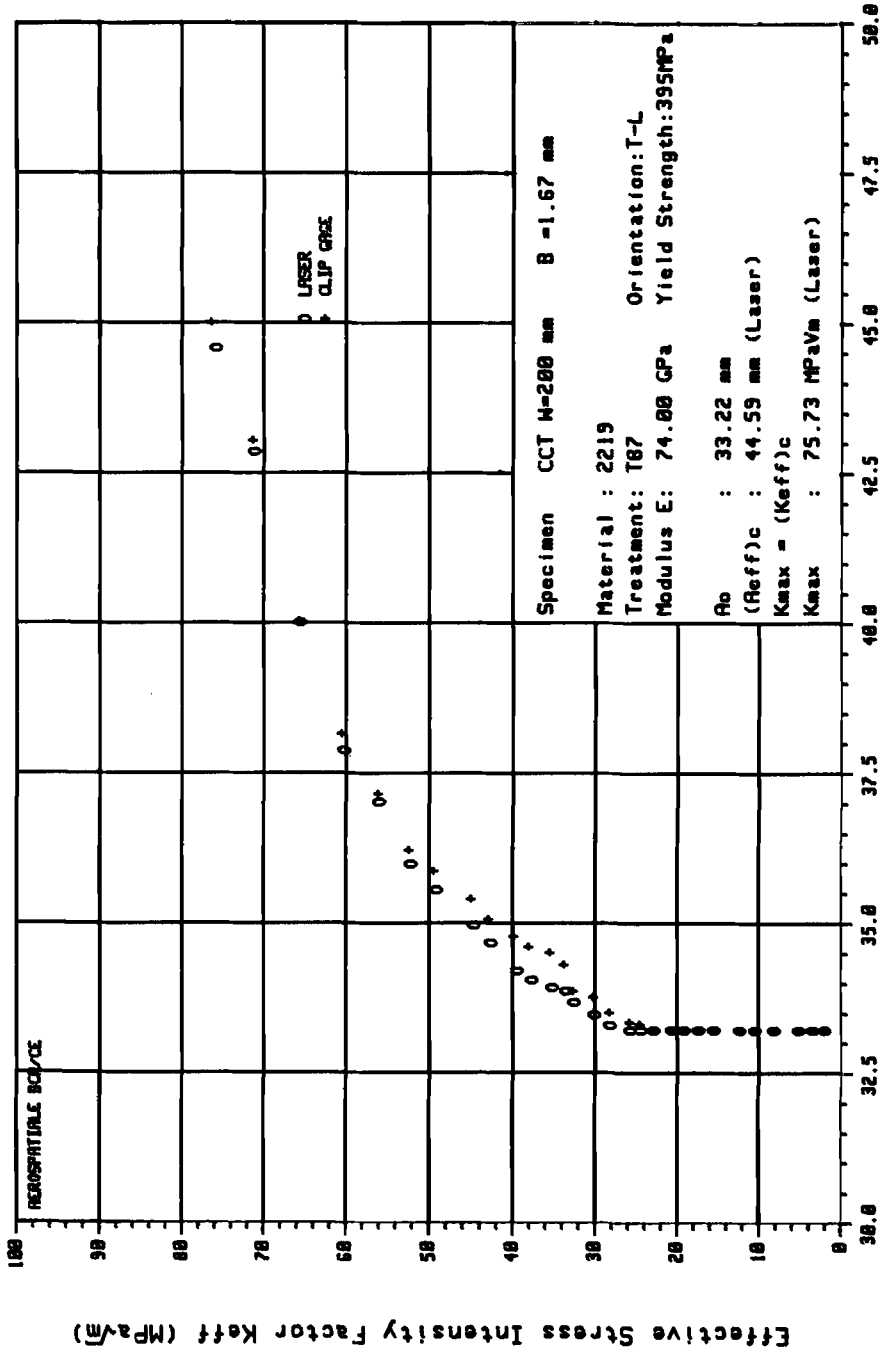

FIG. 8—*Comparison of two compliance methods, Specimen 1.*

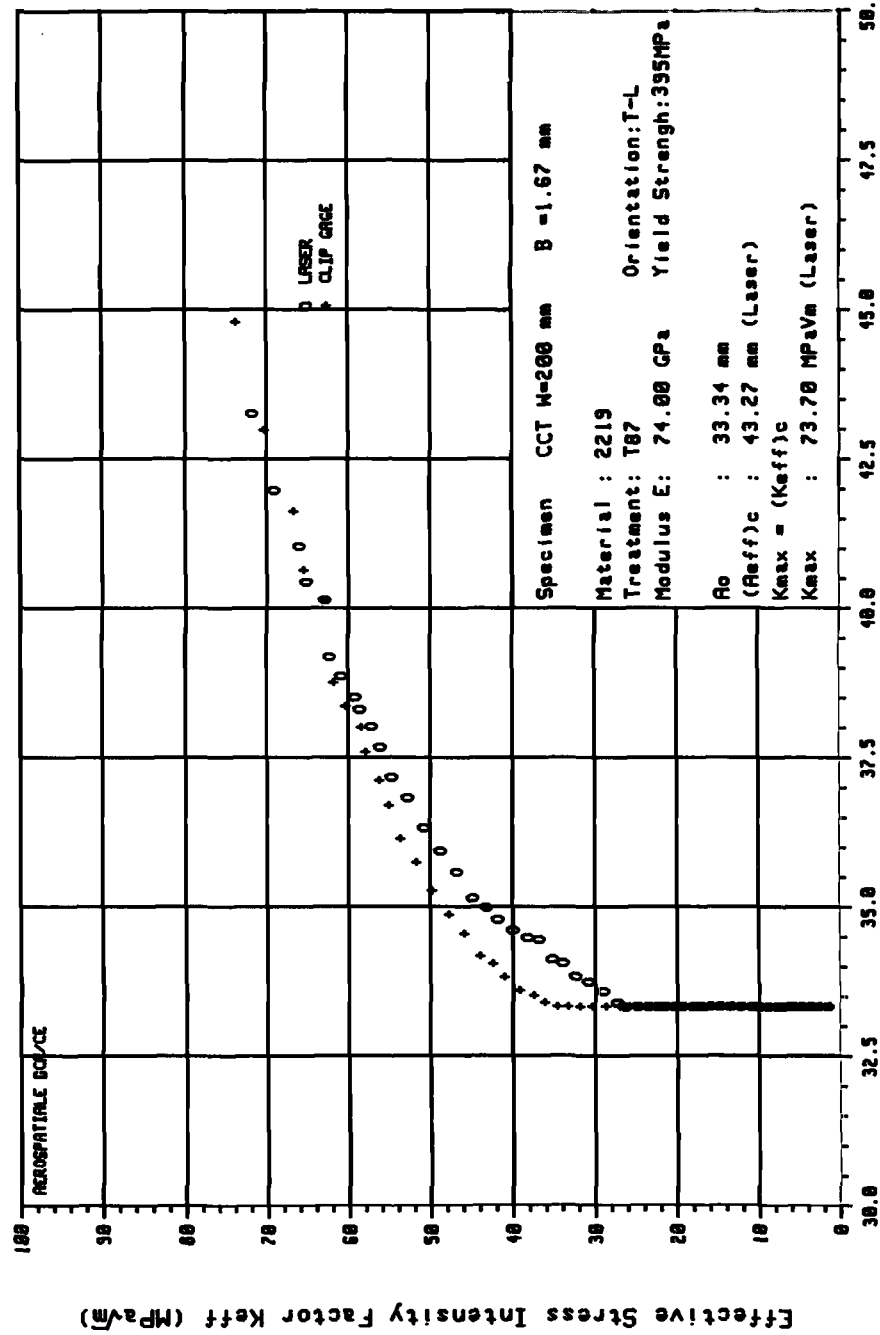

FIG. 9—*Comparison of two compliance methods, Specimen 2.*

TABLE 1—*Clipon gage and laser extensometers measurements differences.*

	Specimen 1	Specimen 2	Mean Values
Laser Young modulus, E_l	72 GPa	71 GPa	71.5 GPa
Clip gage Young modulus, E_g	69 GPa	66 GPa	67.5 GPa
Modulus difference, $1 - E_l/E_g$	−4.4%	−7.8%	−6.1%
K_c laser value, $(K_c)l$	75.7 MPa$\sqrt{m}$	71.7 MPa$\sqrt{m}$	73.7 MPa$\sqrt{m}$
K_c clip gage value, $(K_c)g$	76.3 MPa$\sqrt{m}$	73.7 MPa$\sqrt{m}$	75 MPa$\sqrt{m}$
K_c difference, $1 - (K_c)l/(K_c)g$	1%	2.7%	1.8%
$(A_{effc} - A_0)$ laser value	11.37 mm	9.93 mm	44 mm
$(A_{effc} - A_0)$ clip gage value	11.8 mm	11.46 mm	44.9 mm
Gap, $1 - (A_{eff} - A_0)l/(A_{eff} - A_0)g$	3.6%	13.3%	8.5%

The use of a laser micrometer permits better estimation of the value of the Young's modulus of elasticity of the material, as the accuracy of the linear regression between load and aperture (measurement of DP_0/Dv_0) is not dependent on lateral displacements of the crack edges as when using the gage sensor.

A series of tension tests performed on 2219 T87 provides a mean value of elasticity modulus of $E = 74$ GPa. The laser micrometer (see Table 1) gives an estimation of elasticity modulus of $E = 71.5$ GPa (average value), that is, an underestimate of the order of 3.6% compared to the real modulus. The gage sensor (see Table 1) gives a much lower modulus value $E = 67.5$ GPa, the difference is 8.8%. Thus, the precision of the elasticity modulus determination is maximized by the use of a laser micrometer and is better, as mentioned in ASTM E 561. In addition, the correction of the modulus performed during the processing of data is performed with an accuracy two times better compared with the use of gage sensor.

Conclusion

The *R*-curve test has been totally automated using a laser micrometer. This method was chosen because it is free of the out-of-plane crack opening displacements which usually alter the measurements made by conventional contacting COD extensometer.

The use of a contact-free method by a planar-scan laser micrometer for measuring crack length during a ductile tear test (*R*-curve) permits improvements of the accuracy of the fracture toughness of thin sheets determination. The curves obtained show a more regular appearance and their reproducibility is better. Compared with a compliance method using a gage sensor, this method gives access to more accurate values of maximum allowable defects in the material. A gain in accuracy in the calculation of structures subjected to this type of stress is then expected.

The application of this method to a wide range of environmental conditions, linked to the large work distance of the laser micrometer, is easy to implement and will extend the field of research of such a test.

References

[1] Irwin, G. R., "Fracture Testing of High Strength Sheet Materials Under Conditions Appropriate for Stress Analysis," Report 5486, U.S. Naval Research Laboratory, Washington, DC, 1960.

[2] Heyer, R. H., "Crack Growth Resistance Curves (*R*-Curves), Literature Review," *Fracture Toughness Evaluation by R-Curve Method, ASTM STP 527*, American Society for Testing and Materials, Philadelphia, pp. 3–16.

[3] Krafft, J. M., Sullivan, A. M., and Boyle, R. W., "Effect of Dimensions on Fast Fracture Instability of Notched Sheets," *Proceedings,* Crack Propagation Symposium, College of Aeronautics, Cranfield, UK, Vol. 1, 1961, pp. 8–28.

[4] Heyer, R. H. and McCabe, D. E., "Crack Growth Resistance in Plane Stress Fracture Testing," *Engineering Fracture Mechanics,* Vol. 4, 1972, pp. 413–430.

[5] Heyer, R. H. and McCabe, D. E., "Plane Stress Fracture Toughness Testing Using a Crack-Line-Loaded Specimen," *Engineering Fracture Mechanics,* Vol. 4, 1972, pp. 393–412.

[6] Newman, J. C., Jr., "Crack Opening Displacements in Center-Crack, Compact, and Crack-Line Wedge Loaded Specimen," NASA TN-D 8268, Washington, DC, 1976.

Xiaoguang Chen,[1] *Pedro Albrecht,*[2] *William Wright,*[3] *and James A. Joyce*[4]

Improved Load Ratio Method for Predicting Crack Length

REFERENCE: Chen, X., Albrecht, P., Wright, W., and Joyce, J. A., **"Improved Load Ratio Method for Predicting Crack Length,"** *Special Applications and Advanced Techniques for Crack Size Determination, ASTM STP 1251*, J. J. Ruschau and J. K. Donald, Eds., American Society for Testing and Materials, Philadelphia, 1995, pp. 83–103.

ABSTRACT: The elastic compliance from unloading/reloading sequences in a load-displacement record estimates well crack length in elastic-plastic fracture toughness tests of compact tension [C(T)] and bending type specimens. The need for partial unloading of the specimen makes it difficult to run the test under static loading and impossible under either dynamic loading or very high temperatures. Furthermore, fracture toughness testing in which crack length is determined from elastic compliance requires high precision testing equipment and highly skilled technicians. As a result, such tests are confined usually to research laboratories and seldom used under production settings.

To eliminate these problems, an improved load ratio method of predicting crack length is proposed that utilizes only the recorded load versus load-line displacement curve (or load versus crack-mouth-opening displacement curve) without unloading/reloading sequences. As a result, the instrumentation is much simpler than in the elastic compliance or potential drop methods. If only a monotonic load-displacement record is to be measured the fracture toughness test becomes almost as simple to perform as a tension test.

The method described here improves in three ways the "original load ratio method" proposed by Hu et al. First, a blunting term is added to the crack length before maximum load. Second, a strain hardening correction is included after maximum load. And, third, the initial crack length and the physical (final) crack length measured at the end of the test serve to anchor the predicted crack lengths, forcing agreement between predicted and measured values.

The method predicts crack extension with excellent accuracy in specimens fabricated from A302, A508, and A533B piping and pressure vessel steels, A588 and A572 structural steels, and HY-80 ship steel.

KEYWORDS: load rates, crack length, compact tension, crack opening displacement, fracture toughness

The main drawback of elastic-plastic fracture toughness testing using *J*-integral or crack-tip opening displacement (CTOD) methods is the need to measure crack length with the elastic compliance or potential drop methods. Figure 1 shows, as an example, the periodic unload-reload sequences needed to determine crack length with the elastic compliance method. To eliminate this problem, previous researchers have inferred crack length from

[1] Research associate, Institute for Systems Research, University of Maryland, College Park, MD 20742.
[2] Professor, Department of Civil Engineering, University of Maryland, College Park, MD 20742.
[3] Structural research engineer, Turner-Fairbank Highway Research Center, Federal Highway Administration, 6300 Georgetown Pike, McLean, VA 22101.
[4] Professor, Mechanical Engineering Department, U.S. Naval Academy, Annapolis, MD 21402.

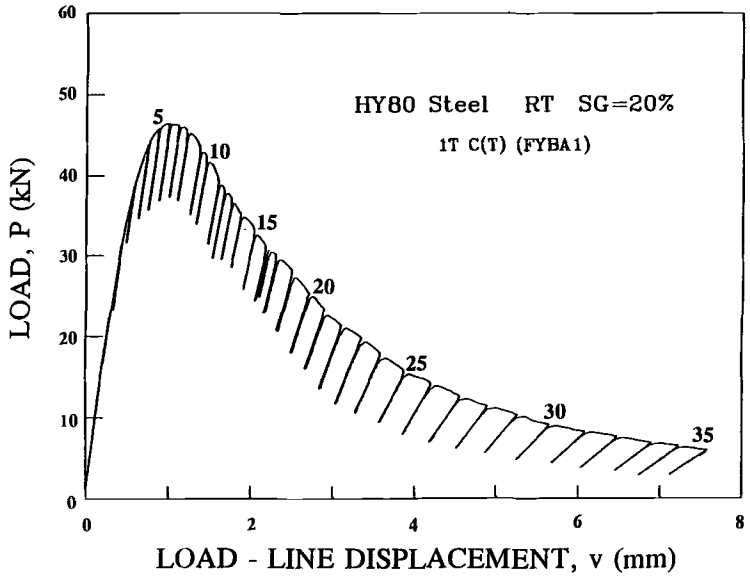

FIG. 1—*Measured load-displacement curve with partial unloadings; 1T C(T) specimen of HY-80 steel.*

load-displacement[5] records using the original load ratio method [*1*], the key curve method [*2*], or the normalization method [*3*].

In the key curve method, a load-displacement record is measured for a small specimen in which the onset of ductile crack extension is delayed by providing a blunt notch at the crack tip. The curve is then normalized to obtain the key curve. Comparison of a specimen's load-displacement record with such a key curve yields the crack extension. Closed-form expressions are fitted to the key curve for use in the analysis.

In the normalization method, the assumed normalization functions are fitted to the test specimen's data (initial and final values of load, displacement, and crack length) yielding the parameters of the normalization functions. The *J*-integral or CTOD can then be evaluated by substituting the normalization function directly in the equations defining *J* in terms of the load and displacement.

The original load ratio method is the simplest of the three methods. Its main shortcoming is that predicted crack lengths are shorter than those obtained with the elastic compliance method. This results from neglecting crack extension before maximum load and assuming elastic-perfectly plastic material behavior. The latter implies constant elastic displacement over the full range of crack extension, which is not correct for strain hardening materials.

Objective

The objective of this sudy is to improve the accuracy of the load ratio method so that it can be used reliably in tests under static and dynamic loading as well as in high temperature tests. Simple and accurate crack length predictions are needed for materials with different degrees of ductility and strain hardening.

[5] In the rest of the paper, the load-line displacement (for C(T) specimen) or crack-mouth-opening displacement (for SEN(B) specimen) are generally referred to as displacement.

The original load ratio method is much simpler than the elastic compliance and potential drop methods of measuring crack length. It is also simpler than the key curve and normalization methods of inferring crack length directly from load-displacement data. In the load ratio method, only load and displacement need to be measured and the test is easily run under, say, a constant displacement rate. Crack extension can also be determined in tests under either dynamic loading or high temperature. During such test conditions, crack opening displacement gages often do not perform adequately.

Original Load Ratio Method

Figure 2 shows a pair of idealized load-displacement curves for a fracture toughness test specimen made of an elastic-perfectly plastic material. If the crack did not extend, meaning the geometry does not change, the specimen would follow curve 1 (OAA″). Since the crack in reality extends, the specimen typically follows curve 2 (OAB″). Both curves are for elastic-perfectly plastic material behavior. The gradual fall of curve 2, beyond maximum load P_{max}, can be thought of as a series of steps. The run B′D of the step between two consecutive points on curve 2 represents yielding without crack extension. The corresponding fall DB″ of the step represents crack extension without yielding. Thus, a displacement increase B′D at constant load P_i must be the result of yielding, with no change in compliance along the run. Conversely, a load decrease DB″ at constant displacement v_i must result from crack extension. In summary, cumulative crack extension causes the load to decrease from the value on curve 1 to that on curve 2.

A specimen whose crack does not extend unloads elastically along lines A′O′ or A″O″ in Fig. 2. The unloading slope equals the initial elastic loading slope OA. If crack extension at

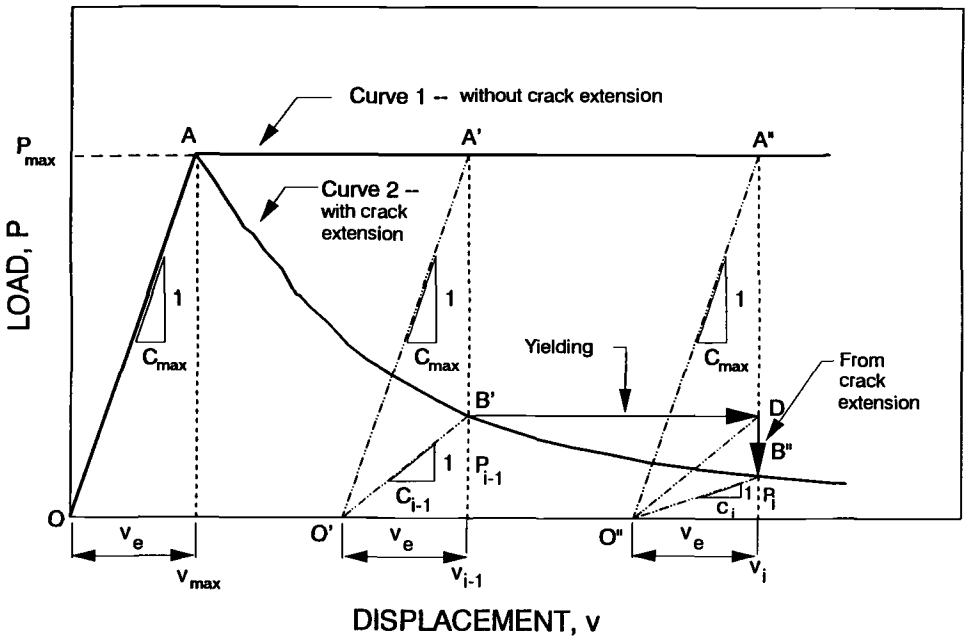

FIG. 2—*Schematic load-displacement curve for specimen made of elastic-perfectly plastic material; basis of original load ratio method.*

constant displacement causes the load to decrease vertically without additional plastic deformation, A′B′ or A″B″, the specimen unloads elastically along B′O′ or B″O″, respectively. It is assumed here, and shown experimentally for some steels in Ref *4*, that the elastic part (v_e) of the total displacement (v) remains nearly constant as the crack extends at fixed total displacement. Beyond maximum load, P_{max}, the elastic displacement v_e remains constant for elastic-perfectly plastic material behavior. This is the case for both curves 1 and 2, that is, irrespective of whether the crack extends.

In developing the original load ratio method, Hu et al. [*1*] assumed that the crack does not extend as the load rises from zero to the maximum load and the steel does not strain harden. These assumptions mean that the elastic part of the total displacement remains constant beyond maximum load during crack extension. Accordingly, the elastic displacement is the product of load (P) and compliance (C)

$$v_e = P_i C_i = P_{i-1} C_{i-1} = \ldots = P_{max} C_{max} \tag{1}$$

Subscripts (i) and ($i - 1$) denote the current and previous values of load and elastic compliance. Eq 1 is solved for the current compliance

$$C_i = \frac{P_{i-1}}{P_i} C_{i-1} = \frac{P_{max}}{P_i} C_{max} \tag{2}$$

Finally, inserting C_i from Eq 2 into the crack length equation for the specimen geometry—here a C(T) specimen—gives the value of current crack length [*5*]

$$\frac{a_i}{W} = 1.000196 - 4.06319u_{LL} + 11.242u_{LL}^2 - 106.043u_{LL}^3 + 464.335u_{LL}^4 - 650.677u_{LL}^5 \tag{3}$$

where

$$u_{LL} = \frac{1}{[B_e E C_i]^{1/2} + 1} \tag{4}$$

and

B_e = effective specimen thickness, and
E = modulus of elasticity.

Thus, knowing the elastic part of the total displacement is the key to accurately predicting crack length with the load ratio method.

To verify the original load ratio method, Hu et al. [*1*] analyzed *J-R* curve test data reported by others for AL5086 aluminum and A302, A533B, and HY-80 steels. Crack extension was predicted most accurately for the smaller degree of strain hardening.

Subsequently, the authors analyzed *J-R* curve data for A572 and A588 structural steels reported by Hartmann et al. [*6*]. The results for these steels were not as good as those previously obtained by Hu et al., because the two structural steels have a high ratio of tensile strength to yield strength and hence a strong strain hardening. In contrast to steels such as HY-80 (Fig. 1), the A572 and A588 structural steels had rounded load-displacement curves

(Fig. 3). When compared with the measured physical crack length, the authors found that the original load ratio method underestimates crack length at the end of the test to such a degree that a correction is needed.

Improved Load Ratio Method

This study improves the accuracy of the load ratio method in three ways, by (1) adding a blunting term to the crack length before maximum load, (2) allowing for strain hardening after maximum load, and (3) matching the crack length estimated from the compliance at the end of the test with the measured physical (final) crack length.

Crack Extension at Maximum Load

The first assumption—zero crack extension up to maximum load—is adequate for brittle and low-ductility materials. In ductile materials, however, some tearing and crack tip blunting occur before maximum load. To account for these effects, the crack length at maximum load (a_{max}) is expressed as the sum of the initial crack length (a_0) plus a blunting term (Δa_{max}):

$$a_{max} = a_0 + \Delta a_{max} \tag{5}$$

The crack extension at maximum load is estimated as [*7*]

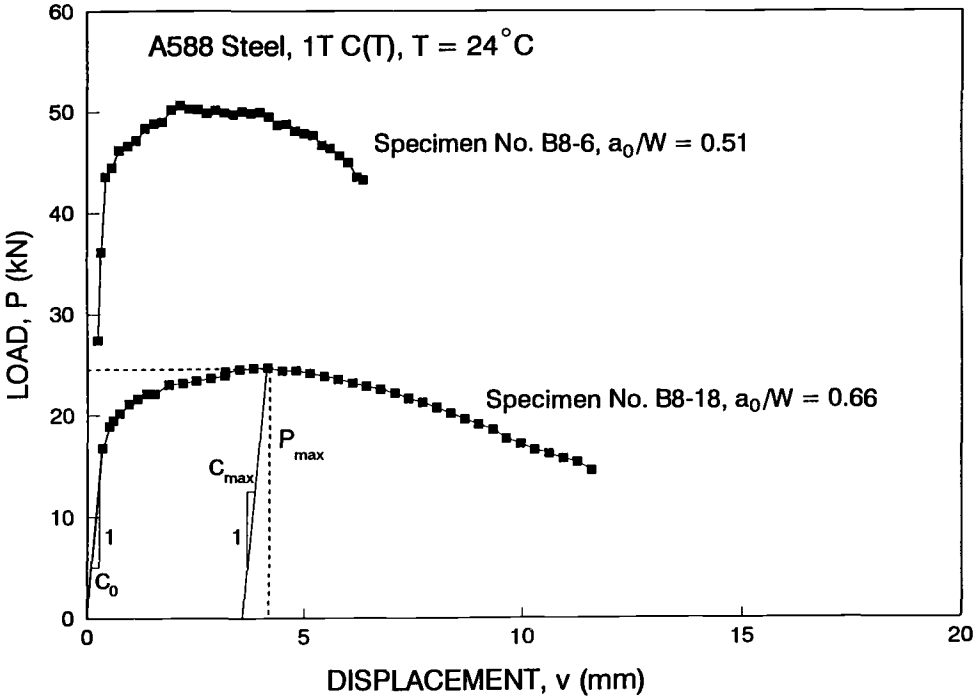

FIG. 3—*Measured load-displacement curve; 1T C(T) specimens of A588 steel.*

$$\Delta a_{max} = \frac{\delta}{1.4} \tag{6}$$

where δ is the crack opening displacement (CTOD) given in the ASTM Test Method for Determining *J-R* Curves (E 1152)

$$\delta = \frac{K_{max}^2(1 - \nu^2)}{2\sigma_y E} + v_{p,max} \frac{r_p(1 - a_0/W)}{a_0/W + r_p(1 - a_0/W)} \tag{7}$$

where the plastic rotation factor at maximum load is given by [*8*]

$$r_p = \frac{1}{1 - a/W}\left[\sqrt{0.633(a/W)^2 + 0.3699} - a/W\right] \tag{8}$$

and

E = modulus of elasticity,
K_{max} = stress intensity factor at maximum load,
$v_{p,max}$ = plastic displacement at maximum load,
W = specimen width,
ν = Poisson's ratio, and
σ_y = yield strength.

To estimate Δa at maximum load with Eqs 6, 7, and 8, the following approximations are made:

(*a*) K_{max} is calculated at maximum load, P_{max}, with initial crack length, a_0.
(*b*) r_p is calculated at the initial crack length a_0.
(*c*) $v_{p,max} = v_{max} - P_{max}C_0$, where v_{max} is the displacement at maximum load and C_0 is the elastic compliance at the initial crack length, a_0.

The blunting correction improves the accuracy in predicting crack length during the initial portion of crack extension for ductile, high toughness steels. The correction becomes increasingly negligible the more the crack extends.

Strain Hardening

Figure 4 illustrates schematically the effect of strain hardening on the load-displacement curve for a steel with linear elastic-strain hardening behavior. Similar to Fig. 2, the specimen follows curve 1 (OAA″) if the crack does not extend and curve 2 (OAB″) if the crack extends. The upward sloping run B′D of the step between two consecutive unloadings represents yielding without crack extension. The corresponding fall DB″ represents crack extension without yielding.

Even when the material strain hardens, a specimen whose crack does not extend unloads elastically along lines O′A′ and O″A″ which are parallel to the initial loading line OA. Hence, since the load increases along curve 1 and the unloading lines remain parallel, the elastic part of the displacement increases in proportion to the load. For a specimen in which the crack extends, the unloading lines from points B′ and B″ on curve 2 pass through points O′ and O″ just as they did for elastic-perfectly plastic material behavior in Fig. 2. The important

point is that the elastic displacement no longer remains constant, but grows in relationship to the amount of strain hardening the material experiences with crack extension.

Beyond point A, a power function describes well the load-displacement curve for a specimen without crack extension. For point A″ on curve 1 (Fig. 4)

$$P_i^* = \gamma v_i^{1/n} \tag{9}$$

where

P_i^* = load from curve 1, without crack extension,
γ = constant, and
n = strain hardening exponent.

Since point A also lies on curve 1, at the reference load P_{max}, Eq 9 becomes

$$P_{max} = \gamma v_{max}^{1/n} \tag{10}$$

Hence, the ratio of loads at A and A″ is

$$\frac{P_i^*}{P_{max}} = \left(\frac{v_i}{v_{max}}\right)^{1/n} \tag{11}$$

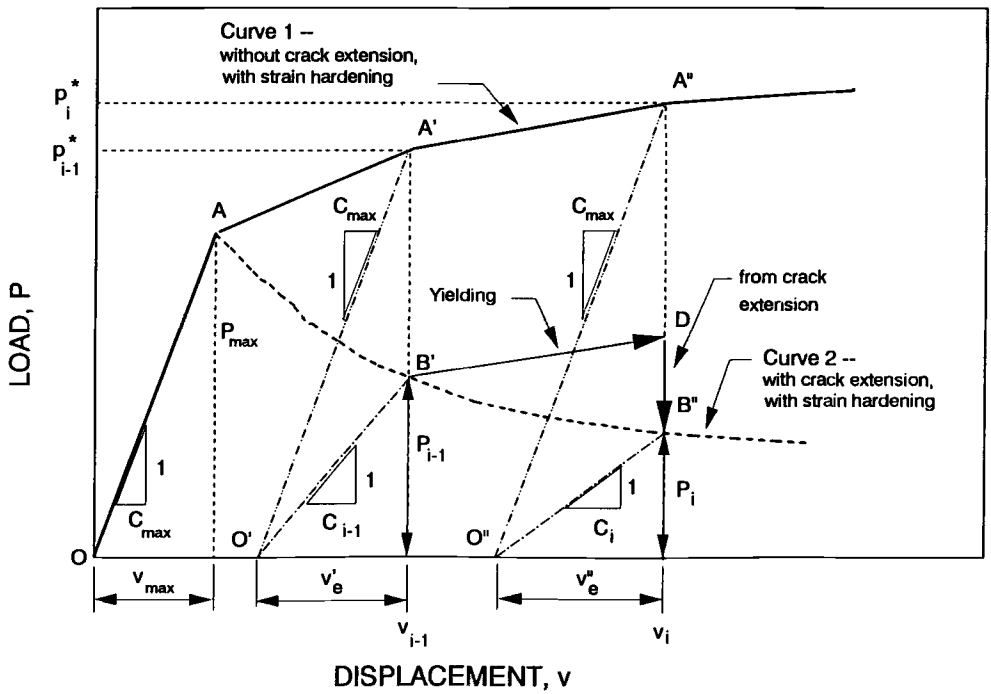

FIG. 4—*Schematic load-displacement curve for specimen made of elastic-strain hardening material; basis of improved load ratio method.*

Given that the elastic part of the displacement may be expressed in terms of the load and compliance associated with points A″ and B″ on both curves 1 and 2 (Fig. 4), then

$$v_e = P_i C_i = P_i^* C_{\max} \tag{12}$$

Solving Eq 12 for P_i^* with

$$P_i^* = P_i \frac{C_i}{C_{\max}} \tag{13}$$

and inserting P_i^* in Eq 11 yields an expression in terms of load and compliance associated with points A and B″ on curve 2 alone

$$\frac{P_i}{P_{\max}} = \frac{C_{\max}}{C_i} \left(\frac{v_i}{v_{\max}} \right)^{1/n} \tag{14}$$

Equation 14 can then be solved for the current compliance

$$C_i = \frac{P_{\max}}{P_i} \left(\frac{v_i}{v_{\max}} \right)^{1/n} C_{\max} \tag{15}$$

where

$(P, v, C)_i$ = current load, displacement, and compliance beyond maximum load and
$(P, v, C)_{\max}$ = load, displacement, and compliance at maximum load.

The bounds on the displacement term in Eq 15 are correct. For elastic materials, $n = 1$ and Eq 15 reduces to $(CP/v)_i = (CP/v)_{\max} = 1$. For elastic-perfectly plastic materials, n is very large, the exponent $1/n$ approaches zero, and Eq 15 reduces to Eq 2.

Matching Crack Lengths

Equation 15 still only approximates a specimen's real behavior for the following reasons:

1. Specimen constraint changes with crack extension as the ratio of net ligament width to specimen thickness becomes smaller.
2. The crack front may be curved or irregular.
3. The specimen's width at the back face increases when the net ligament fully yields and the two halves rotate through a large angle.

Such effects may produce large differences between predicted and actual crack lengths. They are minimized by matching the predicted compliance at the end of the load-displacement curve with the compliance corresponding to the measured physical (final) crack length, a_f.

In the third improvement, then, the load and displacement terms on the right-hand side of Eq 15 are premultiplied by a fitting coefficient β and raised to the power of another fitting coefficient, α

$$C_i = \beta \left[\frac{P_{\max}}{P_i} \left(\frac{v_i}{v_{\max}} \right)^{1/n} \right]^{\alpha} C_{\max} \tag{16}$$

The numerical values of the two fitting coefficients are obtained as follows. At maximum load, $(P, v, C)_i = (P, v, C)_{max}$ and Eq 16 thus yields $\beta = 1$. At the physical (final) crack length, $(P, v)_i$ are known as the last values of the load-displacement record. Inserting the physical (final) crack length in the compliance equation gives $C_i = C_f$. Knowing also $(P, v)_{max}$ from the load-displacement curve and C_{max} from inserting $a_{max} = a_0 + \delta/1.4$ in the compliance equation, Eq 16 can be solved for α.

$$\alpha = \frac{\log\left(\frac{C_f}{C_{max}}\right)}{\log\left[\frac{P_{max}}{P_f}\left(\frac{v_f}{v_{max}}\right)^{1/n}\right]} \tag{17}$$

Results

Materials

The accuracy of the improved load ratio method is demonstrated with analyses of *J-R* curve test data for C(T) compact tension specimens made of the following pressure vessel steels:

A508 Quenched and tempered vacuum-treated carbon and alloy steel forging for pressure vessels.

A302 Manganese-molybdenum and manganese-molybdenum-nickel alloy steel plates for welded boilers and other pressure vessels, Grade B (550-690 MPa tensile strength).

A533B Manganese-molybdenum and manganese-molybdenum-nickel alloy steel plates for use in the quenched and tempered condition for welded pressure vessels.

For structural steels:

A588 High-strength low-alloy structural steel with 345 MPa minimum yield point, for use in welded bridges and buildings.

A572 High-strength low-alloy columbium-vanadium steels of structural quality; for riveted bolted, or welded construction of bridges, buildings and other structures.

and ship steel:

HY-80 Steels for ship hulls.

Table 1 lists the material properties, and Table 2 summarizes the dimensions and test temperatures of the specimens re-analyzed in this study. The elastic compliance data were obtained from Refs *6* and *9* through *12*.

Elastic Displacement

The improved load ratio method is first compared with the elastic compliance method in terms of its ability to predict elastic displacements. To this end, it is assumed that the elastic displacement determined from the compliance at the last unloading is equal to the elastic displacement corresponding to the measured physical crack length. The elastic compliance at the maximum load, C_{max}, is either estimated from the compliance equation in the ASTM

TABLE 1—*Material properties.*

Material	Yield Stress σ_y, MPa	Ultimate Stress σ_u, MPa	Flow Stress σ_o, MPa	Elongation, %	Fracture Toughness J_{Ic}, kJ/m^2	Young's Modulus E, GPa
A533B	462	621	542	26	244	206
A302	459	585	522	19	109	204
A508			553		74	110
HY-80	614	731	672	23	183	200
A572	367	523	445	25		200
A588	390	549	469	21		200

standard (Designation E 813) by inserting the a_{max} from Eq 5, or measured from the unloading compliance method. In the following figures, they are referred to as "estimated C_{max}" or "C_{max} from ECM."

Figures 5 and 6 show elastic displacements of a 1T C(T) specimen with an initial crack length $a_0/W = 0.60$. It was made of HY-80 ship steel and tested at room temperature. Both figures contain elastic displacements predicted with the unloading elastic compliance method (triangular symbols), the original load ratio method (dotted line at constant v_e, with $n = \infty$ and $\alpha = 1$), and the improved load ratio method (solid curve, with $n = 10$ and $\alpha = 1.263$). Figure 5 has, in addition, a dashed curve for elastic displacement whose prediction includes the strain hardening correction but not the matching crack length correction ($n = 10$ and $\alpha = 1$). Conversely, Fig. 6 has a dashed-dotted curve for elastic displacement predicted with a matching crack length correction but not strain hardening correction ($n = \infty$ and $\alpha = 1.189$). All curves in this illustration start at the data point for the elastic displacement measured with the unloading compliance method at maximum load, designated P_{max} in Figs. 5 and 6.

Clearly, each correction markedly improves the result for the HY-80 steel specimen, but both together predict best the elastic displacement v_e as indicated by the solid curves.

Similarly, Figs. 7 and 8 show the effects of strain hardening and matching physical crack length, respectively, on the elastic displacement of a 1T C(T) specimen with an initial crack

TABLE 2—*Specimens analyzed in present study.*

Material	Specimen No.	Specimen Size C(T)	Side Groove, %	Initial Crack Length, a_0/W	Test Temperature, °C
A533B	13A	1T	20	0.55	88
A533B	E3	1T	20	0.62	88
A533B	JB4	1T	20	0.75	88
A302	V50-115	0.5T	20	0.52	82
A302	V50-109	1T	20	0.52	82
A302	V50-105	2T	20	0.52	82
A302	V50-102	4T	20	0.51	82
A302	V50-101	6T	20	0.52	82
A508	66W-33	1.6T	20	0.56	200
HY-80	FYBA1	1T	20	0.60	RT
A572	A2-19	1T	20	0.66	24
A588	B8-6	1T	20	0.52	24
A588	B8-18	1T	20	0.52	24

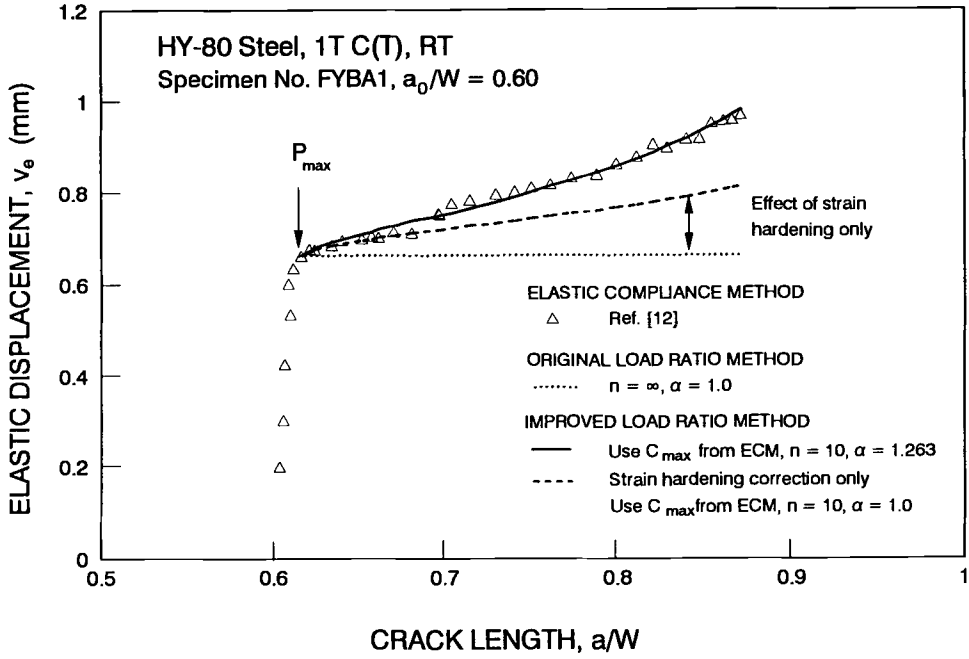

FIG. 5—*Effect of strain hardening correction on predicted elastic displacement; 1T C(T) specimen of HY-80 steel.*

length of $a_0/W = 0.51$. The specimen was made of A588 structural steel and was tested at 24°C [*6*]. Correcting only for strain hardening (the dashed curve in Fig. 7, with $n = 5$ and $\alpha = 1$) overestimates slightly the elastic displacement, while correcting only for matching crack length (dashed-dotted curve in Fig. 8, with $n = \infty$ and $\alpha = 2.543$) greatly underestimates the elastic displacement in the central portion of the curve.

For the A588 steel, the strain hardening correction improves the result much more than does the physical crack length correction. Again, the results are predicted best with both corrections (solid curves in Figs. 7 and 8, with $n = 5$ and $\alpha = 1.081$).

Effect of Strain Hardening

Differences in strain hardening behavior of various steel types are readily apparent from load-displacement curves. For example, the three 1T C(T) specimens of A533B steel, with initial crack lengths of $a_0/W = 0.55$, 0.62, and 0.75, exhibit a behavior typical of highly ductile materials in which the crack extends at limit load after reaching the maximum load (Fig. 9). For materials approaching elastic-perfectly plastic behavior, the strain hardening exponent n is very large, and the strain hardening correction term, $(v/v_{max})^{1/n}$, becomes less important than for the less ductile materials described in the above subsections.

Turner pointed out in Ref *1* that the "pagoda roof" shape of load-displacement curves beyond maximum load, while typical of many piping, pressure vessel and ship steels as shown in Figs. 1 and 9, is not universal. The authors agree. Some structural steels exhibit load-displacement curves with a "roundhouse" shape such as those for A588 steel shown in Fig. 3. A pagoda-roof curve has a short concave peak followed by a long convex tail (Figs. 1 and 9). A roundhouse curve has a long concave peak and a short or negligible

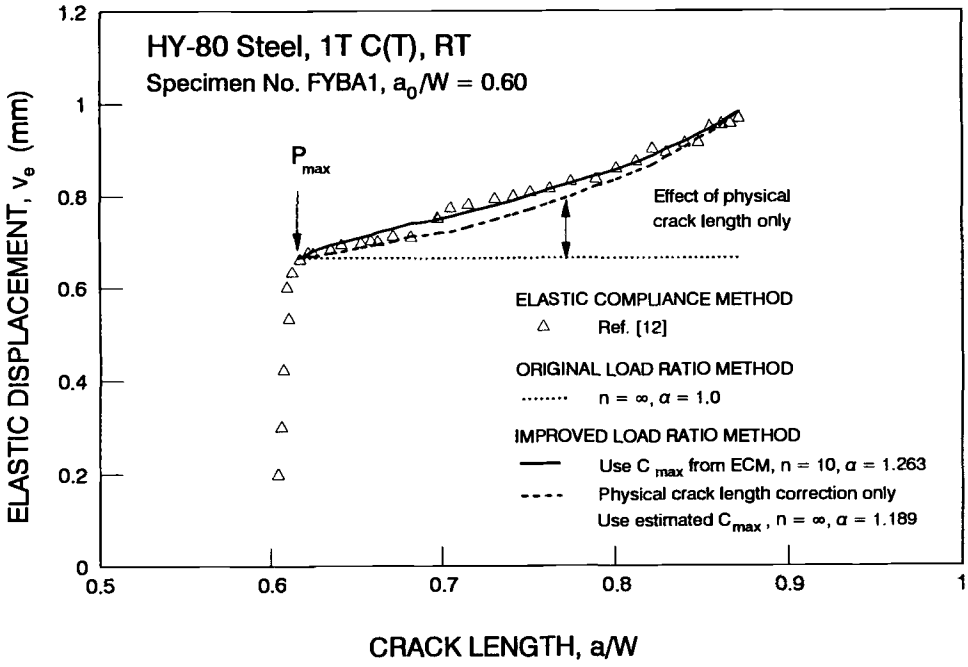

FIG. 6—*Effect of matching physical crack length on predicted elastic displacement; 1T C(T) specimen of HY-80 steel.*

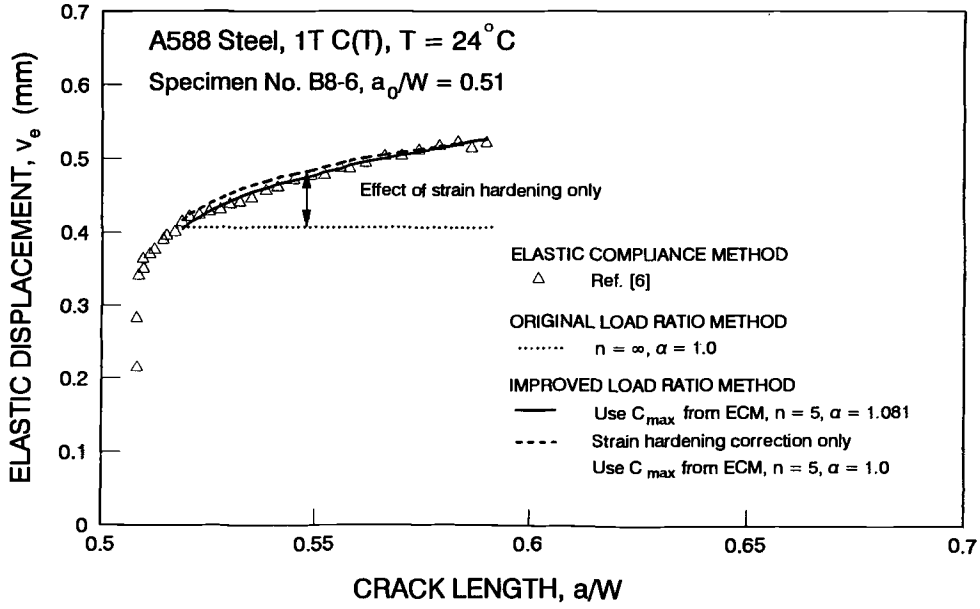

FIG. 7—*Effect of strain hardening on predicted elastic displacement; 1T C(T) specimen of A588 steel.*

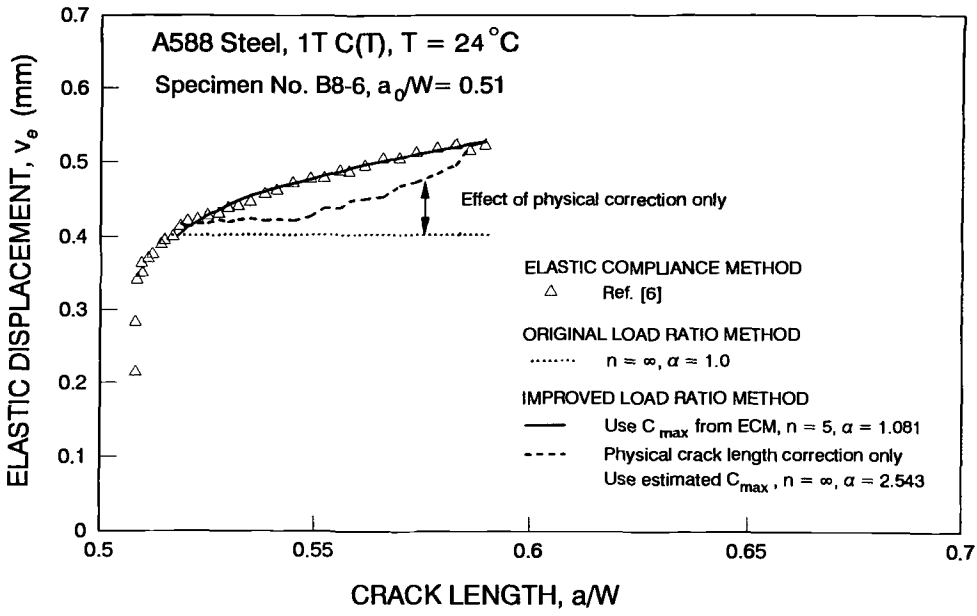

FIG. 8—*Effect of matching physical crack length on predicted elastic displacement; 1T C(T) specimen of A588 steel.*

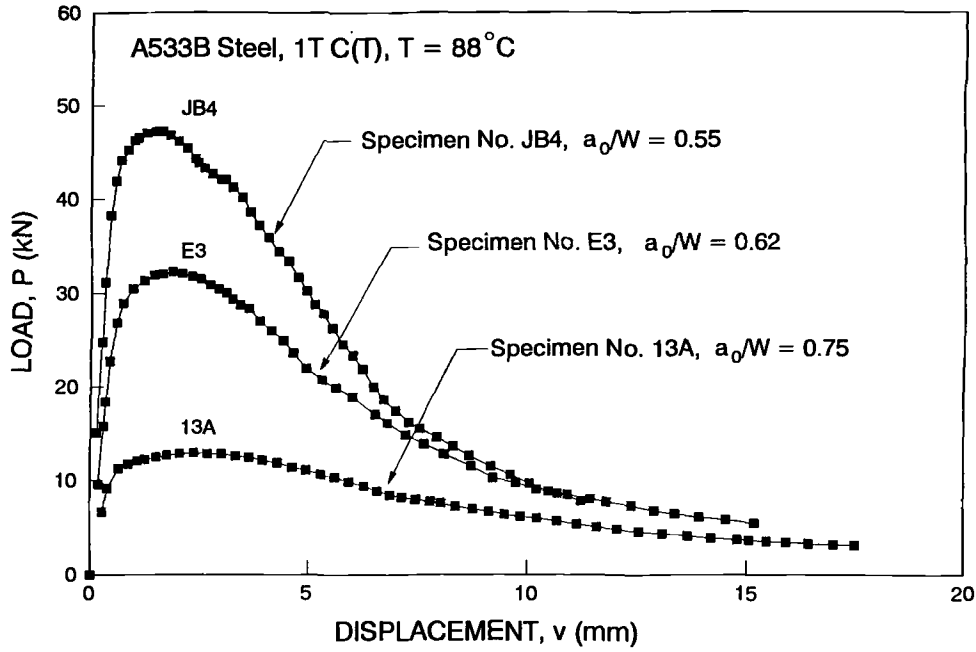

FIG. 9—*Measured load-displacement curves; 1T C(T) specimens of A533B steel.*

convex tail (Fig. 3). The latter is more reminiscent of a tensile stress-strain curve for a highly strain hardening steel. As is shown next, the improved load ratio method increases the accuracy of predicting crack length most for steels with roundhouse curves.

The effect of strain hardening on crack extension is examined in two ways. First, to demonstrate the improvement with strain hardening, crack extensions predicted with and without the $(v/v_{max})^{1/n}$ term are compared with those determined with the elastic compliance method. Figure 10 shows the result for the same 1T C(T) specimen of A588 steel used above to predict elastic displacements [*6*]. For this specimen, the blunting correction slightly underestimates crack extension $\Delta a/W$ at maximum load. The improved load ratio method predicts well crack extension over the full range of the data when the strain hardening correction is included (open triangles in Fig. 10, with $n = 5$ and $\alpha = 1.081$). But it would greatly underpredict crack extension in the central portion if the correction were excluded (rectangles in Fig. 10, with $n = \infty$ and $\alpha = 2.543$). This is the case even though the crack extension at maximum load was estimated with the blunting correction and the final $\Delta a/W$ value was forced to match the compliance result at the end of the test. Thus, strain hardening controls the shape of the crack extension versus displacement curve in the central portion.

The second way of demonstrating the effect of strain hardening on crack extension is to let the exponent vary; that is, $n = 5$, 10, 20, and ∞. As Fig. 11 shows, while the value generally affects the prediction, n could be off by as much as 20% ($n = 5 \pm 1$) and the improved load ratio method would still yield good results. Precise values of the exponent are not needed.

Strain hardening exponents for the materials examined in this study were chosen based on experience. When precise values are needed, a stress-strain curve for the material must be obtained.

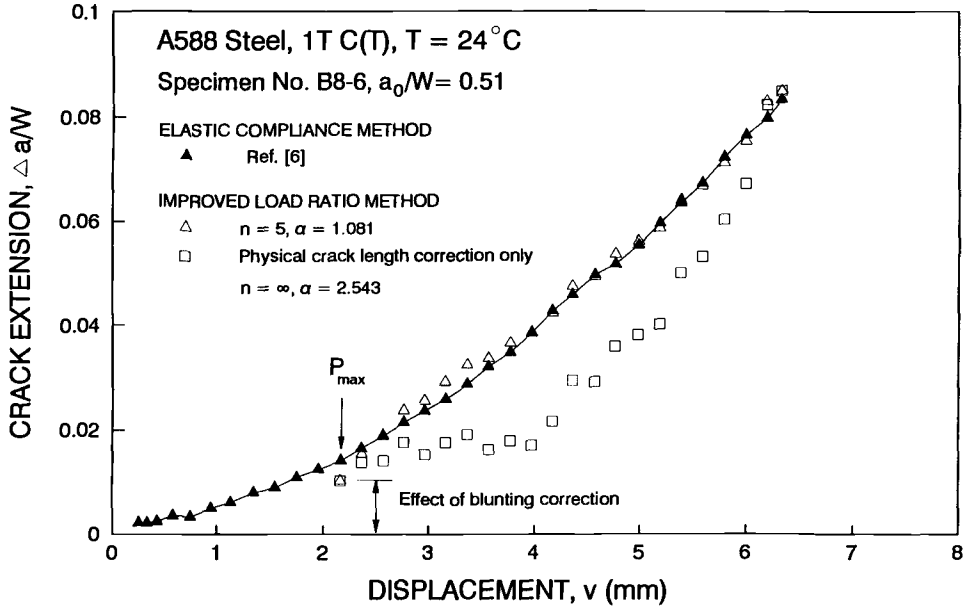

FIG. 10—*Effect of strain hardening correction on predicted crack extension; 1T C(T) specimen of A588 steel.*

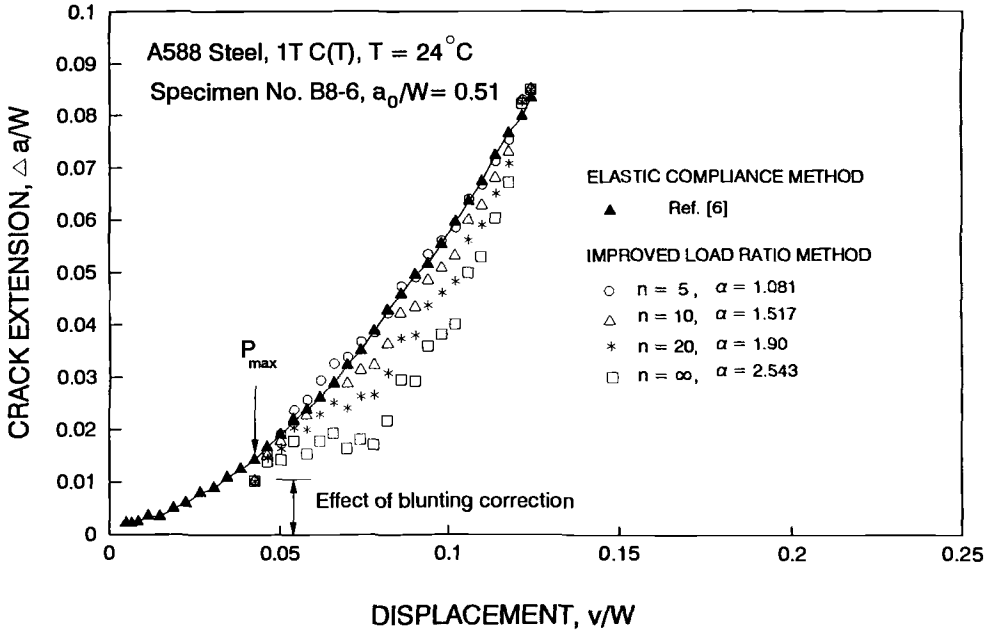

FIG. 11—*Effect of strain hardening exponent on predicted crack extension; 1T C(T) specimen of A588 steel.*

Effect of Physical Crack Length

Estimates of crack length should match the physical crack length measured at the end of the test. The compliance method typically underestimates the final crack extension. Better results are obtained with the improved load ratio method by matching the predicted with the physical crack length (or extension). Crack extensions predicted with the elastic compliance and improved load ratio methods are compared in Fig. 12 for a 2T C(T) specimen of A302 steel from Ref *10*, with $n = 10$ and $\alpha = 1.128$. The physical crack extension is the ordinate of the last open triangle. The match yields a curve that is shifted upward from the elastic unloading compliance results but maintains the same basic shape. It yields a significant improvement over the elastic unloading compliance method. The improved load ratio method predicts well crack extension over the full range of the data despite two instances of unstable crack extension followed by crack arrest.

More examples of the effect of matching final crack extensions are shown in all subsequent figures of crack extension versus displacement.

Effect of Specimen Size

The improved load ratio method was applied to five C(T) specimens of A302 steel ranging in size from 0.5T to 6T. In all specimens, the initial crack length was $a_0/W = 0.52$ and the strain hardening exponent $n = 10$. The tests were performed at a temperature of 82°C [*10*]. Figures 12 through 14 show the results for the 2T, 0.5T, and 6T specimens respectively. Good predictions were obtained for all three specimens despite large variations in specimen size and dramatic differences in elastic-plastic behavior as is apparent in the normalized load

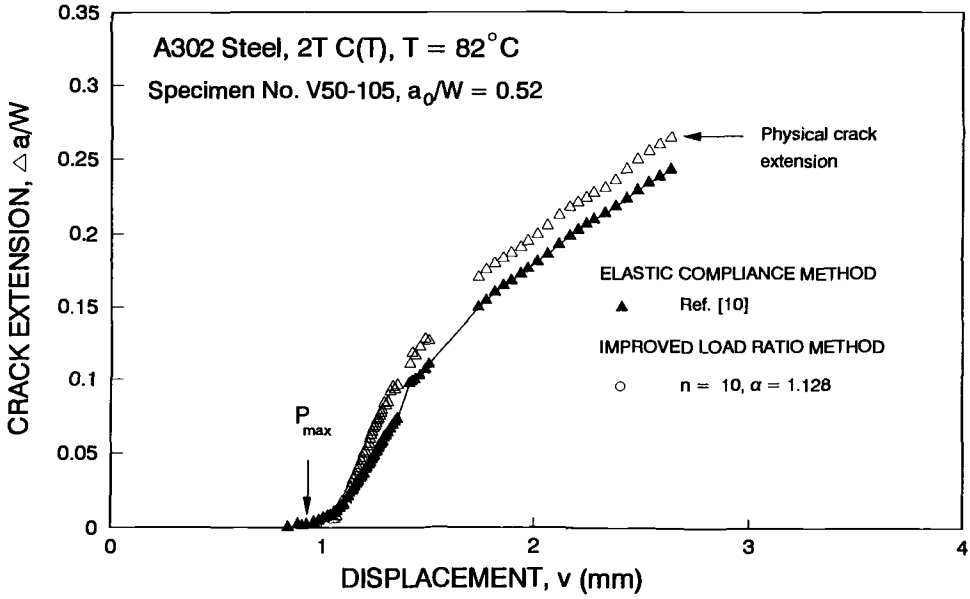

FIG. 12—*Effect of physical crack length on predicted crack extension; 2T C(T) specimen of A302 steel.*

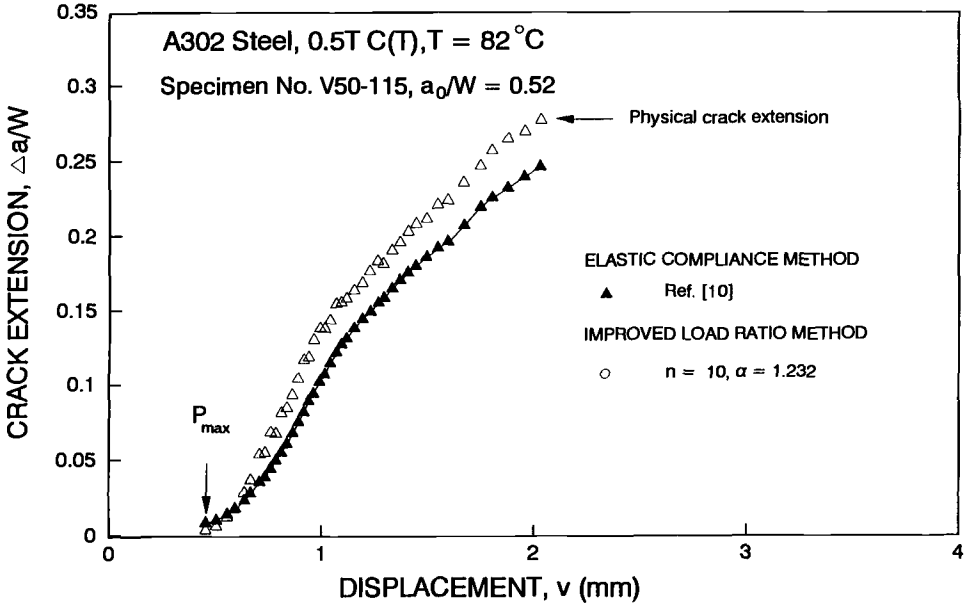

FIG. 13—*Effect of specimen size on predicted crack extension; 0.5T C(T) specimen of A302 steel.*

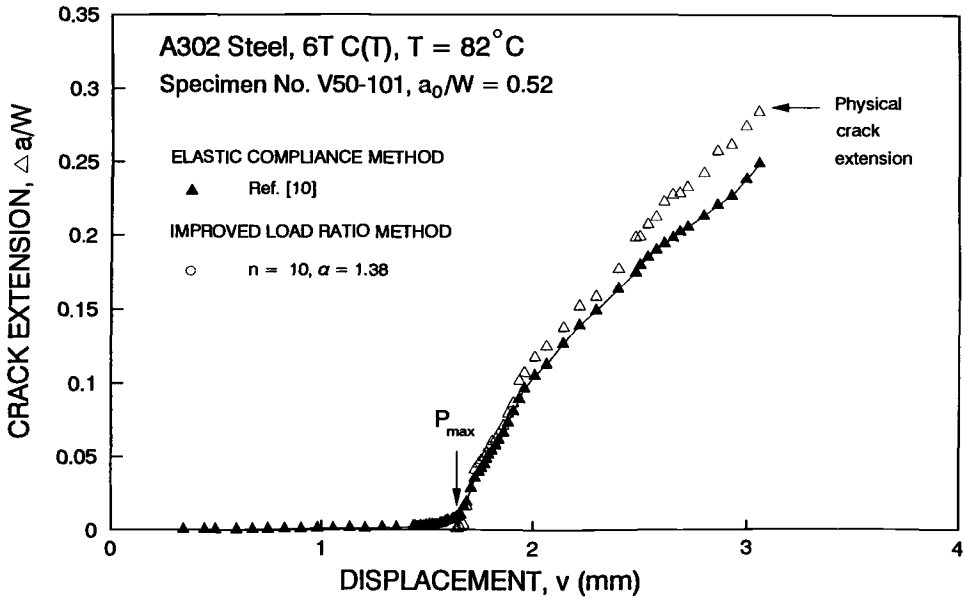

FIG. 14—*Effect of specimen size on predicted crack extension; 6T C(T) specimen of A302 steel.*

versus crack length curves of Fig. 15. The crack extended at a load nearly equal to the limit load in the 0.5T specimen, and at about 75 and 50% of the limit load in the 2T and 6T specimens, respectively.

Effect of Steel Type

The accuracy of the improved load ratio method was verified for many specimens of six different steels. Results were already presented for A588 steel in Figs. 10 and 11, and for A302 steel in Figs. 12 to 14. Additional results are shown in Figs. 16 to 19 for A533B, HY-80, A508, and A572 steels, respectively. In most cases the improved load ratio method performed very well.

A notable exception is the 1T C(T) specimen of A572 steel, with an initial crack length of a_0/W = 0.66, strain hardening exponent n = 3, and fitting parameter α = 1.236 (Fig. 19). This specimen reached the maximum load and failed abruptly after four unloadings beyond maximum load. The crack extended an order of magnitude less than in the A533B, HY-80, and A508 steel specimens (Figs. 16 to 18), but the displacements were about the same in all four. Additional elastic-plastic fracture toughness tests of A572 steel specimens are currently being conducted to clarify this unusual behavior.

Conclusions

The following conclusions can be drawn from the results previously mentioned:

1. A greatly improved load ratio method was developed for predicting crack extension. The method accurately predicts crack extension in C(T) specimens made of pressure vessel, structural, and ship steels.

2. The load ratio method uses the load-displacement curve, initial, and final physical crack lengths, and the strain hardening exponent. It requires no additional equipment, and no

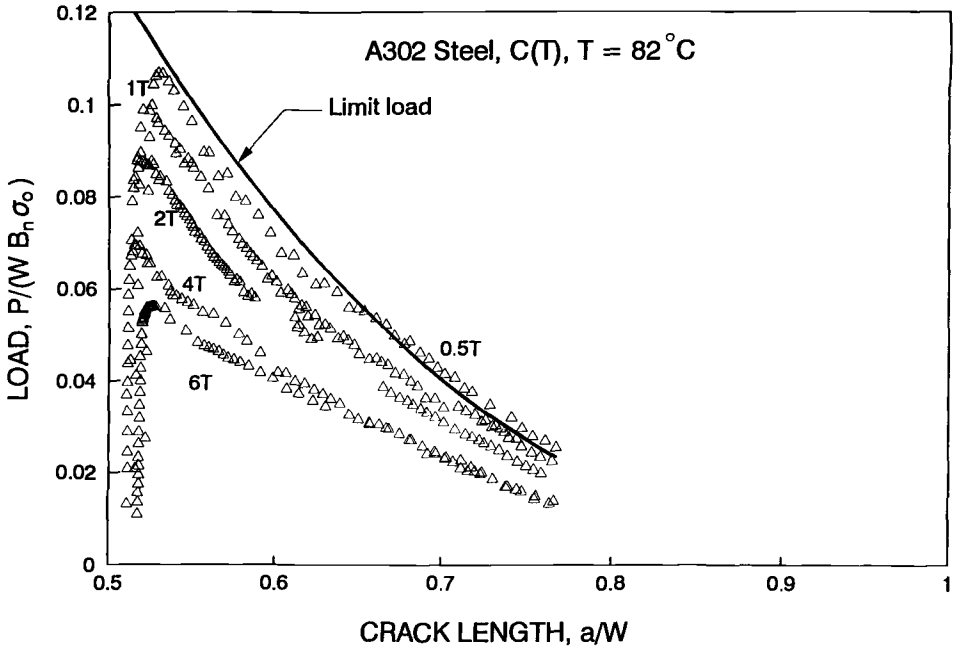

FIG. 15—*Crack extension in 0.5T through 6T C(T) specimens of A302 steel.*

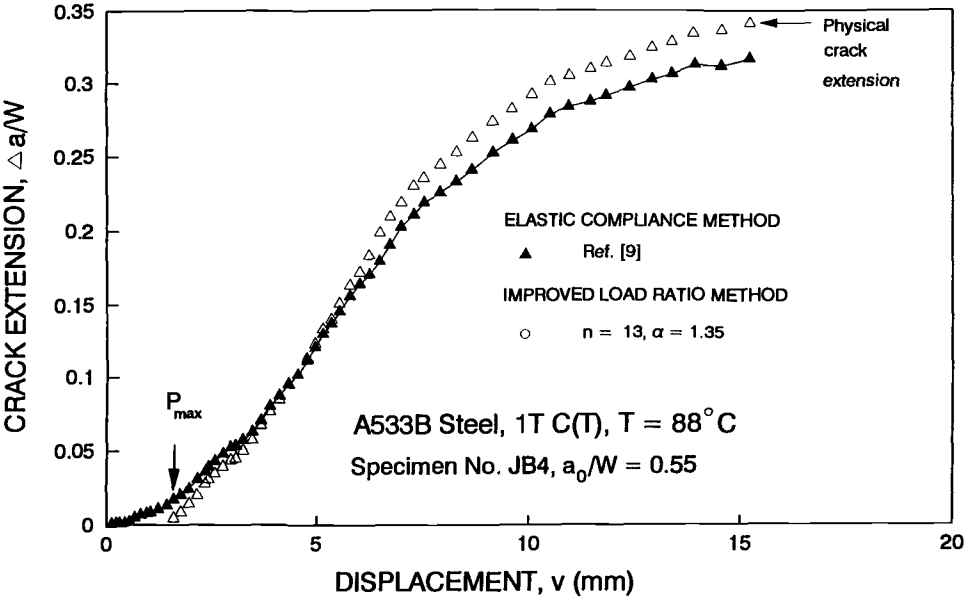

FIG. 16—*Effect of steel type on predicted crack extension; 1T C(T) specimen of A533B steel.*

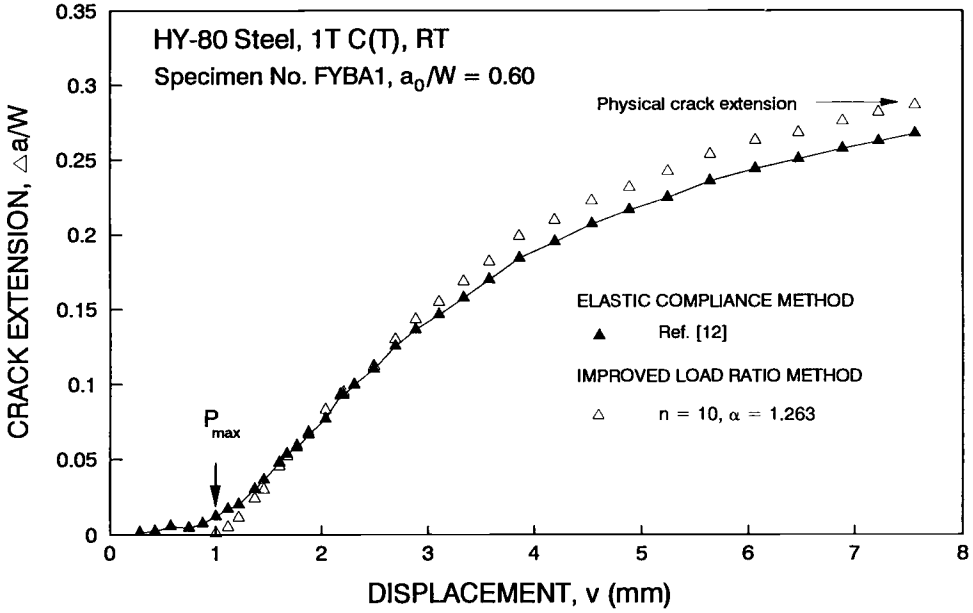

FIG. 17—*Effect of steel type on predicted crack extension; 1T C(T) specimen of HY-80 steel.*

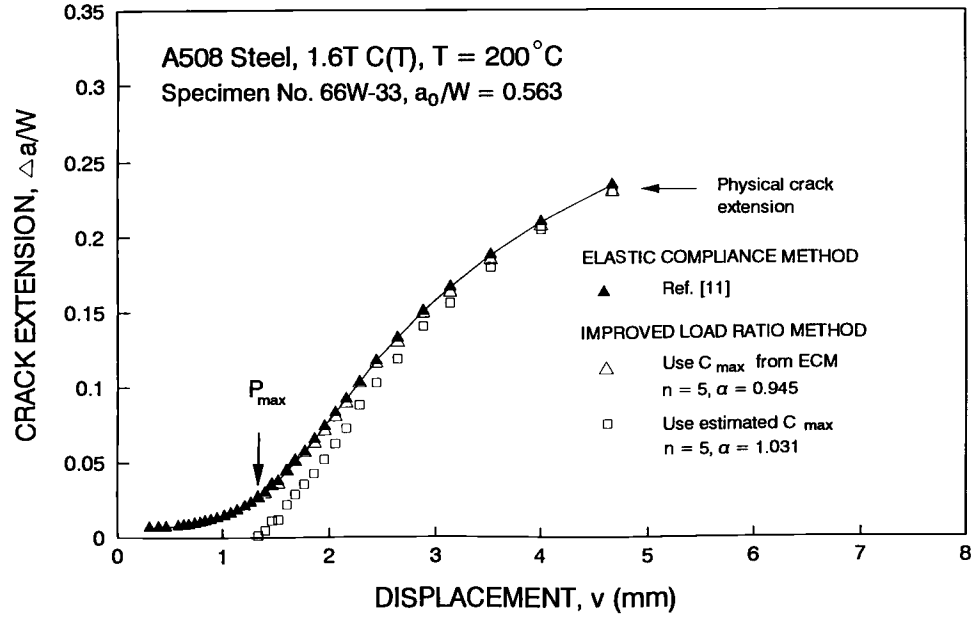

FIG. 18—*Effect of steel type on predicted crack extension; 1.6T C(T) specimen of A508 steel.*

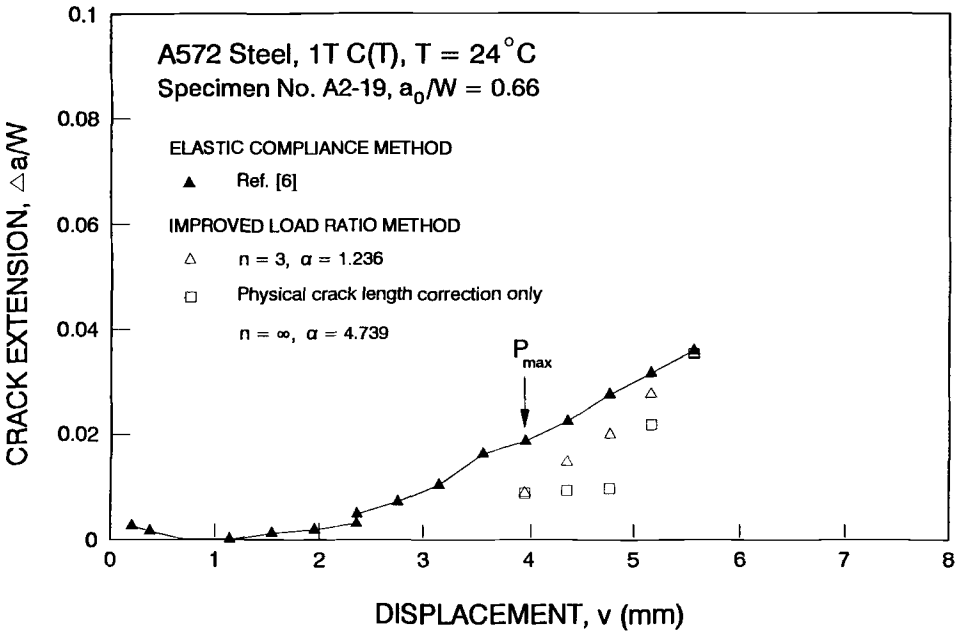

FIG. 19—*Effect of steel type on predicted crack extension; 1T C(T) specimen of A572 steel.*

unloading/reloading sequences. Resolution and noise level of displacement transducers can be equivalent to those of a typical load transducer, rather than the required two orders of magnitude more stringent for the unloading compliance method.

3. The present method improves on the original load ratio method in three ways. Crack extension at maximum load is estimated with a blunting term, strain hardening is accounted for, and the predicted final crack length is forced to match the physical crack length at the end of the test. These improvements greatly enhance the accuracy of predicting crack extension. The blunting and strain hardening corrections have a greater effect on the A572 and A588 structural steels than on the A533B and A508 pressure vessel steels.

4. Because only a monotonic load-displacement curve is needed for the improved load ratio method, it should be applicable to fracture toughness testing under dynamic loading and at very high temperatures.

5. Elastic-plastic fracture toughness measurements are greatly simplified using the improved load ratio method. Savings can be made in technician training, lower equipment requirements, and the time needed to perform a test. Combined with other steps in the fracture toughness test methods and a simple computer program, the method can be moved easily from a research setting to the steel mill for toughness testing of rolled shapes and plates.

References

[*1*] Hu, J. M., Albrecht, P., and Joyce, J. A., "Load Ratio Method of Determining Crack Length," *Fracture Mechanics: Twenty-Second Symposium (Volume 1), ASTM STP 1131,* H. A. Ernst, A. Saxena, and D. L. McDowell, Eds., American Society for Testing and Materials, Philadelphia, 1992, pp. 880–903.

[2] Joyce, J. A., Ernst, H. A., and Paris, P. C., "Direct Evaluation of J-Resistance Curves from Load-Displacement Records," *Fracture Mechanics: Twelfth Symposium, ASTM STP 700,* American Society for Testing and Materials, Philadelphia, 1980, pp. 222–236.

[3] Landes, J. D. and Herrera, R., "A New Look at J-R Curve Analysis," *International Journal of Fracture,* Vol. 36, 1988, pp. R9–R14.

[4] Mecklenburg, M. F., Joyce, J. A., and Albrecht, P., "Separation of Energies in Elastic-Plastic Fracture," *Nonlinear Fracture Mechanics: Volume II—Elastic-Plastic Fracture, ASTM STP 995,* J. D. Landes, A. Saxena, and J. G. Merkle, Eds., American Society for Testing and Materials, Philadelphia, 1989, pp. 594–612.

[5] Saxena, A. and Hudak, S. J., "Review and Extension of Compliance Information for Common Crack Growth Specimens," *International Journal of Fracture,* Vol. 14, No. 5, Oct. 1978, pp. 453–468.

[6] Hartmann, J., Wright, W., and Albrecht, P., *"Fracture Toughness of A572 and A588 Structural Steels,"* Turner-Fairbank Highway Research Center, Federal Highway Administration, McLean, VA, 1995.

[7] Rice, J. R., Drugan, W. J., and Sham, T. L., "Elastic-Plastic Analysis of Growing Cracks," *Fracture Mechanics: Twelfth Symposium, ASTM STP 700,* American Society for Testing and Materials, Philadelphia, 1980, pp. 189–221.

[8] Hu, J. M. and Albrecht, P., "Limit Load Solution and Loading Behavior of C(T) Fracture Specimen," *International Journal of Fracture,* Vol. 52, 1991, pp. 19–45.

[9] Joyce, J. A., *"Ductile to Brittle Toughness Transition Characterization of A533B Steel,"* Report No. NUREG/CR-5142, Nuclear Regulatory Commission, Washington, DC, 1988.

[10] Hiser, A. L. and Terrell, J. B., *"Size Effects on J-R Curves for A302 Plate,"* Report No. NUREG/CR-5265, Nuclear Regulatory Commission, Washington, DC, 1989.

[11] Hiser, A. L., Loss, F. J., and Menke, B. H., *"J-R Curve Characterization of Irradiated Low Upper Shelf Welds,"* Report No. NUREG/CR-3506, Nuclear Regulatory Commission, Washington, DC, April 1984.

[12] Joyce, J. A., Davis, D. A., and Hays, R. A., *"Application of the J-integral and the Modified J-integral to Cases of Large Crack Extension,"* Report No. NUREG/CR-5143, Nuclear Regulatory Commission, Washington, DC, 1989.

D. K. Rehbein,[1] *R. B. Thompson,*[2] *and O. Buck*[3]

Ultrasonic Size Determination of Cracks with Large Closure Regions

REFERENCE: Rehbein, D. K., Thompson, R. B., and Buck, O., **"Ultrasonic Size Determination of Cracks with Large Closure Regions,"** *Special Applications and Advanced Techniques for Crack Size Determination, ASTM STP 1251,* J. J. Ruschau and J. K. Donald, Eds., American Society for Testing and Materials, Philadelphia, 1995, pp. 104–113.

ABSTRACT: A number of investigators have developed acoustic methods for measurement and determination of crack length. These methods have generally fallen into one of three categories, determination of crack area, time of flight to determine crack length, or recognition of the crack tip by changes in the signal response. These methods have been successful in location of the crack tip to within ±0.5 mm. In all cases, however, it was necessary for the crack length or the crack-tip position to be determined with the crack in a fully open state in order to remove the effects of crack closure. Recent work has developed acoustic scanning techniques and subsequent analysis to the point where the same accuracy of ±0.5 mm is now possible through scanning of the crack in an unloaded condition with closure accounted for. A review of the previous methods will be given together with an explanation of the advances in scanning technique and analysis that have allowed this simplification to occur.

KEYWORDS: acoustic, crack closure, crack length, fatigue

Accurate calculation of the stress intensity factor on a given component under load relies on an accurate size determination of the flaws present in the component. The challenge to the nondestructive evaluation (NDE) community has been development of reliable techniques to provide that accurate size determination. Many research groups have investigated this problem using ultrasonic methods with summaries of their techniques and results provided by various authors [*1–3*]. In general, the techniques developed fall into three general categories: (1) determination of crack length from signal amplitude measurements, (2) determination of crack length from time-of-flight measurements, and (3) determination of crack length using interference between diffracted waves. Sketches of representative techniques in each category are shown in Fig. 1.

Background

Crack Length From Signal Amplitude

Figure 1(1) is a sketch of the technique developed by Lumb and co-workers [*4*]. They used a compression wave to monitor the growth of a through-the-thickness crack. A cali-

[1] Associate metallurgist, 206 Metals Development, Ames Laboratory-USDOE, Ames, IA 50011.
[2] Associate director, Science and Technology, 108 Office & Laboratory, Ames Laboratory, Ames, IA 50011.
[3] Program director, Metallurgy and Ceramics, 126 Metals Development, Ames Laboratory-USDOE, Ames, IA 50011.

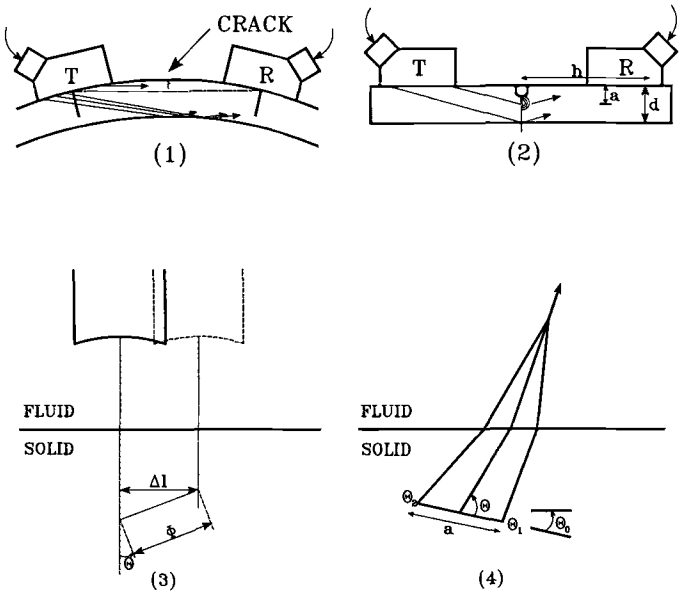

FIG. 1—*Representative techniques used for determining crack length. (1) Signal amplitude (Ref 4). (2) Time of flight: surface breaking crack (Ref 5). (3) Time of flight: subsurface crack (Ref 6). (4) Diffracted wave modulation (Ref 8).*

bration curve of the ultrasonic signal amplitude versus crack depth was developed using milled slots and destructive measurements of part-through fatigue cracks to determine the depth of penetration of in-service cracks. They claim measurement of growth increments accurate to ±0.025 mm and larger amounts of growth accurate to ±0.25 mm.

Particular problems concerning this technique were determined to be the stability of the coupling and temperature induced drift due to attenuation and velocity in the wedges. Additionally, crack closure contributes to inaccuracy of the crack depth measurement since contact between the crack faces allows additional energy to be transmitted that would be blocked if the crack were completely open.

Crack Length From Time-of-Flight

Crack length measurement using the technique shown in Fig. 1(2) as developed by Silk [5] determines the crack length by the time of flight of the wave diffracted by the crack tip and the wave reflected from the back surface. The crack length a is calculated according to

$$a = [(C_1 t/2)^2 - h^2]^{1/2} \tag{1}$$

where

C_1 = acoustic velocity of the wave,
t = time of flight, and
h = distance between crack and receiving transducer.

This result can be checked by using

$$\Delta t = (2/C_1)(d^2 + h^2)^{1/2} - t \tag{2}$$

where

d = sample thickness, and
Δt = difference in flight time of the waves diffracted from the crack tip and reflected from the back surface.

It is recognized that any inaccuracies in the measurements of the separation distance of the receiver from the crack or the acoustic velocity would be reflected in the calculated crack length. It is recommended that the technique be calibrated using saw slots cut into the material of interest in order to correct for possible texture changes. It is also possible that closure in the crack would effectively broaden the diffracted wave being received since diffraction would be occurring at more than one position in the crack, rendering the time measurement more difficult. If the structure is under load, it is possible to measure the crack depth to ± 0.2 mm.

De Vadder and colleagues [*6*] have developed a technique that effectively extends Silk's work to subsurface cracks through the translation of a single transducer to determine the positions of the maximum amplitude of the diffracted wave emanating from the tips of the crack. A typical arrangement is shown in Fig. 1(3). Knowledge of these positions and the time difference between the diffracted waves at these positions allows calculation of the length and orientation of the buried crack according to

$$\Phi = [(C_1\Delta t/2)^2 + \Delta l^2]^{1/2} \tag{3}$$

and

$$\Theta = \tan^{-1}[(C_1\Delta t)/(2\Delta l)] \tag{4}$$

where

Δt = difference in time of flight of the diffracted waves at the positions of maximum amplitude

and the remainder are as shown in Fig. 1(3). The situation shown and equations given are for normal incidence waves investigating the crack. Similar results can be obtained from off-normal incidence when that is more advantageous due to the crack geometry.

Work by Bouami and De Vadder [*7*] has shown that this method is incapable of detecting the actual tip of a closed crack providing the crack is not blunted. The length of the closure region and thus the true crack length can be determined by evaluation of the measurements under zero stress and maximum loaded stress. As with the other techniques developed, it is then necessary to evaluate the crack under load in order to determine the actual crack length.

Crack Length From Interference of Diffracted Waves

Achenbach and co-workers [*8*] have utilized the elastodynamic ray theory [*9*] to predict the scattering field for the situation shown in Fig. 1(4). In this configuration, the crack is completely subsurface similar to that used by De Vadder except that the crack is of insufficient length to allow the diffracted signals from the tips to be separated. The first arriving wave at the receiving transducer then is due to the interference of the longitudinal rays

diffracted at the crack tips. This wave exhibits a modulation in the frequency domain with period, p

$$p = \pi/a[\cos \Theta - \sin \Theta_0] \tag{5}$$

where

a = length of crack,
Θ = angle between crack and center ray of acoustic beam, and
Θ_0 = angle between crack and surface.

Since both a and Θ_0 are unknown, two measurements at different angles are necessary to quantify the crack parameters but with inclusion of the appropriate attenuation values, agreement between their model and the experiment was almost perfect.

It is important to note, however, that one of the objectives of the original theoretical work was to generate a better understanding of the scattering at the tips of fully open cracks embedded in the bulk of a material. Closure in such a crack will contribute additional low amplitude diffracted waves in the closure region, making the determination of the crack length virtually impossible.

Extended Closure

Previous work [*10*] has shown the existence under certain growth conditions of a greatly extended closure region, up to several millimeters. This extended closure region necessitates the application of a tensile load to open the crack in order for the earlier techniques to make a determination of the position of the crack tip. The work currently underway is an attempt to address this problem and determine the crack-tip position without the necessity for the application of tensile loading.

Current Work

Considerable effort has been made to characterize various aspects of the geometry present at the tip of a fatigue crack using a modification of earlier methods suggested by Thompson and Fiedler [*11*]. This method in conjunction with the "distributed spring model" of Baik and Thompson [*12*] characterizes the conditions in the closure region near the crack tip by the use of a broadband pitch-catch transducer system with stepper motor translation of the cracked specimen. This combination allows characterization of the transmission response of a fatigue crack as shown in Fig. 2. The top of the figure is a sketch of the experimental apparatus with two sets of experimental results shown on the bottom. The left-hand graph is the response from a saw slot while the right-hand graph shows the response of an actual fatigue crack grown under a constant stress intensity range, ΔK. The data were taken using focussed 10 MHz transducers of 1.905 cm (0.75 in.) diameter with a focal length of 10.16 cm (4 in.) in water.

In each of these figures as well as the acoustic response curves to be shown later, the transmission coefficient values shown are derived by a normalization process with respect to the uncracked ligament of the specimen. In order to accomplish this normalization, the frequency spectrum obtained at a given position on the specimen is deconvolved with the spectrum obtained by transmission in an uncracked area of the specimen. The values obtained by this deconvolution are the transmission coefficients as a function of frequency, where a transmission coefficient of 1 indicates perfect transmission and 0 indicates no transmitted

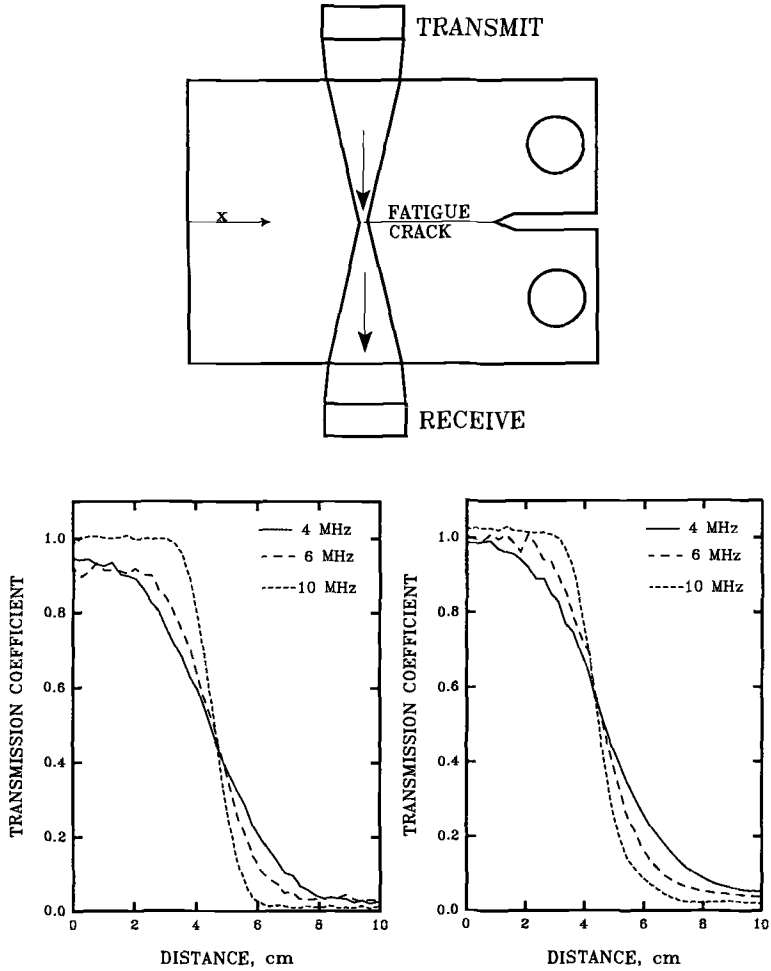

FIG. 2—*Experimental arrangement* (top) *and typical response from saw slot* (bottom-left) *and fatigue crack* (bottom-right).

energy. Due to processes unrelated to the fatigue crack (electronic noise, changes in grain scattering, surface irregularities, etc.), values greater than 1 may be obtained in the uncracked area of the specimen. Since a best-fit analysis will be used to delineate the crack tip later, these essentially random errors will be of slight importance.

The actual differences between the two transmission responses are rather subtle in Fig. 2 but are caused by dramatic differences in the specimens themselves. The left-hand response, that from a saw slot, shows a crossover of the curves at a transmission coefficient of 0.5 due to the overlapping of the effective spot sizes at the tip of the completely open slot. Each spot is half on and half off the slot at the same position leading to a transmission coefficient of 0.5 for each frequency at that position. However, because of closure, the crack shows a transmission coefficient of 0.5 that changes position with frequency due to the changes in transmission characteristics with frequency. The crossover therefore is elevated above 0.5.

In addition, there is a more gradual change from perfect transmission ($T = 1.0$) to no transmission ($T = 0.0$) in the response from the fatigue crack.

Characterization of the closure in the transmission response curve has been accomplished using the distributed spring model based on the work of Baik and Thompson [*12*]. Modeling the contact in the closure region leads to the expression

$$\Gamma^N = C \int_{-00}^{00} dx \frac{1}{1 + j\alpha(x)} e^{-(x-x_1)^2/w^2} \tag{6}$$

where

Γ^N = transmission through a given position normalized by the transmission through the uncracked ligament,
C = constant containing information on the material parameters and the transducer characteristics,
x_1 = center position of the transducer, and
w = effective radius of the ultrasonic beam.

$\alpha(x)$ is characterized according to

$$\alpha(x) = \pi\rho v f/\kappa(x) \tag{7}$$

where

ρ = material density,
v = acoustic velocity, and
f = frequency.

$\kappa(x)$ is the distributed spring constant applied in the cracked region of the specimen and is expressed by

$$\kappa(x) = \kappa_0 e - \beta_x \tag{8}$$

where κ is equal to κ_0 at the crack tip and decreases according to the decay constant β as the beam moves deeper into the crack. In order to fully characterize the crack, then, it is necessary to determine the crack tip position accurately in order to begin applying Eq 8 over the proper region.

Equations 6 to 8 are used in a best fit procedure to determine the optimum values for the crack tip, the spring constant value at the crack tip κ_0, and the decay constant β. A transmission response curve for three individual frequencies is calculated for a given set of the three parameters and compared to the experimental data through calculation of the total error in the transition region of the response curve. The set of parameters that yields the lowest total error is taken to be the optimum set of parameters for that crack.

Experimental Results

Figures 3 and 4 show experimentally determined transmission response curves from cracks in three different specimens with no external loading. Constant ΔK fatigue cracks were grown in two separate specimens of 2024-T6 aluminum. The ultrasonic response from these cracks is shown in Fig. 3. The material was in the as-rolled condition with the crack in the top

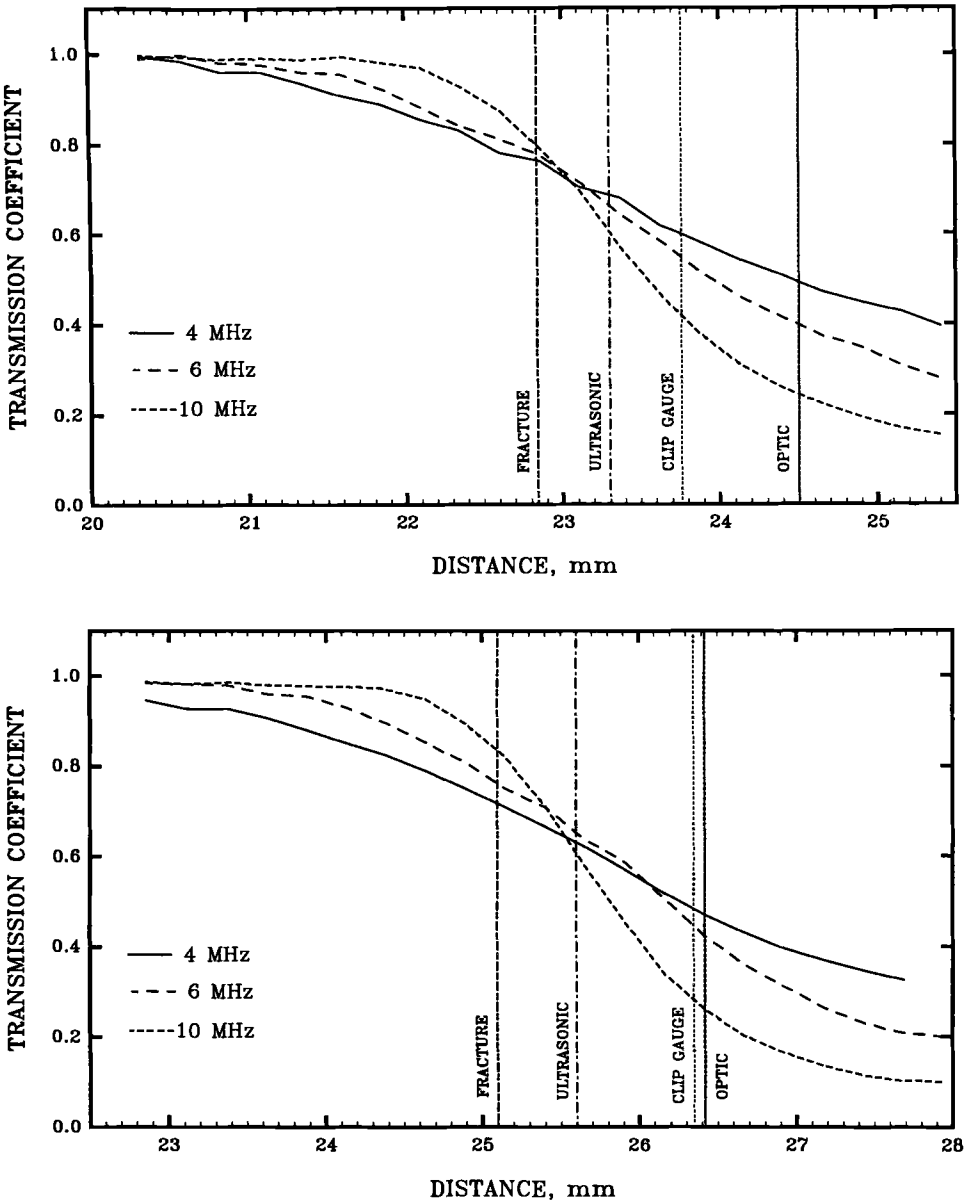

FIG. 3—*Transmission response and crack tip position determined by various means in 2024-T6 aluminum specimens.*

graph grown parallel to the rolling direction, that is, parallel to the elongated grains while the crack in the bottom graph was grown perpendicular to the elongated grains. Also shown are crack tip positions determined by various other means. The position labeled optical was determined on the outside surface of the specimen where the crack intersected the surface. A clip gage was attached at the starter notch opening with the crack position determined by that means labeled. The crack position labeled fracture was determined by physical measurement of the furthest extent of the crack after fracture of the specimen.

The x-axis values shown on Figs. 3 and 4 are determined by registration of the specimen using a reflection scan on a corner of the specimen. This scan is similar to that shown in the left side of Fig. 2 in that the crossover of all frequencies occurs at the same position (when the beam is half on the specimen) and provides an accurate determination of the specimen corner. The x-axis values then represent the remaining uncracked ligament of the specimen. Knowledge of the initial uncracked ligament before crack growth then yields a measurement of the crack length.

In both cases shown in Fig. 3, the ultrasonic determination of the crack tip position lies closest to the actual position as measured on the fracture surface. The discrepancy between the acoustically determined crack length and that actual crack length is within 0.5 mm in each case as compared to 1.0 mm by the other means. The apparent shortening of the crack as determined acoustically is considered to be due to the curvature present in the crack front in these specimens. The acoustic beam may not be completely illuminating the linear portion of the crack front resulting in an apparently shorter crack than is actually present. The curvature undoubtedly results in the greater inaccuracy in the tip position as measured by the clip gage or optically on the surface.

The top of Fig. 4 shows the full response curve for a crack grown in K-Monel with an expanded view of the response immediately around the crack tip shown in the bottom. This crack exhibits a considerable region of extended closure deep into the crack. The crack tip was again measured by various means with the results shown. This crack exhibits considerable less curvature in the crack front, thereby yielding more accurate results. In this case, the acoustic measurement is within 0.25 mm of the actual position again yielding an apparently shorter crack. The clip gage results show a somewhat longer crack than is actually present due to the inherent noise in the measurement.

The significance of Figs. 3 and 4 lies, however, in that the acoustic measurements were taken in the unloaded condition with closure present in all of the cracks and an extended closure region present in the Monel. This is in direct contrast to all of the other measurements of crack tip location (optical, clip gage, fracture) being accomplished with the crack in the fully open condition or broken. Other techniques such as were shown earlier were also able to measure crack length to within 0.5 mm but in all cases were much more accurate with the crack in the loaded condition since these techniques could not take closure into account. The distributed spring model and experimental technique shown here explicitly consider closure in the determination of the crack length.

Conclusions

Under the restriction of being able to operate in through transmission with focussed transducers, it has been shown that the location of the tip of a fatigue crack can be determined to within 0.5 mm in those cases where curvature of the crack front is significant with correspondingly better accuracy as the curvature decreases. Location of the crack tip is accomplished through use of the distributed spring model and also yields information on the residual stresses due to closure. The technique used is able to determine the crack length to

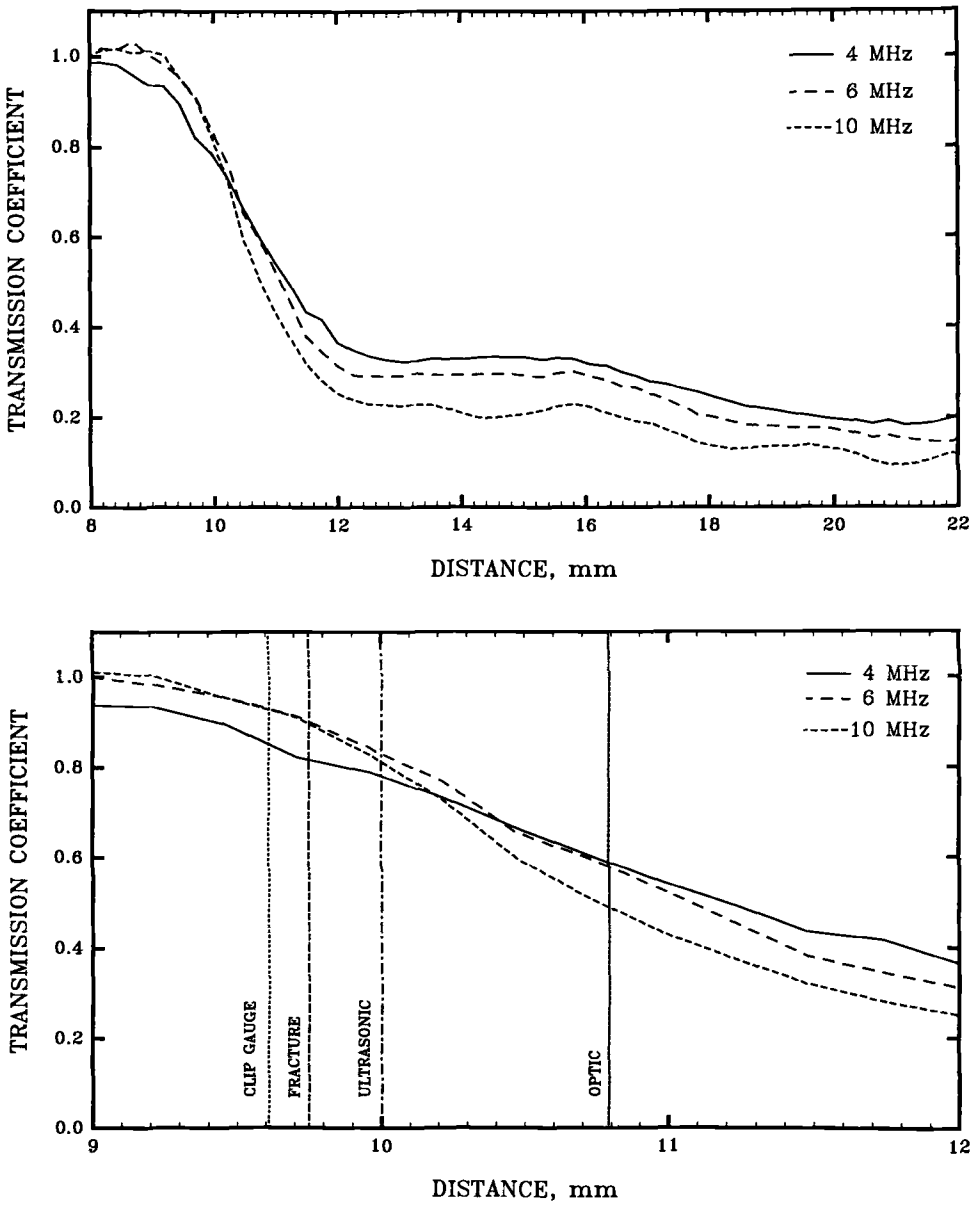

FIG. 4—*Transmission response showing extended closure and crack-tip position determined by various means for fatigue crack in Monel.*

within ±0.5 mm in the unloaded condition in contrast to most of the work done previously, removing the necessity for application of a load sufficient to fully open the crack.

Acknowledgment

Ames Laboratory is operated for the U.S. Department of Energy by Iowa State University under contract W-7405-ENG-82. This work was supported by the Office of Basic Energy Sciences.

References

[1] Coffey, J. M., in *The Measurement of Crack Length and Shape During Fracture and Fatigue,* C. J. Beevers, Ed., Chameleon Press, Ltd., London, 1980, p. 345.
[2] Buck, O. and Tittman, B. R., in *Advances in Crack Length Measurement,* C. J. Beevers, Ed., Chameleon Press, Ltd., London, 1982, p. 413.
[3] Buck, O., in *Fracture Mechanics: Microstructure and Micromechanisms,* S. V. Nair, J. K. Tien, R. C. Bates, and O. Buck, Eds., American Society for Metals, Metals Park, OH, 1987, p. 31.
[4] Lumb, R. F., Hudgell, R. J., and Winship, P., in *Proceedings,* Seventh International Conference on Nondestructive Testing, Paper H-01, Warsaw, 1973.
[5] Silk, M. G., in *Research Techniques in Nondestructive Testing,* Vol. 3, Academic Press, London and New York, 1977, p. 51.
[6] De Vadder, D., Azou, P., and Saglio, R., *Proceedings,* First International Symposium on Ultrasonic Material Characterization, 1978, p. 11.
[7] Bouami, D. and De Vadder, D., *Engineering Fracture Mechanics,* Vol. 3, 1986, p. 913.
[8] Achenbach, J. D., Adler, L., Lewis, D. K., and McMaken, H., *Journal of the Acoustic Society of America,* Vol. 66, 1979, p. 1848.
[9] Karal, F. C. and Keller, J. B., *Journal of the Acoustic Society of America,* Vol. 31, 1959, p. 694.
[10] Rehbein, D. K., Van Wyk, L., Thompson, R. B., and Buck, O., in *Review of Progress in Quantitative Nondestructive Evaluation 7B,* D. O. Thompson and D. E. Chimenti, Eds., Plenum Press, New York and London, 1988, p. 1301.
[11] Thompson, R. B. and Fiedler, C. J., in *Review of Progress in Quantitative Nondestructive Evaluation 3A,* D. O. Thompson and D. E. Chimenti, Eds., Plenum Press, New York and London, 1984, p. 207.
[12] Baik, J.-M. and Thompson, R. B., *Journal of Nondestructive Evaluation,* Vol. 4, 1984, p. 177.

Daniel De Vadder,[1] *Younwon Park,*[2] *and Dominique François*[1]

Apparatus for Ultrasonic In Situ Accurate Crack Size Measurement on Laboratory Test Specimens

REFERENCE: De Vadder, D., Park, Y., and François, D., **"Apparatus for Ultrasonic In Situ Accurate Crack Size Measurement on Laboratory Test Specimens,"** *Special Applications and Advanced Techniques for Crack Size Determination, ASTM STP 1251,* J. J. Ruschau and J. K. Donald, Eds., American Society for Testing and Materials, Philadelphia, 1995, pp. 114–129.

ABSTRACT: Knowledge on the diffraction of ultrasonic waves by crack tips in the nondestructive testing (NDT) field of applications was used to develop a method and a device for the in situ crack size measurements in fatigue test specimens. This single device allows accurate measurements at every stage of the life of the test piece. The standard accuracy is 0.1 mm in the direction of propagation. In many cases we proved that it can reach 0.03 mm. Thanks to the possibility of measurements along the crack front, it is well suited for thick specimens. After some feasibility tests we designed a prototype ready for marketing. It has been used to study the local crack-tip behavior. We could not only trace evolution of the crack profile across the entire specimen thickness but also the crack closure length at any particular point versus increasing load. In this way we confirmed on A533 steel specimens different behaviors of fatigue cracks in the plane stress and in the plane strain regions. Crack closure, the blunting, and the retardation after an overload depend on the position along the front.

KEYWORDS: ultrasound, diffraction, crack tip, crack size measurement, fatigue test specimens, crack closure, curved crack front, overload, retardation

Many techniques are available to measure the evolution of a crack in fracture mechanics specimens: visual examination of the crack at the surface, fractographs, compliance measurements, potential drop measurements, ultrasonic detection, holes drilling near the crack tip etc. These methods do not give indications on the crack front shape except for fractography and ultrasonic detection. The first one requires crack front markings and has to be evaluated after testing. The second one offers attractive possibilities, and it is such a method that we developed. The usual way to detect a crack by ultrasonic testing is to use the reflection of the waves by the defect surface or lack of transmission due to the crack. However, a more accurate manner to take advantage of ultrasonic testing is to use the diffraction by the crack tip [*1*] and preferably by using a focused beam [*2*]. In the present paper we show that this method presents many attractive possibilities, such as early detection of crack initiation, precise determination of the crack front shape and position, measurement of the local crack closure of a fatigue crack, indications about crack tip blunting and measurements of the propagation after an overload.

[1] Research engineer and professor, respectively, Laboratoire Mécanique, C.N.R.S. U.R.A. 850, École Centrale Paris, F92295 Châtenay-Malabry Cedex, France.

[2] Senior researcher, Mechanical Analysis Department, Korea Institute of Nuclear Safety, Daeduk-Danji, Taejeon, Korea 305-606.

We have built a new apparatus based on a patented method [*3*] called MU3F for **M**easurement by **U**ltrasound **F**ocused on **F**atigue **F**ront. In the following we first give a short description of the principle underlying the method. We then present the device and the means we used to make it as simple as possible to operate. The accuracy of the measurements is discussed, and the possibilities of measurements of this device are summarized.

Some examples of particularly significant results that could not be obtained by means of conventional methods are then presented.

Principle of the Method

In pulse-echo technique, when an inclined focused beam is translated over a propagated crack, the "echodynamic," that is, the amplitude of the echo versus the transducer position [*4*], displays three peaks, as shown in Fig. 1.

Peaks I and II are due to diffraction on geometrical discontinuities of the machined notch. They are useful as reference points to measure the true length of the crack—segment BC; peak III is due to diffraction at the crack tip and moves along as the crack propagates.

This phenomenon is used in two ways. First, by recording the echodynamic and determining the position of the maximum, the crack length as a function of time or the number of loading cycles can be measured; this is used for crack propagation determination. Second by stopping the beam on the position giving the maximum echo and then recording the amplitude of the echo versus time, more tenuous determinations can be achieved: detection of crack initiation—by applying a cyclic load—or detection of crack blunting—by applying a slowly varying load.

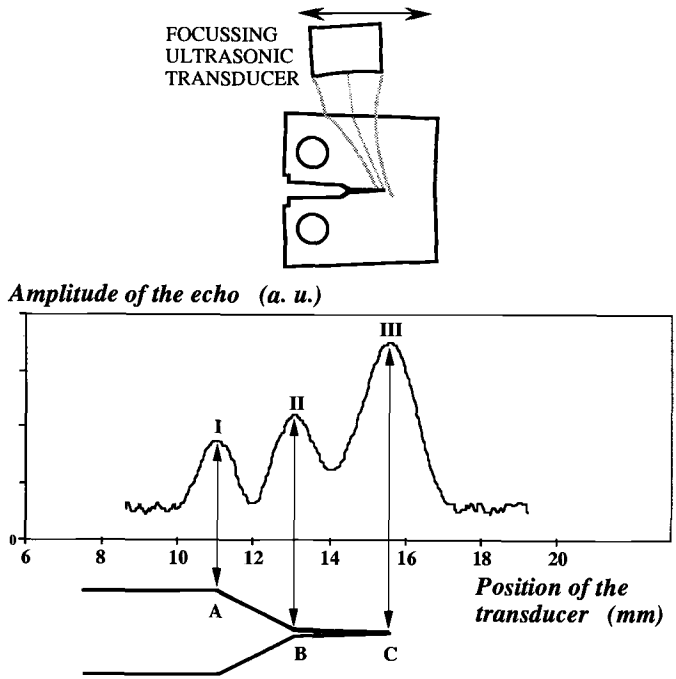

FIG. 1—*Echodynamic of an inclined focused beam translated over a propagated crack.*

A 30-mm diameter focused transducer was used; the center frequency was 4 MHz. The aberrations caused by the nonnormal incidence of the axis of the beam to the interface were corrected by means of an aspheric acoustical lens.

The accuracy of the tip location by the MU3F method can be defined along three orthogonal directions:

1. In a direction perpendicular to the tip (Fig. 2) the accuracy is given by the determination of the maximum of the echodynamic and depends on the processing method used to detect it. By simply looking at the maximum of the peak a standard accuracy of 0.1 mm was reached with a beam whose conventional −6 dB diameter was 1.7 mm. This accuracy was proven by comparison with destructive examination [*4*]. The position of the actual maximum of each peak (I, II or II on Fig. 1) being randomly subject to variations, due to a poor signal to noise ratio of the ultrasonic echoes, an improved accuracy is achieved by a simple procedure to determine the mean axis of each peak as explained in Fig. 3. In this way the estimated accuracy can reach 30 μm. In coarse grain materials the propagation of ultrasound is more or less perturbed by the structure of the material, causing a broadening of each peak, and a possible loss of accuracy.
2. In the direction parallel to the tip the accuracy cannot be better than one half of the 6 dB diameter of the focused beam—here ≈0.8 mm. It depends on ultrasonic frequency and on the probe diameter. Thus it is of no use to scan the crack tip in planes perpendicular to the crack front closer than 0.8 mm to one another.
3. In the direction of the axis of the beam, the accuracy is given by the time of flight measurement. This could detect and measure the deviation of the crack out of the plane of symmetry. This function has not been implemented yet.

Description of the Device

Mechanics

An important choice in using such a device is that of the acoustic coupling between the transducer and the specimen. We choose immersion, because the coupling by contact although simpler is not sufficiently durable for a system subjected to vibrations. The second important choice was to fix the whole mechanical device on the top of the specimen, which has two consequences.

First the mechanical setup was to be as light as possible, and nevertheless very precise for accurate measurements and very rigid against vibrations. The device was designed to

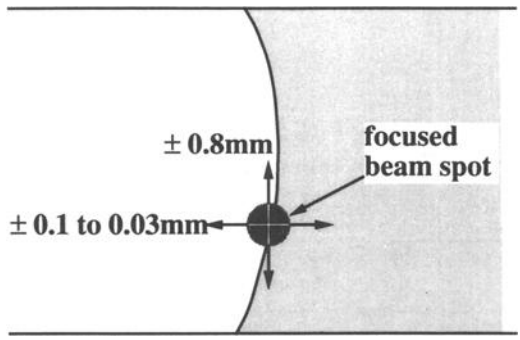

FIG. 2—*Spatial accuracy of the method in the crack propagation plane.*

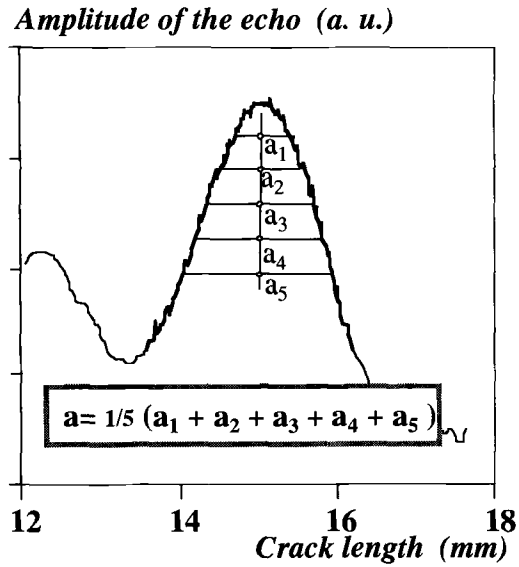

FIG. 3—*Principle of the processing used to enhance the accuracy of the method.*

ensure rigidity under cyclic frequencies up to 20 Hz and displacement amplitudes up to 1 mm.

Furthermore the setup had to be attached to the upper part of the specimen, whose upper surface needed to be in contact with the coupling liquid. Thus the specimen is placed in a window in the base plate of the device. We succeeded in designing a rigid, watertight binding system, leaving the specimen easy to mount and dismount, and, above all, avoiding perturbations during the fatigue process. For this binding the specimen was machined as indicated in Fig. 4.

Two translation and one rotation motions of the probe are provided by stepping motors and precision reduction gear assemblies. The accuracy of the translation parallel to the propagation direction of the crack is about 7 μm. For the rotation the uncertainty is 3 min of arc. Optoelectronic modules are used as zero point references and end-of-run switches. The total weight of the empty setup is 2060 g. Photographs of the mechanical device as designed for CT 25 specimens are shown in Fig. 5. It can be adapted easily to CT 50 ones.

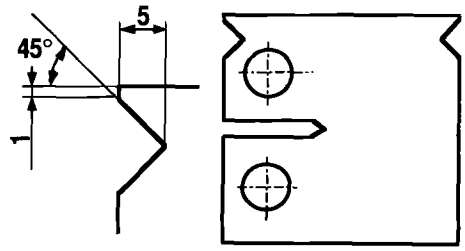

FIG. 4—*Sketch displaying the sole modification necessary to fix the mechanical setup to the CT specimen.*

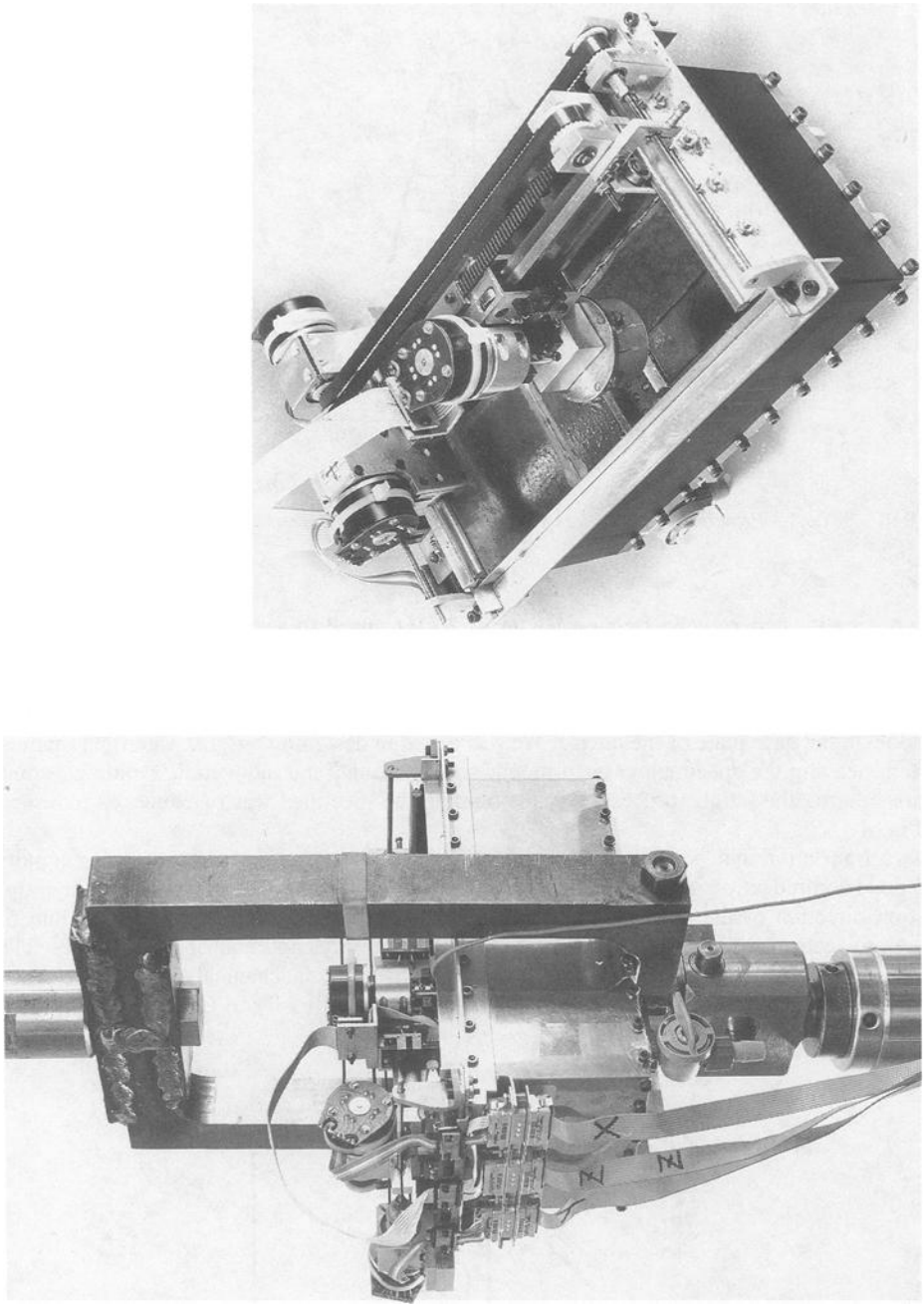

FIG. 5—*Photographs of the mechanical setup. The water tank serves as body to the device. The upper face of the CT specimen under test appears through a window in the base plate of the device.*

Electronics

In order to adapt this hardware to any fatigue machine, we chose to interface by means of analog signals rather than digital ones. For electronics we chose an AT compatible computer fitted with four cards (Fig. 6). Three of these are commercially available—for ultrasonic emitting and receiving, data acquisition from the fatigue machine and IEEE-488 interface.

To be able to drive the testing machine, whether for cyclic or monotonic loads, we choose to generate the signal to be converted to load by means of the computer. This is performed by a specific card including menu and program generation of the shape of the signal and amplification and offset settings. As a by-product of this choice, we can constitute any arbitrary function on the display of the computer by means of mouse clicks.

Digital recordings of load P and crack mouth opening δ are registered. This allows numerical computations to plot the P-δ' curve and to measure the opening load without "human factor bias," or could enable the monitoring of the load by the displacement.

The whole device is driven by a homemade computing program. We built an easy-to-use program based on pull-down menus that permits a nonspecialist of ultrasound to operate the system. This program has a high degree of modularity. At the end of each recording the operator can choose to deviate to any logically permissible measurement. A user-friendly (mouse, pull-down menus, dialog boxes) program was elaborated.

A schematic overview of the program appears in Fig. 7. Measurements of ductile tearing propagation have not yet been fully automated, and the measurement of the deviation of the crack out of the plane of symmetry is not yet implemented.

Performances

The capabilities of the equipment are displayed in a graphical and chronological way in Fig. 8. Let us point out that these are in situ measurements performed using only one device. Likewise these measurements are performed using only one specimen.

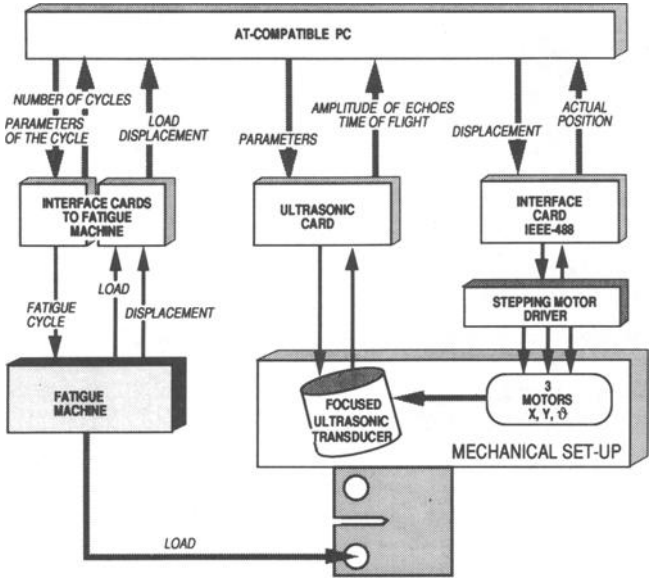

FIG. 6—*Diagram of the prototype of the apparatus developed to use the MU3F method.*

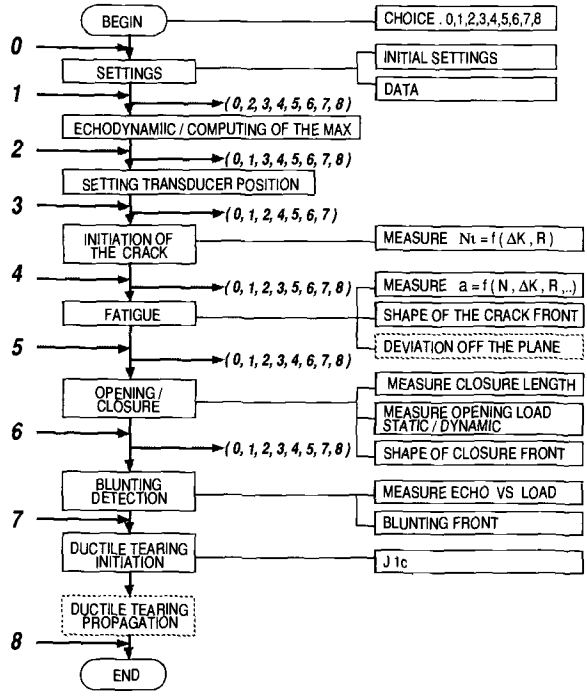

FIG. 7—*Schematic overview of the program driving the device.*

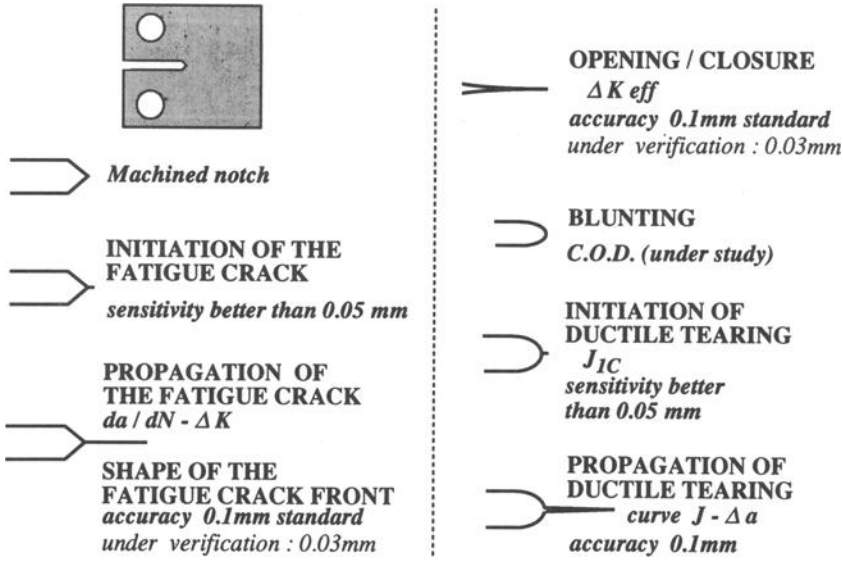

FIG. 8—*Performances of the prototype using the MU3F method.*

Some Significant Results

Initiation of a Crack

The axis of the acoustic beam being positioned at the machined notch root, the amplitude of the ultrasonic echo is plotted against the number of cyclic loads. Before a crack reaches a certain length, which is taken as the definition of the crack initiation, the echo amplitude remains quasi-constant or decreases slightly (Fig. 9). This decrease observed in some materials might be explained by the growth of microcracks, which could affect globally the diffracting power of the region, but this question awaits more detailed studies. The growth of an actual crack produces a monotonous increase of the amplitude of the ultrasonic echo. The actual measurement of very short cracks being difficult, the sensitivity of the method can be estimated by extrapolation from later increases of the crack length. In this way the sensitivity was estimated to be better than 0.05 mm.

Just after the initiation no measurements are possible as far as Peaks I and II cannot be discriminated. This dead zone is one half of the 6 dB diameter of the focused beam—here ≈0.8 mm.

Shape of the Crack Front

In order to investigate the crack tip behavior in the interior of the specimen, that is, under plane strain conditions, the best is certainly to use thick specimens. For the present work, performed for a round robin test program organized under the auspices of "Société Française de Métallurgie et Matériaux," a thickness of 12 mm was chosen for a low alloy steel A533 B which had a yield stress equal to 460 MPa. In order to fulfill this requirement without modifying our ultrasonic equipment, special CT specimens were machined according to the sketch shown on Fig. 10. The initial notch had a depth corresponding to a/W ratio equal to 0.3. The loading frequency was 20 Hz for precracking and crack growth, and the R ratio of minimum to maximum loads was chosen as 0.1. A conventional extensometer was used to monitor the crack mouth opening displacement (CMOD).

Crack Profile Measurement—Scanning the crack with the focused ultrasonic beam allowed the determination of the crack profile as the load was increased. This was limited to 8 mm of the central part owing to a loss of accuracy when nearing the specimen lateral faces. This is due to complex phenomena, including partial shadowing of the aperture of the beam and side wall reflection (these problems could be solved in next version of program by rotating

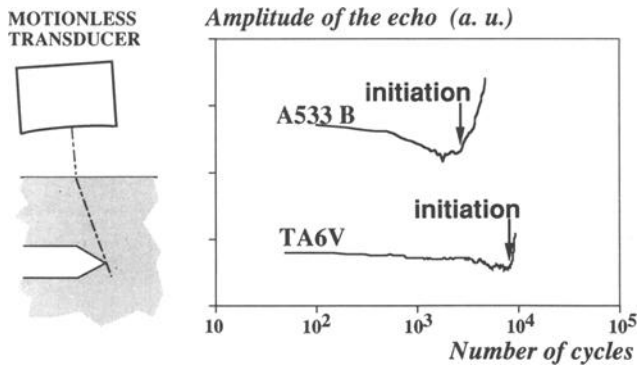

FIG. 9—*Detection of the initiation of a fatigue crack in specimens of steel and titanium alloy.*

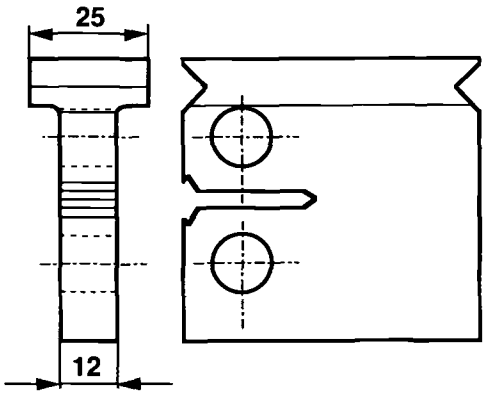

FIG. 10—*Modified CT-type specimen.*

the transducer according to the curved crack profile). Figure 11 shows one of the results obtained.

Determination of the Crack Closure Length

Thanks to the fact that the closed region of the crack is transparent to the propagation of the ultrasonic waves, the source of the diffracted wave is the zone between the fully opened and fully closed crack (Fig. 12). Thus we can detect and measure the extent of the opened and closed regions of the crack [*5*]. In this transition zone which exists between these regions the surfaces are not completely in contact, so there is an uncertainty about the exact location of the closure. This is also reflected by modifications of the acoustical reflection, transmission, and diffraction [*6,7*]. In most of the present cases the shape of the diffracted peak was not affected. In Fig. 13 are displayed the upper parts of some echodynamics by means of which is determined the position of the diffracting front according to Fig. 3. The shape of

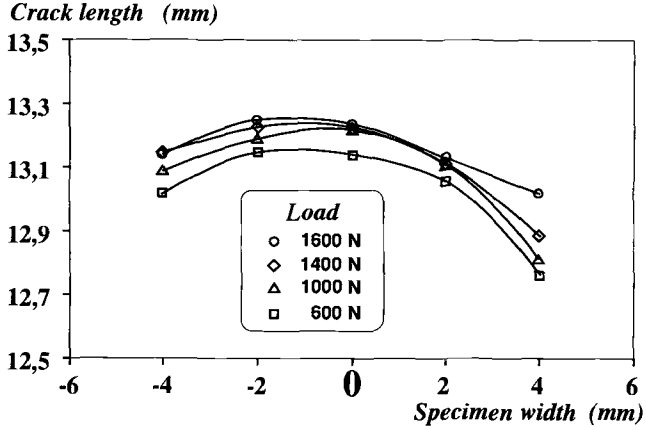

FIG. 11—*Evolution of the crack closure front with increasing load. Notice that the scale in the direction of propagation is enlarged with respect to the one along the width.*

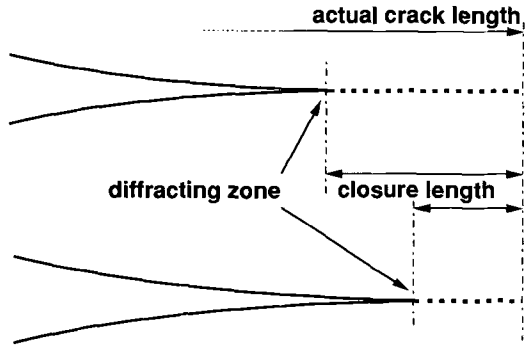

FIG. 12—*Sketch showing the location of the diffracting zone, moving forwards towards the tip as the load is increased.*

the echodynamic for a closed crack (P = 300 N) displays no significant difference with those obtained below the complete opening (P = 2900 N) and for complete opening (P = 3800 N), showing the transition zone to be narrow. In some cases a broadening of the transition peak is observed which is characteristic of a more complex behavior of the zone around the crack tip.

The crack closure length was determined for stepwise increasing loads and subtracting the apparent length from the maximum value corresponding to the complete crack opening. Thus the maximum crack closure length in Fig. 14 corresponds to the values at the minimum of the cyclic load (P_{min} = 560 N). This figure shows the evolution of the crack closure length as a function of load for a specimen with 25.7 mm crack length (midsection length). The closure length decreased with increasing load, and, above a certain load, it became lower than the accuracy of the device; consequently, this load could be considered as an opening load at midsection. The closure length is less than about 0.1 mm. The apparent increase of

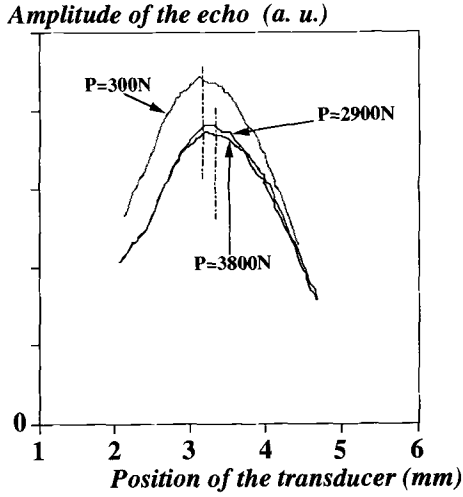

FIG. 13—*Echodynamics over a partially closed crack for different loads.*

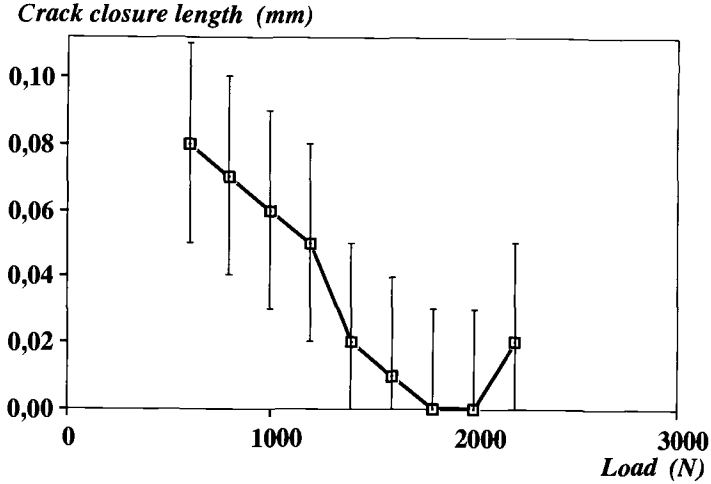

FIG. 14—*Crack length as a function of the load.*

the closure above P_{op} is considered as an artifact. When examining carefully the echodynamic when the load is increased over P_{op}, a yet unexplained broadening of the peak is observed (Fig. 15). This small broadening, being reversible when downloading, cannot be caused by some blunting.

Determination of the Crack Closure Profile

As displayed in Fig. 11 the closure front moved nonuniformly towards the crack tip as the load was increased. The crack opening occurred sooner in the midsection. In this plane

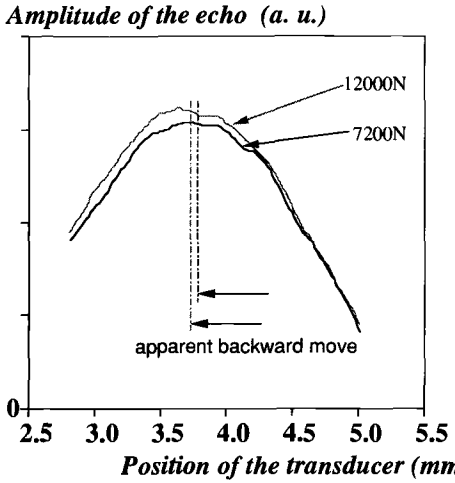

FIG. 15—*Echodynamics representing the backward movement of center line of echodynamics, which is interpreted as apparent increase of the closure above* P_{op}.

strain region, the crack closure annihilation was achieved for 1000 N, whereas crack closure disappeared in the plane stress region at a higher load (about 1600 N), corresponding to the complete opening of the crack. Thus it was confirmed experimentally that the crack remained closed longer near the lateral surfaces than in the midsection. The opening loads determined for the opening of the whole front were in a good agreement with those obtained by CMOD, which was demonstrated to correspond to the closure annihilation in the plane stress region [*8,9*].

Discussion—From the measurements of the opening load the corresponding values of K_{op} were determined using the midsection true crack length. Using the MU3F method two different values could be obtained; the first one—noted K_{op}(US-*C*) with *C* for center—corresponds to the opening at the midsection as shown on Fig. 11, whereas the second one—noted K_{op}(US-*F*) with *F* for front—corresponds to the opening along the entire crack front. As shown in Fig. 11, the crack front line moves forward with increasing load and above 1600 N no measurable progression of any point of the crack closure front is displayed, even with higher load, which means complete opening of crack along the entire crack front. Once P_{op} was determined, K_{op} was calculated by using the formula proposed by Srawley [*10*].

In Fig. 16 these values are compared with the ones obtained with the classical CMOD measurements. It can be seen that there is a good agreement between K_{op}(CMOD) and K_{op}(US-*F*), which confirms that this value corresponds to the full opening of the fatigue crack. On the contrary the K_{op}(US-*C*), corresponding to the opening at the midsection, differs more and more from the first one as the crack grows. Whereas K_{op}(CMOD) and K_{op}(US-*F*) corresponding to the full opening increase, K_{op}(US-*C*) corresponding to the midsection opening tends to remain constant, or even to slightly decrease, until it is absorbed by K_{min}. It confirms that the plane strain region is less influenced by the plasticity-induced crack closure as the plane stress region [*11,12*]. Similar observations of crack opening at the midsection at lower load than near the surface were reported by Pitoniak et al. [*13*] in polymethylmethacrylate. This shows that the fatigue propagation of fully embedded cracks might not follow the propagation law obtained by conventional methods on through cracks.

Our results agree with the ones obtained by the other participants of the round robin organized under the auspices of "Société Française de Métallurgie et Matériaux." Results obtained by means of CMOD clip gage display a rather large scatter, in particular for the

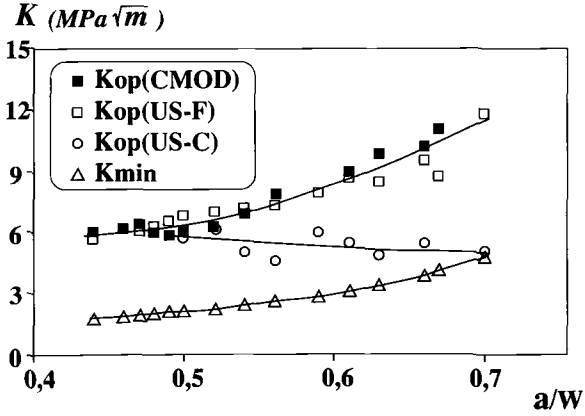

FIG. 16—*Evolution of the stress intensity factor* K_{op} *as a function of the crack length ratio* a/W.

opening load measurements which include a certain degree of subjectivity. In this respect the MU3F method could become a reference.

Overload and Crack Growth Following an Overload

As shown in Fig. 11, before overloading we could observe a forward displacement of the crack profile as a function of the increasing load, due to crack closure annihilation; however, immediately after overloading the crack profiles remained unchanged even at increasing the loads [*14*], showing the complete cancellation of the closure due to the first overload. It was also proven that a second overload had a negligible influence [*14*].

After a 200% overload the crack was grown under normal cyclic loading for 1 mm. A greater crack closure length after crack growth following overloading than before overloading was observed. The crack closure measured at midsection before overloading and after a crack growth following an overload was 0.2 and 0.55 mm, respectively, and the crack opening load went up from 2800 to 3800 N, which confirms the results obtained by other researchers [*15,16*].

The measurement of the crack length at the midsection of the specimen allows us to examine the crack tip response affected by overloading. The measurement of crack growth at the midsection of specimens could be carried out every several hundreds of cycles at a 20 Hz fatigue frequency, which corresponds to a crack growth less than 10 μm, but at the surface the optical measurement obliged us to interrupt fatigue cycling at every 0.3 to about 0.4 mm of crack growth. In Figs. 17 and 18 are shown crack length measurements before and after the application of the overload, at the surface and at the midsection. As shown in Fig. 17, the crack growth behaviors after overloading are not similar in the plane stress and the plane strain regions. At the surface the crack tends to grow continuously longer for about 0.3 to about 0.4 mm after overloading, whereas in the plane strain region its velocity drops immediately [*8,11,15,17*]. These differences are enhanced if we represent the growth rates as a function of crack length as in Fig. 18. After overloading the crack growth rate is slightly

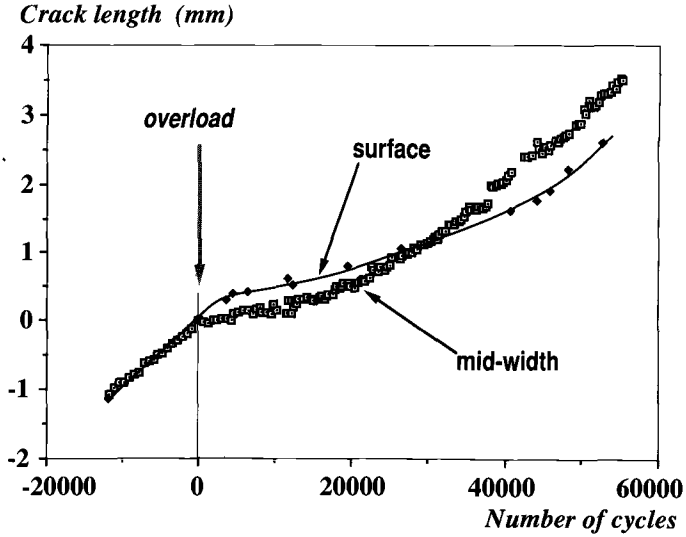

FIG. 17—*Crack length as a function of the number of cycles (200% overload).*

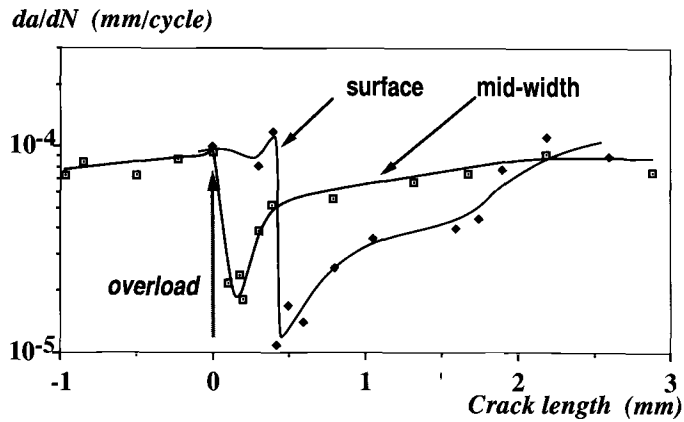

FIG. 18—*Crack growth rate (200% overload).*

accelerated at first at the surface whereas it drops immediately to a minimum value at the mid-section of the specimen.

Future Trends

We may attempt to enhance the capacity of the apparatus to deal with higher fatigue frequency, higher temperature, with other types of specimen, or even structures under test. The foregoing is merely technological improvements, the physical principle remaining valid, as well as the main part of the program.

For adaptation to high temperature fatigue tests, the main problem to be solved was previously that of the probe, as those commonly available could not withstand high temperatures. Recently, commercially available ultrasonic probes have been proposed that work up to 600°C, so that the remaining challenge is to adapt the mechanical setup to high temperature.

For adaptation to higher fatigue frequencies, immersion has to be avoided, requiring the use of a contact probe. The problem is that the focused beam needs to be translated with respect to the specimen. Two solutions are possible. The first one is to design a device ensuring a constant coupling in spite of the vibrations. We are currently testing such a solution. The second one is to take advantage of electronically focused array transducer devices currently under development, in which the translation of the acoustical beam is obtained without any mechanical movement.

Adaptation of the present device to CT50 specimens requires minor modifications. Adaptation to other types of specimens or to structures is a matter of engineering. Such adaptation must take into account the acoustical path of the ultrasonic beam.

In the future, it is likely that signal processing of the diffracted echoes [*18*] will permit enhanced analysis of crack tip behavior.

Conclusion

We have developed the prototype of a device which could be manufactured commercially and which permits the following measurements on CT specimens:

1. Early detection of initiation of a fatigue crack.
2. Automatic tracking of fatigue crack growth.
3. Characterization of crack front shape, even when it has a thumbnail shape.
4. Detection and measurement of both crack closure and opening (length and loads).
5. Detection of initiation of ductile tearing.
6. Monitoring of ductile fracture growth.
7. Characterization of ductile fracture crack fronts.

The accuracy along the direction of propagation is 0.1 mm for all measurements and in many cases can be improved; the sensitivity is better than 0.05 mm for the detection of the initiation of crack or ductile tearing.

Owing to the user-friendly program, the device is easy to operate.

We have demonstrated that the MU3F ultrasonic method yields crack length and full crack opening load measurements which are in excellent agreement with the classical visual and crack mouth opening measurements. The MU3F method provides information on the yet unresolved problems of the crack tip behavior. It allows to determine the crack closure length and the crack opening load both along the crack front and for a particular point (at midsection dominated by plane strain condition). It confirms that the crack opens first at the midsection. In a CT specimen the corresponding K_{op} was found to decrease slightly as the crack grew, contrary to the full opening K_{op}. The behavior of the crack due to overloads and after overloading was found to be different in the plane strain and plane stress regions, for crack closure as well as for crack growth rate.

References

[1] De Vadder, D., Silk, M. G., and Bouami, D., "Review of Knowledge About Diffraction of US by Crack Tips," *Journal of the Mechanical Behavior of Metals,* Vol. 3, No. 1, 1990, pp. 1–34.

[2] De Vadder, D., Azou, P., and Saglio, R., "Determination of Orientation and Size of Badly Oriented Defects by Means of Focused Probes," *Proceedings,* First International Symposium on Ultrasonic Materials Characterization, National Bureau of Standards, Gaithersburg, MD, 7–9 June 1978.

[3] Bouami, D. and De Vadder, D., U.S. Patent No. 4,763,528.

[4] Bouami, D. and De Vadder, D., "Automatic Tracking of Crack Growth with Ultrasonic Focused Probe in CT Specimen," *Ultrasonic '85,* London, June 1985.

[5] Bouami, D. and De Vadder, D., "Detection and Measurement of Crack Closure and Opening by an Ultrasonic Method," *Engineering Fracture Mechanics,* Vol. 23, No. 5, 1986, pp. 913–920.

[6] Baik, J.-M. and Thompson, R. B., "Ultrasonic Scattering from Imperfect Interfaces: A Quasi-Static Model," *Journal of Nondestructive Evaluation,* Vol. 4, Nos. 3/4, 1984.

[7] Thompson, R. B., Skilling, B. J., Zachary, L. W., Schmerr, L. W., and Buck, O., "Effects of Crack Closure on Ultrasonic Transmission," *Review of Progress in Quantitative Nondestructive Evaluation,* Vol. 2, D. O. Thompson and D. E. Chimenti, Eds., Plenum Press, New York, 1983, pp. 325–343.

[8] Fleck, N. A., "Influence of Stress State on Crack Growth Retardation," *Basic Questions in Fatigue, ASTM STP 924,* American Society for Testing and Materials, Philadelphia, 1988, pp. 157–183.

[9] Beevers, C. J., Bell, K., Carson, R. L., and Starke, E. A., "A Model for Fatigue Crack Closure," *Engineering Fracture Mechanics,* Vol. 19, No. 1, 1984, pp. 93–100.

[10] Srawley, J. E., "Wide Range Stress Intensity Factor Expressions for ASTM E 399 Standard Fracture Toughness Specimens," *International Journal of Fracture,* Vol. 12, 1976, pp. 475–476.

[11] Ray, S. K. and Grandt, A. F., Jr., "Comparison of Methods for Measuring Fatigue Crack Closure in a Thick Specimen," *Mechanics of Fatigue Crack Closure, ASTM STP 982,* American Society for Testing and Materials, Philadelphia, 1988, pp. 197–213.

[12] Fleck, N. A., "An Investigation of Fatigue Crack Closure," Ph.D. thesis, CUED/C-MATS/TR.104, 1984, Cambridge University, UK.

[13] Pitoniak, F. J., Grandt, A. F., Montulli, L. T., and Packman, P. F., "Fatigue Crack Retardation and Closure in Polymethylmethacrylate," *Engineering Fracture Mechanics,* Vol. 6, 1974, pp. 663–670.

[*14*] Park, Y., De Vadder, D., and François, D., "In Situ Mid-Width and Near-Surface Measurements of the Retardation of the Propagation of a Crack After an Overload," preprints of the 9th European Conference on Fracture, S. Sedmak, A. Sedmak, and D. Ruzic, Eds., Engineering Materials Advisory Services Ltd., Warley, UK, 1992.

[*15*] Robin, C., "Comportement d'une Fissure de Fatigue sous l'Action d'un Chargement à Amplitude non Constante: Expérience et Modelisation," *Habilitation à Diriger des Recherches*, University de Metz, 1988.

[*16*] Matsuoka, S. and Tanaka, K., *Journal of Material Science*, Vol. 13, 1978, pp. 1335–1353.

[*17*] McEvily, A. J., "On Crack Closure in Fatigue Growth," *Mechanics of Fatigue Crack Closure, ASTM STP 982*, American Society for Testing and Materials, Philadelphia, 1988, pp. 35–43.

[*18*] De Vadder, D. and Dosso, M., "Ultrasonic Characterization of Crack Tips by Digital Signal Processing," 7th International Conference on NDE in Nuclear Industry, Grenoble, Fév., 1985.

Prasanna Karpur,[1] *Theodore E. Matikas,*[2] *Mark P. Blodgett,*[3] *Jay R. Jira,*[4] *and Drew Blatt*[4]

Nondestructive Crack Size and Interfacial Degradation Evaluation in Metal Matrix Composites Using Ultrasonic Microscopy

REFERENCE: Karpur, P., Matikas, T. E., Blodgett, M. P., Jira, J. R., and Blatt, D., **"Nondestructive Crack Size and Interfacial Degadation Evaluation in Metal Matrix Composites Using Ultrasonic Microscopy,"** *Special Applications and Advanced Techniques for Crack Size Determination, ASTM STP 1251,* J. J. Ruschau and J. K. Donald, Eds., American Society for Testing and Materials, Philadelphia, 1995, pp. 130–146.

ABSTRACT: Ultrasonic scanning acoustic microscopy is a nondestructive method useful for material elastic property quantification as well as crack size determination for surface and subsurface cracks. The advantage of the method over destructive methods for crack size determination is that the imaging technique can provide the crack sizing information while helping in the detection of interface degradation and early crack initiation so that their growth can be monitored during interrupted fatigue tests. Various metal matrix composite systems with titanium based matrix and SCS-6 fibers have been evaluated for this study [Ti-24Al-11Nb (atomic percent), Ti-6Al-2Sn-4Zr-2Mo (weight percent), and Ti-15Mo-3Nb-3Al-0.2Si (weight percent)]. The scanning acoustic microscope technique has been applied to materials subjected to both room temperature and elevated temperature fatigue cycling in addition to thermomechanical fatigue (in-phase and out-of-phase) conditions. A 50 MHz scanning acoustic microscope has been used for the imaging and evaluation of the damage initiation and growth of surface/subsurface cracks and interfacial degradation. All the images have been produced by exploiting the surface wave component of the ultrasonic signals from the scanning acoustic microscope because of the higher sensitivity of surface waves to both surface/subsurface cracks and perhaps also due to the changes in interfacial elastic properties. The results shown in this paper provide a very good understanding of the crack initiation and growth as well as interfacial degradation process of titanium based metal matrix composites when subjected to cyclical stresses at elevated temperatures and room temperature. The results indicate that the combination of high temperature and stress is very severe to the interface between the matrix and the fiber.

KEYWORDS: metal matrix composites, thermomechanical behavior, interfacial damage, nondestructive evaluation, ultrasound, scanning acoustic microscope, crack sizing, crack growth, crack initiation, Rayleigh waves, interfacial degradation, environmental effects

[1] Research Institute, University of Dayton, 300 College Park Avenue, Dayton, OH 45469-0127. Also, on-site contract, WL/MLLP, Materials Directorate, Wright Laboratory, Wright Patterson Air Force Base, OH 45433-7817. Contract number F33615-89-C-5612.

[2] National Research Council Associate, WL/MLLP, Materials Directorate, Wright Laboratory, Wright Patterson Air Force Base, OH 45433-7817.

[3] WL/MLLP, Materials Directorate, Wright Laboratory, Wright Patterson Air Force Base, OH 45433-7817.

[4] WL/MLLN, Materials Directorate, Wright Laboratory, Wright Patterson Air Force Base, OH 45433-7817.

Fiber reinforced composite materials are being considered for a number of applications because of their improved mechanical properties as compared to nonreinforced materials. In applications where cyclic loading is expected and where life management is required, consideration must be given to the behavior of the material in the vicinity of stress risers such as notches and holes. It is in these regions that damage initiation and accumulations are expected. In the case of metal matrix composites for aircraft structural and engine components, several damage modes near stress risers have been identified [*1*]. One important damage mode under cyclic loading is the nucleation and growth of matrix cracks perpendicular to the fiber direction. In some composite systems, the matrix crack growth occurs without the corresponding failure of the fibers. This process results in the development of relatively large matrix cracks that are either fully or partially bridged by unbroken fibers. The presence of bridging fibers can significantly influence the fatigue crack growth behavior of the composite. To develop a life prediction methodology applicable to these composite systems, an understanding must be developed of both the matrix cracking behavior as well as the influence of the unbroken fibers on the crack driving force and the affect of interfacial degradation and damage on the eventual failure of the composite.

Paramount to understanding the influence of unbroken fibers is understanding the mechanisms which transfer the load from the matrix to the fiber. The mechanics of matrix cracking and fiber bridging in brittle matrix composites has been addressed [*2,3*]. The analysis is based on the shear lag model to describe the transfer of load from the fiber to the matrix. In the shear lag model, the transfer of load occurs through the frictional shear force (τ) between the fiber and the matrix. The analyses indicate that size of the region on the fiber over which τ acts can have a significant effect on the influence of unbroken fibers on crack growth rate behavior. However, although some indirect ultrasonic experimental techniques have been developed to determine the extent of the influence of τ [*4–6*], no direct nondestructive experimental techniques have been demonstrated to determine the extent of the influence of τ. Another important interfacial phenomenon is the degradation, fracture, or failure of the interface resulting from crack initiation and growth which is the aspect of interest in this paper.

The objective of this paper is to demonstrate the utility and versatility of scanning acoustic microscopy (SAM) for material behavior research of metal matrix composites. Hence, in the work reported in this paper, the SAM technique is utilized for nondestructively determining regions of interfacial degradation while simultaneously providing indications of surface crack length in three metal matrix composite systems. The specimens have been subjected to various test conditions including room temperature, isothermal mechanical fatigue, and thermomechanical fatigue. In the interfacial regions of all the specimens, subsequent destructive evaluations are used to verify the indications revealed by SAM.

Scanning Acoustic Microscopy (SAM)

Scanning acoustic microscopy was developed by Quate et al. [*7,8*]. It has been extensively studied by Briggs et al. [*9–13*] since that time. The most important contrast phenomenon in a SAM is the presence of Rayleigh waves which are leaking toward the transducer and are very sensitive to local mechanical properties of the materials being evaluated. The generation and propagation of the leaky Rayleigh waves are modulated by the material properties, thereby making it feasible to image even very subtle changes of the mechanical properties.

A SAM transducer is schematically shown in Fig. 1. The transducer has a piezoelectric active element situated behind a delay line made of silica crystal oriented such that the 1-1-1 axis is parallel to the direction of sound propagation. The thickness of the active

element is suitable to excite ultrasonic signals (with a nominal frequency of 50 MHz in this case) when an electrical spike voltage is delivered to the piezoelectric element. The silica delay has a spherical acoustical concave lens (Fig. 1) which is ground to an optical finish. The numerical aperture (NA, ratio of the diameter of the lens to the focal distance) is 1.25 for the transducer used for this study. An NA of more than 1 (or F number, focal distance/diameter, of the lens less than 1) is essential for the SAM technique to effectively generate and receive surface waves in the specimen being imaged.

The principle of operation of a SAM transducer is based on the production and propagation of surface acoustic waves (SAW) as a direct result of a combination of the high curvature of the focusing lens of the transducer and the defocus of the transducer into the specimen [*7,14*]. The contrast of the images obtained using SAM is based on the attenuation and

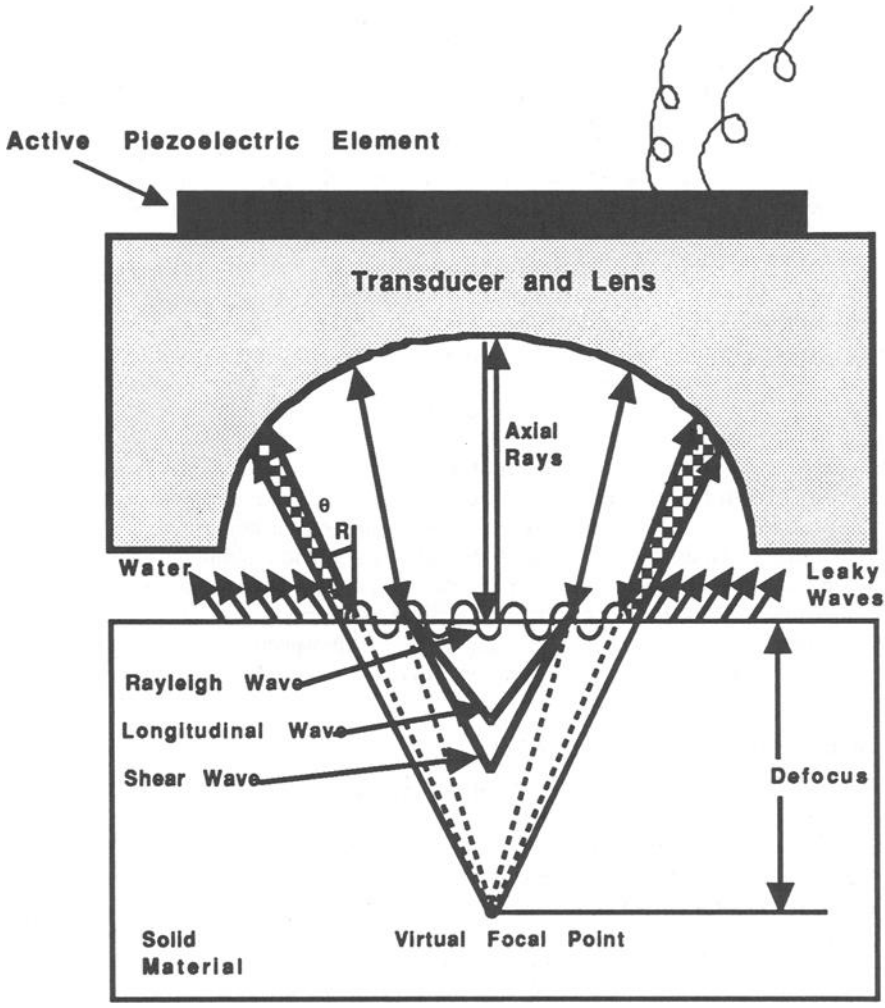

FIG. 1—*Schematic of a SAM. The diagram shows the active piezo electric element, focusing lens, and the Rayleigh wave generated due to the sharp focusing of the ultrasonic beam.*

reflection of SAW. In addition, the sensitivity of the SAW signals to the surface and the subsurface features depend on the degree of defocus and has been well documented in the literature as the $V(z)$ curves [*15*]. The defocus distance also has another important effect on the SAW signal obtained by the SAM transducer: the degree of defocus dictates whether the SAW signal is well separated from the specular reflection or interferes with it. Thus, depending on the defocus, the SAM technique can be used either to map the interference phenomenon in the first layer of subsurface fibers or to map the surface and subsurface features (reflectors) in the specimen.

Test Specimens

The SAM was used in conjunction with several on-going material behavior investigations [*16–18*] to evaluate the extent of damage accumulated during the respective test procedures. Specimens were removed during or after testing and evaluated using the SAM. Thus, composite materials composed of a range of different matrix materials could be evaluated. All the specimens are titanium matrix composites reinforced with a silicon-carbide based fiber, commercially designated SCS-6, that has a double pass carbon rich coating. The matrix materials include a beta processed titanium alloy, Ti-15Mo-3Nb-3Al-0.2Si (weight percent: Specimens 1, 2, and 3), a conventional titanium alloy Ti-6Al-2Sn-4Zr-2Mo (weight percent: Specimen 4), and an alpha-two titanium aluminide alloy, Ti-24Al-11Nb (atomic percent: Specimen 5). The Ti-24Al-11Nb and Ti-15Mo-3Nb-3Al-0.2Si composites were manufactured using the foil-fiber-foil process, and the Ti-6Al-2Sn-4Zr-2Mo was manufactured using the plasma spray technique.

Experimental Configuration

The ultrasonic imaging was done by using a 50 MHz nominal frequency SAM transducer with a focal spot size of approximately 15 μm (theoretical) when focused on the surface of the specimen. The ultrasonic beam was defocused into the specimens to generate leaky Rayleigh waves propagating along the surface. The defocus was enough to avoid interference of the surface wave with the specular reflection from the front surface of the specimen (the exact defocus distance for each specimen to generate and receive leaky Rayleigh waves, however, is dependent on the properties of the matrix material). The depth of penetration of 50 MHz surface waves is about 140 μm (theoretical). The SAM transducer was raster scanned in a plane parallel to the surface of the specimen while simultaneously producing and receiving Rayleigh waves. The digitally recorded Rayleigh wave signals were software gated [*19*], and the resulting amplitude was plotted to generate the acoustic micrographs shown in this paper.

Results

The results of SAM applied to metal matrix composites (MMC's) will be presented under several subsections based on the type of composite system being imaged. The fatigue test parameters for each specimen will be outlined for each specimen in the corresponding subsections.

Specimen 1: SCS-6/Ti-15Mo-3Nb-3Al-0.2Si

One benefit of the SAM is that it provides a nondestructive indication of the extent of interfacial damage. To demonstrate its utility, a notch (hole) fatigue experiment was peri-

odically interrupted and the specimen was scanned using the SAM to evaluate the development of damage during the life of the specimen. After each SAM evaluation, the specimen was returned for further fatigue cycling. The fatigue cycling was terminated after the third interruption at 9.66×10^5 cycles. For this test, the composite consisted of a cross-ply layup of fibers in the $[0/90]_s$ configuration. Prior to testing, a SAM image was made of the specimen to establish the initial integrity of the material. The pretesting image is shown in Fig. 2*a* and shows no damage to the interfaces prior to testing.

After the initial scan, the specimen was fatigued isothermally at 650°C with a maximum remote stress of 200 MPa applied at 1 Hz along the fibers with reference to the image in Fig. 2*a*. The fatigue test was stopped after 1.54×10^5 cycles or approximately 43 h at the specified high temperature. One matrix crack could be seen on each side of the hole. One

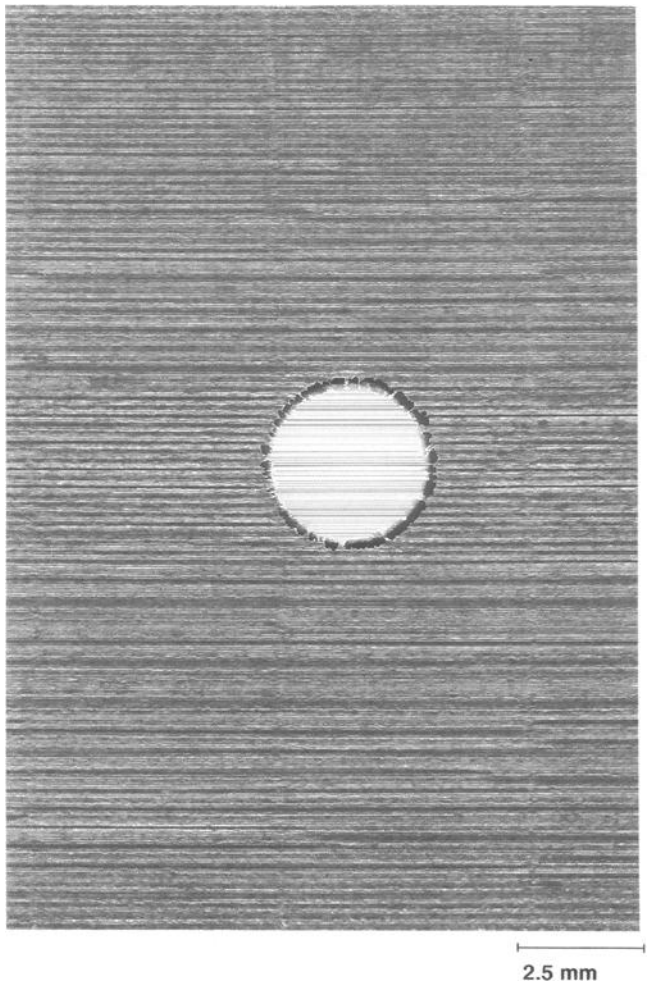

FIG. 2*a*—*The SAM image of a Ti-15Mo-3Nb-3Al-0.2Si (weight percent) specimen before an isothermal (650°C) fatigue test.*

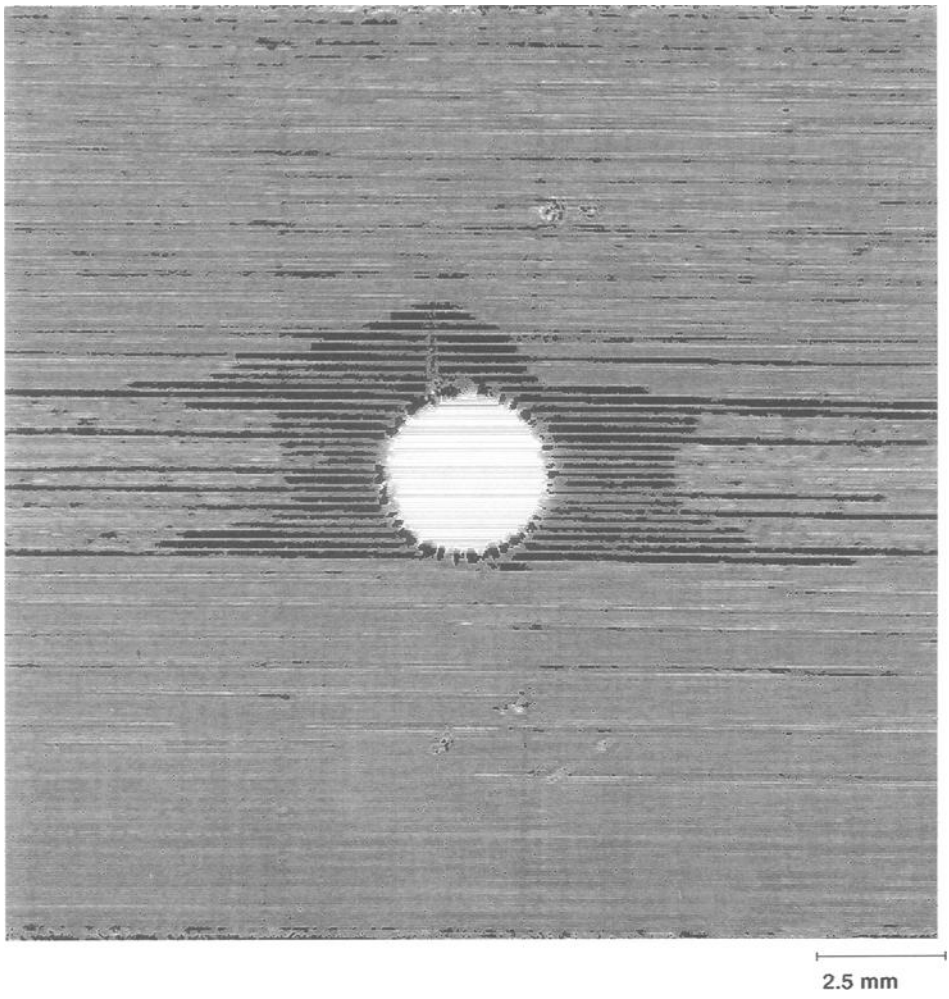

FIG. 2*b*—*The SAM image of the Ti-15Mo-3Nb-3Al-0.2Si (weight percent) specimen in Fig.* 2a *after* 1.54×10^5 *cycles or approximately 43 h of isothermal (650°C) fatigue test.*

crack initiated earlier in the test and had a surface length of 2.36 mm from the edge of the hole while the crack on the other side had reached a length of 0.54 mm from the edge of the hole. The specimen was removed from testing and imaged using the SAM. The resulting image is shown in Fig. 2*b*. In this figure, the damage (as indicated by the high contrast regions) originates at the top and bottom of the hole and proceeds away from the hole along the fibers. The damage is also seen to originate at the crack plane, where the crack exposes the interior of the specimen to the environment. The actual crack length is longer than the length over which the high contrast region is observed. This difference corresponds to approximately three fibers at each crack tip and appears to be related to the relatively recent extension of the crack into this region and perhaps the consequential shorter duration over

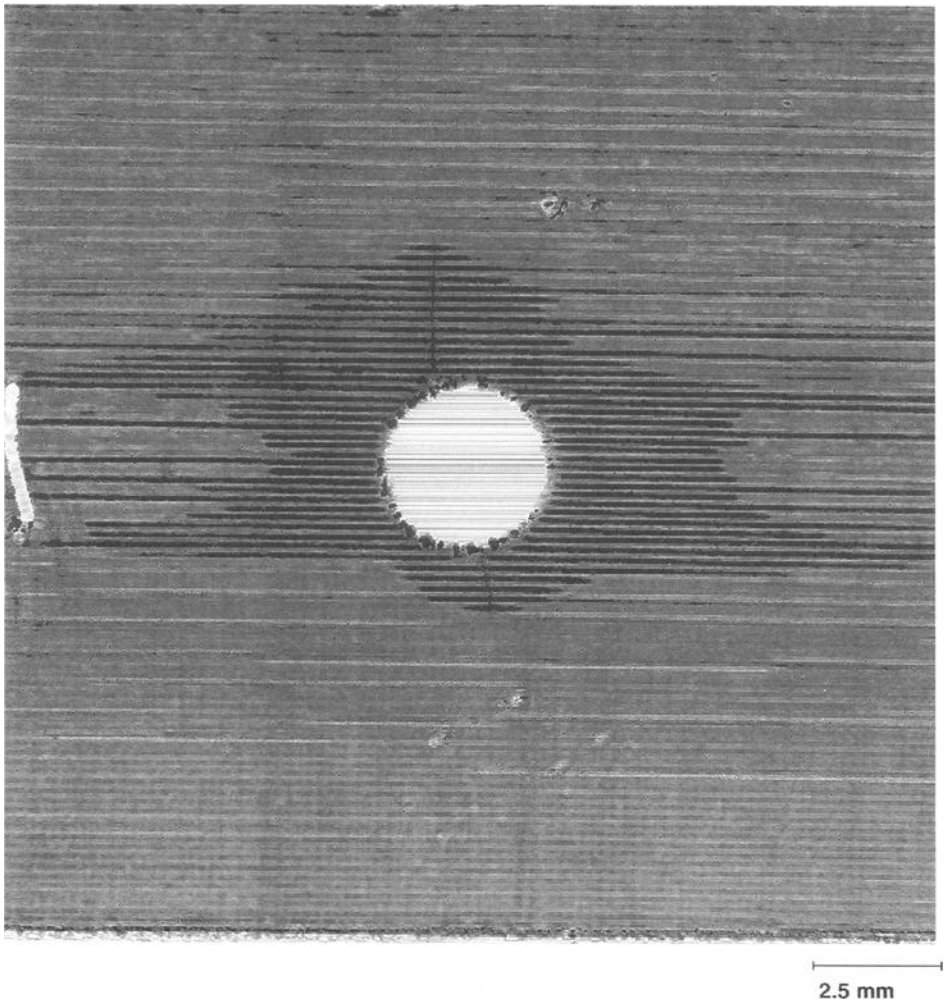

FIG. 2*c*—*The SAM image of the Ti-15Mo-3Nb-3Al-0.2Si (weight percent) specimen in Fig.* 2a *after* 2.51×10^5 *cycles or approximately 70 h of isothermal (160°C) fatigue test.*

which the environment has had access to those fiber-matrix interfaces. The shorter crack on one side of the hole is only beginning to develop an affected zone and is barely visible in the ultrasonic image although the crack extends about three fiber diameters at the surface.

Figure 2*c* is the SAM image after an additional 9.66×10^4 cycles were applied for a total of 2.51×10^5 cycles and total time of 70 h at the specified high temperature. In this figure, the cracks on each side of the hole can be seen clearly. The larger crack had grown to a surface length of 2.88 mm from the edge of the hole while the crack on the other side had reached a length of 1.77 mm from the edge of the hole. The region of high contrast has expanded along the cracks as well as to the left and right of the hole. However, in the SAM

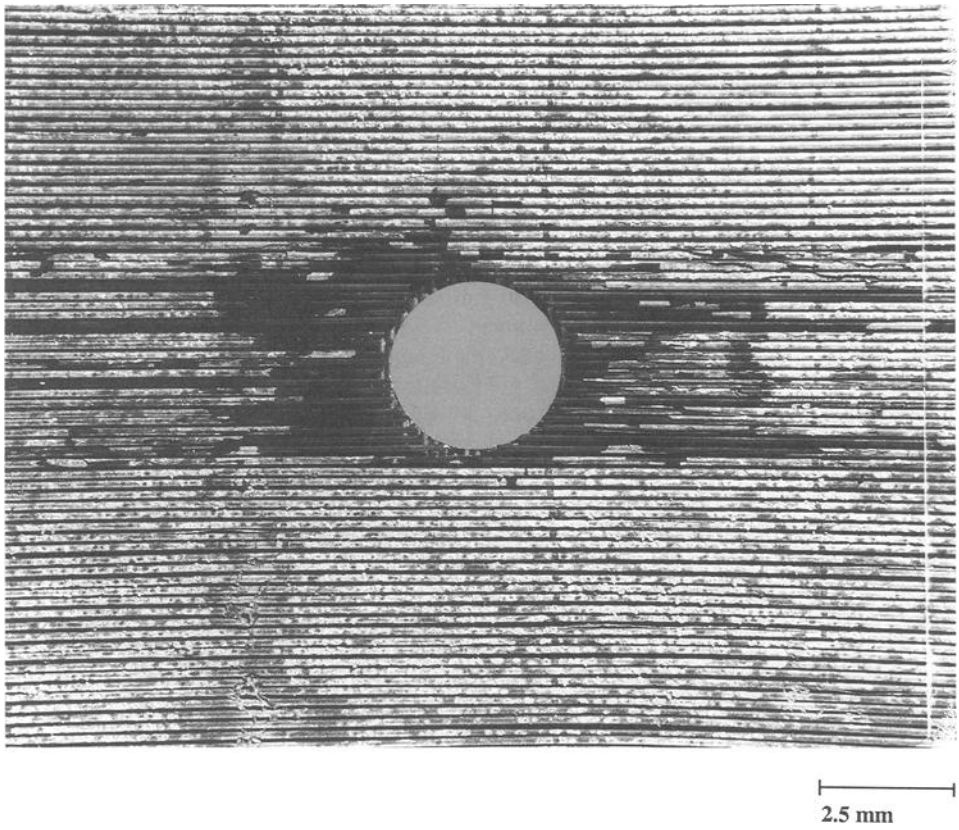

FIG. 2*d*—*Metallography of specimen in Fig.* 2a *through* 2c.

image in Fig. 2*c*, the last three fibers at the tips of both the cracks did not show any interfacial damage.

To substantiate the indications made by the SAM, the outer layer of matrix material on Specimen 1 was etched away using a saturated solution of tartaric acid in 10% bromine in methanol. The etched specimen was cleaned ultrasonically in acetone, photographed, and is shown in Fig. 2*d*. Throughout most of the exposed layer of fibers, the outer coatings of the fibers have remained intact and appear white. The dark regions above and below the hole indicate the cracking of the coating. In most cases, when the environmental exposure time is maximum, the coatings have been removed completely, exposing the dark silicon carbide fibers beneath the coating. The cross-ply (90°) fibers in the second layer can also be detected. From the metallographic image in Fig. 2*d*, the hypothesis of gradual degradation of the interface is suggested because the interfaces of the fibers cut by the circumference of the hole were exposed the longest to the severe environmental conditions and show enough damage to lose the interfacial coating during cleaning. However, the longer and older of the two cracks show some damage to the interface whereas the shorter crack shows almost no damage in the metallography although ultrasonic images indicate otherwise. Plans are un-

derway to conduct elevated temperature experiments in inert atmosphere to further evaluate the effect of oxygen on the interfacial degradation process.

Specimen 2: SCS-6/Ti-15Mo-3Nb-3Al-0.2Si

Specimen 2 is a four-ply, unidirectionally reinforced composite of SCS-6 fibers in Ti-15Mo-3Nb-3Al-0.2Si matrix. This beta processed matrix material was chosen for composite applications because of its improved environmental resistance at high temperatures. As such, Specimen 2 was fatigued at an elevated temperature (650°C) to investigate the notch and fatigue crack growth behavior of this composite system. The specimen was rectangular in shape with a width of 19 mm, length of 150 mm, and had a 4.76 mm diameter hole machined in the center. The fatigue loading was applied to the specimen in the direction of the fibers at a frequency of 1 Hz and at a maximum remote applied stress of 350 MPa. Fatigue cracks initiated quickly in the circular hole and grew until the specimen fractured after 1.82×10^5 cycles. This corresponded to approximately 50 h of high temperature exposure during the life of this specimen. After testing, the specimen was evaluated using the SAM.

Figure 3 is a SAM image of Specimen 2. The fractured edge of the specimen including the remaining portion of the circular hole is on the right-hand side of the figure. Four cracks initiated around the hole, with one crack on each side of the hole dominating and eventually leading to failure. One of the nonfailure cracks, labeled E, is visible in Fig. 3. Note that the fiber locations are easily distinguished throughout the SAM image.

A region of high contrast, evident in Fig. 3, appears to extend along the fibers. The shape of the high contrast regions suggest that both the local stresses and the duration of exposure to the high temperature environment influence the extent of damage. The zones labeled A and B on the figure are regions of stress concentration near the notch. Cracks initiated in this region, exposing the interior of these regions to the environment early in the fatigue life. Consequently, the largest affected length of fibers appear to originate near A and B. In contrast, the affected fiber length between G and H is considerably less, even though the fiber ends at the hole were exposed to the environment from the beginning of the test. The geometry of the notch leads to fiber stresses in this region which are considerably smaller in magnitude than the stresses near A and B. It appears that the different stress state in this region has affected the rate of environmental interaction. The zones beginning at labels C and D and extending to each edge of the specimen are the regions of fast-fracture. In this region, the SAM did not detect strong differences from the virgin material. Finally, in the crack growth region shown by CA, BE, and BD, a gradient of affected fiber lengths is evident, presumably related to the duration of exposure after matrix cracking. These observations indicate that the effect detected by the SAM is related to both stress and exposure duration.

Specimen 3: SCS-6/Ti-15Mo-3Nb-3Al-0.2Si

A thermomechanical fatigue (TMF) crack growth test was conducted on a four-ply unidirectional composite with a titanium matrix reinforced with silicon-carbide, SCS-6, fibers [*18*]. The crack was grown perpendicular to the fiber and loading direction. The single-edge notch (SE(T)) specimen with clamped ends [*20*] was 25.37 mm wide and 0.96 mm thick with the initial EDM notch length equal to 7.593 mm. The specimen was subjected to a constant P_{max} throughout the test of 3.3 kN at an R (stress ratio $R = s_{min}/s_{max}$) of 0.1 out-of-phase with a thermal cycle between 150 and 538°C. Out-of-phase means that the maximum load and minimum temperature occur at the same time during each cycle. The specimen

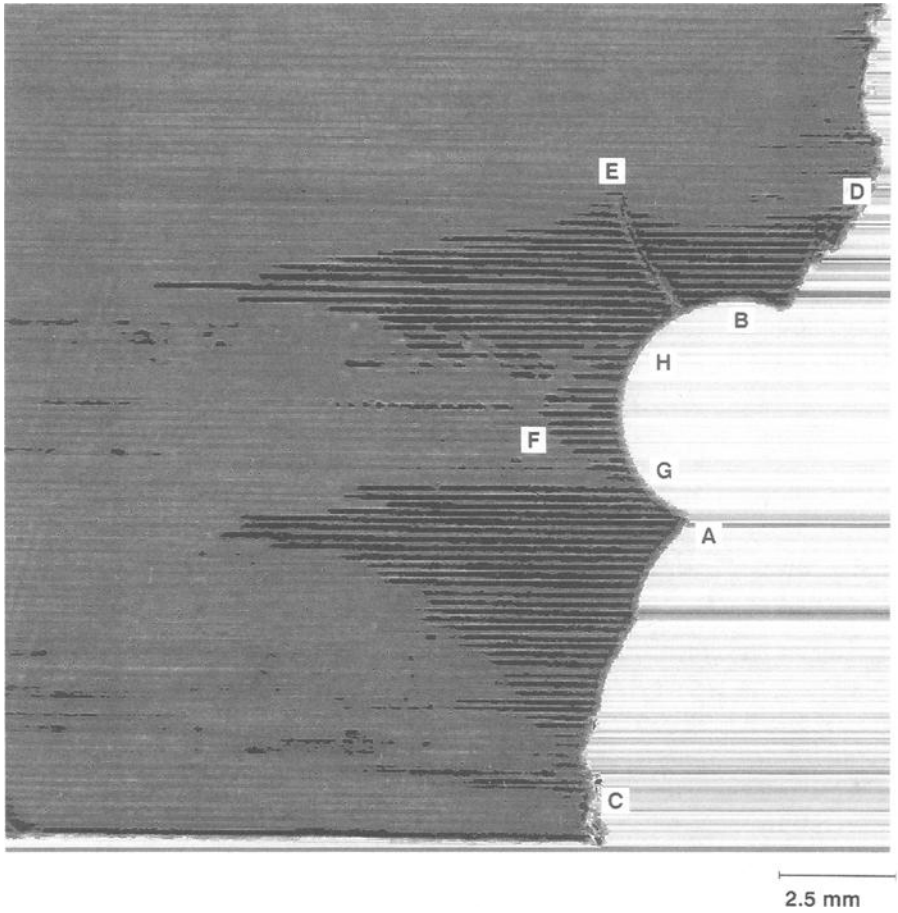

FIG. 3—*The SAM image of a Ti-15Mo-3Nb-3Al-0.2Si (weight percent) specimen after an isothermal (650°C) fatigue test (1.82×10^5 cycles).*

was subjected to 14 612 thermomechanical cycles over 36 days (0.0056 Hz). Further details of the test configuration can be found in the literature [*18*].

The first indication of the presence of an extensive zone of damage associated with the dominant matrix cracks was evidenced by a conventional "glass reflector plate" C-scan of the specimen [*18*]. Glass reflector plate technique [*21*] is a global method and provides the accumulated macro-damage in the entire thickness of the specimen. A well-defined damage zone was seen in the C-scan and prompted a further micro-evaluation of the area using SAM. Figure 4*a* shows the SAM image of the specimen. The image clearly shows the two dominant cracks, A and B (also visible on the surface to the naked eyes), growing from the tip of the notch. However, the ultrasonic SAM image shows a host of other features which provide invaluable information about the elevated temperature behavior as well as the degradation and failure mechanisms due to the combination of elevated temperature, applied stresses, presence of oxygen, and the duration of exposure.

The effects of the stress, temperature, and duration of exposure to elevated temperature can be seen clearly in Fig. 4*a*. The image is labeled to show seven zones, 1 through 7. Also, cracks are labeled A through D. In zone 1, where the effect of stress is gradually increasing toward the notch tip, the interface shows corresponding increasing lengths of degradation. The interfacial degradation and damage at the tip of the notch (zone 2) show a sudden increased length indicating that the stress in the first continuous fiber and the total time of exposure to elevated temperature have a devastating combined effect on the integrity of the interface. At zone 3 where the matrix crack tip is growing, the pointed shape of the interfacial oxidation followed by "parabolic" growth of the damage profile indicates that at the crack tip, the interfacial damage is not instantaneous. Zones 4 and 5 are cracks growing from the site of spot welds used to secure control thermocouples. The zones show similar crack and interfacial damage mechanism as zones 1, 2, and 3. In addition, the areas labeled 6 and 7 on Fig. 4*a* show the process where interfacial damage from zone 4 as well as zone 5 are

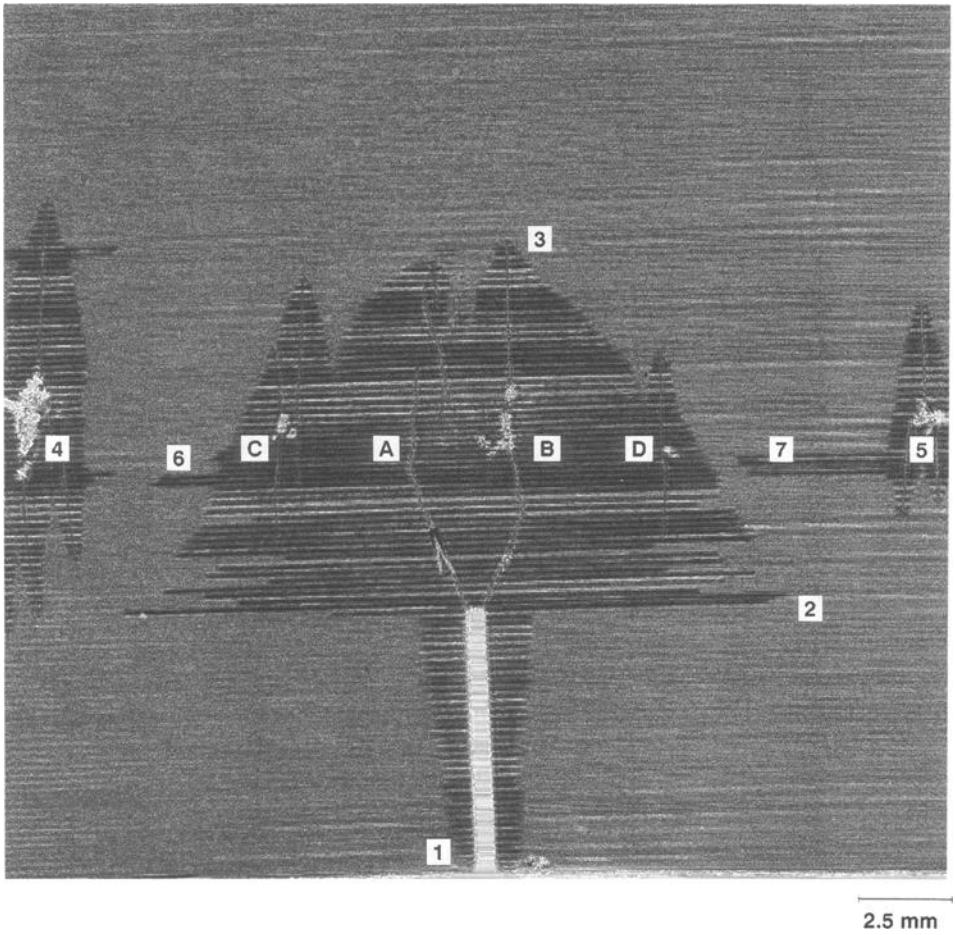

FIG. 4*a*—*The SAM image of a Ti-15Mo-3Nb-3Al-0.2Si (weight percent) specimen after the specimen was subjected to 14 612 thermomechanical cycles over 36 days (0.0056 Hz).*

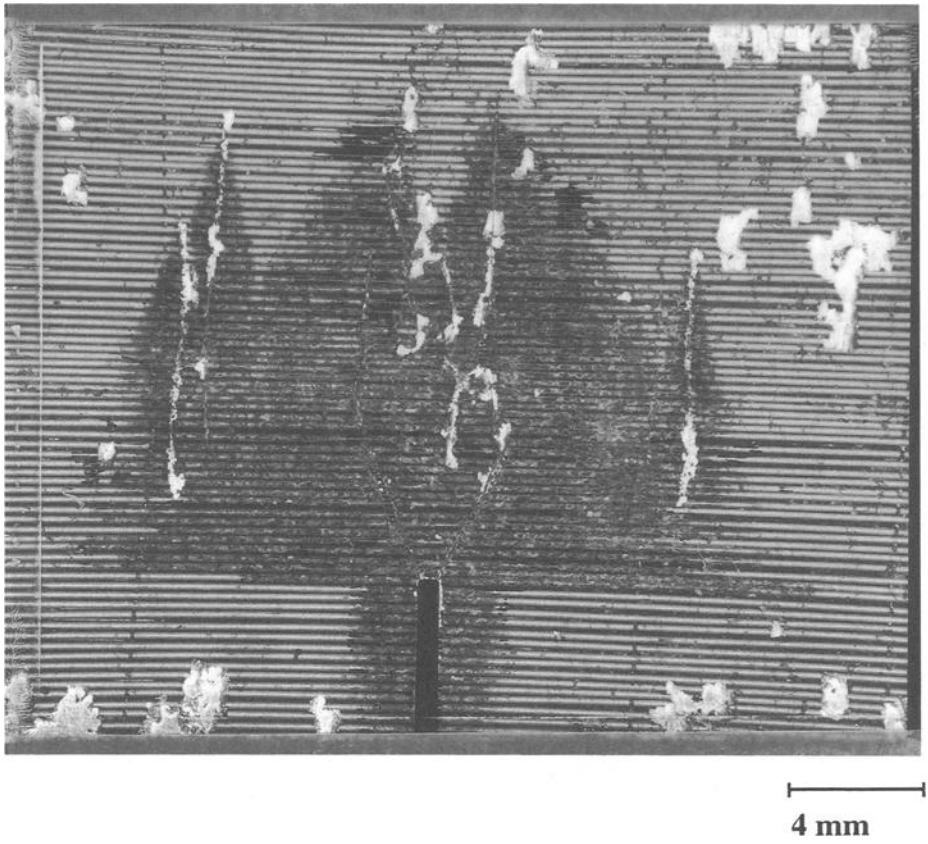

FIG. 4*b*—*Metallography of specimen in Fig. 4*a.

approaching the interfacial damage from cracks A, B, C, and D (C and D are cracks growing from unintentional weld spots on the surface). This behavior indicates that similar growth and merging behavior around cracks A, B, C, and D has resulted in the large mushroom shaped interfacial degradation and damage zone around the slot and the cracks.

Following the same procedure used for Specimen 1, the matrix was etched away to expose the first layer of fibers that were scanned (Fig. 4*b*). The photomicrograph in Fig. 4*b* shows a high degree of correlation with the SAM image. An examination of the etched specimen under the optical microscope revealed that the first layer of fibers showed a pattern of darkened fiber coatings that exactly matched the ultrasonic signature from the SAM. Closer inspection of the fiber coatings under a scanning microscope showed severe coating spalling in the darkened region. The coatings in the unaffected zone showed little damage, and what damage was visible was thought to be caused by the etching solution. The same effect of stress in the continuous fibers on the extent of damage was similar to that found in Specimens 1 and 2. The extent of fiber coating damage was greatly increased where the fibers were continuous (load carrying) and exposed to the environment due to matrix cracking. The stress-free fiber ends along the notch exhibited much less environmentally assisted damage along the fiber/matrix interface than the load carrying fibers left in the wake of the advancing

crack tip. It is important to note here that, at termination of the experiment, the crack tip was growing at a rate of approximately 0.1 mm during every 6 days. Thus, most of the interfacial degradation imaged by SAM is also seen by metallography, perhaps because of the extended duration of environmental exposure due to the slow crack growth rate of about 0.00069 mm/h.

Specimen 4: SCS-6/Ti-6Al-2Sn-4Zr-2Mo

A TMF crack growth test was conducted [*22*] on a four-ply unidirectional composite of Ti-6Al-2Sn-4Zr-2Mo matrix reinforced with silicon-carbide, SCS-6, fibers. The crack was grown perpendicular to the fiber and loading direction. The specimen, a single-edge notch (SE(T)) with clamped ends [*20*], was 25.07 mm wide and 0.83 mm thick with the initial EDM notch length equal to 7.481 mm. The specimen was subjected to a constant P_{max} throughout the test of 4.0 kN at an R of 0.1 in-phase with a thermal cycle between 150 and 538°C. In-phase means that the maximum load and maximum temperature occur at the same time during each cycle. The test frequency was 0.00833 Hz.

Figure 5 shows the SAM image of the specimen after 35 733 cycles were applied. The image clearly shows the two cracks, which are also visible to the naked eye, growing from the tip of the notch. Each crack has an average projected crack length of 8.9 mm. The distinct ultrasonic feature (dark areas) evident around the EDM notch and to a greater extent around the cracks indicates possible environment degradation of the carbon rich fiber-matrix

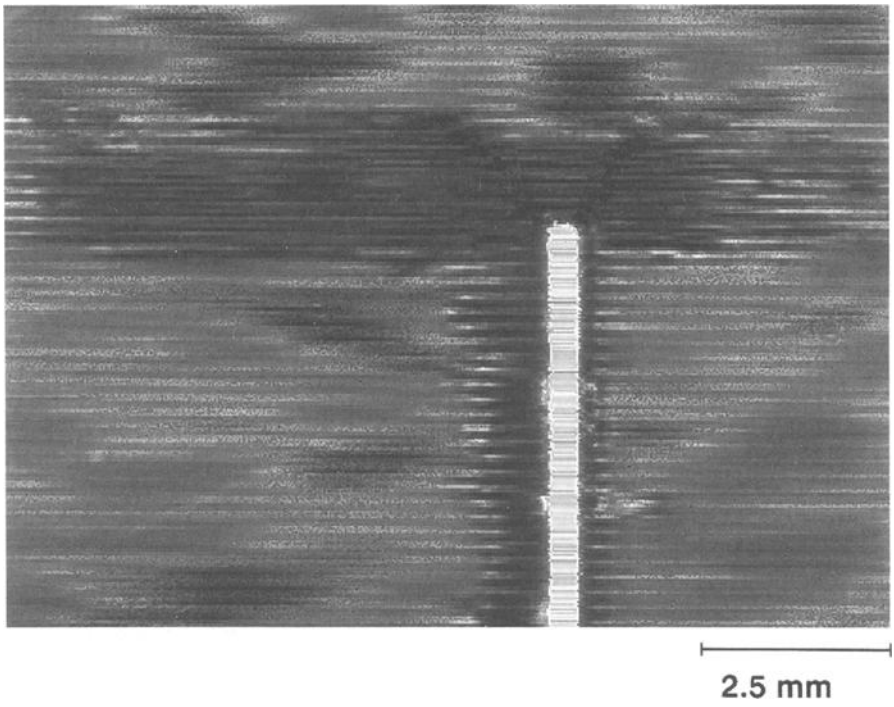

FIG. 5—*The SAM image of a SCS-6/Ti-5Al-2Sn-4Zr-2Mo specimen after 35 733 cycles at 0.00933 Hz.*

interfacial region. To confirm this, the matrix was etched away using a saturated solution of tartaric acid in 10% bromine in methanol. A visual inspection of the first layer of fibers after matrix removal showed a pattern of darkened fiber coatings that exactly matched the ultrasonic signature from the SAM.

Specimen 5: SCS-6/Ti-24Al-11Nb

In a recent investigation [*16*], the initiation and fatigue crack growth rates of cracks emanating from circular holes were investigated in an eight-ply, unidirectional layup of SCS-6/Ti-24Al-11Nb. Constant amplitude fatigue crack growth tests were conducted at a wide range of stress levels at a constant R equal to 0.1. In the investigation, it was found that cracks initiate at four locations around the hole very early in the fatigue life. Crack bridging by unbroken fibers was found to dominate the fatigue crack growth life as evidenced by the characteristic decrease in crack growth rates as the crack length increased during fatigue cycling. The SAM technique was applied to a specimen from this investigation to observe the matrix damage and evaluate the characteristics of a fully bridged matrix crack. The specimen was rectangular in shape with a width of 12.5 mm, length of 150 mm, and had a 3.2 mm diameter hole machined in the center. They were subjected to 1.01×10^5 cycles at a maximum remote applied stress of 580 MPa at a frequency of 1 Hz. The fatigue loading direction was in the direction of the fibers with reference to Fig. 6.

Figure 6 shows the SAM image of a typical specimen after fatigue cycling at room temperature. It is clear from the figure that the primary cracks grew radially from the notch but turned to follow a direction perpendicular to the loading axis within a distance of one radius of the hole. Some secondary cracking can be seen near the primary cracks although these cracks formed later in the fatigue life and did not appear to participate in the final fracture. The locations of the fibers in the first layer can be seen easily as well as the location of a crossweave binder material used to hold the fibers in place during consolidation.

Discussion

The results from SAM imaging as well as metallography of Specimens 1 through 5 provide some very interesting and intriguing insight into the behavior and failure mechanisms of titanium based metal matrix composites with SCS-6 fibers. The results indicate, especially at elevated temperatures, that a chain of events occurs leading to eventual failure of the composites. The various events and the mechanisms observed will be discussed further with reference to each specimen tested and evaluated here.

The invaluable information that can be obtained from SAM in specimens tested at elevated temperatures is demonstrated clearly in Figs. 2 to 5. The interfacial degradation and damage evident in Fig. 2*c*, Fig. 3, Fig 4*a*, and Fig. 5 were also corroborated by metallography. It is evident from the combination of SAM image and metallography that the extent of fiber coating damage was greatly increased where the fibers were continuous (load carrying) and exposed to the environment due to matrix cracking. The fiber ends exposed along the notch did accumulate some damage along the fiber-matrix interface but to a much lesser extent because they were in a stress free condition. This phenomenon in combination with larger damage near high stress areas such as the notch tips and hole circumference indicates that (1) when the stresses are negligible at the edge of the specimen, the interfacial degradation and damage is minimum even though the fiber/matrix interface was exposed to the temperature cycling during the entire duration of testing, and (2) the interfacial degradation is related directly to the fiber and matrix stresses which increase near the notch tip.

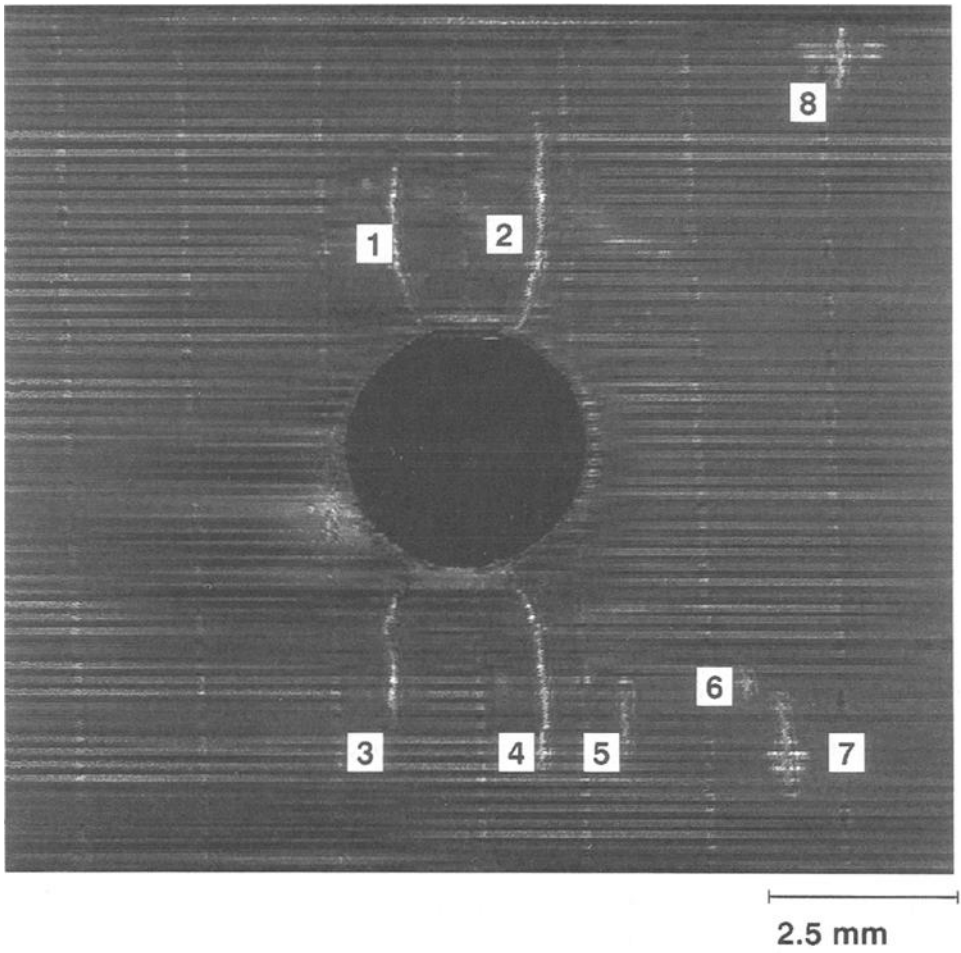

FIG. 6—*The SAM image of a SCS-6/Ti-24Al-11Nb (atomic percent) specimen after room temperature.*

It is apparent from the results that the crack tip merely provides access for environmental damage to attack the interface and that ahead of the crack tip no noticeable environmental damage occurs. Once the interface is exposed to the environment of elevated temperature and stresses, the interfacial degradation proceeds as indicated by the boundaries of the interfacial damage behind the crack tip. Thus, the relative size of the affected regions indicates that the extent of damage is related to the magnitude of the local stress level and the duration of exposure to elevated temperature. The stress level dependence is indicated by the relative size of the affected zones at the edge of the notch (a high stress region) when compared to the size at the top of the hole (a relatively low stress region). The time dependence is evidenced by a region near the crack tip where no fiber damage is indicated by the SAM. In this region, where the crack growth has occurred most recently, insufficient time has passed for the environment to be detrimental. Fibers which have been exposed to the environment later in life by the advance of the crack are affected less than fibers which were exposed early in life by the hole.

The utility of SAM for the assessment of room temperature fatigue behavior of SCS-6/Ti-24Al-11Nb composite can be seen from Fig. 6. The SAM technique can easily detect primary cracking in the composite which normally can also be easily observed visually on the surface. However, the SAM also detects the presence of secondary cracking which is not always as evident as the primary cracks.

Conclusions

Scanning acoustic microscopy has been shown to provide an invaluable insight into the fatigue crack growth behavior of titanium based metal matrix composites with SCS-6 fibers. The elastic waves produced by the SAM transducer are very sensitive to the local changes in elastic properties of the interfacial region. As a result, the technique is capable of detecting the onset of and monitoring the growth of interfacial damage, especially at elevated temperature.

The behavior of titanium based MMC's with SCS-6 fibers at both room temperature and elevated temperature has been analyzed in this study by conducting SAM analysis at room temperature. The results obtained from both SAM and metallography have provided invaluable information regarding the initiation and progress of interfacial damage. It has been found that the initiation of matrix cracking provides the necessary passage for the environment to reach the interfacial region. However, it has been shown that the environmental access alone is not sufficient for an accelerated interfacial degradation because it appears from the specimens in this study that temperature, stress, and duration of exposure are the three necessary factors for the degradation phenomenon to progress to maturity when most of the exposed interfacial region will be damaged.

Acknowledgment

We would like to thank Mr. Jeffrey A. Fox of the University of Dayton Research Institute for his prompt software support without which timely completion of this paper would not have been possible.

References

[1] Harmon, D. and Saff, C., "Metal Matrix Composites: Testing, Analysis, and Failure Modes," *Damage Initiation and Growth in Fiber Reinforced Metal Matrix Composites, ASTM STP 1032,* E. W. S. Johnson, Ed., American Society for Testing and Materials, Philadelphia, 1988, pp. 237–250.

[2] Marshall, D. B., Cox, B. N., and Evans, A. G., "The Mechanics of Matrix Cracking in Brittle-Matrix Fiber Composites," *Acta Metallurgica*, Vol. 33, No. 11, 1985, pp. 2013–2021.

[3] McCartney, L. N., "Mechanics of Matrix Cracking in Brittle-Matrix Fibre-Reinforced Composites," *Proceedings of the Royal Society, London*, Vol. A409, 1987, pp. 329–350.

[4] Karpur, P., Matikas, T. E., Krishnamurthy, S., and Ashbaugh, N., "Ultrasound for Fiber Fragmentation Size Determination to Characterize Load Transfer Behavior of Matrix-Fiber Interface in Metal Matrix Composites," *Review of Progress in Quantitative NDE,* D. O. Thompson and D. E. Chimenti, Eds., La Jolla, CA, 19–24 July 1992, Vol. 12B, 1992, pp. 1507–1513.

[5] Karpur, P., Matikas, T. E., and Krishnamurthy, S., "Matrix-Fiber Interface Characterization in Metal Matrix Composites Using Ultrasonic Imaging of Fiber Fragmentation," *Seventh Technical Conference on Composite Materials, Mechanics and Processing,* America Society of Composites, Pennsylvania State University, University Park, PA, Vol. 1, 1992, pp. 420–427.

[6] Matikas, T. E. and Karpur, P., "Matrix-Fiber Interface Characterization in Metal Matrix Composites Using Ultrasonic Shear-Wave Back-Reflection Coefficient Technique," *Review of Progress in Quantitative NDE,* D. O. Thompson and D. E. Chimenti, Eds., La Jolla, CA, 19–24 July 1992, Vol. 12B, 1992, pp. 1515–1522.

[7] Quate, C. F., Atalar, A., and Wickramasinghe, H. K., "Acoustic Microscopy with Mechanical Scanning—A Review," *Proceedings of the IEEE*, Vol. 67, Aug. 1979, pp. 1092–1114.

[8] Lemons, R. A. and Quate, C. F., "A Scanning Acoustic Microscope," *IEEE Ultrasonics Symposium*, 1973, pp. 18–21.

[9] Briggs, G. A. D., *An Introduction to Scanning Acoustic Microscopy*, Microscopy Handbooks, Oxford University Press, Royal Microscopical Society, Oxford, UK, Vol. 12, 1985.

[10] Briggs, G. A. D., *Acoustic Microscopy*, Oxford University Press, Oxford, UK, 1992.

[11] Lawrence, C. W., Briggs, G. A. D., Scruby, C. B., and Davies, J. R. R., "Acoustic Microscopy of Ceramic-Fibre Composites; Part I: Glass-Matrix Composites," *Journal of Materials Science*, Vol. 28, 1993, pp. 3635–3644.

[12] Lawrence, C. W., Briggs, G. A. D., and Scruby, C. B., "Acoustic Microscopy of Ceramic-Fibre Composites; Part II: Glass-Ceramic-Matrix Composites," *Journal of Materials Science*, Vol. 28, 1993, pp. 3645–3652.

[13] Lawrence, C. W., Briggs, G. A. D., and Scruby, C. B., "Acoustic Microscopy of Ceramic-Fibre Composites; Part III: Metal-Matrix Composites," *Journal of Materials Science*, Vol. 28, 1993, pp. 3653–3660.

[14] Bertoni, H. L., "Rayleigh Waves in Scanning Acoustic Microscopy," *Rayleigh-Wave Theory and Application*, E. A. Ash and E. G. S. Paige, Eds., The Royal Institution, London, Vol. 2, 1985, pp. 274–290.

[15] Liang, K. K., Kino, G. S., and Khuri-Yakub, B. T., "Material Characterization by the Inversion of V(z)," *IEEE Transactions on Sonics and Ultrasonics*, Vol. SU-32, No. 2, 1985, pp. 213–224.

[16] Jira, J. R. and Larsen, J. M., "Fatigue of Unidirectional SCS-6/Ti-24Al-11Nb Composite Containing a Circular Hole (Part II)," companion paper submitted to *Metallurgical Transactions A*, Carnegie Mellon University, Pittsburgh, PA (Metallurgical Transactions), 1993.

[17] John, R., Jira, J. R., Larsen, J. M., and Ashbaugh, N. E., "Fatigue Crack Growth in Unidirectional SCS-6/Ti-24Al-11Nb Composite Containing a Circular Hole (Part II)," companion paper submitted to *Metallurgical Transactions A*, Carnegie Mellon University, Pittsburgh, PA (Metallurgical Transactions), 1993.

[18] Blatt, D., Karpur, P., Stubbs, D. A., and Matikas, T. E., "Observations of Interfacial Damage in the Fiber Bridged Zone of a Titanium Matrix Composite," *Scripta Metallurgica et Materialia*, Vol. 29, 1993, pp. 851–856.

[19] Buynak, C. F., Moran, T. J., and Martin, R. W., "Delamination and Crack Imaging in Graphite-Epoxy Composites," *Materials Evaluation*, Vol. 47, April 1989, pp. 438–447.

[20] Blatt, D., John, R., and Coker, D., "Stress Intensity Factor and Compliance Solutions for a Single Edge Notched Specimen with Clamped Ends," submitted to *Engineering Fracture Mechanics*, 1993.

[21] Krautkramer, J. and Krautkramer, H., *Ultrasonic Testing of Materials*, Springer-Verlag, New York, 1990.

[22] Blatt, D., "Fatigue Crack Growth of Metal Matrix Composites Under Thermomechanical Loading," Ph.D. thesis, Purdue University, West Lafayette, IN, Dec. 1993.

William F. Schmidt,[1] *Otto H. Zinke,*[2] *and Seifollah Nasrazadani*[3]

Characterization of a Crack in an Aluminum Bar Using an AC Magnetic Bridge

REFERENCE: Schmidt, W. F., Zinke, O. H., and Nasrazadani, S., **"Characterization of a Crack in an Aluminum Bar Using an AC Magnetic Bridge,"** *Special Applications and Advanced Techniques for Crack Size Determination, ASTM STP 1251*, J. J. Ruschau and J. K. Donald, Eds., American Society for Testing and Materials, Philadelphia, 1995, pp. 147–163.

ABSTRACT: A hairline crack was introduced in a 27.9 cm long by 7.62 cm wide by 1.3 cm thick (11 by 3 by 0.5 in.) 6061-4 aluminum specimen by repeated bending. The size of the crack was limited by stopping the bending at the initial stage of crack formation. Measurements were then made using an AC magnetic bridge which detected the presence of the crack and enabled characterization of its form. The extent, the orientation, and the depth from the surface along the crack length were obtained from the measurement. This paper outlines the principle of the bridge operation and details related to interpreting the output from the bridge as the bridge is moved over the surface of the aluminum specimen. Verification of the bridge measurements was made by destructive evaluation of the specimen using a scanning electron microscopic examination.

KEYWORDS: fatigue crack, magnetic bridge, flaw location, nondestructive testing, electromagnetic testing

A fatigue crack which was produced by bending a 1.27-cm thick 6061-4 aluminum bar has been examined electromagnetically through the use of a modified AC magnetic Wheatstone bridge [*1*]. In other uses such as measuring the strain from applied stress [*2,3*], the thickness of metal coatings plated to metals [*4*], and corrosion-type losses in simulated aircraft seams [*5*], the bridge response either exceeds or equals the sensitivity of electromagnetic examination through eddy-current coils. Woodward [*6*] has shown that at liftoffs (gap between the bridge and test surface) of less than 0.001 mm, the unusual pole structure of the bridge gives rise to scanning patterns through which both the thickness and depth of saw cuts in a material can be determined simultaneously. Woodward also applied the bridge to a fatigue crack produced in a compact-tension specimen and was able to measure crack growth. Woodward's measurements were based on offnull operation of the bridge, that is, the bridge was nulled on a nonflawed section of the specimen, and the offnull voltages produced by the flaws were measured.

This work differs from Woodward's in two respects: a larger value of liftoff was used, and renull measurements were made. In renull measurements the resistances and capacitances which are required to renull the bridge for each measurement are recorded and converted into real and imaginary reluctance changes through equations given next. Both real and

[1] Professor and department head, Mechanical Engineering Department, University of Arkansas, Fayetteville, AR 72701.

[2] President, International Validators, Inc., 807 N. Jackson, Fayetteville, AR 72701.

[3] Assistant professor, Mechanical Engineering Department, University of Arkansas, Fayetteville, AR 72701.

imaginary reluctance yield predictions for the location of the flawed region although the predictions seem to differ slightly. The imaginary reluctance results seem particularly rich in detail and may contain information pertinent to determining the location of the crack tip. A one-to-one relation between real and imaginary reluctance variations and the characteristics of flaws in a material requires a large amount of research involving destructive evaluation of test specimens. The work presented is a first effort. However, since real reluctance generally depends on the energy stored in magnetic fields (which, in turn, determines the geometrical configuration of the fields) and imaginary reluctance generally depends on the dissipation of energy (which depends in part on the conductivity of the specimens), it can be assumed that real reluctance variations occur, primarily, because of flaw geometry and imaginary reluctance depends, primarily, on changes in conductivity. Possibly, this is the result of cold working or other grain boundary movement produced in or near a flaw.

Finally, an attempt was made to calculate crack depth by assuming that the flaw observed was a simple crack and that the depth of it could be calculated by calibration using fine saw cuts. The calibration assumption implies that an extrapolation can be made to crack widths which cannot be seen due to residual stress. A simple cubic polynomial fit was made to the saw cut data and then applied to the data obtained from the current specimen. The results for the depth based on using the calibration curve and those found by destructive measurement were remarkably close in value.

Measurement Techniques—Magnetic Bridge

Since modified AC magnetic bridges are not in general usage, a brief description of the operation, construction, and method of use is given. The bridge is schematized in Fig. 1,

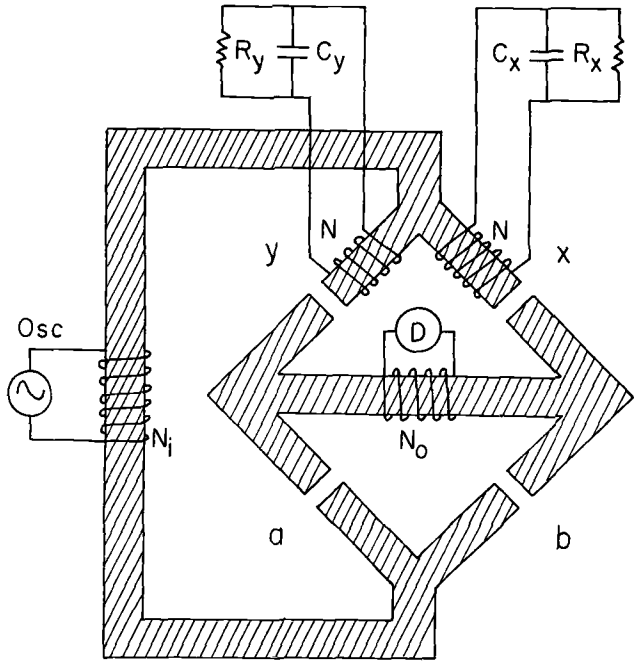

FIG. 1—*Schematic of AC magnetic bridge.*

where the hatched area is ferrite. An oscillator (Osc) provided 100 milliamps input at 500 Hz. The number of turns (N_i) on the input leg of the bridge and the number of turns (N_o) on the output leg were both 200. Coils of 120 turns also appear on the arms of the bridge designated x and y, respectively. Resistances R and capacitances C attached to these arms allow the adjustment of the real and imaginary reluctances in the arms of the bridge and thus allow the bridge to be nulled in much the same way that an AC electrical bridge is nulled. Zinke and Schmidt [7] have shown that changes in real reluctance *Re* and imaginary reluctance *Im* can be related to changes in R and C in a particular arm of the bridge as follows

$$\Delta Re = N^2\omega^2\,\Delta C \tag{1}$$

$$\Delta Im = -N^2\omega/\Delta R \tag{2}$$

where N equals the number of turns and ω is the frequency.

In the construction of the bridge, arms a and b are ground to be as geometrically identical as possible. The assumption is then made that the complex reluctance of gap a is equal to the complex reluctance of gap b, and bridge equations coupled with Eqs 1 and 2 are used to determine the changes of real and imaginary reluctances produced by variations in the test specimens. For balancing, a compensating piece of specimen material is sometimes placed in the y gap. In these experiments, no compensating specimen was placed in the y gap, that is, the y gap was empty. Italicized quantities will be used here to represent complex quantities.

The complex reluctances of the empty x and y gaps will be designated R_{ex} and R_{ey}, respectively. These assumptions immediately lead to the expression

$$R_s = R_{ex} - R_e \tag{3}$$

where R_s is the complex reluctance of the specimen and R_e is the measured complex reluctance. The bridge is first nulled with no specimen in either gap, and the values of resistance (R_{rx} or R_{ry}) and capacitance (C_{rx} or C_{ry}) necessary to null the bridge are recorded. The bridge is then nulled with the test specimen, and the values R_{sx} or R_{sy} and C_{sx} or C_{sy} are recorded. Under these circumstances R_e is given by the following expression

$$R_e = N\omega^2(C_{sy} - C_{ry} - C_{sx} + C_{rx}) + iN^2(-1/R_{sy} + 1/R_{ry} + 1/R_{sx} - 1/R_{rx}) \tag{4}$$

where i is the square root of -1. Equation 4 is rewritten as

$$R_e = Re + iIm \tag{5}$$

with *Re* and *Im* the real and complex parts of the reluctance.

All reluctance values presented here are measured values and are in units of megaamperes/weber, the most convenient unit for work done with the AC magnetic bridge.

The basic AC magnetic bridge described previously is modified through the inclusion of a piece of conducting copper inserted in each gap in such a manner that the flux in the gap is converted completely into fringing flux for better specimen access. In fact, the bridge is made of two ferrite pieces glued to opposite sides of a single piece of copper as shown in Fig. 2. The locations of the coils shown in Fig. 1 are indicated in Fig. 2. If the bridge did not have extensions on the x and y arms, it could be pictured as two ferrite H's, one crossed on the other on opposite sides of the copper insert which is cut flush with each gap face.

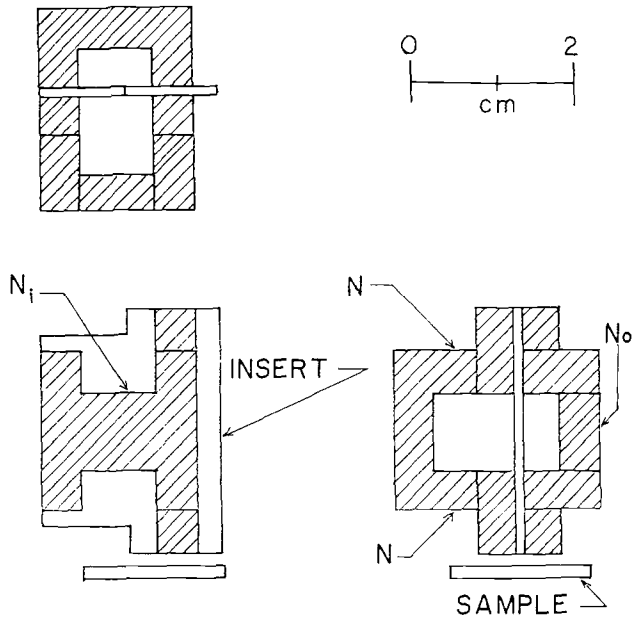

FIG. 2—*Construction of modified AC magnetic bridge showing insert and position of specimen.*

The gap face is in a plane which is parallel to the specimen surface indicated in Fig. 2. The two poles present faces to the specimen which are 0.48 by 0.48 cm. The copper insert is 0.056 cm thick. Note that the magnetic field produced by this gap face has a preferred direction in which the field lines are perpendicular to the plane of the copper insert. In this respect it differs from magnetic fields produced by eddy-current coils. For these experiments, the plane of the insert was oriented so that it crossed the fatigue crack at approximately right angles, that is, the magnetic field was parallel to the gap. This will be called a "parallel scan" which is a reversal of Woodward's notation where "parallel" and "perpendicular" referred to the relative directions of the insert and the flaw.

Zinke and Schmidt [*8*] have carried out some approximate calculations of the strength of magnetic fields in the vicinity of the insert which show that they are quite large, larger than those which would be expected from eddy-current coils, because of the concentrating effect of the insert. Further, measurements showed that the magnetic fields arise from a very small fraction of the area of the gap face, a fraction which is in a strip which is parallel to the insert.

Test Procedure

A drawing of the test specimen containing the induced fatigue crack is shown in Fig. 3. The crack in the specimen [*8*] was produced through bending and was initiated using an EDM notch which was later milled away. In an attempt to develop a calibration for flaw depth and width, four 0.0254-in. wide saw cuts were made in the specimen on the side opposite the fatigue crack at roughly 9, 11.5, 16.3, and 19.3 cm. The 19.3-cm saw cut was at 45 degrees and was not used in these studies. The saw cuts at 9, 11.6, and 16.3 cm were 0.635, 0.159, and 0.381 cm deep, respectively. These cracks were used to calibrate the real

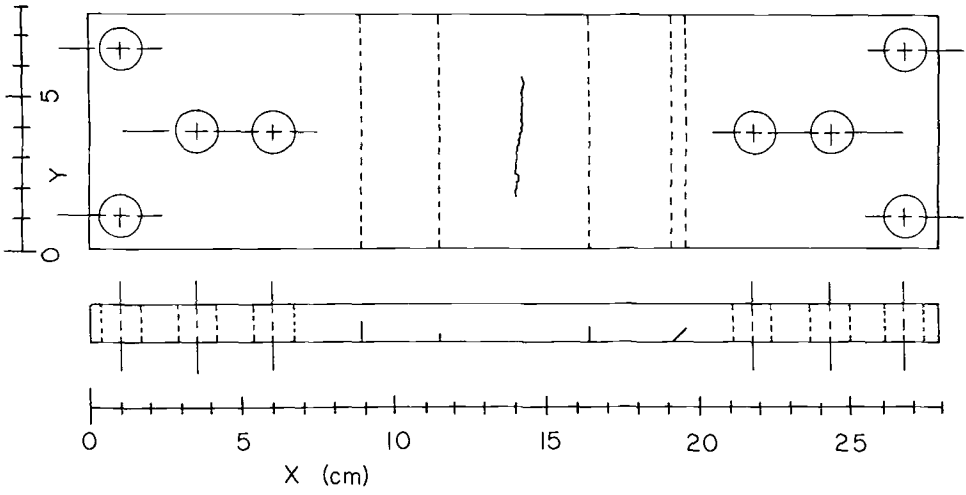

FIG. 3—*Aluminum 6061-4 specimen showing flaw position and saw cuts.*

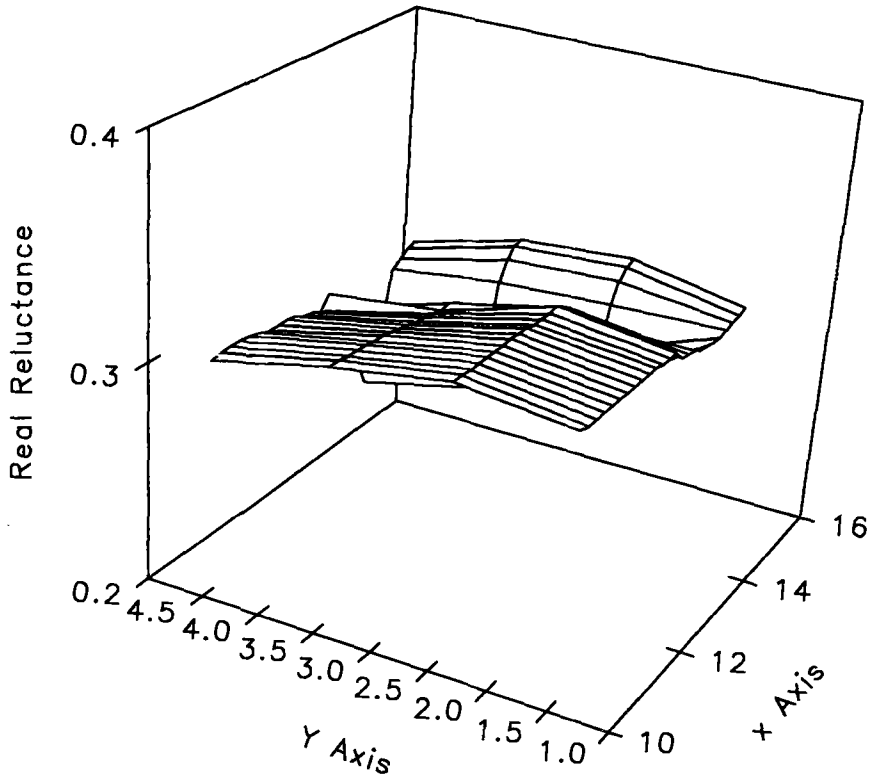

FIG. 4—*Real-reluctance coarse scan results.*

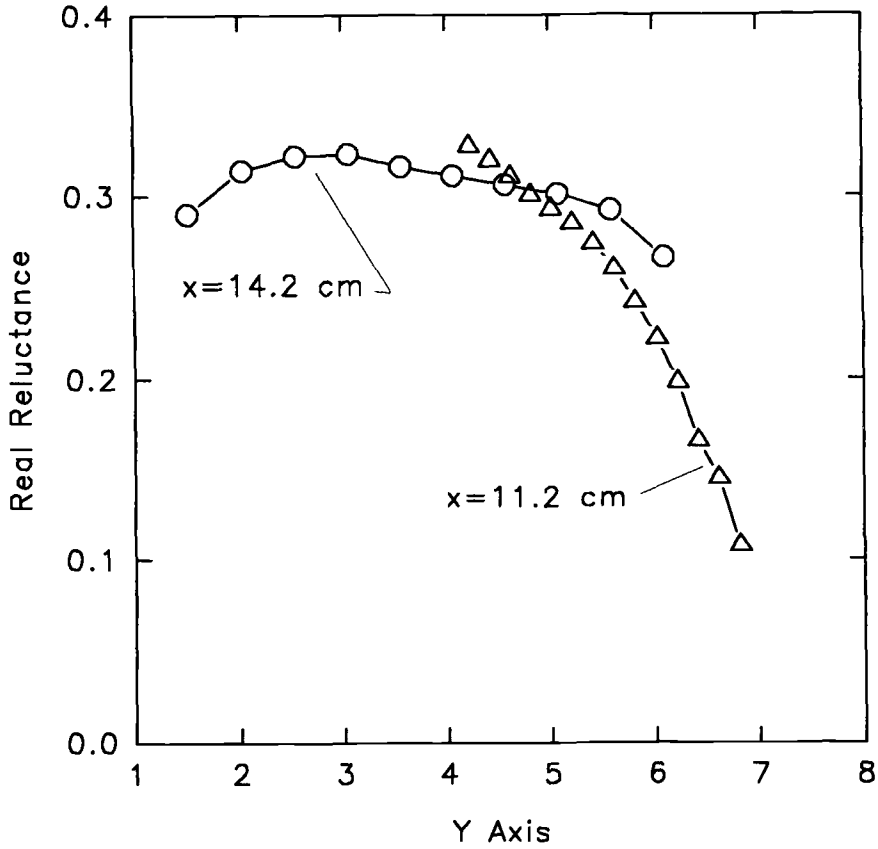

FIG. 5—*Edge effect on flaw side of specimen* (circles) *and opposite side of specimen* (triangles).

reluctance of Eqs 4 and 5. Directions of x and y, now corresponding to the specimen rather than to the bridge arms, are shown in Fig. 3. The location of the fatigue crack as determined from results using the magnetic bridge is indicated at approximately x = 14.1 cm where only a small portion of it between y = 4 cm and y = 4.5 cm was visible to the unaided eye.

The flaw and the saw cuts were both scanned along the x-direction at 0.2-cm intervals on the y-axis and 0.051-cm intervals on the x-axis unless otherwise indicated. The liftoff for the scans was 0.01 cm, which was obtained by placing a precision plastic film between the bridge and the specimen. All scans were parallel scans.

After the specimen was scanned with the bridge, sections were cut for examination by optical techniques. An ISI 40 scanning electron microscope (SEM) using a 30 KeV beam and Unitron Versamet photomicrographic microscope were used. Two cuts in the y direction were made at x = 12.75 cm and x = 15.25 cm to produce a 2.5 cm wide section of the specimen. These cuts were necessary in order to allow placement in the SEM vacuum chamber. The surface of this 2.5-cm wide section was then examined. Internal cross sections of the 2.5-cm section were exposed by cutting this reduced specimen at y = 3.73, 4.06, and 4.57 cm using a Buehler ISOMET™ 11-1180 low speed precision saw with a 12.7 cm (5

in.) diameter diamond saw (series 20HC) having a 0.4 mm thickness. After cutting, the surfaces were sanded and then polished using a solution containing 0.3μ Al_2O_3 and a rotational speed of 125 rpm for a billiard cloth-covered polishing wheel. The polished cross sections were then examined using both the SEM and optical microscope.

Results

Initial results using the bridge were obtained by a coarse scan of the specimen from x = 10.3 cm to x = 15.1 cm for values of y of 1.52, 2.54, 3.56, and 4.57 cm to determine both the location of any flaws and the reaction of the bridge in unflawed regions of the specimen. The real reluctance from this set of scans is shown in Fig. 4. Note that the crack causes a downward trend in the real reluctance and that while the real reluctance is relatively constant in the x direction in the unflawed part of the scan, there is a downward trend at smaller and larger values of y. This trend occurs because of the sensitivity of the real reluctance to the edge of the specimen; the same sensitivity which should cause the bridge to be effective in the detection of flaws. The edge effect is illustrated in Fig. 5. The open circles are results obtained at x = 14.2 cm and y varying from 1.52 cm to 6.10 cm in 0.508-cm intervals. The specimen was then turned over and scanned at x = 11.2 cm with y varying from 4.22 cm to 6.82 cm in 0.2 cm increments. The results of this scan appear as triangles on Fig. 5. The open-circle scan has the same profile as seen in the unflawed section in Fig. 4. However, the real reluctance as represented by the triangles decreases by more than 60% between y =

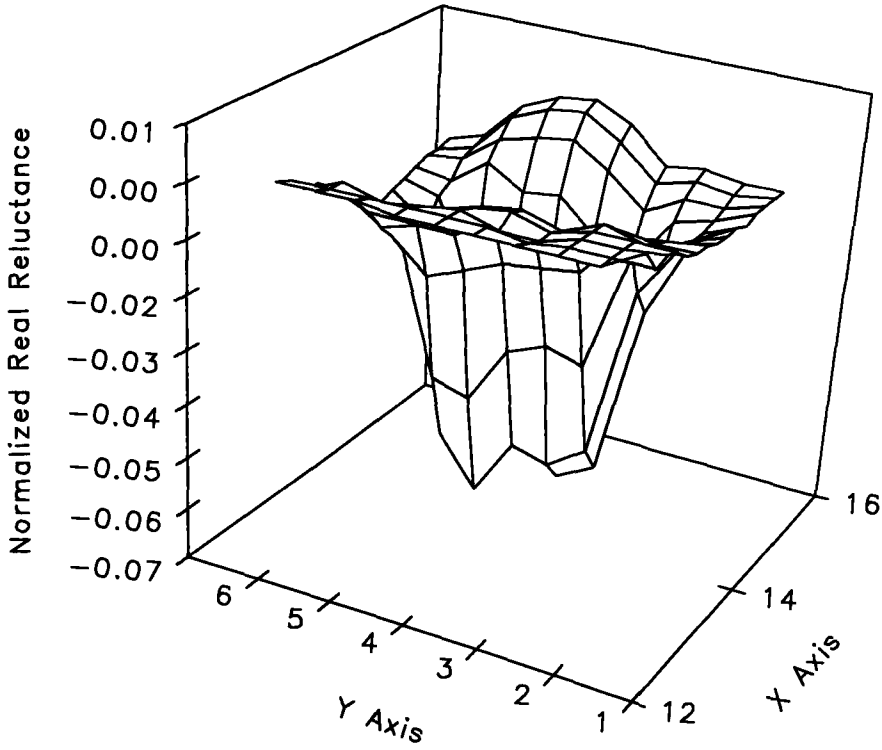

FIG. 6—*Normalized real-reluctance variations in the region of the flaw.*

4.22 and 6.82 cm, about 0.8 cm from the edge of the specimen illustrating the influence of the edge. The imaginary reluctance demonstrated a decrease of about 16% in the same interval, and that decrease occurred principally for values of y greater than 5.25.

The coarse scan indicates the existence of a flaw or abnormality in the material near the line $x = 14$ cm. Therefore, the specimen was scanned between $x = 12.1$ cm and $x = 15.1$ cm at constant y-values from 1.52 cm to 6.10 cm in 0.5 cm increments. Due to the edge effect on the real reluctance, each curve was normalized by subtracting the value of the reluctance at $x = 12.3$ cm for each y measurement. A three-dimensional plot of the variation of the normalized real reluctance over the crack appears as Fig. 6. A similar plot for the normalized imaginary reluctance appears as Fig. 7. The real reluctance shows a downward excursion except for a positive hump for larger x parts of the scan and central values of y. The imaginary reluctance exhibits a very interesting behavior in that while it is positive for the central part of the flaw, at each end of the flaw a negative excursion appears. It is possible that this negative excursion is characteristic of conditions near the crack tip. Figures 8 and 9 display the individual scans associated with the three-dimensional plots of Figs. 6 and 7. The existence of a flaw near the central region at $x = 14$ cm is very evident from the figures.

Parallel scans were used to inspect this specimen because the definition of the bridge in the y direction is better in the parallel scan than in the perpendicular scan. A crack had been observed in the y direction. The scans were to establish the spatial extent of the flaw in the y direction. Since the magnetic field issues from the gap face very close to the insert, then with a parallel scan the magnetic field of the bridge in the y direction is of the order of 0.2

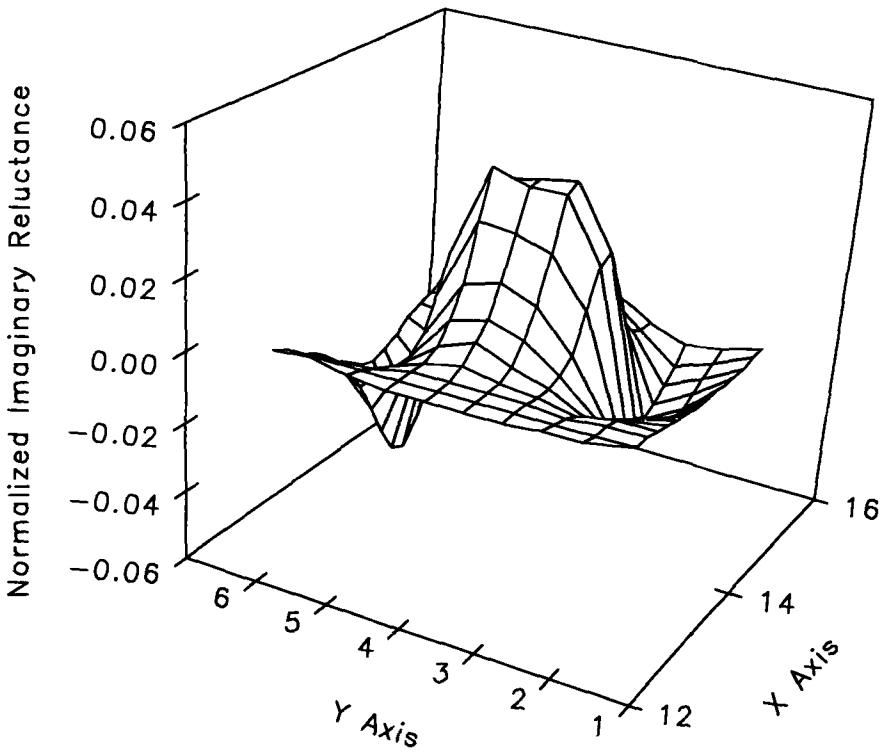

FIG. 7—*Normalized imaginary-reluctance variations in the region of the flaw.*

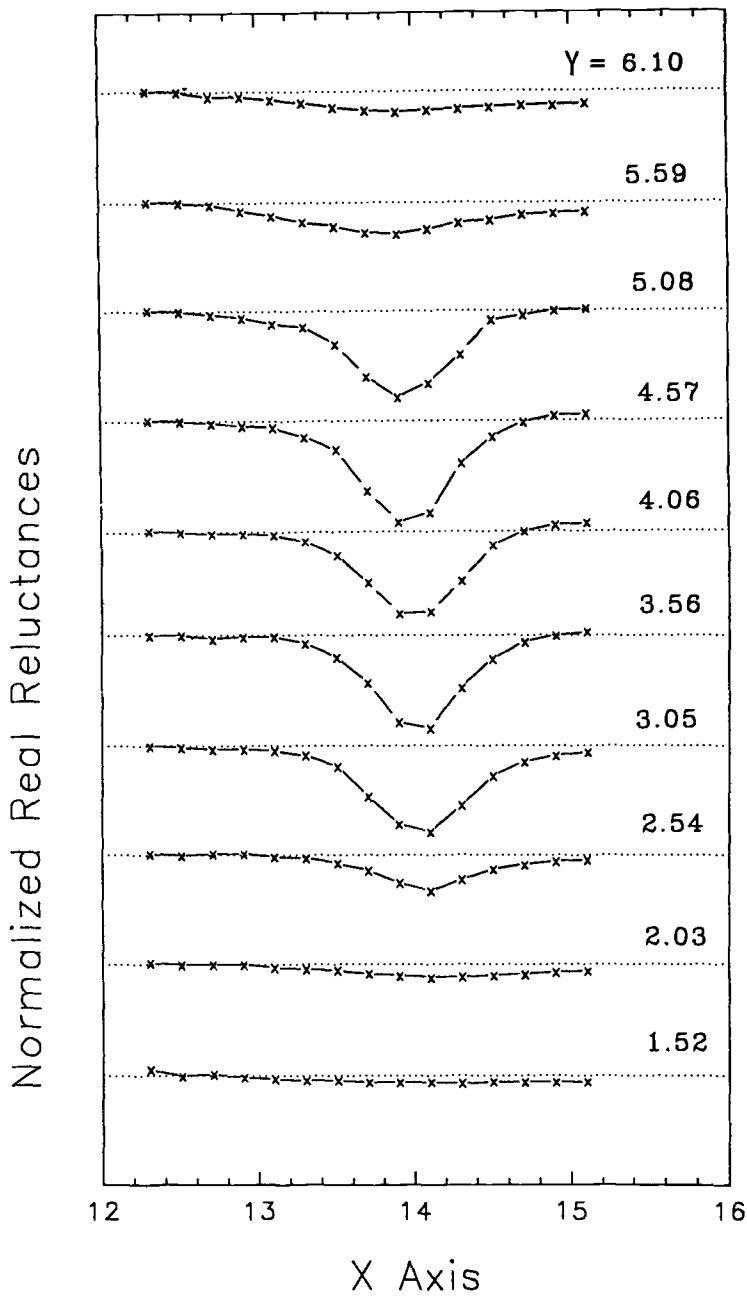

FIG. 8—*Individual scans of normalized real reluctance at constant values of* y.

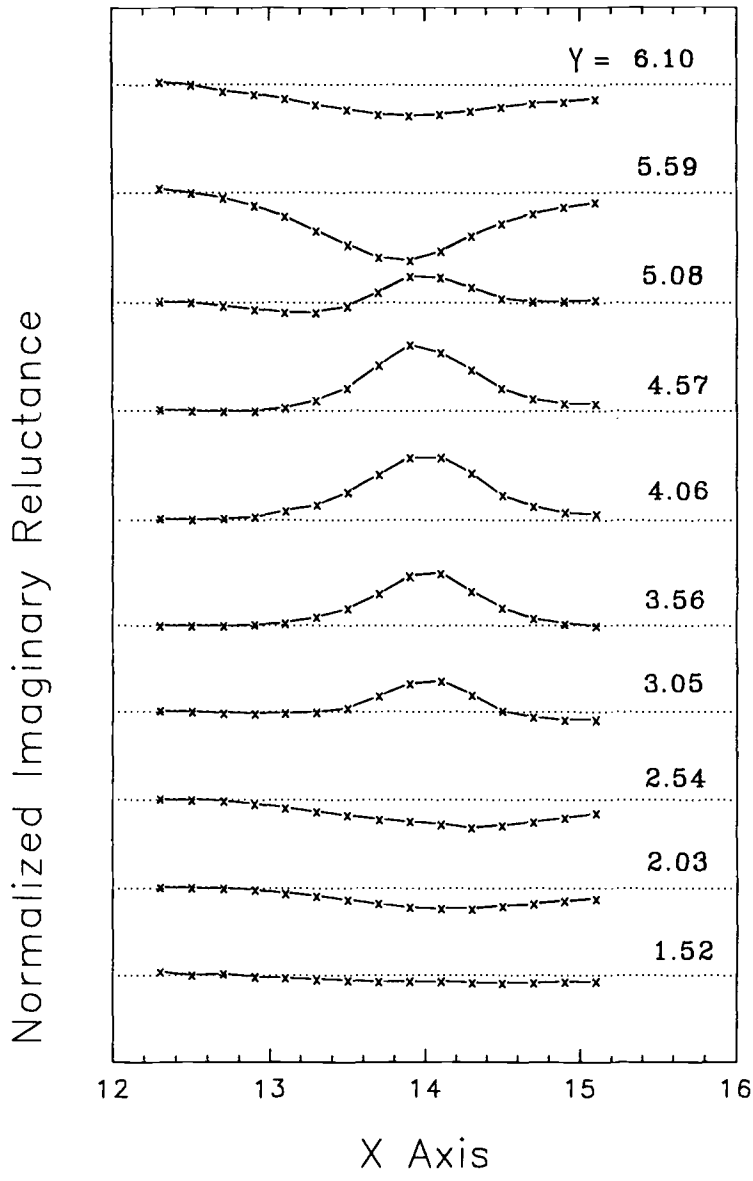

FIG. 9—*Individual scans of normalized imaginary reluctance at constant values of* y.

plus or minus 0.1 cm for the insert used in this work. Thus, the y representations in Figs. 6 through 9 are probably very accurate. It is clear from the normalized real reluctance curves of Fig. 8 that the flaw, whatever it is, extends minimally from $y = 2.54$ to 5.59. The normalized imaginary reluctance curves indicate that the flaw or other abnormality may extend about 0.5 cm past that predicted by the real reluctance. Inspection of the three-dimensional plot of Fig. 7 indicates that this extension is in the area where the excursion of the imaginary

reluctance is negative, that is, where the reaction of the bridge is atypical of the region in which a flaw is thought to exist.

The imaginary reluctance has positive excursions in the center of the flawed area indicating that the conductivity in this region is less than the unflawed aluminum. However, at both ends of the flawed regions there are negative excursions indicating an increased conductivity of the metal in this region. There are two possible explanations for this effect. One of these is that metal deformation produces a change in liftoff in this region. The other explanation is that there is actually a change in conductivity of the metal at the ends of the flawed area.

The lift-off explanation requires that the liftoff at the end of the flawed regions be reduced. Deformations of the metal could account for this if the metal in this region were raised above the surrounding metal. Lift-off work done with thick aluminum specimens indicates that the deformations would have to protrude at least 0.25 mm above the surrounding metal. Such protrusions would appear in the examination of the specimen with a microscope, and none were noticed. Further, in the studies cited in Ref *6* the deformations at the end of the flawed areas were below the surrounding surface rather than above it.

In Ref *9* was noted that the directional resistance as measured with the modified bridge changed with direction of measurement on rolled shim stock indicating that grain orientation may affect conductivity. Plasticity effects and resulting residual stresses at the ends of the flawed area offer a possible explanation since this may increase the conductivity. Increasing

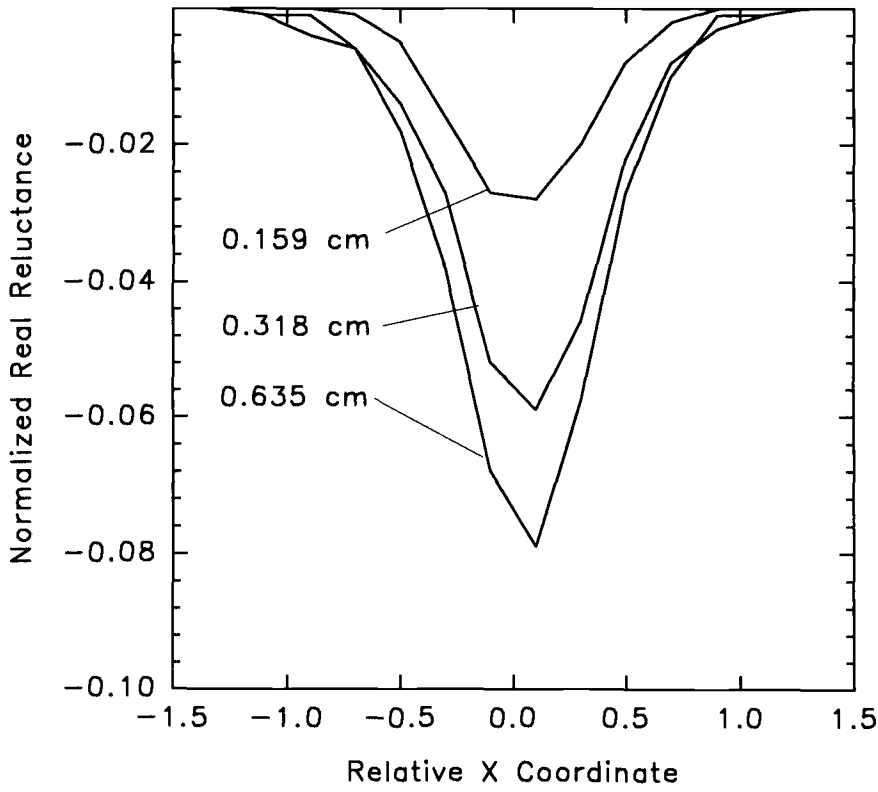

FIG. 10—*Calibration curves of normalized real reluctance over the 0.025-cm wide saw cuts.*

the definition of the bridge through the use of the parallel scan has the undesirable effect of decreasing the definition in the x direction. From Fig. 2, it can be seen that a length of the gap amounting to one side of the pole faces passes over the flaw in the x direction. That length is 0.48 cm and coupled with expected edge effects (if the crack is well defined), the width of the scanning peak in the x direction should be somewhat greater than that.

How much edge effect a well-defined flaw could add can be answered by examining the real reluctance curves for the saw cuts placed in the specimen. The normalized real-reluctance curves shown in Fig. 10 were taken over three 0.025-cm saw cuts which were (from the bottom peak to the top) 0.635, 0.318, and 0.159-cm deep. Measurements were made at constant y = 3.81 cm from 1.5 cm before the cut to 1.5 cm following the cut along the x-axis. The half-width of all three of these curves was about 0.7 cm. The same is true of normalized imaginary reluctance curves taken at the same time. Thus, the edge effect does not appear to increase with depth of cut. But this is somewhat larger than the 0.48 cm which was expected. The average of all the half-widths of the curves for real reluctance in Fig. 8 is 0.65 cm with a standard deviation of 0.01 cm. The average of all the half-widths of the positive imaginary reluctance curves is 0.65 with a standard deviation of 0.1 cm. The average of all the half-widths of the negative curves of the imaginary reluctances of Fig. 9 is 1.45 with a standard deviation of 0.3. Four of these curves have a half-width of 1.6 cm and the

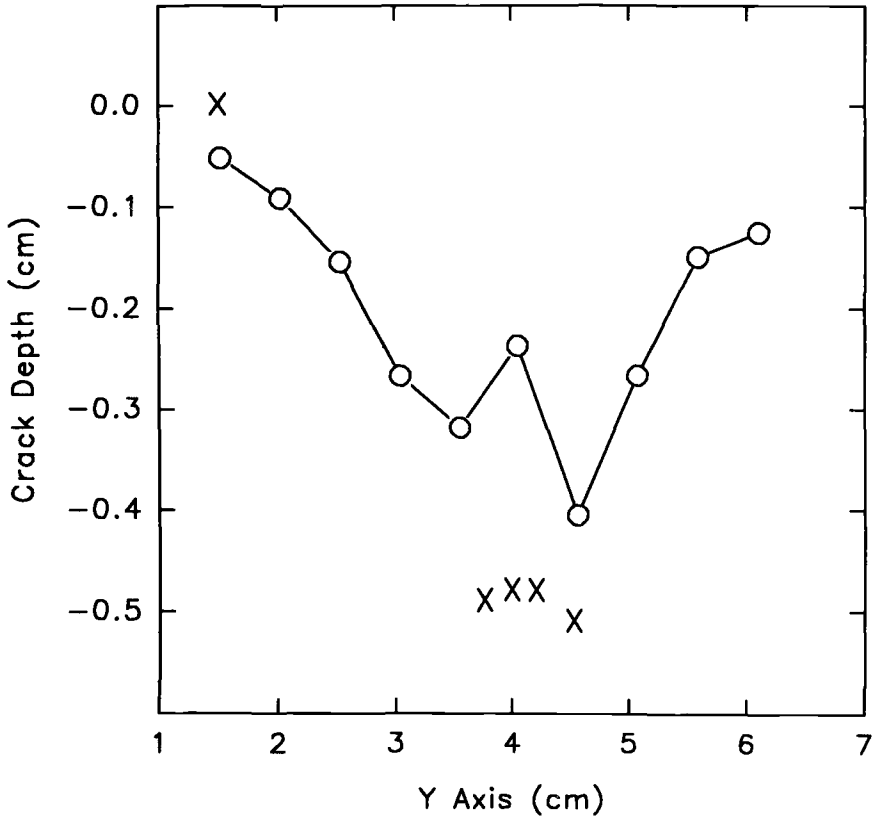

FIG. 11—*Calculated crack depth along the indicated flaw and measured values* (x's).

fifth, which reduces the average, is somewhat asymmetric. This is another indication that the negative excursions are indicative of some physical phenomenon which differs greatly from that which produces the positive peaks of the imaginary reluctance.

A simplistic approach was used to calibrate the reluctance peaks for depth of crack, assuming that there was a well-defined crack. The peaks of Fig. 10 produced a calibration curve as follows

$$D = 3.777\ Re_m - 32.682\ (Re_m)^2 - 130.93\ (Re_m)^3 \tag{6}$$

Here, D is the depth of the saw cut in centimeters, and Re_m is the maximum of the real reluctances exhibited in Fig. 10. This curve was applied to the profile of the maxima of the real reluctances in Fig. 8. The first six points having a maximum are at $x = 14.1$ cm, and the last four are at $x = 13.9$ cm. From Eq 6 and the maxima of Fig. 8 a depth profile was calculated which is shown in Fig. 11. Also shown are measured crack depths found as outlined in the following text.

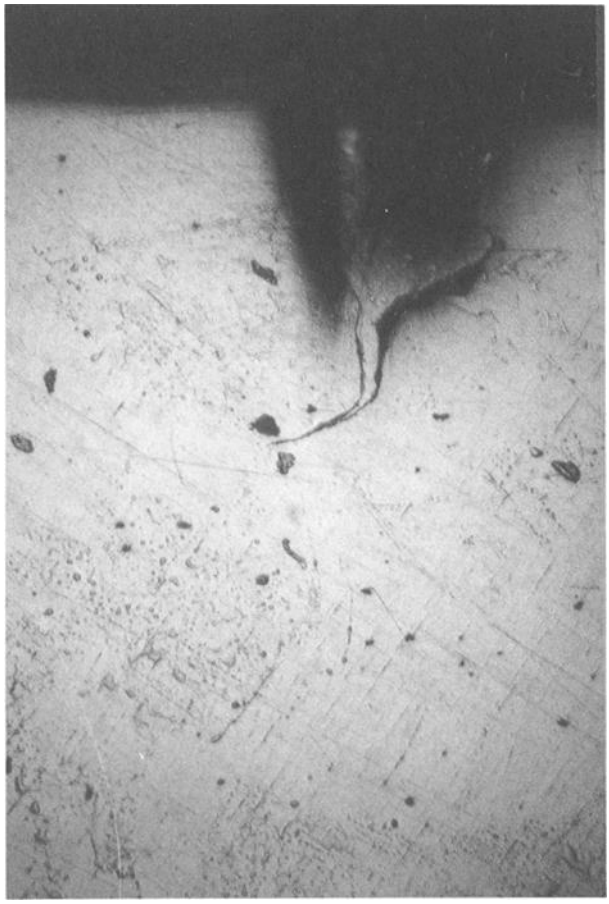

FIG. 12—*Test specimen cross section at* y = *4.1 cm prior to opening crack. The shallow visible crack intersects the surface at* x = *13.9 cm* (×*100*).

At this stage in the investigation the test specimen was cut to allow microscopic examination. The first area of observation was the surface of the specimen near $x = 13.9$ cm for various y-values. There were two noticeable characteristics on the surface. The major morphological feature was the existence of raised sections of material forming the flaw. Nearby, approximately 0.075 mm in the positive x-direction, was a second flaw which appears to be the first stages of the formation of another raised section. The existence of this second flaw line may account for the unexpectedly large values of the half-widths in the real reluctance mentioned earlier.

After surface examination the 2.5 cm wide section was cut along the $y = 1.5$, 3.7, 4.1, and 4.6-cm lines to expose inside surfaces of the specimen. Each of these exposed surfaces was polished and examined using both the SEM and optical microscopes. In addition, the top surfaces of the two thin sections from $y = 3.7$ to 4.1 cm and from $y = 4.1$ to 4.6 cm were polished and examined. These top surfaces revealed the existence of a tightly closed crack which appeared as a fine line at magnifications of $\times 1000$. There was also a small notch shaped (a portion of the raised section observed on the surface) flaw near the edge $y = 4.1$ cm on the section cut at $y = 3.7$ cm. Figure 12 shows a microphotograph of the

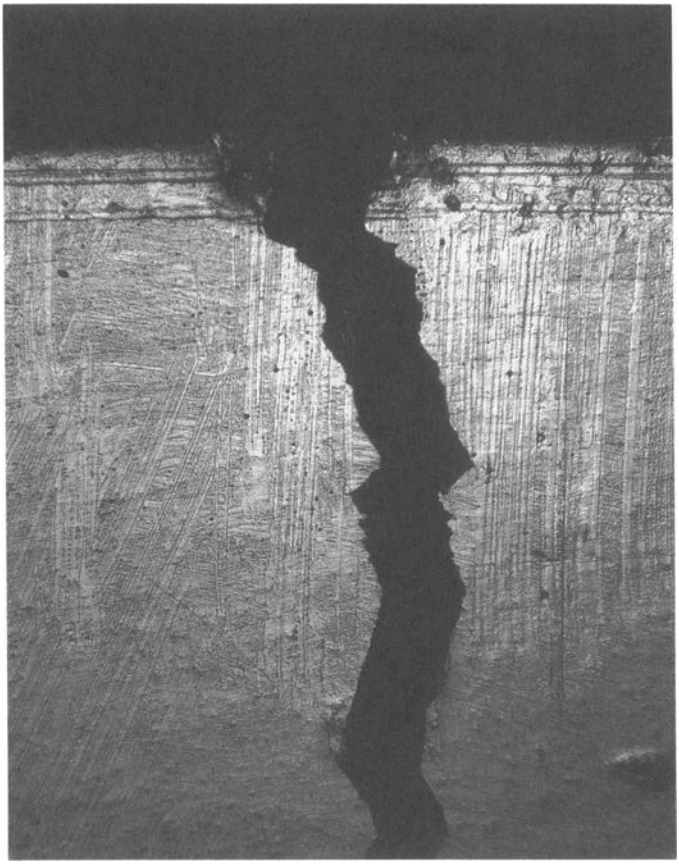

FIG. 13—*Test specimen cross section at* y = *4.1 cm after opening the crack. The crack intersects the surface at* x = *13.9 cm* (×*50*).

side face of this section (y = 4.1 cm). As can be seen, a shallow crack is visible. This crack came from both sides of the notched area on the top surface. The dark shadows are the result of the triangular shaped section being slightly out of the plane of the remainder of the surface. The triangular shape again helps to explain the larger half-widths mentioned earlier.

The side faces of the polished specimens at y = 3.7, 4.1, and 4.6 under ×1000 magnification showed a fine jagged line which was believed to be a crack. To determine the extent of the crack 0.6 cm of the bottom surface was milled off from each section to provide a thinner cross section which could be bent to open a crack if one existed. Once the bottom portion was removed the small section was bent by holding each end in one's hand. This bending made visible the crack in the section. Figure 13 shows the same side surface at ×50 following the bending as was shown in Fig. 12. The small triangular shaped section is on the left side in the photograph. The crack extended to a depth of 0.48 cm.

Figure 14 shows the top surface of the section between y = 4.1 and 4.6 cm at ×50 after bending. The crack is very evident, and its location agrees with the magnetiç bridge scans shown in Fig. 8. A side view of this section at y = 4.1 cm is shown at ×50 in Fig. 15. The depth of this crack was 0.48 cm.

FIG. 14—*Test specimens surface between* y = *4.2 and 4.6 cm after opening the crack. Edge of the crack at bottom of photograph is at* x = *13.9 cm* (×*50*).

FIG. 15—*Test specimen cross section at* y = *4.6 cm after opening the crack. The crack intersects the surface at* x = *14.0 cm* (×*50*).

The bottom portion of the section between $y = 0$ and 1.5 cm was also milled to remove 0.6 cm of material. Bending of this thinner section into the plastic range using mechanical force did not reveal any indication of a crack which, again, agrees with the results of the magnetic bridge scans shown in Fig. 9. The measured crack depths for the sections which were bent to open the crack are shown by the "x" in Fig. 11. The results of the measured depth agree well with those computed using the empirical relationship based on saw cuts.

Conclusions

The magnetic bridge successfully determined the location and extent of a fatigue crack in the test specimen. The existence and location were verified by destructive evaluation and microscopic examination. The depth of the crack was predicted using saw cuts to develop a calibration curve for the bridge. The simple calibration scheme was surprisingly successful. Using the calibration curves, crack depths were predicted which were within 30% of the actual depth located in the destructive verification.

The results of this paper show that the bridge has the advantage of testing, in a simple manner, the existence of cracks as well as providing an estimate of the depth. The bridge is a simple device which is easy to use requiring minimal instrumentation. Due to the nature of the field produced by the bridge, it can for equal size devices, provide a higher resolution than eddy-current devices. Unfortunately, there is not a standard test specimen which is used to compare results of various techniques. The authors are currently in the process of proposing a study which would compare results of several techniques with all measurements being conducted on the same set of test specimens. We are particularly interested in comparing them to several of the eddy-current techniques in use.

The results show that a large amount of information is contained in the output from the magnetic bridge. However, a large amount of work remains in order to relate the bridge output to a detailed description of the flaw in the material.

Acknowledgments

We are very grateful to Charles Salkowski, NDT Laboratory, NASA, Johnson Space Center, Houston, Texas, for this specimen. The authors would also like to thank the reviewers for the helpful suggestions regarding the destructive evaluation. Their remarks lead to the process used to determine the actual crack depths.

References

[1] Zinke, O. H., U.S. Patent No. 4,901,017, 13 Feb. 1990.

[2] Zinke, O. H. and Schmidt, W. F., "Measurement of Stress with AC Magnetic Bridges," *Review of Progress in Quantitative Nondestructive Evaluation*, Vol. 8, pp. 2051–59, D. O. Thompson and D. E. Chimenti, Eds., Plenum Press, New York, 1989.

[3] Schmidt, W. F. and Zinke, O. H., "Response of Tensile and Bending Specimens Using an AC Magnetic Bridge," *Review of Progress in Quantitative Nondestructive Evaluation*, Vol. 11, D. O. Thompson and D. E. Chimenti, Eds., Plenum Press, New York, 1992, pp. 1163–1168.

[4] Zinke, O. H. and Derby, R. W., "Nondestructive Measurements of Plating Thicknesses of Copper and Nickel on Shim Stock and of Nickel on Steel," *Review of Progress in Quantitative Nondestructive Evaluation*, Vol. 11, D. O. Thompson and D. E. Chimenti, Eds., Plenum Press, New York, 1992, pp. 1953–1958.

[5] Zinke, O. H. and Schmidt, W. F., "Modified AC Magnetic Bridge Scanning Patterns of Samples Simulating Flaws in Aircraft Seams," *Review of Progress in Quantitative Nondestructive Evaluation*, Vol. 12, D. O. Thompson and D. E. Chimenti, Eds., Plenum Press, New York, 1993, pp. 1885–1890.

[6] Woodward, M. R., "Detection and Characterization of Fatigue Damage in 6061-T6 Aluminum Using the Magnetic Bridge Sensor," a thesis submitted in partial fulfillment of the requirements for the degree of Masters of Science, Department of Mechanical Engineering, University of Arkansas, Fayetteville, AR 72701.

[7] Zinke, O. H. and Schmidt, W. F., "Linear AC Magnetic Circuit Theory," IEEE Transactions on Magnetics, Vol. 29, 1993, pp. 2207–2212.

[8] Schmidt, W. F. and Zinke, O. H., "Reluctance Variation as a Result of Lift Off for an AC Magnetic Bridge," *Review of Progress in Quantitative Nondestructive Evaluation*, Vol. 12, D. O. Thompson and D. E. Chimenti, Eds., Plenum Press, New York, 1993, pp. 1885–1890.

[9] Zinke, O. H. and Derby, R. W., "Nondestructive Measurements of Plating Thicknesses of Copper and Nickel on Shim Stock and of Nickel on Steel," *Review of Progress in Quantitative Nondestructive Evaluation*, Vol. 11, D. O. Thompson and D. E. Chimenti, Eds., Plenum Press, New York, 1992, pp. 1953–1958.

ISBN 0-8031-2003-6